Groeien met Groen Staal

EXMENTE

Reducing Electric Furnace Material Physical Property Infrastructure

Theory Manual

2025-12-17

Revision 5

Document Purpose

The purpose of this manual is to empower readers to pursue new innovations in the field of pyrometallurgical material property modelling by equipping them with knowledge and understanding of the models available in auxi-mpp.

Target Audience

This user manual is intended for the Groeien met Groen Staal (GGS) consortium involved in developing new Reducing Electric Furnace (REF) technologies, particularly the Theme II partners. It guides users through the underlying theory the material physical property models in auxi-mpp is based on.

The Theme II partners include process, metallurgical, chemical, and mechanical engineers from Tata Steel Netherlands, along with PhD students and their supervisors from TU Delft, TU Eindhoven, and the University of Twente.

Document Overview

The manual is divided into four parts.

Part I (Executive Summary) provides an overview of the purpose, contents, and outcomes of this manual. Part II (Slag Material Properties) covers the theory and validation of the models that describe slag physical properties. Part III (Liquid Alloy Material Properties) covers the theory and validation of the models describing liquid alloy physical properties. Similarly, Part IV (Gas Material Properties) covers the theory and validation of the models describing gas physical properties. Finally, Part V (Appendices) contains definitions of terms and abbreviations used throughout the document.

Disclaimer

This Report has been prepared for the purpose set out in the brief provided to Ex Mente by GGS by Groeien met Groen Staal: WP-II.6 (GGS) and was not prepared for any third party or for any other purpose than that detailed in the engagement terms with GGS.

The contents of this document relate specifically to the project referenced herein, and Ex Mente cannot accept responsibility for use of the contents of this document other than for its intended purpose.

The information contained in this document is current as of the date of the Report, and may not reflect any event or circumstance which occurs after the date of the Report. The opinions contained herein are expressed in good faith and whilst every care has been taken in preparing this Report in accordance with standards of engineering practice (customary in the engineering profession for services of a similar nature), Ex Mente shall not, in any event, be liable for any indirect or consequential damages, including, without limitation, loss of profit or interruption of business arising from the recipient's use of this document or the contents hereof.

Document Identification

Distribution Statement	
Project Label **Project Name**	NLG-176-603 Material Data Framework
Document Name **Document Number** **Release Date**	Reducing Electric Furnace Material Physical Property Infrastructure - Theory Manual NLG-176-603-DOC-1228 Rev. 5 2025-12-17
Compiled For	Groeien met Groen Staal: WP-II.6 Contact person: Vinod Dhiman Tel.: +31 (0)251 49 35 62 E-mail: Vinod.Dhiman@tatasteeleurope.com
Compiled By	Ex Mente Technologies (Pty) Ltd Postal address: P.O. Box 10214, Centurion, 0046, SOUTH AFRICA Tel.: +27 87 808 1903 E-mail: info@ex-mente.co.za Website: www.ex-mente.co.za

Document Authorisation

Release	Name	Signature
Author	Stefan Koning	Stefan Koning Digitally signed by Stefan Koning Date: 2025.12.17 16:47:45 +02'00'
Reviewer	Dr Johan Nell	Johan Nell Digitally signed by Johan Nell Date: 2025.12.17 16:31:42 +02'00'
Approver	Dr Johan Nell	Johan Nell Digitally signed by Johan Nell Date: 2025.12.17 16:31:54 +02'00'

Document History

Revision	Release Date	Description
Rev. 5	2025-12-17	Fourth formal release to GGS.
Rev. 4	2025-12-10	
Rev. 3	2025-11-27	
Rev. 2	2025-09-17	Third formal release to GGS.
Rev. 1	2025-07-01	Second formal release to GGS.
Rev. 0	2025-02-18	First formal release to GGS.
Draft 1	2025-02-14	Draft 1 release for internal review.

Contents

List of Figures

List of Tables

Part I

Executive Summary

Chapter 1

Introduction

The pyrometallurgy industry plays an important role in the global economy but faces growing challenges that demand innovative solutions. These challenges include stricter environmental regulations, such as the EU's target of a 30% reduction in CO_2 emissions by 2030, alongside the rising global demand for high-grade steel and increased reliance on lower-quality ores due to the depletion of high-grade resources. Consequently, traditional Blast Furnace-Basic Oxygen Furnaces (BF-BOFs) must be replaced with more efficient smelting technologies, such as the proposed REF process unit, to help the industry adapt.

Innovation requires advancements in existing tools, particularly in pyrometallurgy. There is a growing need to describe processes more fundamentally through improved material property models, process models, and multiphysics models. These improved models can assist the industry in developing new REF process units more quickly and cost-effectively.

This manual supports the GGS Theme II partners in developing new REF processes with well documented theory on material property models. The property models documented here are implemented in an open-source python package called auxi-mpp. This manual therefore gives the theoretical background and insight necessary to arrive at better innovations using the models available in auxi-mpp.

Chapter 2

Focus

This iteration of the manual describes physical property models for slags and liquid alloys. The covered properties include density (molar volume), viscosity, and electrical conductivity for both material types, as well as diffusivity for slags and thermal conductivity for liquid alloys.

Future versions will expand to include material physical property models for gases, single pellet, and multiphase materials like pellet beds, all accessible through auxi-mpp.

The models take temperature, pressure, composition, and for multi-component models also phase constituent activities, as inputs. The underlying theory for each property model is explained to help readers understand its operation and the specific component systems for which it is valid. The models have been validated against extracted model and experimental data to demonstrate accurate implementation in auxi-mpp.

Chapter 3

Highlights

3.1 Slag Material Properties

Density Model (Thibodeau): The Thibodeau density model, which estimates slag density via molar volume, has been successfully implemented in auxi-mpp. This model is fundamentally based on the structural Q-species concept, accounting for variations in melt composition and temperature. The auxi-mpp implementation demonstrates good agreement with literature models and experimental data for unary, binary, ternary, and quaternary Fe-free systems. For Fe-bearing systems, while parameters have been refitted due to changes in Fe bond fraction parameters in the underlying Modified Quasi-chemical Model (MQM) model, further refinement is still required to fully align with extracted literature model data.

Electrical Conductivity Models:

1. **Thibodeau Electrical Conductivity (ThibodeauEC) Model**: This structural model uses the Nernst-Einstein relationship and relies on the molar volume and diffusivity models to estimate electrical conductivity . The auxi-mpp implementation of this model closely reproduces literature and experimental data for unary, binary, and ternary Fe-free systems. For Fe-bearing systems, there is an increasing deviation from literature data as the fraction of iron oxides increases. This is likely due to a parameter change for FeO in the underlying thermodynamic database.
2. **Hundermark Electrical Conductivity Models**: This unified, semi-empirical model is particularly useful for Fe-bearing slags, although it can apply to others. For non-Fe bearing systems, auxi-mpp's implementation generally reproduces literature models well, with some exceptions for Al2O3-containing systems. Fe-bearing systems, current auxi-mpp estimates deviate slightly from literature data as the amount of iron oxides increases. This is thought to be caused by updated thermodynamic parameters for FeO in the FactSage database.

Diffusivity Model (Thibodeau): This model calculates diffusivity from slag polymerisation and is integral to the electrical conductivity calculation within the ThibodeauEC model. While not independently validated due to a lack of direct literature data for comparison, its successful incorporation and indirect validation through the accurate performance of the Thibodeau electrical conductivity model indicate its correctness.

Viscosity Model (Grundy-Kim-Brosch): The Grundy-Kim-Brosch viscosity model has been implemented and successfully validated against literature models and experimental data across unary, binary, and multicomponent systems. For multicomponent Fe-bearing systems, auxi-mpp generally performs well; however, visible deviations from literature for systems like $CaO-Fe_2O_3-SiO_2$ and $Al_2O_3-CaO-Fe_2O_3-SiO_2$ were observed, where auxi-mpp's results align more closely with FactSage 8.3, suggesting potential inaccuracies in the original literature data or changes in underlying thermodynamic databases.

3.2 Liquid Alloy Material Properties

Density Models: Several models for liquid alloy density have been implemented in auxi-mpp. The primary model, based on volumetric thermal expansion, has been successfully validated for unary metallic elements, the binary Fe-Ni system, and the ternary Cu-Fe-Ni system, showing good agreement with experimental data. Supported unary elements for the volumetric thermal expansion model include: Al, Sb, Bi, Cd, Cr, Co, Cu, Ga, Hf, In, Fe, Pb, Mo, Ni, Nb, Si, Ag, Ta, Tl, Sn, Ti, W, V, Zn, and Zr. Additional empirical models for binary alloys containing non-metallics (e.g., Fe-C, Fe-S) and specific commercial alloys (e.g., stainless steel 304) have also been implemented and validated where data was available.

Electrical Conductivity Model (Polynomial Fit): Due to the complexity of modelling liquid alloys with transition metals, an empirical approach using polynomial fits to experimental resistivity data has been implemented. The models for unary (Fe, Ni, Si), binary (Fe-C, Fe-Si, Fe-Mn, Fe-Ni), and ternary (Fe-C-Si) systems have been validated. Second-degree polynomials are generally recommended as they provide a good balance of accuracy and stability, avoiding the overfitting issues seen with higher-order fits.

Viscosity Models: Two distinct viscosity models have been implemented.

1. Andrade-Type Model: For unary liquid metals, this model has been successfully validated against recommended reference data across all supported elements. Supported elements include: Al, Sb, Bi, Cd, Co, Cu, Ga, In, Fe, Pb, Hg, Ni, Si, Ag, Tl, Sn, and Zn.
2. Deng Model: This linear, empirical model for binary and multi-component iron-based alloys (Fe-C-X, where X = Si, Mn, P, S, or Ti) shows good agreement with experimental data across all validated systems.

Thermal Conductivity Model (Wiedemann-Franz Law): Thermal conductivity is estimated by applying the Wiedemann-Franz law to the electrical conductivity polynomial models. Validation against the Fe-Ni system, the only one with sufficient experimental data, indicates that the model underestimates thermal conductivity by 20–38%, a finding consistent with other literature. Users should be aware that the fundamental assumptions of the Wiedemann-Franz law are violated for pig iron compositions, and the model should be used with caution.

3.3 Gas Material Properties

Density Models (Clapeyron): The Clapeyron models use the ideal gas law to estimate density for CO, CO_2, N_2, Ar, H_2, H_2O, and O_2. The auxi-mpp implementation performs reliably against NIST reference data for pure gases and back-calculated binary data, justifying its use for high-temperature engineering applications.

Viscosity Models:

1. **Unary Viscosity Model (Lemmon-Hellmann-Laesecke-Muzny)**: This composite model unifies correlations for all supported gases. It demonstrates strong agreement with reference data, showing only minor deviations for CO and H_2 near their temperature limits.

2. **Binary Viscosity Model (Wilke)**: The Wilke mixing rule estimates mixture viscosity from pure component data. Despite observable deviations in aqueous mixtures like $H_2O - Ar$, the model consistently captures the correct physical trends across validated temperature ranges.

Diffusivity Models:

1. **Self-Diffusivity Model (Burgess)**: This model accurately estimates coefficients for Ar, CO, CO_2, H_2, N_2, and O_2 but is currently limited to narrow temperature ranges ($\sim$450 K). Parameters for H_2O are unavailable.

2. **Binary Diffusivity Model (Hellmann)**: Based on kinetic theory, this model estimates coefficients for specific pairs (e.g., $Ar - H_2O$, $CO_2 - N_2$). Validation confirms that these coefficients are effectively independent of mixture composition.

Thermal Conductivity Models:

1. **Unary Thermal Conductivity Models**: A combination of high-performing models (Chung, Lemmon, Huber, Assael) covers all supported species. Validation against NIST data is successful, with minor deviations noted only for the Chung model applied to CO and CO_2.

2. **Mixture Thermal Conductivity Model (Mason and Saxena)**: This mixing rule estimates mixture thermal conductivity. It performs reasonably well for validated binary systems, though validation for multi-component mixtures remains a future task.

Total Emissivity Models:

1. **Exponential Wide Band Model (EWB)**: Implemented for CO, this model exhibits deviations from comparative literature data, likely due to differences in the underlying reference models.

2. **Chart Model (Leckner)**: Used for H_2O, CO_2, and their mixtures, this model matches zero-partial pressure limits well. However, deviations are noted in ternary mixtures at extreme temperatures and pressure path lengths.

Part II

Slag Material Properties

Chapter 4

Background

Slags are integral to pyrometallurgical processes, serving crucial roles in metal extraction, purification, and environmental control. These molten materials, predominantly composed of metal oxides, form during the smelting, refining, and alloying of metals. Slags not only facilitate the separation of metals from their ores but also play a significant role in controlling reactions, heat transfer, and minimising environmental impacts such as emissions and waste generation. Controlling the slag properties is therefore essential for optimal yields and minimal waste. To effectively control slag properties, it is important to understand the underlying principles that govern them.

The physical properties of slags are intricately interconnected, primarily due to the slag's structure. This structure, specifically the degree of polymerisation (Q) of the silicate network, acts as the fundamental characteristic influencing the slag's properties like diffusivity (D), viscosity (μ), electrical conductivity (σ), thermal conductivity (κ), and density (ρ) (Mysen and Richet 2019).

A highly polymerised network, characterised by long, interconnected chains of silicate tetrahedra, restricts the movement of all slag components. This restricted movement results in higher μ, as the slag becomes more resistant to flow. Similarly, D decreases, as the interconnected network hinders the movement of ions. σ is also reduced, as the movement of charge-carrying cations is impeded by the tightly bound structure. κ is increased, as the interconnected structure presents a lower resistance to the flow of phonons, resulting in higher thermal conductivity.

Conversely, a less polymerised network with more non-bridging oxygen atoms, allows for greater freedom of movement. This leads to lower μ, higher D, increased σ, but decreased κ. The molar volume ($\bar{V}$) and ρ is also affected by Q, as the arrangement of silicate tetrahedra and the packing of cations influence the overall volume occupied by the slag.

The structure of silicate melts is characterised by the three types of bridging oxygen atoms. A free oxygen separates a metal-metal (M – M) pair, a non-bridging oxygen separates a metal-silicon (M – Si) pair, and a bridging oxygen separates a silicon-silicon (Si – Si) pair. From the Si atom's perspective, silicon atoms are always tetrahedrally bonded to four oxygen ions such that the basic silicate melts mainly consist of M^{q+}, O^{2-}, and $SiO_4{}^{4-}$. As the silica content increases beyond the orthosilicate composition, the $SiO_4{}^{4-}$ tetrahedra begin to polymerise, forming more bridging oxygens and gradually creating a three-dimensional network.

The degree of polymerisation of a slag is described by the Q^{n}-species which is the fraction of $SiO_4{}^{4-}$ ions that contains n bridging oxygens. In pure SiO_2, all four oxygens surrounding each silicon are bridging oxygens, with the Q^4-species fraction being 1.0, whereas an isolated $SiO_4{}^{4-}$ ion is a Q^0-species (Kim et al. 2012a).

The structure of a slag is significantly affected by both temperature (T) and composition (x). Increasing T generally leads to a decrease in polymerisation, as the thermal energy breaks the bonds between silicate tetrahedra, resulting in shorter chains and a more fluid slag. x also plays a crucial role, with network-forming oxides like SiO_2 and Al_2O_3 promoting polymerisation by forming extensive interconnected networks. Conversely, network-modifying oxides such as CaO, MgO, Na_2O, and K_2O disrupt the network by breaking the Si – O – Si bonds, resulting in shorter chains and a less polymerised structure. Al_2O_3 is also amphoteric and may act as a network modifier depending on the availability of other network-modifying oxides, such as CaO or Na_2O, to charge compensate for Al^{3+} ions.

In short, the specific type and concentration of these oxides, along with T, ultimately determine the structure and resulting physical properties of slag.

Chapter 5

Density

5.1 Thibodeau Density Model

A model developed by Thibodeau et al. (2016a).

5.1.1 Introduction

The density is closely related to the molar volume of a slag, it is essentially the reciprocal thereof. Estimation of the density is therefore not limited to models strictly for density, as molar volume models will achieve the same goal. Hence, the structural molar volume model developed by Thibodeau et al. (2016a) was implemented with the intention to estimate slag density.

5.1.2 Model Overview

This model is based on the concept of silicate tetrahedral Q-species. Q-species represent different structural units defined by silicon tetrahedra with varying numbers of bridging oxygens (oxygen atoms shared between two tetrahedra), non-bridging oxygens (oxygen atoms bonded to only one silicon atom), and free oxygens (oxygen atoms not bonded to silicon).

The original literature model uses the MQM found in ChemApp for Python and the FactSage FToxid database to calculate the quantity of each Q-species in a given melt (Thibodeau et al. 2016a). Each Q-species is assigned a molar volume that changes linearly with temperature. The model calculates the total molar volume of the melt by summing the contributions from each Q-species and free oxide species. This allows the model to account for the non-linear behaviour of molar volume in silicate melts that arises from the changing distribution of Q-species with composition and temperature.

It is important to note that this model is formulated strictly for liquid slag systems – the user should therefore ensure that his/her system is above the liquidus temperature before performing calculations. Also, we recommend the model to be used within the validation ranges specified in Table 5.2. The validation ranges are based on selected figures from the original articles. To peruse the full range of systems the model were validated for, the user is directed to the original article.

Finally, for systems containing Fe, the correct ratio of Fe(II) and Fe(III) has to be provided. This means the user needs to know the oxidation environment of the system, and from that estimate this ratio before passing it on to the model.

5.1.3 Model Formulation

Molar volume for a multicomponent system is typically expressed with Equation (5.1).

$$\bar{V}_{\mathrm{slag}} = \frac{\sum_i \bar{m}_{\mathrm{i}} \cdot x_{\mathrm{i}}}{\rho_{\mathrm{slag}}} \tag{5.1}$$

However, the molar volume of the metal oxide melt (slag) can also be expressed as the sum of molar volumes for each phase constituent scaled by its mole fraction in the slag, according to Equation (5.2).

$$\bar{V}_{\mathrm{slag}} = \sum_i \bar{V}_{\mathrm{i}} \cdot x_{\mathrm{i}} \tag{5.2}$$

Thibodeau et al. (2016a) and Thibodeau et al. (2016b) developed more fundamental, structure-based equations based on Equations (5.1) and (5.2) to model the molar volume in binary and multicomponent slag systems containing $Li_2O - Na_2O - K_2O - MgO - CaO - MnO - PbO - Al_2O_3 - SiO_2$. This model was further extended to include FeO and Fe_2O_3 in Thibodeau et al. (2016c), demonstrating its applicability across a wide range of SiO_2-based slag systems. The following information describes the model and its implementation.

Unary

The molar volume of a unary system is simply calculated as a linear combination of a pure oxide's parameters at a specific temperature, as shown in Equation (5.3).

$$\bar{V}^{T}_{\mathrm{slag}} = \mathrm{a} + \mathrm{b}T \tag{5.3}$$

Binary

The level of oxygen in slag determines the types and quantities of bonding scenarios that develop between non-oxygen atoms. There are types of bonding scenarios corresponding to the three possible structural states for oxygen shown in Equation (5.4). O^0 represents a bridging oxygen; Si – O – Si, O^{-2} refers to a free oxygen; M – O – M, and O^- denotes a non-bridging oxygen; Si – O – M.

$$\mathrm{O}^0 + \mathrm{O}^{2-} \rightleftharpoons 2\mathrm{O}^- \tag{5.4}$$

If we are dealing with one mole of slag, the total moles of oxygen per mole of slag is calculated by summing the oxygen contributions from each species in the slag system, as shown in Equation (5.5).

$$n_\mathrm{t} = x_{\mathrm{M_2O}} + x_{\mathrm{MO}} + 3x_{\mathrm{M_2O_3}} + 2x_{\mathrm{MO_2}} \tag{5.5}$$

The number of bridging oxygen atoms is calculated using Equation (5.6), which incorporates the bond fraction of Si – O – Si contacts and can be obtained from the MQM model found in ChemApp for Python. Likewise, Equation (5.7) is used to determine the number of M – O – M contacts.

$$n_{\mathrm{O^0}} = x_{\mathrm{Si-Si}} \cdot n_\mathrm{t} \tag{5.6}$$

$$n_{\mathrm{M-M}} = x_{\mathrm{M-M}} \cdot n_\mathrm{t} \tag{5.7}$$

Now, the number of Si – O^0 bonds per mole of solution is simply twice the number of bridging oxygens; $2n_{\mathrm{O^0}}$. The average number of bridged oxygens per silicon atom is therefore $2n_{\mathrm{O^0}}/x_{\mathrm{SiO_2}}$. Assuming that all Si atoms are tetrahedrally coordinated with four oxygens, the probability that one of the oxygens will be bridging is therefore a quarter of this, as given by Equation (5.8).

$$P_{\mathrm{O^0}} = \frac{1}{4} \cdot \frac{2n_{\mathrm{O^0}}}{x_{\mathrm{SiO_2}}} = \frac{n_{\mathrm{O^0}}}{2x_{\mathrm{SiO_2}}} \tag{5.8}$$

If the probability of an oxygen in a Q-species being a bridging oxygen is known, the probability to have a given Q^n (where $\mathrm{n} = 0, 1, 2, 3,$ or 4) can be calculated with Equation (5.9);

$$W_\mathrm{n} = \frac{4!}{(4-\mathrm{n})!\mathrm{n}!} P_{\mathrm{O^0}}^{\mathrm{n}} (1 - P_{\mathrm{O^0}})^{(4-\mathrm{n})} \quad \mathrm{n} = 0, 1, 2, 3, \text{or } 4 \tag{5.9}$$

The amount of each Q-species per mole of slag can be determined from their probabilities to form, calculated with Equation (5.10). This is achieved by multiplying W_n with $x_{\mathrm{SiO_2}}$, since the latter gives the mole fraction of all Q-species combined;

$$n_{\mathrm{Q^n}} = W_\mathrm{n} \cdot x_{\mathrm{SiO_2}} \text{ for } \mathrm{n} = 0, 1, 2, 3, \text{or } 4 \tag{5.10}$$

The molar volume is then calculated by Equation (5.11) as a linear combination of the molar volume for each species, weighted by the amount of the associated species present.

$$\bar{V}_{\mathrm{slag}}^{T} = n_{\mathrm{Q^4}} \bar{V}_{\mathrm{SiO_2}}^{T} + \sum_{\mathrm{n}=0}^{3} n_{\mathrm{Q^n}} \bar{V}_{\mathrm{Q^n}}^{T} + n_{\mathrm{M-M}} \bar{V}_{\mathrm{M-M}}^{T} \tag{5.11}$$

In Equation (5.11), the species specific molar volume is calculated with Equation (5.12), where the two empirical parameters a and b were fitted to the pure oxide slags, assuming that their molar volumes varies linearly with temperature.

$$\bar{V}_\mathrm{i} = \mathrm{a_i} + \mathrm{b_i} T \tag{5.12}$$

Multicomponent

To calculate the molar volume for multicomponent systems, Equation (5.11) was adapted to account for the different cations that Si can be connected to and for the different ways in which the cations can connect to each other. This is given in Equation (5.13). The molar volume of a given Q-species is therefore calculated as a linear combination of the different non-bridging oxygen, Si – M$_j$, scenarios. The contribution from free oxygen contacts, $\bar{V}_{\mathrm{M_i-M_j}}$, are taken as the average of their pure oxides' molar volumes as per Equation (5.14).

$$\bar{V}^{T}_{\mathrm{slag}} = n_{\mathrm{Q^4}}\bar{V}^{T}_{\mathrm{SiO_2}} + \sum_{\mathrm{n=0}}^{3} n_{\mathrm{Q^n}} \frac{\sum_i x_{\mathrm{Si-M_i}}\bar{V}^{T}_{\mathrm{Q^n}}}{\sum_i x_{\mathrm{Si-M_i}}} + \sum_i \sum_j n_{\mathrm{M_i-M_j}}\bar{V}^{T}_{\mathrm{M_i-M_j}} \tag{5.13}$$

$$\bar{V}^{T}_{\mathrm{M_i-M_j}} = \frac{\bar{V}^{T}_{\mathrm{M_i}} + \bar{V}^{T}_{\mathrm{M_j}}}{2} \tag{5.14}$$

Density

Once the molar volume is known, the density can be calculated. The density can be calculated from molar volume with Equation (19.12).

$$\rho_{\mathrm{slag}} = \frac{\sum_i \bar{m}_{\mathrm{i}}x_{\mathrm{i}}}{\bar{V}_{\mathrm{slag}}} \tag{5.15}$$

If the molar volume model proofs to be accurate, accurate density values can be calculated from it.

5.1.4 Variable Declarations

The parameters used in Equation (5.12) is tabulated in Table 5.1

Table 5.1: Empirical model parameters for molar volume calculation of SiO_2 slags.

	Q^3		Q^2		Q^1		Q^0		Pure Oxide	
Oxides	a	b$\times10^3$	a	b$\times10^3$	a	b$\times10^3$	a	b$\times10^3$	a	b$\times10^3$
SiO_2	-	-	-	-	-	-	-	-	27.3	0.00
Li_2O	29.96	2.80	35.73	5.00	41.66	6.50	48.18	8.20	13.52	3.30
Na_2O	34.41	3.50	43.11	8.00	53.22	10.0	63.78	13.0	25.32	5.95
K_2O	38.17	6.00	54.75	12.00	68.92	16.50	87.63	21.00	37.85	8.83
MgO	30.42	1.00	34.79	2.40	37.66	4.00	42.34	5.00	14.05	0.70
CaO	32.60	1.70	35.60	3.50	42.60	6.00	50.70	7.00	19.54	0.85
MnO	31.00	1.60	34.50	3.50	38.80	6.50	43.00	7.00	16.09	0.95
PbO	39.00	1.00	44.50	3.00	56.00	5.00	65.00	8.30	23.86	3.21
Al_2O_3	35.98	0.00	36.89	0.00	47.69	0.00	50.30	0.00	11.15	0.47
FeO*	29.90	3.50	31.10	2.00	40.80	5.20	48.70	6.70	13.46	1.17
Fe_2O_3*	40.60	0.00	48.20	0.00	82.60	0.00	44.20	0.00	10.05	1.38

* The model parameters for FeO and Fe_2O_3 had to be refitted due to a change in Fe parameters used in the MQM model of ChemApp for Python.

5.1.5 Assumptions

The structural molar volume model for oxide slags is based on several key assumptions.

1. It relies on accurately estimated molar volumes of pure liquid oxide components.
2. It assumes that the molar volume of each component, including pure oxides and Q-species, changes linearly with temperature.
3. The model uses Q-species as the fundamental structural units, assuming they are the minimal units needed to explain silicate melt volumes.
4. It considers the excess molar volume from medium-range structures formed by Q-species to be negligible.
5. It assumes that the MQM, with the FactSage FToxid database, accurately calculates bond fractions.
6. It assumes a single liquid melt without solid phases or liquid miscibility gaps.
7. It assumes Al_2O_3 to be a network modifier.
8. It assumes other potentially important anions (e.g. S^{2-}, ${SO_4}^{2-}$, ${CO_3}^{2-}$, etc.) will not disrupt the oxygen network.

5.1.6 Model Validation

Molar Volume, Fe-free Systems

The Thibodeau density model implemented in auxi-mpp, was evaluated by comparing its inverse (molar volume) against both the literature model and experimental data. Data were extracted directly from figures in Thibodeau et al. (2016a) and Thibodeau et al. (2016b). The models were validated for the systems and temperatures shown in Table 5.2.

Table 5.2: Molar Volume Validation Ranges

Model	Systems	Composition ($\mathrm{mol\,mol^{-1}}$)	Temperature (K)
Unary	SiO_2	pure substance	$0 - 3000$
	Al_2O_3	pure substance	$2000 - 3250$
	MgO	pure substance	$300 - 4000$
	CaO	pure substance	$300 - 3500$
Binary	$Al_2O_3 - SiO_2$	$x_{\mathrm{Al_2O_3}} = 0 - 1$	2073
	$CaO - SiO_2$	$x_{\mathrm{CaO}} = 0 - 1$	$1773, 1973$
	$MgO - SiO_2$	$x_{\mathrm{MgO}} = 0 - 1$	1973
Ternary	$CaO - MgO - SiO_2$	$x_{\mathrm{MgO}} = 0 - 1, x_{\mathrm{SiO_2}}/x_{\mathrm{CaO}} = 1$	$1723, 1873$
	$CaO - MgO - SiO_2$	$x_{\mathrm{CaO}} = 0 - 1, x_{\mathrm{SiO_2}}/x_{\mathrm{MgO}} = 2$	$1723, 1873$
	$Al_2O_3 - MgO - SiO_2$	$x_{\mathrm{SiO_2}} = 0 - 1, x_{\mathrm{MgO}}/x_{\mathrm{Al_2O_3}} = 1$	$1873, 1973$
	$Al_2O_3 - MgO - SiO_2$	$x_{\mathrm{MgO}} = 0 - 0.5, x_{\mathrm{SiO_2}} = 0.5$	$1873, 1973$
	$Al_2O_3 - CaO - SiO_2$	$x_{\mathrm{SiO_2}} = 0 - 1, x_{\mathrm{CaO}}/x_{\mathrm{Al_2O_3}} = 1$	$1773, 1873$
	$Al_2O_3 - CaO - SiO_2$	$y_{\mathrm{Al_2O_3,CaO,SiO_2}} = 0 - 1$	1873
	$CaO - MgO - SiO_2$	$y_{\mathrm{CaO,MgO,SiO_2}} = 0 - 1$	1873
Quaternary	$Al_2O_3 - CaO - MgO - SiO_2$	$y_{\mathrm{Al_2O_3,CaO,SiO_2}} = 0 - 0.9, y_{\mathrm{MgO}} = 0.1$	1873
	$Al_2O_3 - CaO - MgO - SiO_2$	$y_{\mathrm{CaO,MgO,SiO_2}} = 0 - 0.8, y_{\mathrm{Al_2O_3}} = 0.2$	1873
	$Al_2O_3 - CaO - MgO - SiO_2$	$y_{\mathrm{CaO,MgO,SiO_2}} = 0 - 0.7, y_{\mathrm{Al_2O_3}} = 0.3$	1873

The auxi-mpp model agrees well with the literature model across unary, binary, ternary and quaternary systems. Figure 5.1 shows that auxi-mpp aligns with the literature model ("2016: Thibodeau et al.") for unary systems, plotting molar volume against temperature.

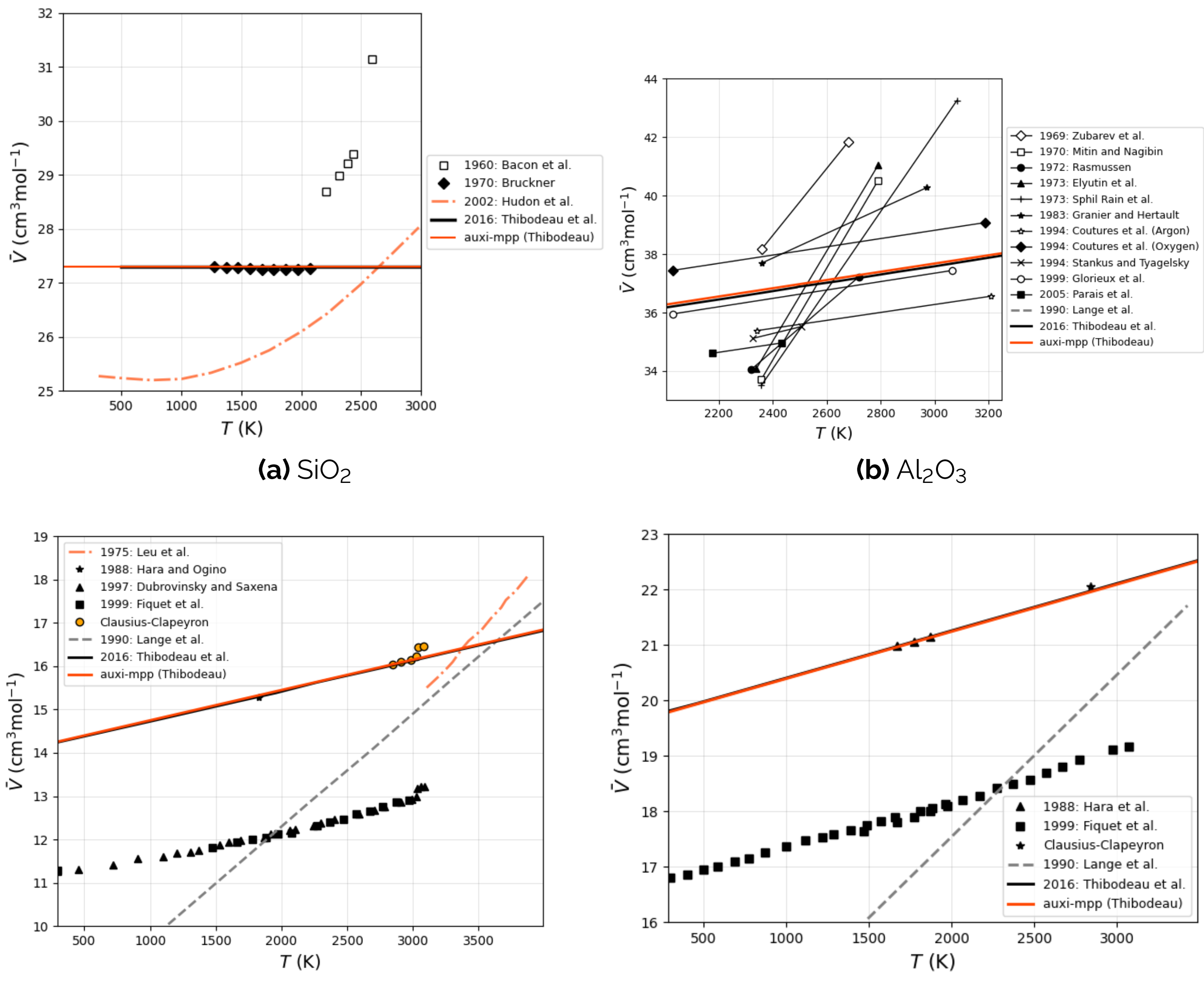

(a) SiO_2 **(b)** Al_2O_3

(c) MgO **(d)** CaO

Figure 5.1: Molar volume vs temperature of unary systems.

Similarly, Figure 5.2 and Figure 5.3 confirm this agreement for binary and ternary systems, where molar volume is plotted against mole fraction.

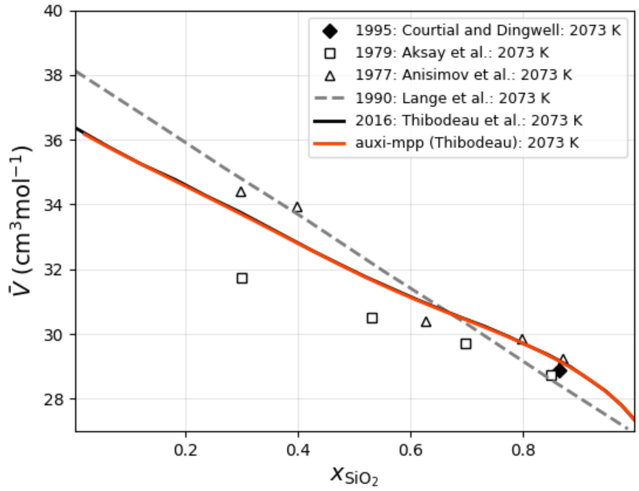

(a) $Al_2O_3 - SiO_2$

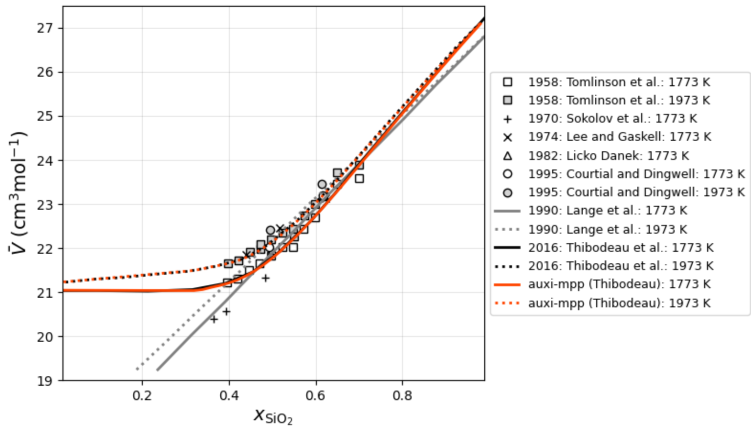

(b) $CaO - SiO_2$

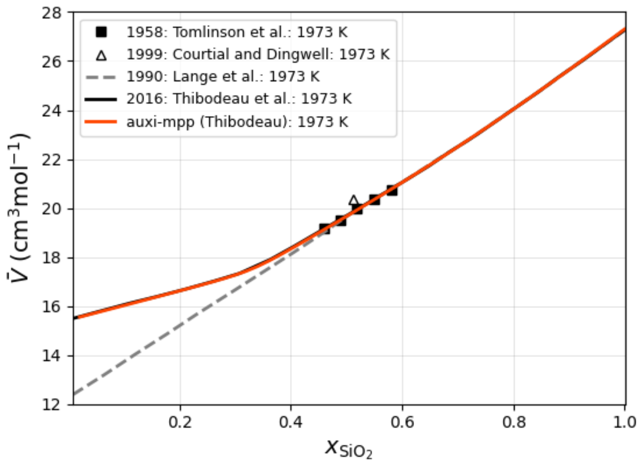

(c) $MgO - SiO_2$

Figure 5.2: Molar volume vs mole fraction of binary systems.

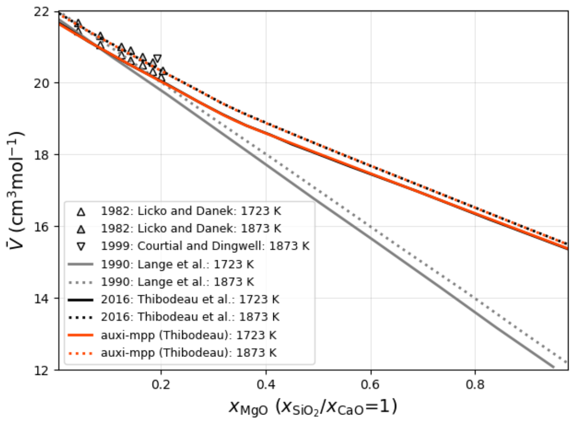

(a) $CaO - MgO - SiO_2$

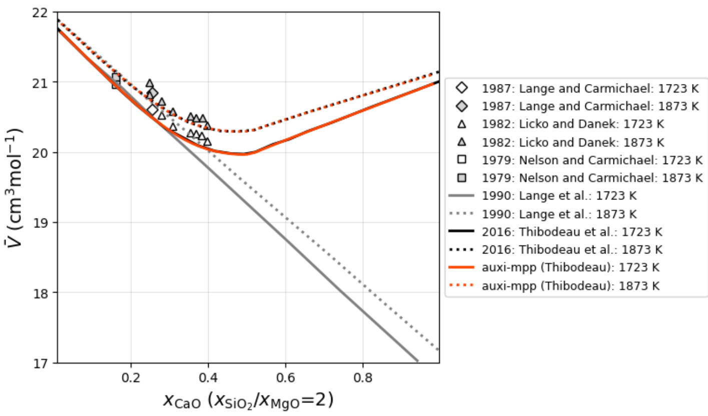

(b) $CaO - MgO - SiO_2$

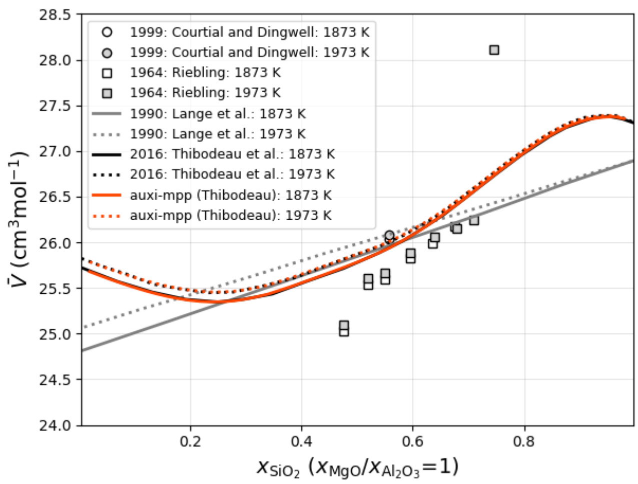

(c) $Al_2O_3 - MgO - SiO_2$

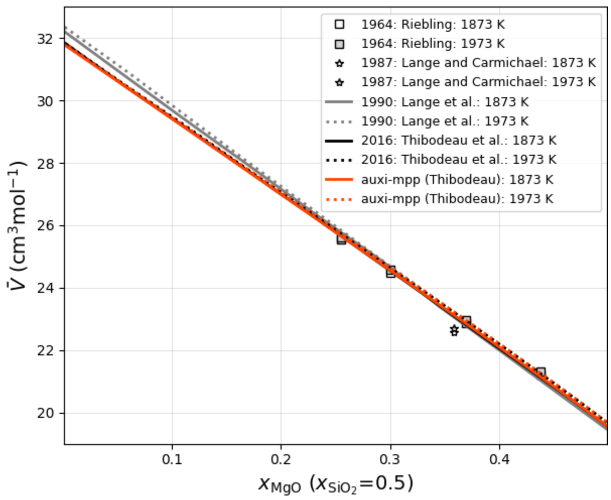

(d) $Al_2O_3 - MgO - SiO_2$

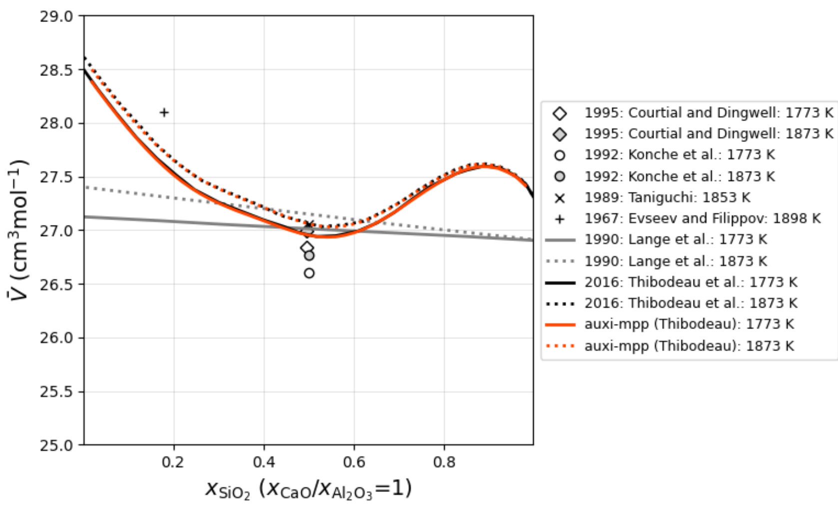

(e) $Al_2O_3 - CaO - SiO_2$

Figure 5.3: Molar volume vs mole fraction for the ternary systems.

auxi-mpp was also validated for $Al_2O_3 - CaO - MgO - SiO_2$. In Figure 5.4, the ternary diagrams display the molar volume contour lines as calculated by Thibodeau et al. (2016b). For each point on the contour line, the composition were extracted and used to calculate the molar volume using auxi-mpp to see if the contour line's value could be reproduced.

The green points in Figure 5.4 indicate auxi-mpp's estimations that lies within a 1% error threshold compared to the value of the contour line.

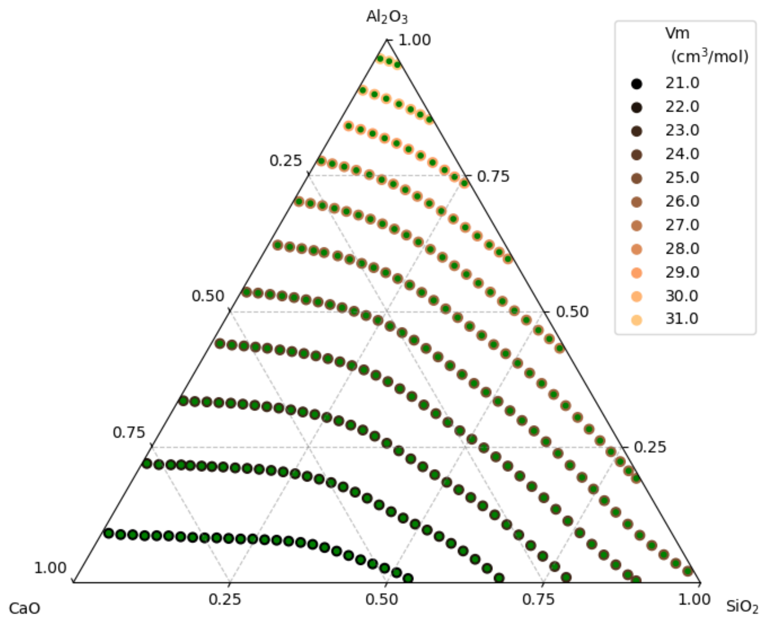

(a) $Al_2O_3 - CaO - MgO - SiO_2$ system at 1873 K and $y_{\mathrm{MgO}} = 0.1$

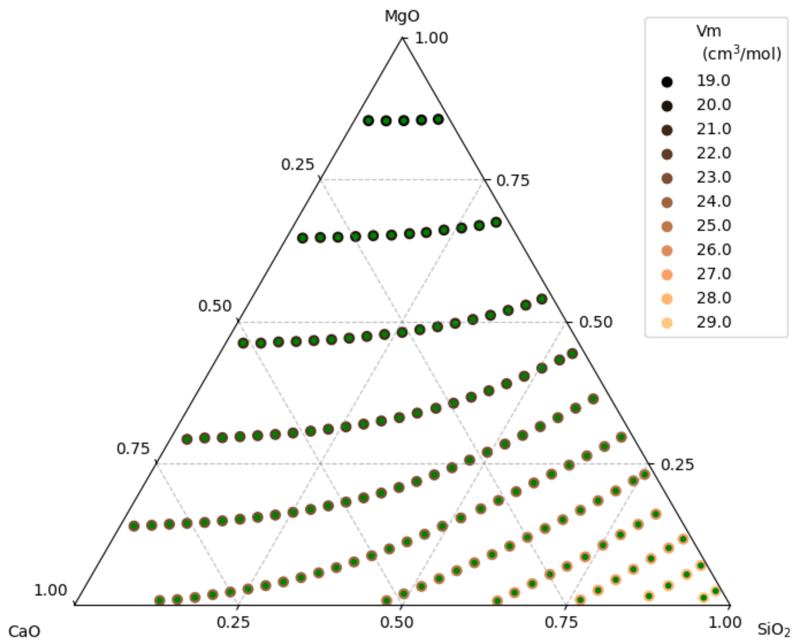

(b) $Al_2O_3 - CaO - MgO - SiO_2$ system at 1873 K and $y_{\mathrm{Al_2O_3}} = 0.3$

Figure 5.4: Molar volume vs mole fraction for quaternary systems.

Finally, Figure 5.5 gives an oversight of how auxi-mpp compares with literature for ternary and quaternary systems.

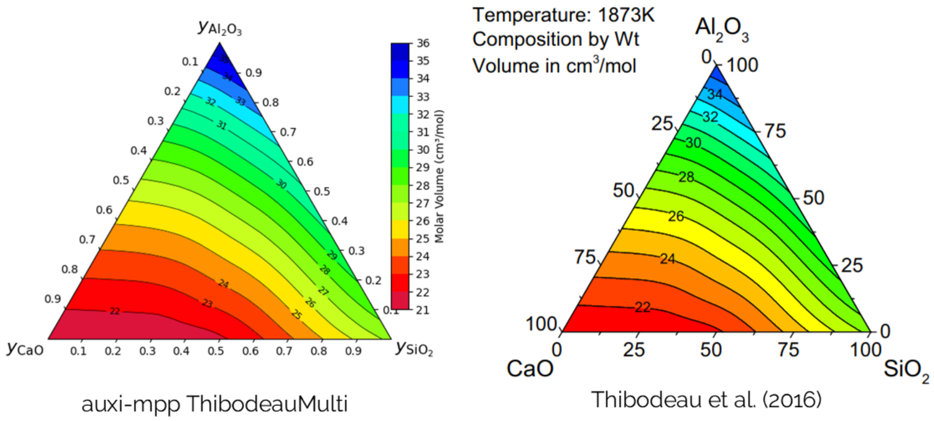

(a) $Al_2O_3 - CaO - SiO_2$

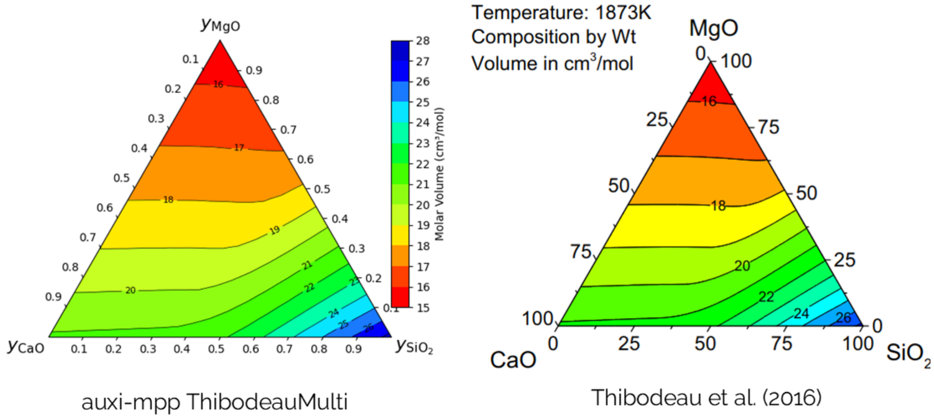

(b) $CaO - MgO - SiO_2$

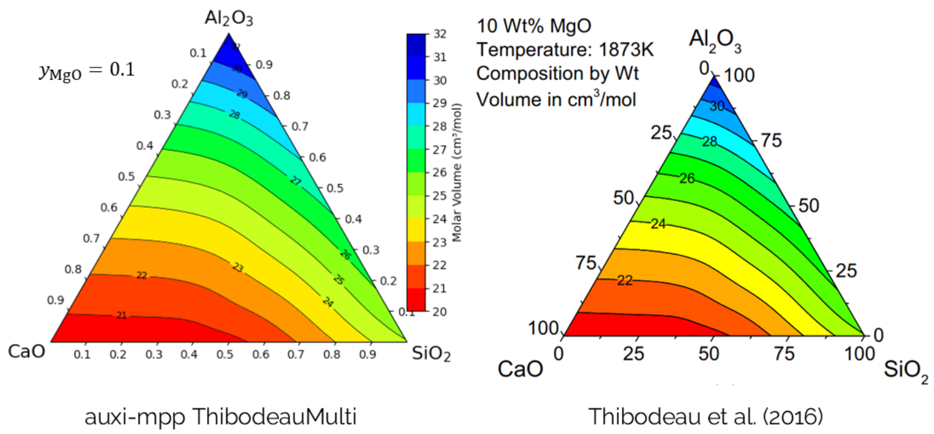

(c) $Al_2O_3 - CaO - MgO - SiO_2$

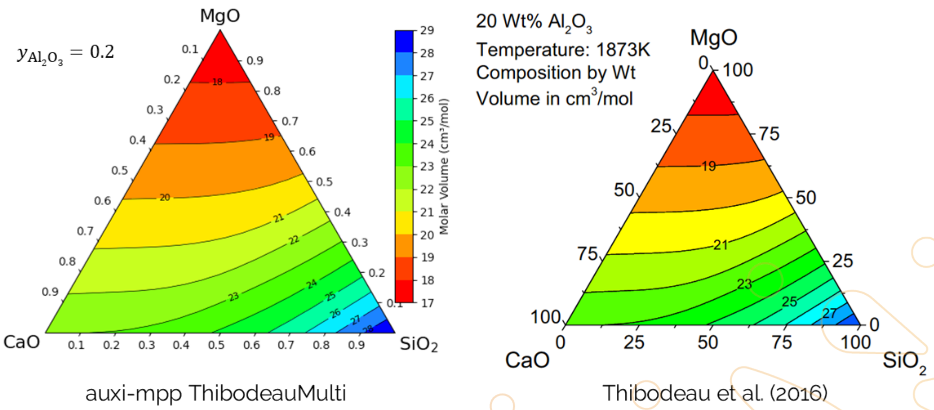

(d) $Al_2O_3 - CaO - MgO - SiO_2$

Figure 5.5: Comparing auxi-mpp's contour plots with literature.

Molar Volume, Fe-bearing Systems

The original parameters were refitted due to a change in the Fe parameters used in the MQM model of ChemApp for Python which resulted in a change in bond fraction estimates. This is shown with Figure 5.6 for the fraction of non-bridging oxygens in the $SiO_2 – FeO$ system compared to $SiO_2 – CaO$ and $SiO_2 – MgO$ systems.

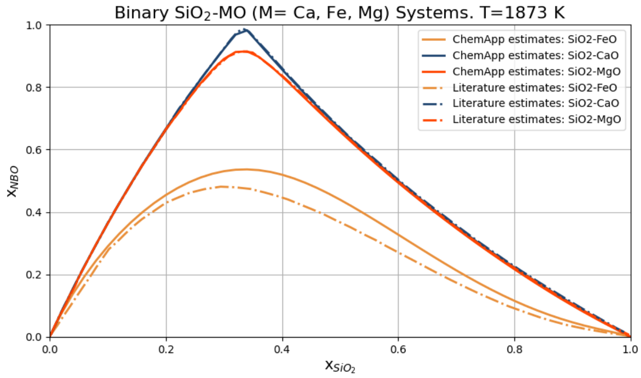

Figure 5.6: Fraction of non-bridging oxygens for binary systems.

Correlation plots were generated for the following Fe-bearing systems using both the original and the updated parameters for FeO and Fe_2O_3 from Table 5.1. There is still deviation between the extracted model data and estimated model data from auxi-mpp with respect to temperature as shown in Figure 5.8. Further refinement of the parameters are required and will be addressed in a later update.

1. $FeO – SiO_2$ (Hypothetical)
2. $Fe_2O_3 – SiO_2$ (Hypothetical)
3. $Fe_2O_3 – FeO – SiO_2$
4. $CaO – Fe_2O_3 – FeO – SiO_2$

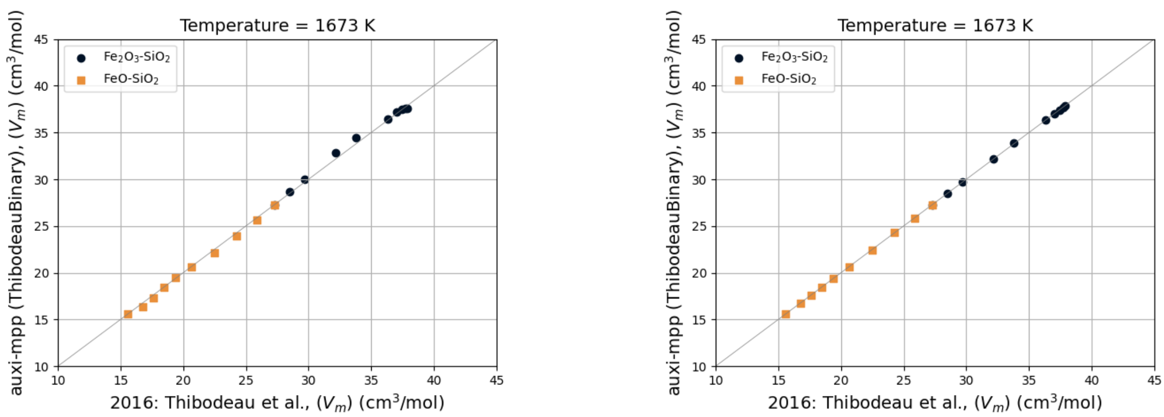

(a) **(b)**

Figure 5.7: auxi-mpp vs Thibodeau (2014) for correlation plots for hypothetical Fe-bearing binary systems, original (left) and updated (right) for FeO and Fe_2O_3 parameters.

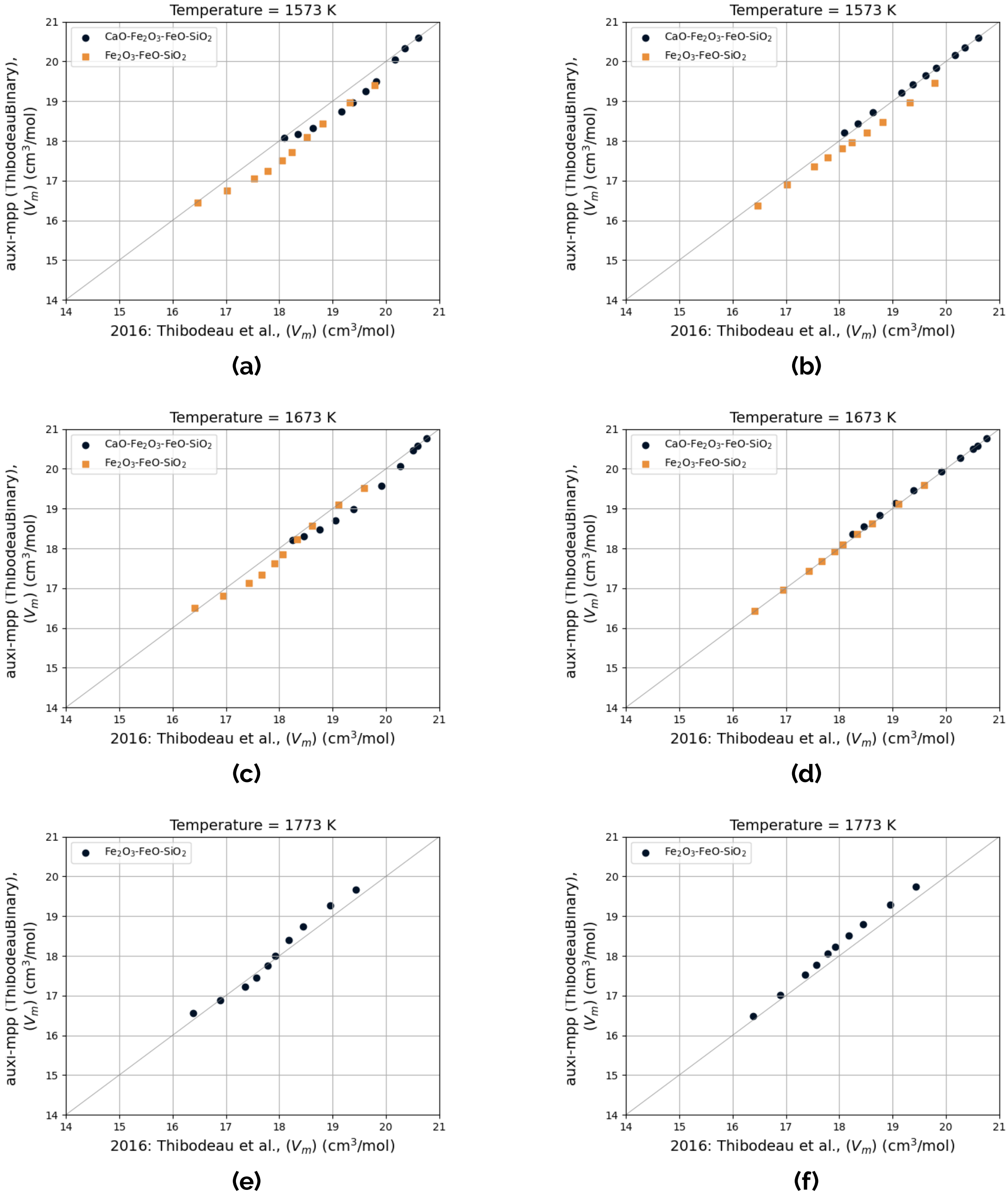

Figure 5.8: auxi-mpp vs Thibodeau (2014) correlation plots, original (left) and updated (right) for FeO and Fe_2O_3 parameters.

Chapter 6

Electrical Conductivity

6.1 Thibodeau Electrical Conductivity Model

A model developed by Thibodeau (2016).

6.1.1 Introduction

The electrical conductivity model is a structural model that uses the Nernst-Einstein relationship to predict the electrical conductivity of oxide melts. The model is built on the concept of ionic conduction, where cations act as charge carriers, and their movement is influenced by the slag's polymerisation. The electronic contribution are also accounted for when iron oxides are present.

6.1.2 Model Overview

The model relies on Thibodeau's molar volume (density) model, Chapter 5, to calculate the degree of polymerisation (Q), enabling it to account for variations in melt composition. Its parameters for individual cations are derived from unary and binary silicate systems, allowing it to estimate the electrical conductivities of higher-order systems without additional parameters.

The model deals with the role of ionic conduction in the electrical conductivity of all oxide melts and only accounts for an electronic contribution from iron oxides. When these melts contain substantial amounts of iron oxide and manganese oxide (transition metal oxides), they can host significant quantities of both divalent and trivalent Fe and Mn cations. In such instances, the contribution of electronic conduction must also be considered.

It is important to note that this model is formulated strictly for liquid slag systems – the user should therefore ensure that his/her system is above the liquidus temperature before performing calculations. Also, we recommend the model to be used within the validation ranges specified in Table 6.1. The validation ranges are based on selected figures from the original article as well as Thibodeau's dissertation.

6.1.3 Model Formulation

This model is based on the work of Thibodeau (2016) and Thibodeau (2014). It mainly estimates the total electrical conductivity based on ionic conduction (see Equation (6.1)), assuming that only iron oxides contribute to electronic conduction. The electronic contribution due to iron oxides are estimated using Equation (6.3).

$$\sigma_{\text{ionic}} = \sum_i \sigma_{\text{i}} \tag{6.1}$$

For each cationic species, electrical conductivity is defined as per Equation (6.2), indicating a dependence on molar volume and diffusivity;

$$\sigma_{\text{i}} = \frac{n_{\text{i}} x_{\text{i}} z_{\text{i}}^2 F^2}{\bar{V} RT} D_{\text{i}} \tag{6.2}$$

The molar volume and diffusion coefficient values are obtained from the models described in Chapter 5 and Chapter 7, respectively.

For iron oxides, Equation (6.3) are used to estimate the electronic contribution.

$$\sigma_{\text{electronic}} = \frac{A}{T} D_{\text{Fe}^{2+}} c_{\text{Fe}}^2 y(1-y) \tag{6.3}$$

Here, A has a value of 4×10^{14}, c_{Fe} is the total iron concentration and y is the fraction of Fe^{2+}. The total electrical conductivity is then as shown in Equation (6.4).

$$\sigma_{\text{total}} = \sigma_{\text{ionic}} + \sigma_{\text{electronic}} \tag{6.4}$$

6.1.4 Assumptions

Equation (6.2) makes several assumptions.

1. It assumes that all cations are available to carry charge, meaning there are no neutral species or complexes.
2. It is assumed that the mechanism for ionic conductivity is the same as tracer diffusion.
3. It assumes that the velocity of an ion is determined solely by the forces acting on that specific ion. Thus, the electric field does not influence the medium through which the cations diffuse.
4. It is assumed that only iron oxides contribute to electronic conduction.

6.1.5 Literature Inaccuracies

The contour mapping of electrical conductivity shown in Thibodeau (2016) Figure 34 is likely incorrect. auxi-mpp were successfully validated against all Cartesian plots in Thibodeau (2016), but could not reproduce their contour mapping – see Figure 6.4. Figure 6.4a shows all composition slices for which auxi-mpp were successfully validated, yet the contour plot for $Al_2O_3 - CaO - SiO_2$ differs. Single point calculations for several selected compositions on Figures 6.4b to 6.4c also consistenty agreed with auxi-mpp's contour mapping. Finally, the same method to create the ternary plots in Figure 6.4 were used to create those in Figure 5.5 where there were no issues.

6.1.6 Model Validation

The Thibodeau electrical conductivity (ThibodeauEC) model implemented in auxi-mpp was validated against the literature model and experimental data extracted from Thibodeau (2016). The systems and temperatures for which the models were validated are given in Table 6.1.

Table 6.1: Electrical Conductivity Thibodeau Model Validation Ranges

Model	Systems	Composition	Temperature (K)
Unary	SiO_2	pure substance	$1500 - 3000$
	Al_2O_3	pure substance	$2200 - 3200$
	MgO	pure substance	$2000 - 3400$
	CaO	pure substance	$1800 - 3400$
Binary	$Al_2O_3 - SiO_2$	$x_{Al_2O_3} = 0 - 1$	$1873, 1973, 2073$
	$CaO - SiO_2$	$x_{CaO} = 0.2 - 0.7$	$1823, 1873, 1923$
	$MgO - SiO_2$	$x_{MgO} = 0.2 - 0.8$	$1873, 1973, 2073$
Ternary	$Al_2O_3 - CaO - SiO_2$	$y_{Al_2O_3} = 0 - 1$, $y_{CaO}/y_{SiO_2} = 1$	$1673, 1773, 1873$
	$Al_2O_3 - CaO - SiO_2$	$y_{CaO} = 0 - 0.9$, $y_{SiO_2} = 0.1$	$1673, 1773, 1873$
	$Al_2O_3 - CaO - SiO_2$	$y_{CaO} = 0 - 0.8$, $y_{SiO_2} = 0.2$	$1673, 1773, 1873$
	$Al_2O_3 - CaO - SiO_2$	$y_{CaO} = 0 - 0.7$, $y_{SiO_2} = 0.3$	$1673, 1773, 1873$
	$Al_2O_3 - CaO - SiO_2$	$y_{CaO} = 0 - 0.6$, $y_{SiO_2} = 0.4$	$1673, 1773, 1873$
	$Al_2O_3 - CaO - SiO_2$	$y_{CaO} = 0 - 0.95$, $y_{Al_2O_3} = 0.05$	$1673, 1773, 1873$
	$Al_2O_3 - CaO - SiO_2$	$y_{CaO} = 0 - 0.9$, $y_{Al_2O_3} = 0.1$	$1673, 1773, 1873$
	$Al_2O_3 - CaO - SiO_2$	$y_{CaO} = 0 - 0.8$, $y_{Al_2O_3} = 0.2$	$1673, 1773, 1873$
	$Al_2O_3 - MgO - SiO_2$	$y_{MgO} = 0 - 0.5$, $y_{SiO_2} = 0.5$	$1873, 1973, 2073$
	$CaO - MgO - SiO_2$	$x_{MgO} = 0 - 0.4$, $x_{CaO}/x_{SiO_2} = 1$	$1773, 1823, 1873$
	$Al_2O_3 - CaO - SiO_2$‡	$y_{Al_2O_3,CaO,SiO_2} = 0 - 1$	1873
	$CaO - MgO - SiO_2$‡	$y_{CaO,MgO,SiO_2} = 0 - 1$	1873
Quaternary‡	$Al_2O_3 - CaO - MgO - SiO_2$	$y_{CaO,MgO,SiO_2} = 0 - 0.9$, $y_{Al_2O_3} = 0.1$	1873
	$Al_2O_3 - CaO - MgO - SiO_2$	$y_{Al_2O_3,CaO,SiO_2} = 0 - 0.9$, $y_{MgO} = 0.1$	1873
Iron Containing	$Fe_2O_3 - FeO - SiO_2$	$x_{SiO_2} = 0.2 - 0.5$, Fe sat.	$1573, 1673, 1773$
	$Fe_2O_3 - FeO - MgO - SiO_2$	$x_{MgO} = 0 - 0.65$, $x_{SiO_2} = 0.35$, Fe sat.	$1673, 1723, 1773$
	$Fe_2O_3 - FeO - MgO - SiO_2$	$x_{MgO} = 0 - 0.6$, $x_{SiO_2} = 0.4$, Fe sat.	$1673, 1723, 1773$
	$Fe_2O_3 - FeO - CaO - SiO_2$	$x_{CaO} = 0 - 0.67$, $x_{SiO_2} = 0.33$, Fe sat.	$1573, 1673, 1773$
	$Fe_2O_3 - FeO - CaO - SiO_2$	$x_{CaO} = 0 - 0.575$, $x_{SiO_2} = 0.425$, Fe sat.	$1573, 1673, 1773$

‡ See Figure 6.4

For Fe-free systems, auxi-mpp's ThibodeauEC model closely reproduces the literature model, which itself shows good agreement with experimental data (Thibodeau 2016).

See Figures 6.1 to 6.4 for model performance for unary, binary, ternary and quaternary systems.

For Fe-bearing systems there is a increasing deviation from literature the greater the fraction of iron oxides present. We assume this to be due to a parameter change for FeO in the FactSage's database, as is also mentioned in Section 5.1.6. The effect are presented in Figure 6.5.

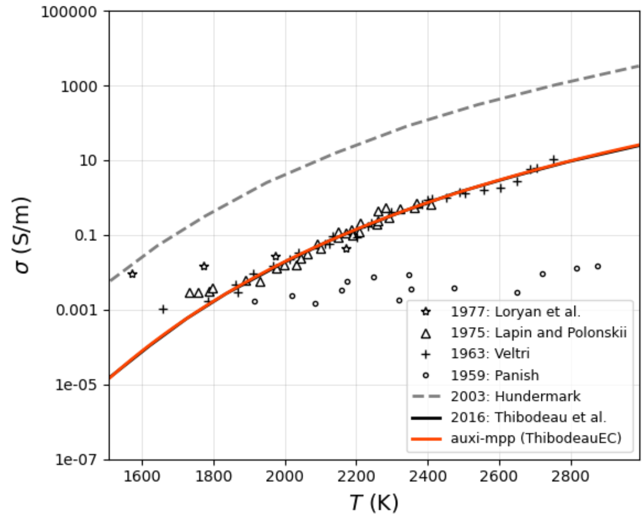

(a) SiO_2

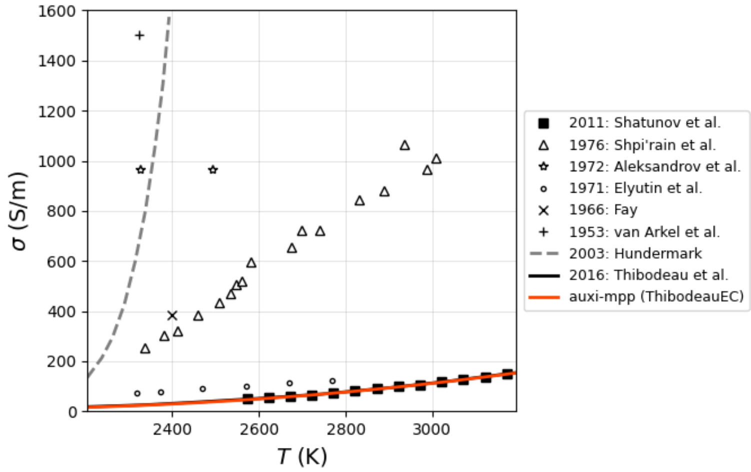

(b) Al_2O_3

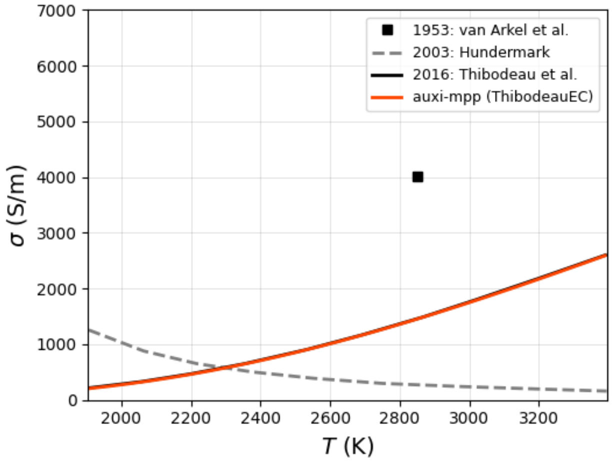

(c) CaO

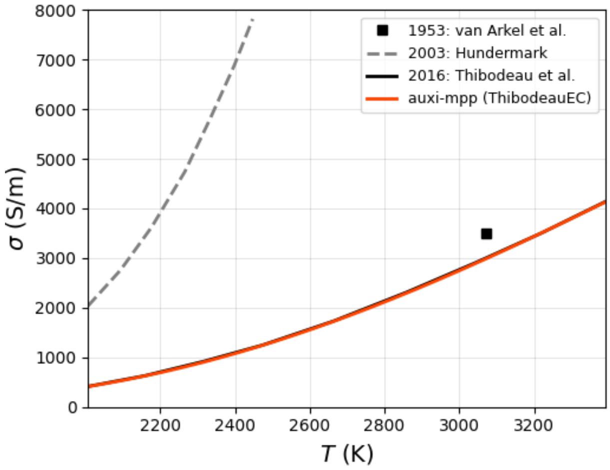

(d) MgO

Figure 6.1: Electrical conductivity vs temperature for unary systems.

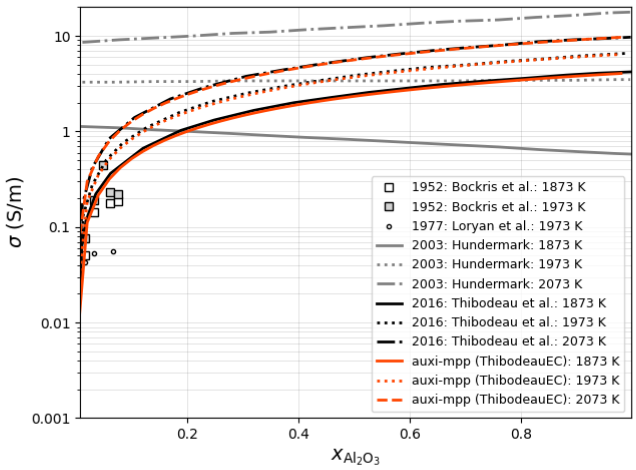

(a) $Al_2O_3 - SiO_2$

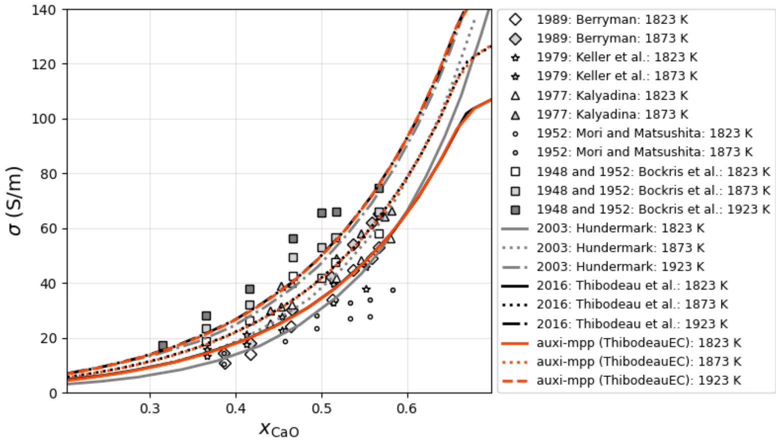

(b) $CaO - SiO_2$

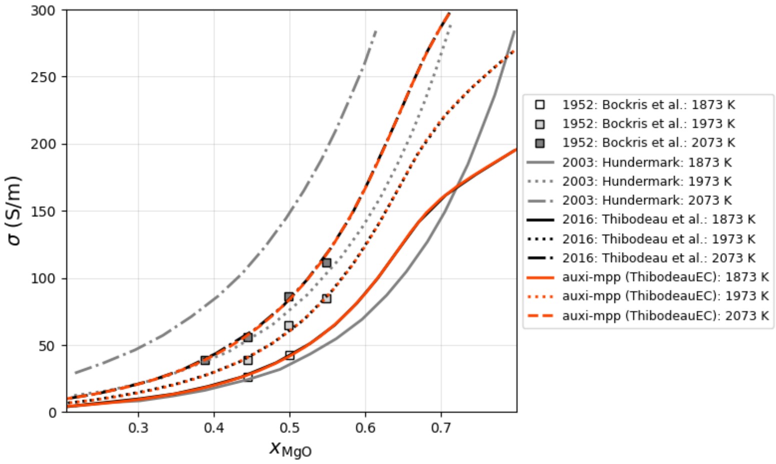

(c) $MgO - SiO_2$

Figure 6.2: Electrical conductivity vs mole fraction of binary systems.

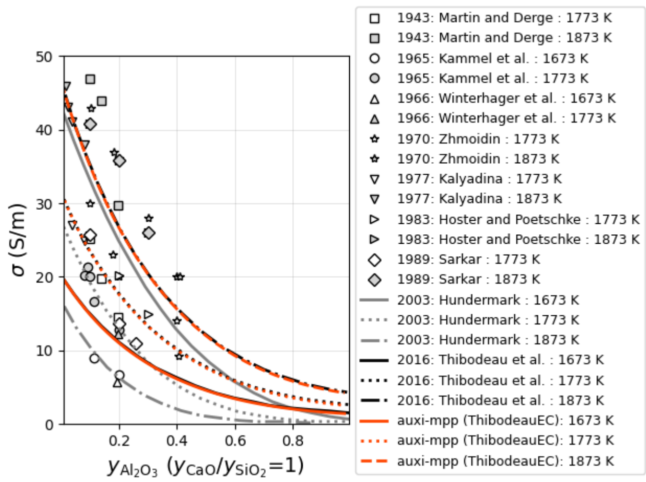

(a) $Al_2O_3 - CaO - SiO_2$

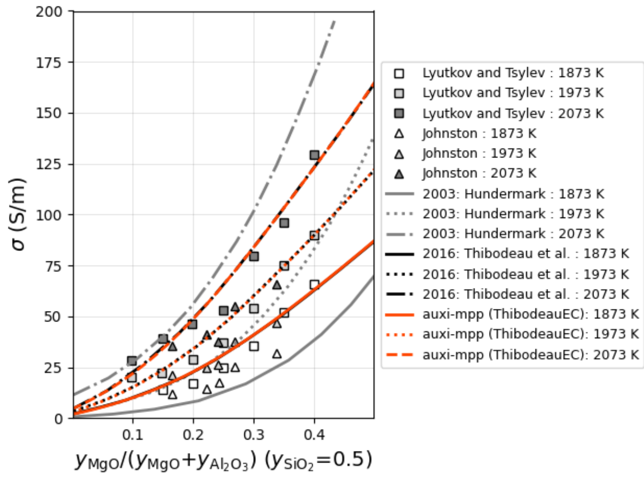

(b) $Al_2O_3 - MgO - SiO_2$

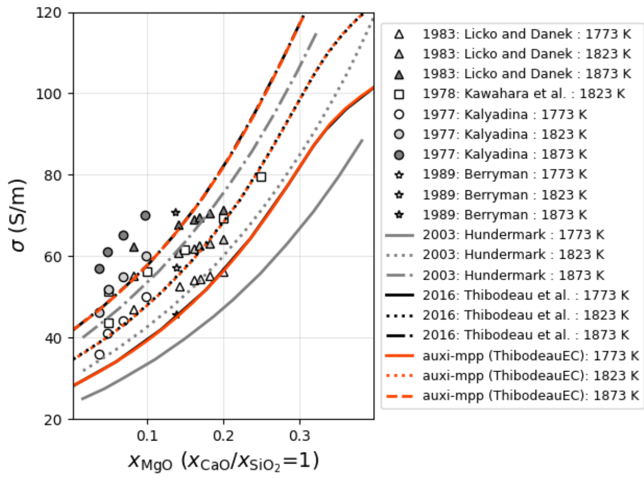

(c) $CaO - MgO - SiO_2$

Figure 6.3: Electrical conductivity vs mole fraction of ternary systems.

When reproducing the contour mapping of electrical conductivity for ternary and quaternary systems, as shown in Figure 6.4, there is not an exact agreement with literature, however.

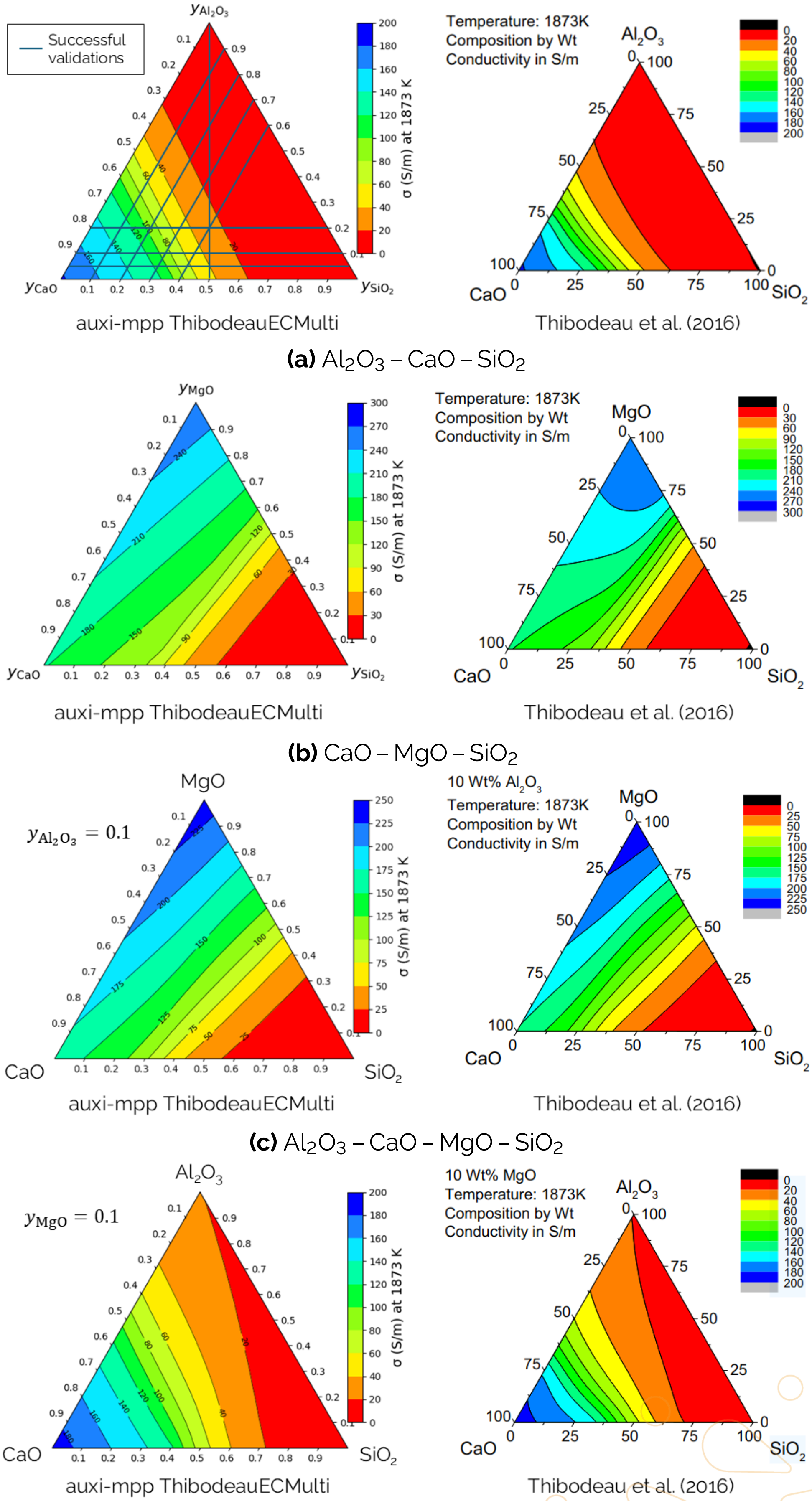

(a) $Al_2O_3 - CaO - SiO_2$

(b) $CaO - MgO - SiO_2$

(c) $Al_2O_3 - CaO - MgO - SiO_2$

(d) $Al_2O_3 - CaO - MgO - SiO_2$

Figure 6.4: Comparing auxi-mpp's contour mapping of electrical conductivity with literature.

We believe this to be a mistake in the literature plots for a few good reasons. Figure 6.4a shows all composition slices for which the model were successfully validated against Thibodeau's own figures. There were no Cartesian plot in Thibodeau (2016) that auxi-mpp could not reproduce. Secondly, the method used to create the plots could exactly reproduce the contour mapping for ternary and quaternary systems for molar volume – see Figure 5.5. This also confirms that there are no issues with the bond fractions used. Finally, calculations performed on selected points in Figures 6.4b to 6.4d consistently agreed with auxi-mpp's mapping. Nevertheless, the contour mappings are relatively close to that in literature.

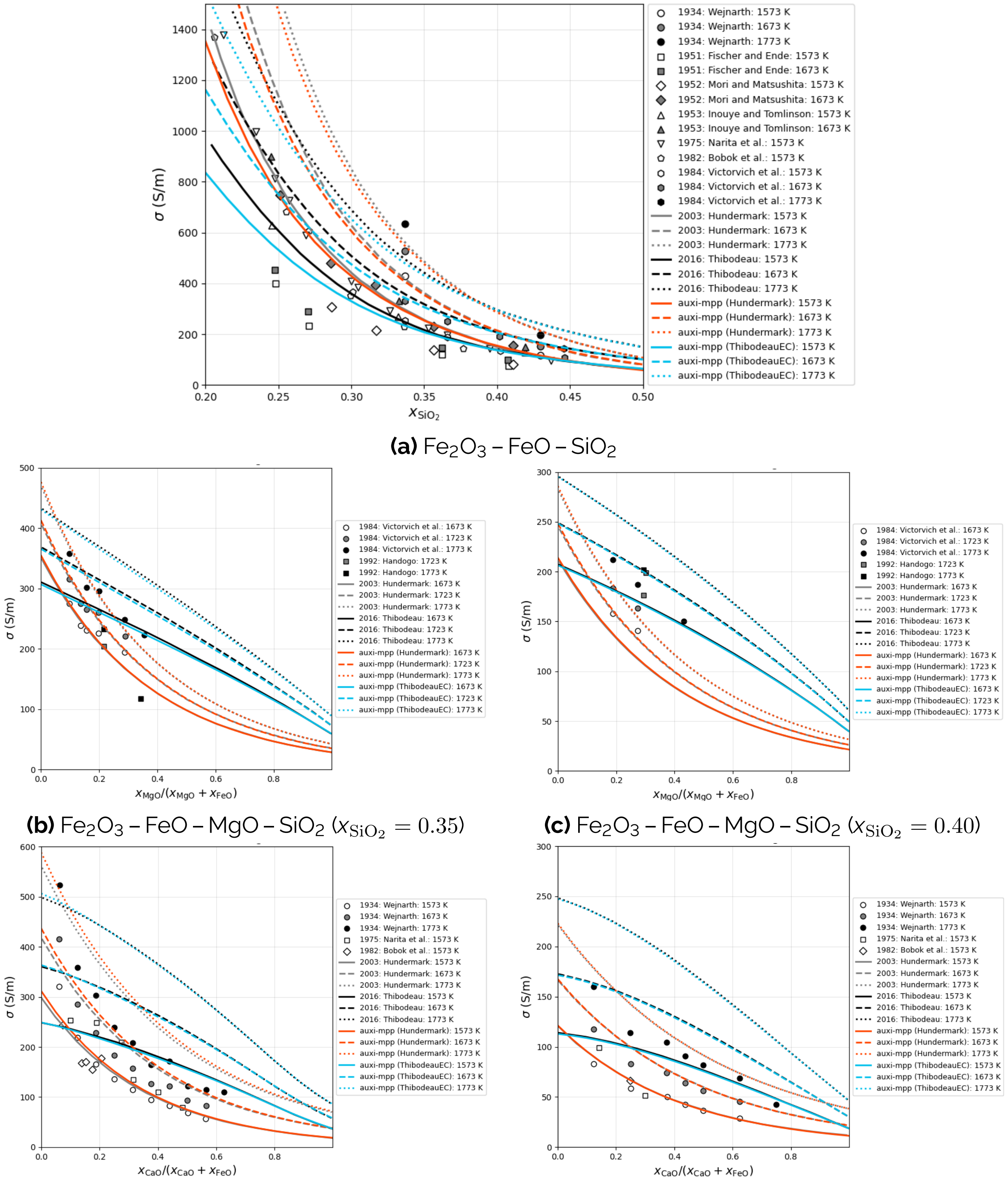

(a) $Fe_2O_3 - FeO - SiO_2$

(b) $Fe_2O_3 - FeO - MgO - SiO_2$ ($x_{SiO_2} = 0.35$)

(c) $Fe_2O_3 - FeO - MgO - SiO_2$ ($x_{SiO_2} = 0.40$)

(d) $CaO - Fe_2O_3 - FeO - SiO_2$ ($x_{SiO_2} = 0.33$)

(e) $CaO - Fe_2O_3 - FeO - SiO_2$ ($x_{SiO_2} = 0.425$)

Figure 6.5: Electrical conductivity vs mole fraction of iron containing systems at iron saturation conditions.

Issues

There likely was a parameter change in FactSage's database for FeO, resulting in a different equilibrium ratio between FeO and Fe_2O_3, and thus also different bond fractions. If we apply Thibodeau's electrical conductivity model to Fe-bearing systems, we no longer obtain the results we were meant to obtain. Luckily, the deviation is not significant enough to render the model unusable.

6.2 Hundermark Electrical Conductivity Models

Models developed by Hundermark (2003).

6.2.1 Introduction

The unified model for estimating the electrical conductivity of melter-type slags, developed by Hundermark (2003), originated from challenges in the electrical control of furnaces used by South African platinum producers. The initial design was an iron-free model for $Al_2O_3 - CaO - MgO - SiO_2$ slags, based on the principle of ionic conduction as the sole operating mechanism. This foundational work was later integrated with data from iron-containing systems to create the comprehensive unified model.

6.2.2 Model Overview

Hundermark's unified model estimates the electrical conductivity of melter-type slags based on their composition, temperature, and oxidation state (Hundermark 2003). It is applicable to slags containing two or more of the following components: Al_2O_3, CaO, FeO_x, MgO, and SiO_2. The model is particularly useful for Fe-bearing slags where other models, like Thibodeau's, have shown to be unreliable (Thibodeau 2014). While empirical, the model provides reasonably accurate estimates for a wide range of slag systems, achieving an average correlation coefficient of 0.9743 with experimental values.

The model was developed by integrating two separate datasets. The first part was a foundational Fe-free model for the $Al_2O_3 - CaO - MgO - SiO_2$ system represented by Equation (6.5). This initial model, which assumed that ionic conduction is the sole mechanism, used multiple linear regressions to correlate slag composition with conductivity, yielding a correlation coefficient of 0.8358 for temperatures between 1623 to 2023 K.

The second part incorporated data from Fe-containing systems. By combining both datasets, the unified model, represented by eq. (6.6), explicitly accounts for the fractions of ferrous (Fe^{2+}) and ferric (Fe^{3+}) ions, allowing it to estimate conductivity changes with varying slag oxidation states.

It is important to note that this model is formulated strictly for liquid slag systems – the user should therefore ensure that his/her system is above the liquidus temperature before performing calculations. Also, we recommend the model to be used within the validation ranges specified in Table 6.2. The validation ranges are based on selected figures from the original articles. To peruse the full range of systems the model were validated for, the user is directed to the original article.

Finally, for systems containing Fe, the correct ratio of Fe(II) and Fe(III) has to be provided. This means the user needs to know the oxidation environment of the system, and from that estimate this ratio before passing it on to the model.

6.2.3 Model Formulation

The model formulation is the foundational Fe-free model is given by Equation (6.5), while the unified model, which includes the contribution of ferrous and ferric ions, is represented by Equation (6.6).

$$\ln \sigma = \left(31.6 - \frac{68048}{T}\right) x_{\mathrm{Al_2O_3}} + \left(-2.2 - \frac{9006}{T}\right) x_{\mathrm{CaO}} + \left(10.5 - \frac{15049}{T}\right) x_{\mathrm{MgO}} + \left(17.1 - \frac{40544}{T}\right) x_{\mathrm{SiO_2}} \tag{6.5}$$

$$\ln \sigma = \left(19.9 - \frac{47348}{T}\right) x_{\mathrm{Al_2O_3}} + \left(15.4 - \frac{24087}{T}\right) x_{\mathrm{CaO}} + \left(9.2 - \frac{14151}{T}\right) x_{\mathrm{MgO}} + \left(-0.5 - \frac{7478}{T}\right) x_{\mathrm{SiO_2}} + \left(10.0 - \frac{9140}{T}\right) x_{\mathrm{FeO}_x} \cdot x_{\mathrm{Fe^{2+}}} + \left(65.4 - \frac{82447}{T}\right) x_{\mathrm{FeO}_x}^2 \cdot x_{\mathrm{Fe^{2+}}} \cdot x_{\mathrm{Fe^{3+}}} + \left(-2.6 + \frac{6642}{T}\right) x_{\mathrm{FeO}_x} \cdot x_{\mathrm{Fe^{3+}}} \tag{6.6}$$

Where σ represents the electrical conductivity, with units of $\mathrm{S\,cm^{-1}}$, x_i is the mole fraction of component i, and T is the temperature in Kelvins. x_{FeO_x} is the equivalent mole fraction of the total ferrous and ferric oxide in the slag, while $x_{\mathrm{Fe^{2+}}}$ and $x_{\mathrm{Fe^{3+}}}$ refer to the ferrous and ferric fractions, respectively.

In auxi-mpp, Equation (6.5) is used when there is no iron in the system, and the unified model given by Equation (6.6) is used when iron is present.

6.2.4 Assumptions

Several assumptions were made in the development of the Hundermark model, which are important to consider when applying the model. These assumptions include:

1. A primary assumption for the Fe-free model is that ionic conduction is the only mechanism operating in these Fe-free systems and it results solely from the movement of cations like Mg^{2+} and Ca^{2+}.
2. The Fe-free model assumes that the temperature dependence of the conductivity obeys the Arrhenius relationship. Furthermore, it was observed and incorporated into the model that the activation energy for conduction and the natural logarithm of the pre-exponential factor are linearly related, following a compensation law.
3. The Fe-free model is specifically developed for slags containing Al_2O_3, CaO, MgO, and SiO_2 in a temperature range of 1623 to 2023 K.
4. The models are fundamentally semi-empirical, meaning they are based on observed relationships and regressions techniques rather than being derived purely from first principles of slag structure or ion transport mechanisms.
5. The unified model is specifically designed for slags containing two or more of Al_2O_3, CaO, FeO_x, MgO, and SiO_2 components, and a temperature range of 1623 to 2023 K.
6. Only electrical conductivity data for fully molten slags (above their liquidus temperature) were considered for the models' development to avoid inconsistencies arising from the presence of solid phases.

6.2.5 Literature Inaccuracies

To validate the implemented Hundermark model, we had to test it against the model performance as presented by Thibodeau (2016) and Thibodeau (2014), due to a lack of performance figures in Hundermark's documentation. The performance validated against is therefore not from the original author, adding a layer of uncertainty to it. We reason that this extra link in the chain is the cause of the deviation seen when validating systems containing Al_2O_3. We discovered that when Al_2O_3's temperature coefficient in Equation (6.5) is entered as 69048 instead of 68048, the model's performance match with that presented by Thibodeau (2016), as shown in Figures 6.6 and 6.7.

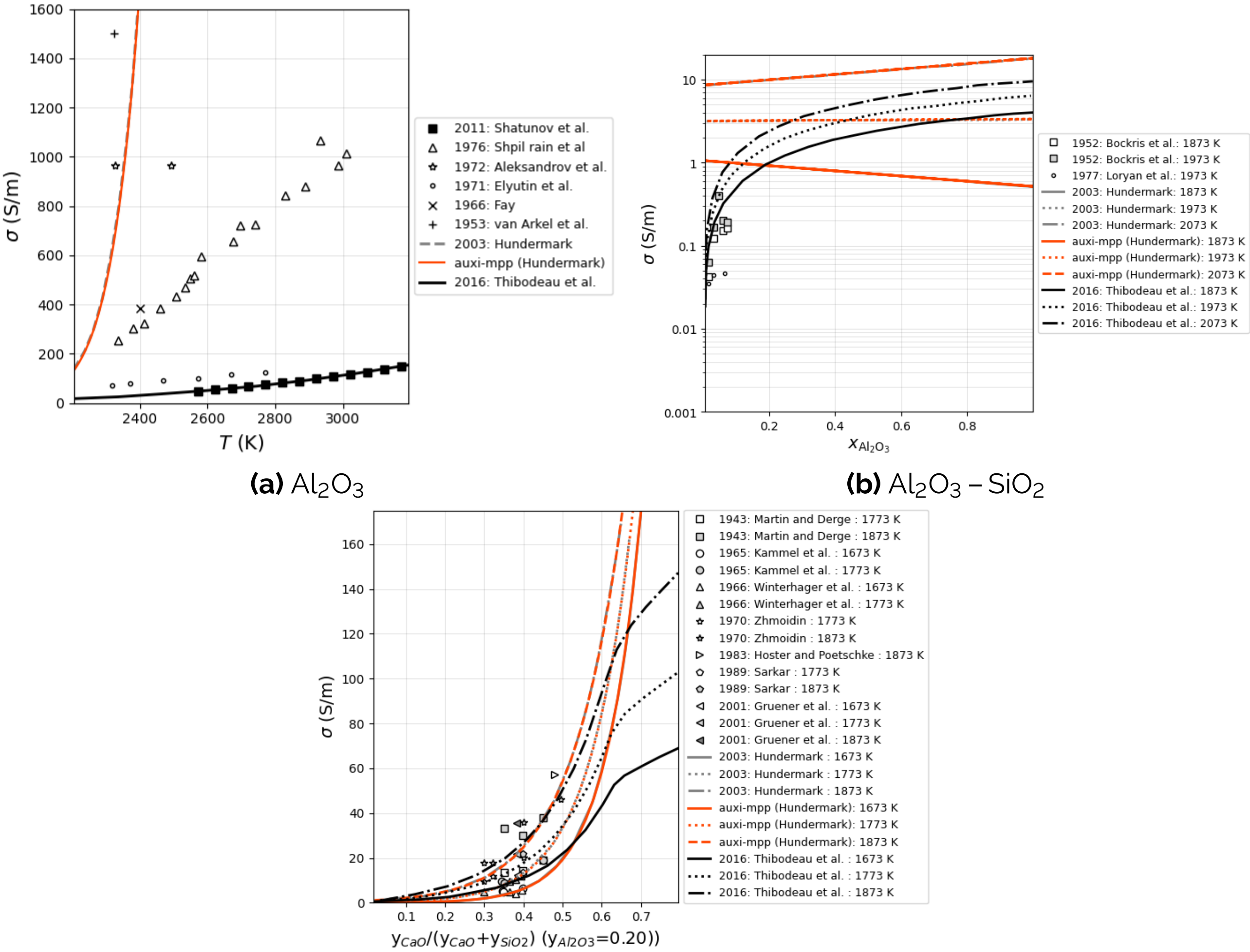

(a) Al_2O_3 **(b)** $Al_2O_3 - SiO_2$

(c) $Al_2O_3 - CaO - SiO_2$

Figure 6.6: Hundermark's performance with Al_2O_3's temperature coefficient as 69048, instead of 68048.

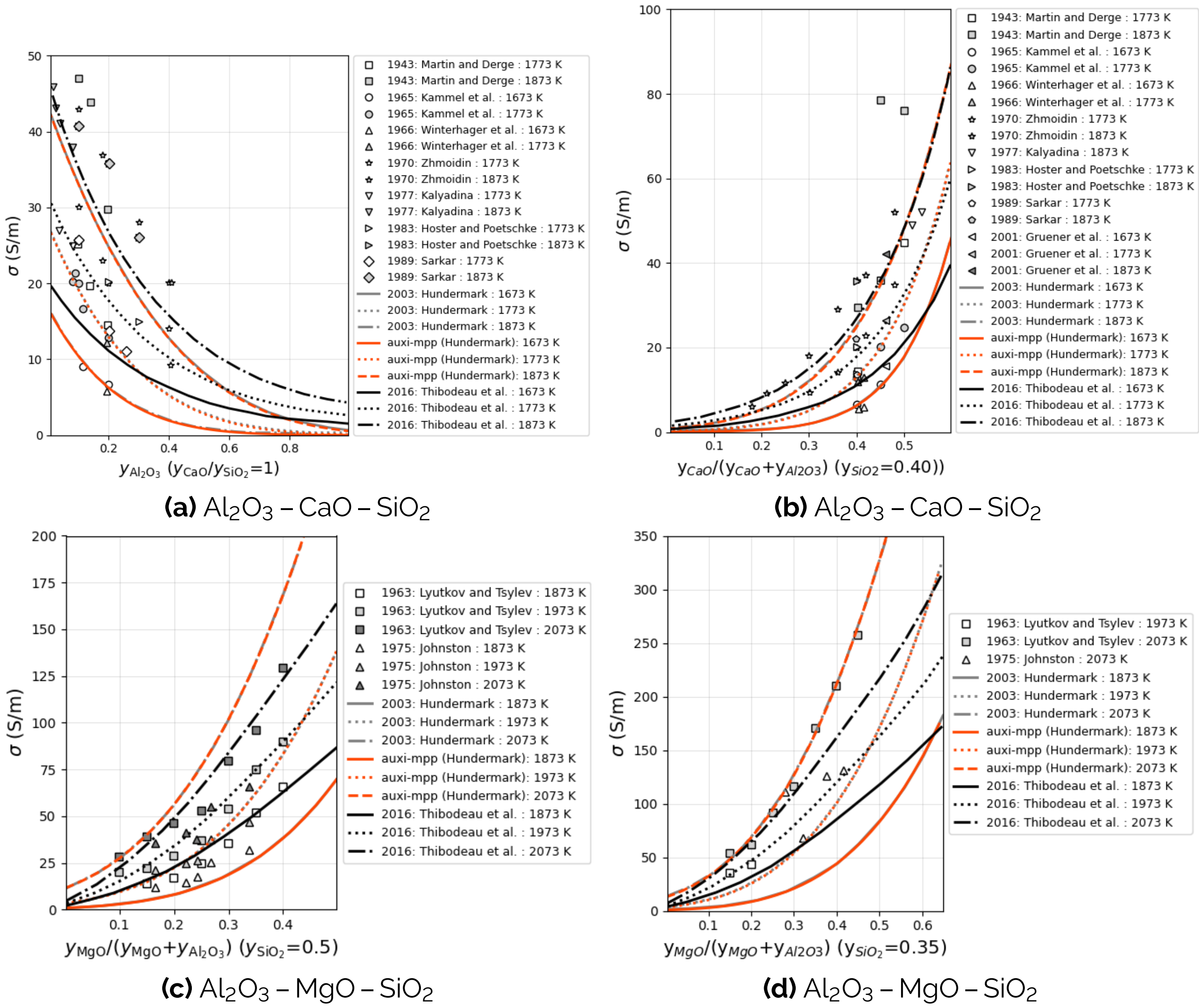

(a) $Al_2O_3 - CaO - SiO_2$ **(b)** $Al_2O_3 - CaO - SiO_2$

(c) $Al_2O_3 - MgO - SiO_2$ **(d)** $Al_2O_3 - MgO - SiO_2$

Figure 6.7: Hundermark's performance with Al_2O_3's temperature coefficient as 69048, instead of 68048.

As the original value for this coefficient, as determined by Hundermark himself, is 68048, we will assume this to be the correct value, and thus assume that Thibodeau made an error here.

6.2.6 Model Validation

Hundermark's electrical conductivity model, implemented in auxi-mpp, was validated against literature model data and experimental data extracted from Thibodeau (2016) and Thibodeau (2014), as Hundermark (2003) did not offer such plots for validation. The systems and temperatures for which the models were validated are given in Table 6.2.

Table 6.2: Electrical Conductivity Hundermark Model Validation Ranges

Model	Systems	Composition	Temperature (K)
Unary	SiO_2	pure substance	$1500 - 3000$
	Al_2O_3	pure substance	$2200 - 2400$
	MgO	pure substance	$2000 - 2450$
	CaO	pure substance	$1800 - 3400$
Binary	$Al_2O_3 - SiO_2$	$x_{\mathrm{Al_2O_3}} = 0 - 1$	$1873, 1973, 2073$
	$CaO - SiO_2$	$x_{\mathrm{CaO}} = 0.2 - 0.7$	$1823, 1873, 1923$
	$MgO - SiO_2$	$x_{\mathrm{MgO}} = 0.2 - 0.8$	$1873, 1973, 2073$
Ternary	$Al_2O_3 - CaO - SiO_2$	$y_{\mathrm{Al_2O_3}} = 0 - 1$, $y_{\mathrm{CaO}}/y_{\mathrm{SiO_2}} = 1$	$1673, 1773, 1873$
	$Al_2O_3 - CaO - SiO_2$	$y_{\mathrm{CaO}} = 0 - 0.8$, $y_{\mathrm{SiO_2}} = 0.2$	$1673, 1773, 1873$
	$Al_2O_3 - CaO - SiO_2$	$y_{\mathrm{CaO}} = 0 - 0.6$, $y_{\mathrm{SiO_2}} = 0.4$	$1673, 1773, 1873$
	$Al_2O_3 - MgO - SiO_2$	$y_{\mathrm{MgO}} = 0 - 0.65$, $y_{\mathrm{SiO_2}} = 0.35$	$1873, 1973, 2073$
	$Al_2O_3 - MgO - SiO_2$	$y_{\mathrm{MgO}} = 0 - 0.5$, $y_{\mathrm{SiO_2}} = 0.5$	$1873, 1973, 2073$
	$CaO - MgO - SiO_2$	$x_{\mathrm{MgO}} = 0 - 0.4$, $x_{\mathrm{CaO}}/x_{\mathrm{SiO_2}} = 1$	$1773, 1823, 1873$
Iron Containing	$Fe_2O_3 - FeO - SiO_2$	$x_{\mathrm{SiO_2}} = 0.2 - 0.5$, Fe sat.	$1573, 1673, 1773$
	$Fe_2O_3 - FeO - MgO - SiO_2$	$x_{\mathrm{MgO}} = 0 - 0.65$, $x_{\mathrm{SiO_2}} = 0.35$, Fe sat.	$1673, 1723, 1773$
	$Fe_2O_3 - FeO - MgO - SiO_2$	$x_{\mathrm{MgO}} = 0 - 0.6$, $x_{\mathrm{SiO_2}} = 0.4$, Fe sat.	$1673, 1723, 1773$
	$Fe_2O_3 - FeO - CaO - SiO_2$	$x_{\mathrm{CaO}} = 0 - 0.67$, $x_{\mathrm{SiO_2}} = 0.33$, Fe sat.	$1573, 1673, 1773$
	$Fe_2O_3 - FeO - CaO - SiO_2$	$x_{\mathrm{CaO}} = 0 - 0.575$, $x_{\mathrm{SiO_2}} = 0.425$, Fe sat.	$1573, 1673, 1773$

For the validation of systems containing Al_2O_3, we accept that Thibodeau (2016) likely made a simple error in the temperature coefficient for Al_2O_3 in Equation (6.5), as explained in Section 6.2.5. With that said, for Fe-free systems auxi-mpp's implementation of Hundermark's Fe-free model closely reproduces the literature model for all systems tested. See Figures 6.8 to 6.10 for model performance for unary, binary and ternary systems.

On the other hand, auxi-mpp's implementation of Hundermark's unified model, which incorporates iron, slightly deviates from literate the greater the fraction of iron oxides present. We assume this to be due to a parameter change for FeO in the FactSage's database, as is also mentioned in Section 5.1.6. The effect are presented in Figure 6.11.

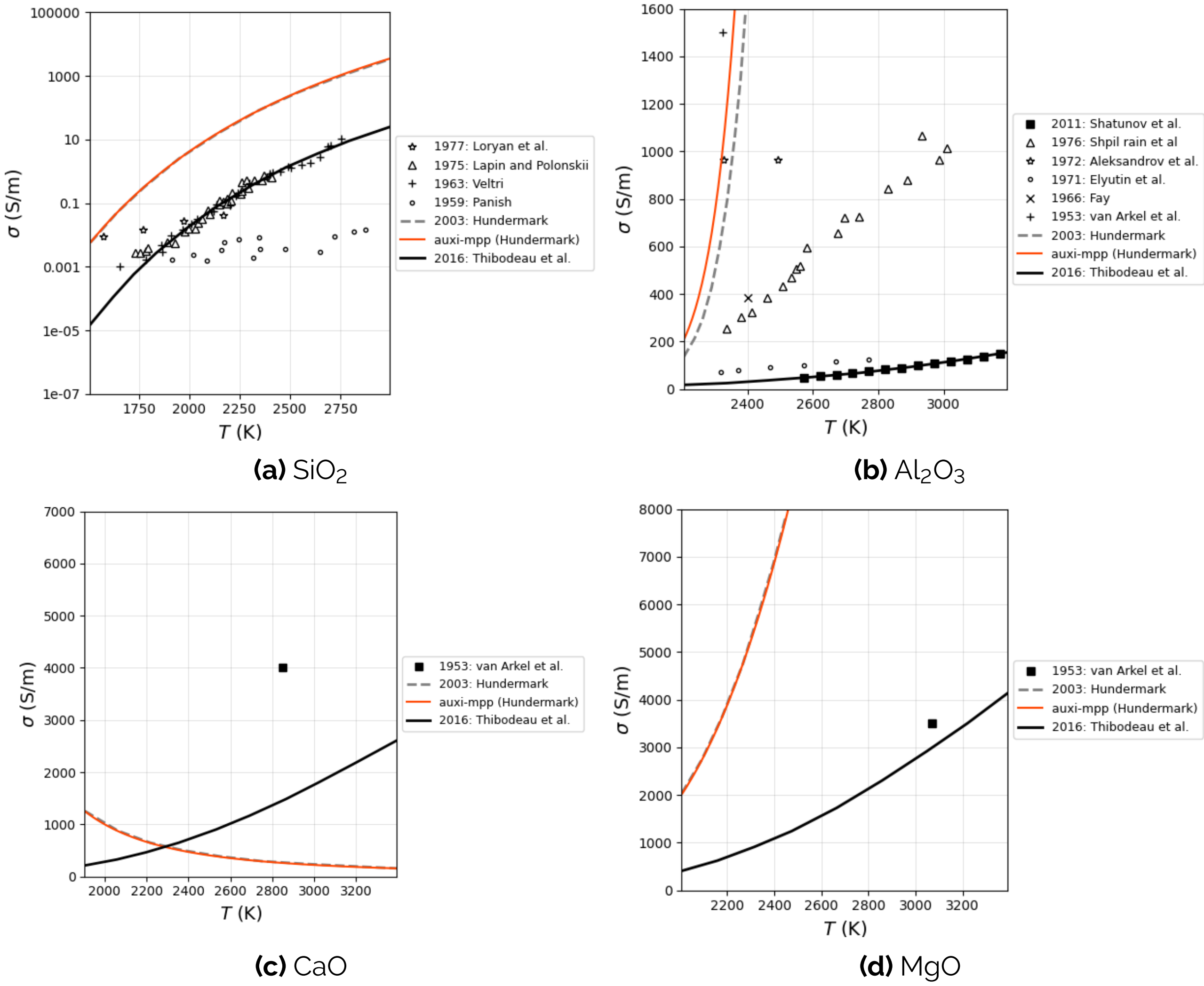

Figure 6.8: Electrical conductivity vs temperature for unary systems.

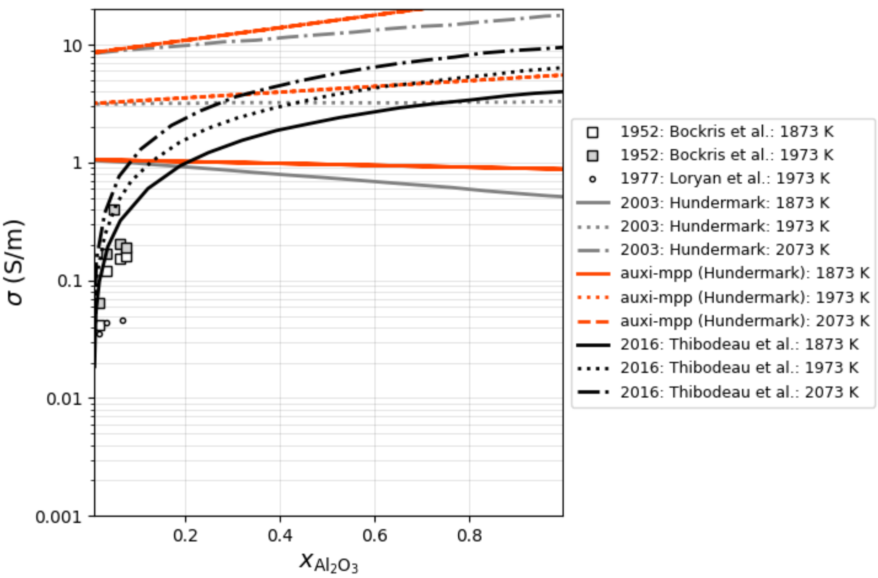

(a) $Al_2O_3 - SiO_2$

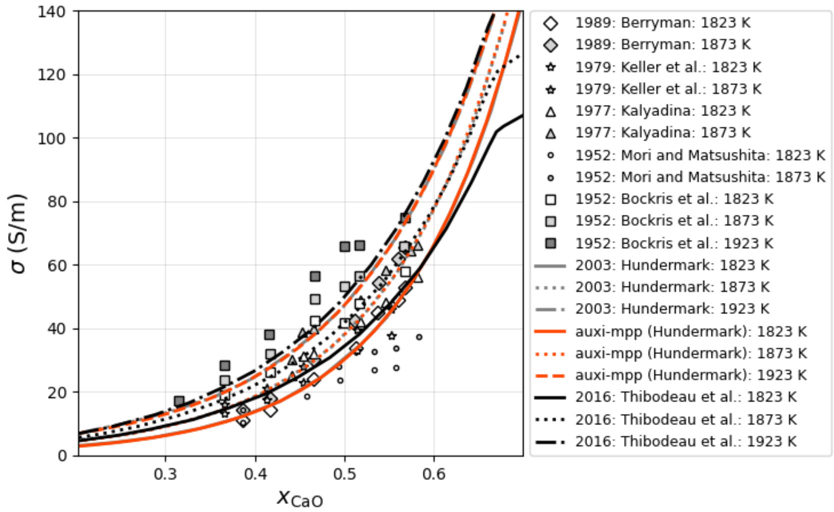

(b) $CaO - SiO_2$

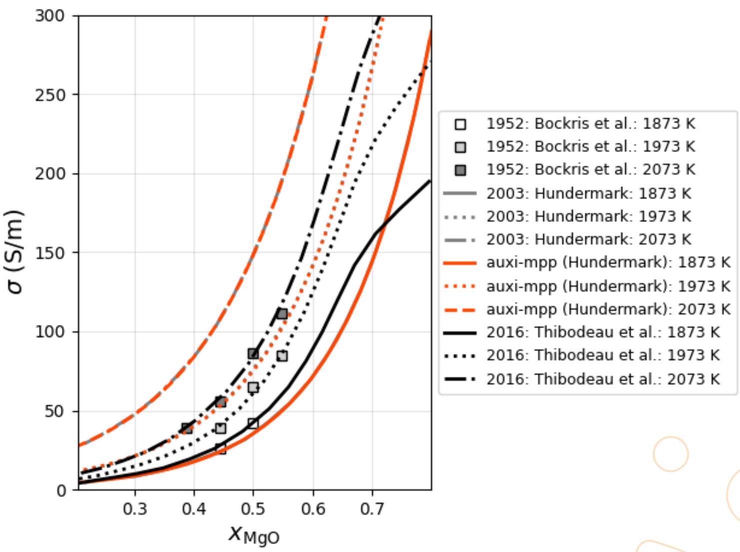

(c) $MgO - SiO_2$

Figure 6.9: Electrical conductivity vs mole fraction of binary systems.

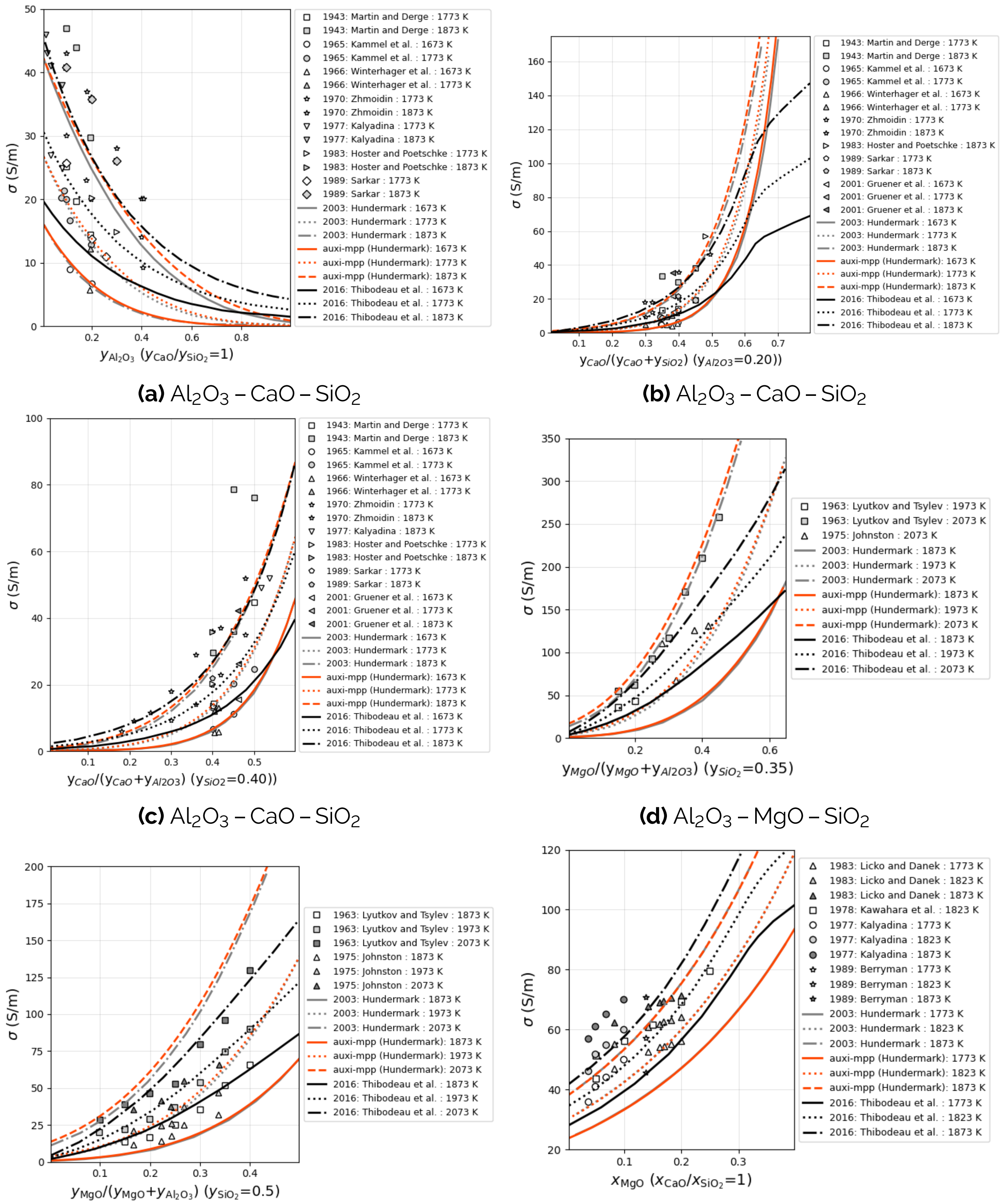

(a) $Al_2O_3 - CaO - SiO_2$ **(b)** $Al_2O_3 - CaO - SiO_2$

(c) $Al_2O_3 - CaO - SiO_2$ **(d)** $Al_2O_3 - MgO - SiO_2$

(e) $Al_2O_3 - MgO - SiO_2$ **(f)** $CaO - MgO - SiO_2$

Figure 6.10: Electrical conductivity vs mole fraction of ternary systems that does not contain iron.

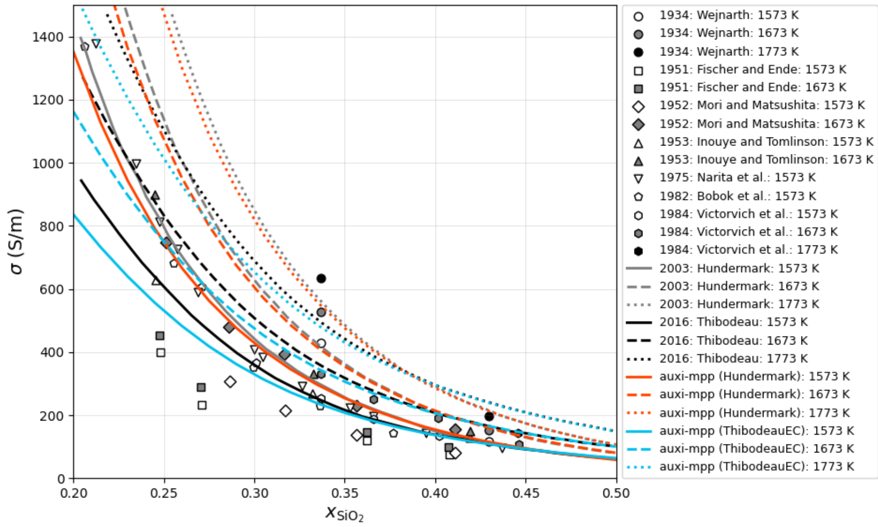

(a) $Fe_2O_3 - FeO - SiO_2$

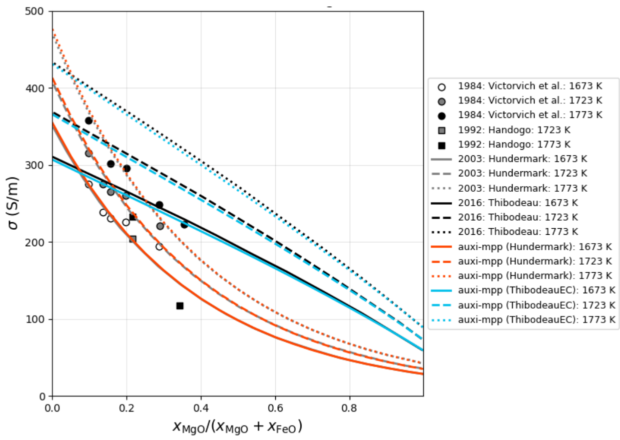

(b) $Fe_2O_3 - FeO - MgO - SiO_2$ ($x_{SiO_2} = 0.35$)

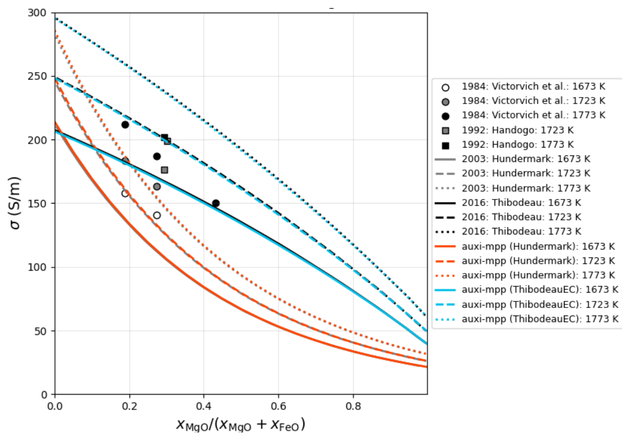

(c) $Fe_2O_3 - FeO - MgO - SiO_2$ ($x_{SiO_2} = 0.40$)

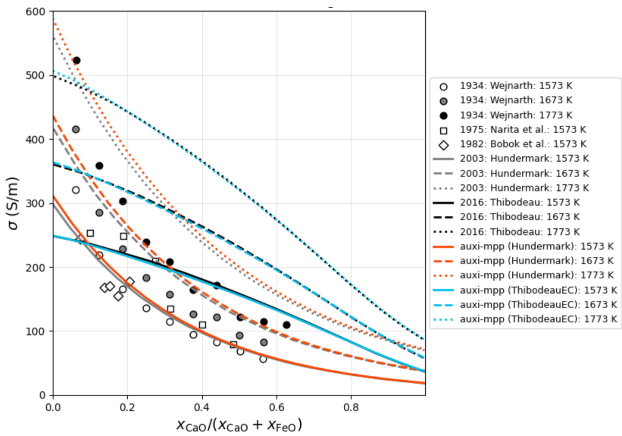

(d) $CaO - Fe_2O_3 - FeO - SiO_2$ ($x_{SiO_2} = 0.33$)

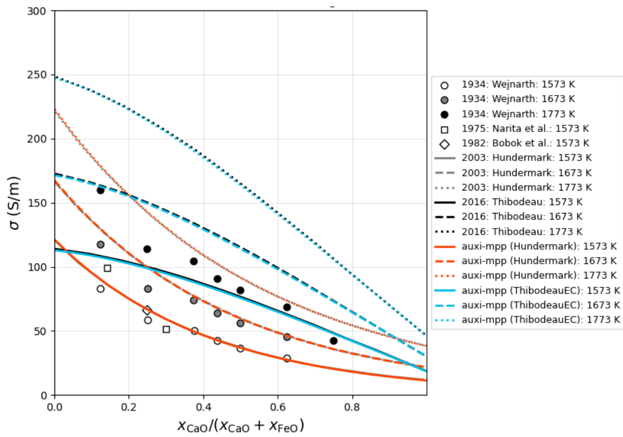

(e) $CaO - Fe_2O_3 - FeO - SiO_2$ ($x_{SiO_2} = 0.425$)

Figure 6.11: Electrical conductivity vs mole fraction of iron containing systems at iron saturation conditions.

Issues

There likely was a parameter change in FactSage's database for FeO, resulting in a different equilibrium ratio between FeO and Fe_2O_3. If we then maintain the coefficients of Hundermark's model, we no longer obtain the results we were meant to obtain. Luckily, the deviation is not significant enough to render the model unusable.

Chapter 7

Diffusivity

7.1 Thibodeau Diffusivity Model

A model implemented by Thibodeau (2016).

7.1.1 Introduction

As with all physical properties, the diffusivity is also affected by the structure of the slag. The higher the polymerisation, the more rigid the slag structure and therefore the more difficult particles will diffuse through it. A model that calculates diffusivity (diffusion coefficients) from slag polymerisation is thus presented here.

7.1.2 Model Overview

Variations in slag composition affecting polymerisation are accounted for using bond fractions, calculated with the MQM model in ChemApp for Python and data from FactSage's FToxid database. The model's parameters for individual cations are determined using data from unary and binary silicate systems, and is capable of estimating the electrical conductivity of higher-order systems without additional parameters.

The bond fractions with the model parameters are then used to scale the activation energy that dictates the rate of diffusion. This is done in an Arrhenius-like equation which is similar to Equation (7.1). Arrhenius-like equations are typically used to calculate temperature dependence for reaction rates.

$$D = A\exp\left(-\frac{E}{RT}\right) \tag{7.1}$$

It is important to note that this model is formulated strictly for liquid slag systems – the user should therefore ensure that his/her system is above the liquidus temperature before performing calculations. Finally, for systems containing Fe, the correct ratio of Fe(II) and Fe(III) has to be provided. This means the user needs to know the oxidation environment of the system, and from that estimate this ratio before passing it on to the model.

7.1.3 Model Formulation

The diffusivity used in the calculation of the electrical conductivity described in Equation (6.2), is determined in Equation (7.2) with parameters for systems containing network formers such as SiO_2 and Al_2O_3.

$$D_{\mathrm{i}} = A_{\mathrm{i}}\exp\left(-\frac{B_{\mathrm{i}} + C_{\mathrm{i-SiSi}}x_{\mathrm{Si-Si}} + C_{\mathrm{i-SiAl}}x_{\mathrm{Si-Al}} + C_{\mathrm{i-AlAl}}x_{\mathrm{Al-Al}}}{RT}\right) \tag{7.2}$$

The bond fractions ($x_{\mathrm{i-j}}$) calculated from the MQM model are combined with the parameters A_{i}, B_{i}, and C_{i} from Thibodeau (2016).

This model is limited to the following cations; Mg^{2+}, Ca^{2+}, Mn^{2+}, Pb^{2+}, Fe^{2+}, Fe^{3+},Al^{3+}, and Si^{4+}.

7.1.4 Variable Declarations

The parameters used in the model are extracted from Thibodeau (2014) and are given in Table 7.1.

Table 7.1: Electrical Conductivity Parameters (Thibodeau 2014)

	A_{i} ($\mathrm{cm^2\,s^{-1}}$)	B_{i} ($\mathrm{kJ\,mol^{-1}}$)	$C_{\mathrm{i-SiSi}}$ ($\mathrm{kJ\,mol^{-1}}$)	$C_{\mathrm{i-AlAl}}$ ($\mathrm{kJ\,mol^{-1}}$)	$C_{\mathrm{i-AlSi}}$ ($\mathrm{kJ\,mol^{-1}}$)
Mg^{2+}	0.03448	118.6	42.1	10.0	10.0
Ca^{2+}	0.02600	115.0	35.0	35.0	35.0
Mn^{2+}	0.05421	104.2	55.4	20.0	20.0
Pb^{2+}	0.00936	65.4	90.4	90.4	90.4
Fe^{2+}	0.04200	95.0	-	-	-
Fe^{3+}	0.00358	158.3	-	-	-
Al^{3+}	0.00358	158.3	-	-	-
Si^{4+}	5.22600	380.9	-	-	-

7.1.5 Assumptions

In this diffusivity model, the following assumptions were made.

1. It is assumed that the activation energy of the ionic conductivity is linearly increasing with the bond fractions of Si – Si and Al – Al.
2. It is assumed that that $C_{\mathrm{i-SiAl}}$ will be equal to $C_{\mathrm{i-AlAl}}$, instead of the average between $C_{\mathrm{i-AlAl}}$ and $C_{\mathrm{i-SiSi}}$. This is because it will be significantly more likely for the cations to take the lower energy route, which is on the Al side of the bond.
3. It is assumed that Al_2O_3 behaves like a network former, despite its amphoteric behaviour.
4. Parameters for Fe^{3+} were fixed to the same values as Al^{3+} as there was no data available capable of providing a better first estimate.

7.1.6 Simplifications

For applying Equation (7.2), interactions between diffusing network modifier cations are neglected. This simplifies the model, allowing it to estimate diffusion coefficients of higher-order systems from unary and binary parameters without additional parameters.

7.1.7 Model Validation

This model is not independently used or implemented due to lack of literature data for comparison. However, Chapter 6's electrical conductivity estimates incorporate the diffusivity model's results. This model was successfully validated and thereby indirectly validates the diffusivity model.

Chapter 8

Viscosity

8.1 Grundy-Kim-Brosch Viscosity Model

Model developed by Grundy et al. (2008b), Grundy et al. (2008b), Kim (2011), and Brosh et al. (2012).

8.1.1 Introduction

The Grundy-Kim-Brosch viscosity model, which accounts for silicate structure estimated using the MQM model with ChemApp for Python and the FactSage FToxid database, is currently implemented for unary through multi component systems containing SiO_2, CaO, MgO, Al_2O_3, FeO and Fe_2O_3.

8.1.2 Model Overview

The principle equation implemented in the model to calculate the viscosity (μ) for a slag is an Arrhenius-like equation, Equation (8.1). It is a function of both temperature and composition where μ is the viscosity in Pa s, R is the gas constant and T is the temperature in Kelvin.

$$\ln(\mu) = A + \frac{E}{RT} \tag{8.1}$$

The parameters A and E depends on the slag composition. For unary systems the compound specific A and E parameters are simply plugged into Equation (8.1) together with the system temperature. However, with silicate binary or multicomponent systems, A and E are not only determined by the pure substance character, but also by the interaction between the components and by the degree of polymerisation.

It is important to note that this model is formulated strictly for liquid slag systems – the user should therefore ensure that his/her system is above the liquidus temperature before performing calculations. Also, we recommend the model to be used within the validation ranges specified in Table 8.3 and Figure 8.8. The validation ranges are based on selected figures from the original articles. To peruse the full range of systems the model were validated for, the user is directed to the original article.

Finally, for systems containing Fe, the correct ratio of Fe(II) and Fe(III) has to be provided. This means the user needs to know the oxidation environment of the system, and from that estimate this ratio before passing it on to the model.

8.1.3 Unary and Binary Model Formulation

Unary Model

For unary systems, Equation (8.1) is used directly, where A and E are unique to each component. For systems containing two or more components, the structure of the slag becomes more complex, requiring A and E to be estimated based on several structural contributions.

Binary Model

Starting with the Arrhenius-like equation, Equation (8.1), instead of using a single parameter for A and E, these are weighted based on different structural contributions. For binary sytsems, A is calculated as in Equation (8.2);

$$A = A_{\mathrm{M}} x_{\mathrm{M}}^{\$_0} + x_{\mathrm{Si}}^{\$_0} [A^{*}_{\mathrm{SiO_2}} + A^{\mathrm{E}}_{\mathrm{SiO_2}} p^{40} + A_{\mathrm{M-Si}} x_{\mathrm{M}}^{\$_0} + A^{\mathrm{R}}_{\mathrm{M-Si}} (p^4 - p^{40})] \tag{8.2}$$

and E is calculated as in Equation (8.3);

$$E = E_{\mathrm{M}} x_{\mathrm{M}}^{\$_0} + x_{\mathrm{Si}}^{\$_0} [E^{*}_{\mathrm{SiO_2}} + E^{\mathrm{E}}_{\mathrm{SiO_2}} p^{40} + E_{\mathrm{M-Si}} x_{\mathrm{M}}^{\$_0} + E^{\mathrm{R}}_{\mathrm{M-Si}} (p^4 - p^{40})] \tag{8.3}$$

where p is a probability factor used to estimate the degree of polymerisation in the system, and is calculated in Equation (8.4).

Estimating Polymerisation

Silicate melt structure is defined by the bridging behaviour of oxygen atoms, influencing the polymerisation of SiO_4 tetrahedra into three-dimensional networks. The degree of polymerisation, quantified by the average number of bridging oxygens around silicon, can be estimated from bond fractions calculated using the MQM. The first step to estimate the degree of polymerisation is to know the probability for a given Si atom to form one Si – Si bridge. This propapility is given by p in Equation (8.4).

$$p = \frac{2n_{\mathrm{Si-Si}}}{2n_{\mathrm{Si-Si}} + \sum_M n_{\mathrm{Si-M}}} \tag{8.4}$$

$$= \frac{x_{\mathrm{Si-Si}}}{2x_{\mathrm{Si-Si}} + \sum_M x_{\mathrm{Si-M}}} \tag{8.5}$$

As a first approximation, p can be calculated by dividing the total number of Si – Si bridges from all silicon atoms by the combined total of Si – Si and Si – M bridges. Each Si – Si bridge is counted twice since an O^0 bond emanates from each silicon atom in the bridge.

The probability that a given silicon atom is a Q^4-species is p^4, as this atom is connected to four Si – Si bridges. This principle extends to Si – Si bridges forming chains. The probability of encountering m Si – Si bridges connected to form a chain of length m is proportional to p^{m}.

Thus, p^{m}, where m is a natural number, serves as a measure of the abundance of various Si – Si cluster sizes present in the slag (Kim et al. 2012a). A critical cluster size can be defined to represent the formation of a percolating SiO_2 network. Once this cluster size is reached, the μ increases dramatically. Analysis of the viscosity data suggests that a cluster of 40 interconnected Si – Si pairs is an appropriate choice for the critical cluster size (Kim et al. 2012a).

8.1.4 Multicomponent Model Formulation

Systems Without Alumina

For the implemented model, both A and E are functions of slag composition, $\boldsymbol{x}$, and are expressed in terms of multiple additional contributing parameters shown in Equation (8.6) and Equation (8.7). These equations provide estimates for A and E for unary, binary, and multi-component systems, with the primary constraint of having the appropriate optimised binary parameters to describe the system of interest. As indicated by Equation (8.6) and Equation (8.7), each individual parameter within these equations are multiplied with ionic compositions of $x_{\mathrm{Si}}^{\$_0}$ or $x_{\mathrm{M}}^{\$_0}$ to account for their contributions to the overall viscosity of the slag.

Therefore, it is important to note that the input compositions that are generally expressed with the formulas of the oxide components, need to be converted to ionic compositions ($x_{\mathrm{SiO_2}}^{\$_{\mathrm{f}}} \rightarrow x_{\mathrm{Si}}^{\$_0}$) to be used in the model.

$$
\begin{aligned}
A = & \sum_{\mathrm{M=Na,Ca,Mg,...}} A_{\mathrm{M}} x_{\mathrm{M}}^{\$_0} + A_{\mathrm{Si}}^{*} x_{\mathrm{Si}}^{\$_0} + A_{\mathrm{Si}}^{E} x_{\mathrm{Si}}^{\$_0} p^{40} \\
& + \sum_{\mathrm{M}} A_{\mathrm{M-Si}} x_{\mathrm{M}}^{\$_0} x_{\mathrm{Si}}^{\$_0} + x_{\mathrm{Si}}^{\$_0} (p^4 - p^{40}) \times \sum_{\mathrm{M}} A_{\mathrm{M-Si}}^{R} \frac{x_{\mathrm{M}}^{\$_0}}{\sum_{\mathrm{M}} x_{\mathrm{M}}^{\$_0}}
\end{aligned}
\tag{8.6}
$$

$$
\begin{aligned}
E = & \sum_{\mathrm{M=Na,Ca,Mg,...}} E_{\mathrm{M}} x_{\mathrm{M}}^{\$_0} + E_{\mathrm{Si}}^{*} x_{\mathrm{Si}}^{\$_0} + E_{\mathrm{Si}}^{E} x_{\mathrm{Si}}^{\$_0} p^{40} \\
& + \sum_{\mathrm{M}} E_{\mathrm{M-Si}} x_{\mathrm{M}}^{\$_0} x_{\mathrm{Si}}^{\$_0} + x_{\mathrm{Si}}^{\$_0} (p^4 - p^{40}) \times \sum_{\mathrm{M}} E_{\mathrm{M-Si}}^{R} \frac{x_{\mathrm{M}}^{\$_0}}{\sum_{\mathrm{M}} x_{\mathrm{M}}^{\$_0}}
\end{aligned}
\tag{8.7}
$$

Background to these individual parameters is given as follows.

The parameters A_{M} and E_{M} are the contributions to the viscosity of the pure liquid oxides MO_x, Equation (8.8). These are non-network formers.

$$
\ln \mu_{\mathrm{MO_x}} = A_{\mathrm{M}} + \frac{E_{\mathrm{M}}}{RT}
\tag{8.8}
$$

Similarly, Equation (8.9), describes the hypothetical viscosity of SiO_2 if it behaved as a basic oxide and did not form a network.

$$\ln \mu^{*}_{\mathrm{SiO_2}} = A^{*}_{\mathrm{Si}} + \frac{E^{*}_{\mathrm{Si}}}{RT} \tag{8.9}$$

The excess contribution per Si atom from large clusters of Q^4-species, where a silicon atom is at the center of a group containing at least 40 interconnected Si – Si pairs, is proportional to p^{40}. This contribution is expressed through $A^{\mathrm{E}}_{\mathrm{Si}}$ and $E^{\mathrm{E}}_{\mathrm{Si}}$. For a system with a composition of $x^{\$_0}_{\mathrm{Si}}$, the clustering effect is given by $x^{\$_0}_{\mathrm{Si}} \cdot p^{40}$, as shown in Equation (8.6) and Equation (8.7).

By combining the contributions of $A^{\mathrm{E}}_{\mathrm{Si}}$ and $E^{\mathrm{E}}_{\mathrm{Si}}$ with those of A^{*}_{Si} and E^{*}_{Si}, and assuming that the excess contributions of the silica network are independent of other cations M, the viscosity of pure SiO_2 can be calculated using Equation (8.10).

$$\ln \mu_{\mathrm{SiO_2}} = (A^{*}_{\mathrm{Si}} + A^{E}_{\mathrm{Si}}) + \frac{(E^{*}_{\mathrm{Si}} + E^{E}_{\mathrm{Si}})}{RT} \tag{8.10}$$

The excess contribution per Si atom from the remaining Q^4-species, particularly from smaller clusters with fewer than 40 interconnected Si – Si pairs, is proportional to (p^4 - p^{40}). These smaller clusters, containing less than 40 Si – Si pairs, also affect viscosity and interact more directly with other oxides in the slag. The M cations are positioned closer to a given Si atom, making their contribution to viscosity system-dependent, and are combined with the binary parameters $A^{\mathrm{R}}_{\mathrm{M-Si}}$ and $E^{\mathrm{R}}_{\mathrm{M-Si}}$.

Finally, the binary parameters $A_{\mathrm{M-Si}}$ and $E_{\mathrm{M-Si}}$, are cross-terms used to account for small nonlinearities of the viscosity, if any, for binary systems M – Si and are therefore multiplied by the concentrations of both respective ions, $x^{\$_0}_{\mathrm{M}}$ and $x^{\$_0}_{\mathrm{Si}}$, associated with a binary oxide system.

The parameters A^{*}_{Si}, $A^{\mathrm{E}}_{\mathrm{Si}}$, E^{*}_{Si} and $E^{\mathrm{E}}_{\mathrm{Si}}$ are properties of pure SiO_2 and so are common for all binary systems. $(A^{*}_{\mathrm{Si}} + A^{\mathrm{E}}_{\mathrm{Si}})$ and $(E^{*}_{\mathrm{Si}} + E^{\mathrm{E}}_{\mathrm{Si}})$ are equal to experimentally determined viscosity parameters A_{Si} and E_{Si} from pure SiO_2.

The parameters $A_{\mathrm{M-Si}}$, $E_{\mathrm{M-Si}}$, $A^{\mathrm{R}}_{\mathrm{M-Si}}$ and $E^{\mathrm{R}}_{\mathrm{M-Si}}$ are characteristic of each binary system and are the only true binary viscosity parameters. The values for these parameters were optimised using critically evaluated experimental viscosity data. For binary systems studied, except for the $AlO_{1.5}$ – SiO_2 system, the parameters $A_{\mathrm{M-Si}}$ and $A^{\mathrm{R}}_{\mathrm{M-Si}}$ were not required and are set to zero. The optimised parameters for the model are shown in Table 8.1 (Kim 2011; Kim et al. 2012b).

Systems Containing Al_2O_3 or Fe_2O_3

In the binary $AlO_{1.5}$ – SiO_2 system, Al^{3+} is assumed to be octahedrally coordinated by six oxygens, similar to its coordination in the aluminosilicate minerals mullite and sillimanite. In this state, Al^{3+} disrupts the silica network, forming non-bridging oxygens and acts as a network modifier, which lowers the viscosity of the silicate melt. However, in a melt containing both $AlO_{1.5}$ and MO_x, Al^{3+} can partially substitute for Si^{4+} in the silica network, acting as a network former. This substitution is possible as long as the network-forming Al^{3+} remains associated with the M^{1+} or M^{2+} ions that compensate for the missing charge. The same concept applies to Fe_2O_3, where Fe^{3+} will act as a network former. This concept is known as the charge-compensation effect, and has become generally accepted. Due to its ability to act both as a network former and a network modifier, $AlO_{1.5}$ and $FeO_{1.5}$ are termed "amphoteric" components.

The thermodynamic database of the MQM parameters, which the viscosity model is based on to determine $x_{\mathrm{Si-Si}}$, does not consider the different structural roles of Al^{3+} and Fe^{3+} because the thermodynamic properties do not strongly depend on the different structural states. Therefore, to model a viscosity maximum induced by the amount of network-forming Al^{3+} and Fe^{3+} in a slag, they have to be separately evaluated.

It is assumed that the charge-compensated Al^{3+} and Fe^{3+} in the silicate network have the same impact on viscosity as Si^{4+}. The quantity of network-forming associate species, in relation to temperature and composition, can be determined from the equilibrium constant (K) of the following equilibria, Equations (8.11) to (8.14).

$$2\,\mathrm{AlO_{1.5}} + \mathrm{CaO} \leftrightarrow \mathrm{CaAl_2O_4} \tag{8.11}$$
$$2\,\mathrm{AlO_{1.5}} + \mathrm{MgO} \leftrightarrow \mathrm{MgAl_2O_4} \tag{8.12}$$
$$2\,\mathrm{AlO_{1.5}} + \mathrm{FeO} \leftrightarrow \mathrm{FeAl_2O_4} \tag{8.13}$$
$$2\,\mathrm{FeO_{1.5}} + \mathrm{CaO} \leftrightarrow \mathrm{CaFe_2O_4} \tag{8.14}$$
$$\tag{8.15}$$

The concentrations of the associate species, $x^{\$_1}_{\mathrm{CaAl_2}}$, $x^{\$_1}_{\mathrm{MgAl_2}}$, $x^{\$_1}_{\mathrm{FeAl_2}}$ and $x^{\$_1}_{\mathrm{CaFe_2}}$ correspond to the concentration of network formers while the concentration of $x^{\$_1}_{\mathrm{Al_{15}}}$, $x^{\$_1}_{\mathrm{Fe}}$ and $x^{\$_1}_{\mathrm{Fe_{15}}}$ corresponds to the concentration of network modifiers. By increasing the Si content by the amount of the associate species calculated from Equations (8.11) to (8.14) it is possible to estimate values of A and E for Al-containing systems with Equation (8.6) and Equation (8.7).

Therefore, to accurately model the viscosity, equilibrium constants, Equations (8.16) to (8.19), of the reactions are required.

$$K_{\mathrm{CaAl_2}} = \frac{\gamma_{\mathrm{CaAl_2}}}{\gamma^2_{\mathrm{Al}} \cdot \gamma_{\mathrm{Ca}}} \tag{8.16}$$
$$K_{\mathrm{MgAl_2}} = \frac{\gamma_{\mathrm{MgAl_2}}}{\gamma^2_{\mathrm{Al}} \cdot \gamma_{\mathrm{Mg}}} \tag{8.17}$$
$$K_{\mathrm{FeAl_2}} = \frac{\gamma_{\mathrm{FeAl_2}}}{\gamma^2_{\mathrm{Al}} \cdot \gamma_{\mathrm{FeO}}} \tag{8.18}$$
$$K_{\mathrm{CaFe_2}} = \frac{\gamma_{\mathrm{CaFe_2}}}{\gamma^2_{\mathrm{FeO_{1.5}}} \cdot \gamma_{\mathrm{Ca}}} \tag{8.19}$$
$$\tag{8.20}$$

The activity coefficients γ_{i} of the species Al, Na, Ca, and Mg can be obtained from the implemented MQM model in FactSage. However, the activities of the associated species are not available, as they are not included in the thermodynamic database. Therefore, it is assumed that the activities of all species in Equations (8.16) to (8.19) can be approximated by their concentrations, i.e., $x^{\$_1}_{\mathrm{i}}$.

Using an equation for K, the concentration of an associate species can be determined by calculating the Gibbs free energy of the reaction, Equation (8.21), coupled with an optimised value for ΔG°, from Table 8.2.

$$\Delta G^{\circ} = -RT \ln K \tag{8.21}$$

An example case is provided for Equation (8.11) to determine the composition of the associate species $x^{\$_1}_{\mathrm{CaAl_2}}$, using the combined equations Equations (8.16) and (8.21) and the optimised value of $\Delta G^{\circ}_{\mathrm{CaAl_2}}$ from Table 8.2. The combined equation, Equation (8.22), is expressed in terms of compositions $x^{\$_1}_{\mathrm{i}}$, with the superscript $\$_1$ indicating compositions that now include the associate species.

$$5000 - 100000 x^{\$_0}_{\mathrm{Si}} = -RT \ln \frac{(x^{\$_1}_{\mathrm{CaAl_2}})}{(x^{\$_1}_{\mathrm{Al}})^2 \cdot (x^{\$_1}_{\mathrm{Ca}})} \tag{8.22}$$

The compositions $x^{\$_1}_{\mathrm{CaAl_2}}$, $x^{\$_1}_{\mathrm{Ca}}$, and $x^{\$_1}_{\mathrm{Al}}$ can be expressed in terms of n_{i} with Equations (8.23) to (8.27).

$$x^{\$_1}_{\mathrm{CaAl_2}} = \frac{n^{\$_1}_{\mathrm{CaAl_2}}}{n^{\$_1}_{\mathrm{Total}}} = \frac{n^{\$_1}_{\mathrm{CaAl_2}}}{(n^{\$_1}_{\mathrm{CaAl_2}} + n^{\$_1}_{\mathrm{Al}} + n^{\$_1}_{\mathrm{Ca}})} \tag{8.23}$$

$$x^{\$_1}_{\mathrm{Ca}} = \frac{n^{\$_1}_{\mathrm{Ca}}}{n^{\$_1}_{\mathrm{Total}}} = \frac{n^{\$_1}_{\mathrm{Ca}}}{(n^{\$_1}_{\mathrm{CaAl_2}} + n^{\$_1}_{\mathrm{Al}} + n^{\$_1}_{\mathrm{Ca}})} \tag{8.24}$$

$$x^{\$_1}_{\mathrm{Al}} = \frac{n^{\$_1}_{\mathrm{Al}}}{n^{\$_1}_{\mathrm{Total}}} = \frac{n^{\$_1}_{\mathrm{Al}}}{(n^{\$_1}_{\mathrm{CaAl_2}} + n^{\$_1}_{\mathrm{Al}} + n^{\$_1}_{\mathrm{Ca}})} \tag{8.25}$$

$$n^{\$_1}_{\mathrm{Ca}} = n^{\$_0}_{\mathrm{Ca}} - n^{\$_1}_{\mathrm{CaAl_2}} \tag{8.26}$$

$$n^{\$_1}_{\mathrm{Al}} = n^{\$_0}_{\mathrm{Al}} - 2n^{\$_1}_{\mathrm{CaAl_2}} \tag{8.27}$$

A careful evaluation of Equations (8.22) to (8.27) reveals that $n^{\$_1}_{\mathrm{CaAl_2}}$ is the only unknown. This value can be determined through a root-finding procedure constrained by an elemental mass balance, ensuring the correct root is selected to satisfy mass conservation.

For MeO_x – $AlO_{1.5}$/$FeO_{1.5}$ – SiO_2 systems, ΔG° varies linearly as a function of SiO_2 content, with no temperature dependence. It becomes more negative with increasing SiO_2 concentration (Kim 2011).

Finally, calculating A and E using Equation (8.6) and Equation (8.7) requires updating the mole fractions to "equivalent" mole fractions $x^{\$_2}_{\mathrm{i}}$, as shown in Equations (8.28) to (8.31). This adjustment accounts for the network-forming effect of the associated species. In this approach, the slag is considered to have the same viscosity as an "equivalent" slag without network-forming Al^{3+}, which is compensated by $x^{\$_2}_{\mathrm{i}}$.

$$x^{\$_2}_{\mathrm{Si}} = [x^{\$_1}_{\mathrm{Si}} + 2x^{\$_1}_{\mathrm{CaAl_2}} + 2x^{\$_1}_{\mathrm{MgAl_2}} + 2x^{\$_1}_{\mathrm{FeAl_2}} + 2x^{\$_1}_{\mathrm{CaFe_2}}]/N_{tot} \tag{8.28}$$
$$x^{\$_2}_{\mathrm{Al}} = [x^{\$_1}_{\mathrm{Al}}]/N_{tot} \tag{8.29}$$
$$x^{\$_2}_{\mathrm{Ca}} = [x^{\$_1}_{\mathrm{Ca}}]/N_{tot} \tag{8.30}$$
$$x^{\$_2}_{\mathrm{Mg}} = [x^{\$_1}_{\mathrm{Mg}}]/N_{tot} \tag{8.31}$$
$$x^{\$_2}_{\mathrm{FeO}} = [x^{\$_1}_{\mathrm{FeO}}]/N_{tot} \tag{8.32}$$
$$x^{\$_2}_{\mathrm{FeO_{1.5}}} = [x^{\$_1}_{\mathrm{FeO_{1.5}}}]/N_{tot} \tag{8.33}$$
$$\tag{8.34}$$

with:

$$\begin{aligned} N_{tot} =& x^{\$_1}_{\mathrm{Si}} + x^{\$_1}_{\mathrm{Al}} + x^{\$_1}_{\mathrm{Ca}} + x^{\$_1}_{\mathrm{Mg}} + x^{\$_1}_{\mathrm{FeO}} + x^{\$_1}_{\mathrm{FeO_{1.5}}} \\ &+ 2x^{\$_1}_{\mathrm{CaAl_2}} + 2x^{\$_1}_{\mathrm{MgAl_2}} + 2x^{\$_1}_{\mathrm{FeAl_2}} + 2x^{\$_1}_{\mathrm{CaFe_2}} \end{aligned} \tag{8.35}$$

8.1.5 Variable Declarations

Table 8.1: Optimised viscosity parameters

System	A (Pa s)	E (J mol^{-1})
$\mathrm{SiO_2}$	$A^*_{\mathrm{Si}} = -10.56$ $A^E_{\mathrm{Si}} = -6.13$	$E^*_{\mathrm{SiO_2}} = 217200$ $E^E_{\mathrm{SiO_2}} = 298500$
$\mathrm{AlO_{1.5}}$	$A_{\mathrm{Al_{15}}} = -9.22$	$E_{\mathrm{Al}} = 120400$
CaO	$A_{\mathrm{Ca}} = -12.27$	$E_{\mathrm{Ca}} = 137650$
MgO	$A_{\mathrm{Mg}} = -10.58$	$E_{\mathrm{Mg}} = 117160$
FeO	$A_{\mathrm{Fe}} = -8.75$	$E_{\mathrm{Fe}} = 52500$
$\mathrm{FeO_{1.5}}$	$A_{\mathrm{Fe_{15}}} = -8.63$	$E_{\mathrm{Fe_{15}}} = 47250$
$\mathrm{SiO_2 - AlO_{1.5}}$	$A^R_{\mathrm{Al-Si}} = -12.30$	$E_{\mathrm{Al-Si}} = -75000$ $E^R_{\mathrm{Al-Si}} = 303500$
$\mathrm{SiO_2 - CaO}$	-	$E_{\mathrm{Ca-Si}} = -101750$ $E^R_{\mathrm{Ca-Si}} = 81400$
$\mathrm{SiO_2 - MgO}$	-	$E_{\mathrm{Mg-Si}} = -86250$ $E^R_{\mathrm{Mg-Si}} = 72600$
$\mathrm{SiO_2 - FeO}$	-	$E_{\mathrm{Fe-Si}} = -115000$ $E^R_{\mathrm{Fe-Si}} = 87525$
$\mathrm{SiO_2 - FeO_{1.5}}$	-	$E_{\mathrm{Fe_{15}-Si}} = -107500$ $E^R_{\mathrm{Fe_{15}-Si}} = 88500$

Table 8.2: Optimised values of ΔG° for the associate species for slag systems containing $AlO_{1.5}$ (Grundy et al. 2008a).

System	
$CaO - AlO_{1.5} - SiO_2$	$\Delta G^\circ_{\mathrm{CaAl_2}} = 5000 - 100000x^{\$_0}_{\mathrm{Si}}$
$MgO - AlO_{1.5} - SiO_2$	$\Delta G^\circ_{\mathrm{MgAl_2}} = 13000 - 105000x^{\$_0}_{\mathrm{Si}}$
$FeO - AlO_{1.5} - SiO_2$	$\Delta G^\circ_{\mathrm{FeAl_2}} = -66944x^{\$_0}_{\mathrm{Si}}$
$CaO - FeO_{1.5} - SiO_2$	$\Delta G^\circ_{\mathrm{CaFe_2}} = 2092 - 5335x^{\$_0}_{\mathrm{Si}}$

8.1.6 Assumptions

The following assumptions was made to formulate this model.

1. Where no experimental data were available, viscosity parameters for unary systems are extrapolated from binary viscosity data.
2. For pure silica, two contributions to the viscosity are assumed. The first is that there is a contribution to viscosty that is independent on the formation of a polymer network. The second is that the silicate network itself contributes to the viscosity.
3. It is assumed that the effect of network-forming Al^{3+} and Fe^{3+} on the viscosity will be the same as that of Si^{4+}.
4. For solving the equilibrium equations of the associate species, the activities of all species are assumed to be accurately approximated by their concentrations.
5. For systems not containing Al_2O_3 or Fe_2O_3 it is assumed that $\ln(\mu)$ can be calculated from a linear combination of A and E of binary systems.

8.1.7 Simplifications

The following simplifications was made in this model. The critical group size for SiO_4 clusters is set to be $n = 40$ interconnected Si – Si pairs. Also, the interaction between MgO and Fe_2O_3 is not accounted for as it is for that between CaO and Fe_2O_3.

8.1.8 Literature Inaccuracies

Background

During development of the multicomponent model catered for systems containing Al_2O_3, we experienced significant difficulty to navigate uncertainties caused by literature inaccuracies. To ensure the user do not go through the same trouble, these are listed here.

Inaccuracies

1. Calculating ΔG

   Grundy et al. (2008a) reported that ΔG which dictates the equilibrium constant for the formation of $CaAl_2O_4$ and $MgAl_2O_4$ should be calculated as

   $\Delta G^{\circ}_{\mathrm{CaAl_2}} = 5000 - 100000 x^{\$_0}_{\mathrm{Si}}$ and $\Delta G^{\circ}_{\mathrm{MgAl_2}} = 13000 - 105000 x^{\$_0}_{\mathrm{Si}}$,

   while Kim et al. (2012a) reported

   $\Delta G^{\circ}_{\mathrm{CaAl_2}} = -5000 - 100000 x^{\$_0}_{\mathrm{Si}}$ and $\Delta G^{\circ}_{\mathrm{MgAl_2}} = -13000 - 105000 x^{\$_0}_{\mathrm{Si}}$.

   Grundy et al. (2008a) reported it correctly.

2. Calculating $x^{\$_2}$

   Grundy et al. (2008a) reported the calculation of $x^{\$_2}_{\mathrm{Si}}$ to be

$$x^{\$_2}_{\mathrm{Si}} = [x^{\$_1}_{\mathrm{Si}} + x^{\$_1}_{\mathrm{NaAl}} + 2x^{\$_1}_{\mathrm{CaAl_2}} + 2x^{\$_1}_{\mathrm{MgAl_2}}]/N_{\mathrm{tot}} \tag{8.36}$$

where

$$N_{\text{tot}} = x_{\text{Si}}^{\mathcal{S}_1} + x_{\text{Al}}^{\mathcal{S}_1} + x_{\text{Na}}^{\mathcal{S}_1} + x_{\text{Ca}}^{\mathcal{S}_1} + x_{\text{Mg}}^{\mathcal{S}_1} - x_{\text{NaAl}}^{\mathcal{S}_1} - x_{\text{CaAl}_2}^{\mathcal{S}_1} - x_{\text{MgAl}_2}^{\mathcal{S}_1} \tag{8.37}$$

while Kim et al. (2012a) reported the same calculation for $x_{\text{Si}}^{\mathcal{S}_2}$ but with

$$N_{\text{tot}} = x_{\text{Si}}^{\mathcal{S}_1} + x_{\text{Al}}^{\mathcal{S}_1} + x_{\text{Na}}^{\mathcal{S}_1} + x_{\text{Ca}}^{\mathcal{S}_1} + x_{\text{Mg}}^{\mathcal{S}_1} + x_{\text{NaAl}}^{\mathcal{S}_1} + 2x_{\text{CaAl}_2}^{\mathcal{S}_1} + 2x_{\text{MgAl}_2}^{\mathcal{S}_1} \tag{8.38}$$

Here, Kim et al. (2012a) reported it correctly.

3. Incorrect plots presented in Grundy et al. (2008b) and Grundy et al. (2008a).

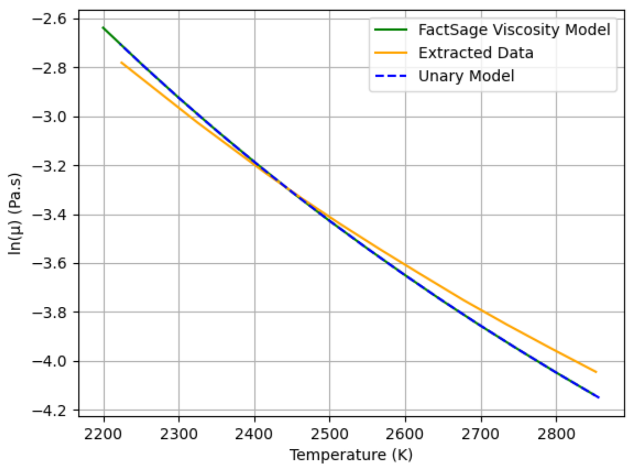

(a) Al_2O_3 – Grundy et al. (2008b) Fig. 7. 'Extracted Data' represents Grundy's model and 'Unary Model' represents auxi-mpp's model.

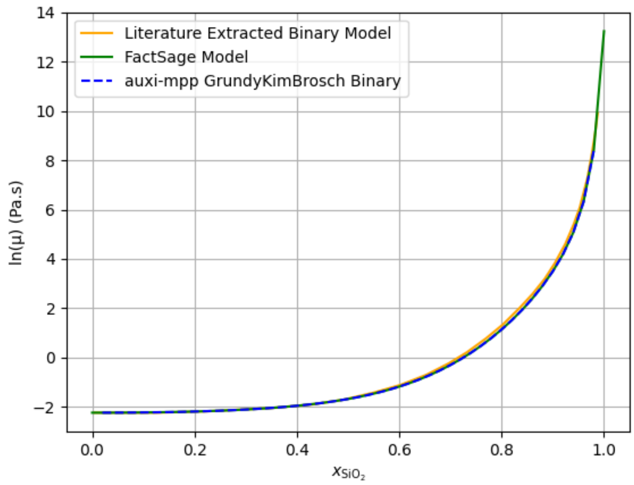

(b) $Al_2O_3 - SiO_2$ – Grundy et al. (2008b) Fig. 8. 'Literature Extracted Binary Model' represents Grundy's model.

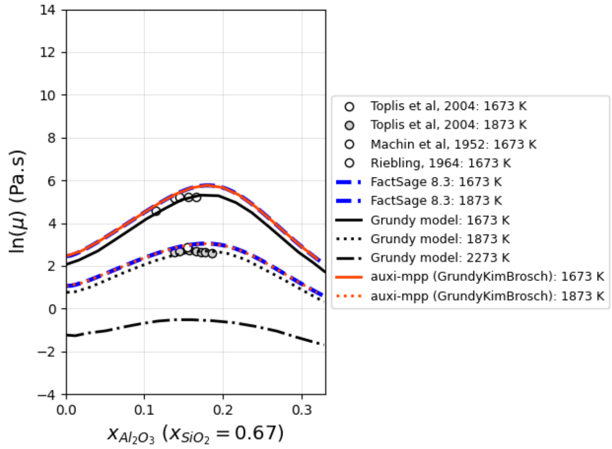

(c) $Al_2O_3 - MgO - SiO_2$ – Grundy et al. (2008a) Fig. 32

Figure 8.1: Inaccurate plots.

The seemingly small deviation present in Figure 8.1b at $x_{\text{SiO}_2} = 0.8$, was found to be double the deviation found in Figure 8.1a at $T = 2800$K. These deviations were confirmed not to be due to erroneous data extraction. The deviation in Figure 8.1c is also a definite inaccuracy since Fig. 31 and 33 matches correctly with auxi-mpp and FactSage's model, and Grundy's binary model agrees with the calculated viscosity at $x_{\mathrm{Al_2O_3}} = 0$. The same problem is present for Fig. 23 of Grundy et al. (2008a).

4. Incorrect plot presented in Kim et al. (2021a).

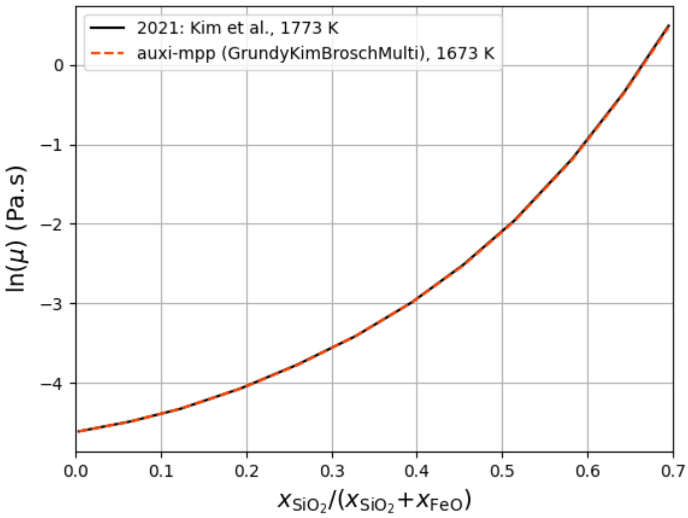

Figure 8.2: CaO – FeO – SiO_2

In Figure 8.2, auxi-mpp plotted the same compositions but 100 K lower than the literature plot at 1773 K. There is an exact match, implying that Kim et al. (2021a) provided the incorrect temperature label.

5. Incorrect plot section defined.

The original figure from which the literature data in Figure 8.2 were extracted is Figure 9 in Kim et al. (2021a). The section to plot is there defined as (81.24 mol % FeO, 13.76 mol % CaO) to (86.75 mol % SiO_2, 13.25 mol % CaO). The first endpoint does not border and is therefore incorrect. The correct endpoint is (**86.24** mol % FeO, 13.76 mol % CaO).

8.1.9 Model Validation

This section details the current status of the Grundy-Kim-Brosch viscosity model implementation in auxi-mpp and presents results for various slag systems. The auxi-mpp model results were compared against the literature model and experimental data extracted from Grundy et al. (2008b), Grundy et al. (2008a), Kim et al. (2021a), and Kim et al. (2021b). auxi-mpp were validated by means of literature figure reproduction as well as with a correlation plot. Validation by figure reproduction is summarised in Table 8.3, and those by correlation plot is listed thereafter.

Table 8.3: Viscosity Validation Ranges

Model	Systems	Composition ($\mathrm{mol\,mol^{-1}}$)	Temperature (K)
Unary	SiO_2	pure substance	$1250-3250$
	FeO	pure substance	$1100-2100$
	Fe_2O_3	pure substance	$1100-1850$
Binary	$Al_2O_3-SiO_2$	$x_{\mathrm{Al_2O_3}}=0-1$	$2073, 2173$
	$CaO-SiO_2$	$x_{\mathrm{CaO}}=0-1$	$1773, 1873, 2073$
	$MgO-SiO_2$	$x_{\mathrm{MgO}}=0-1$	$1773, 1873, 2073$
	$FeO-SiO_2$	$x_{\mathrm{FeO}}=0.3-1$	$1473, 1573, 1673, 1773$
Ternary	$CaO-MgO-SiO_2$	$y_{\mathrm{SiO_2}}=0.3-0.75$, $y_{\mathrm{SiO_2}}/y_{\mathrm{MgO}}=1$	$1673, 1773, 1873$
	$CaO-MgO-SiO_2$	$y_{\mathrm{SiO_2}}=0.3-0.8$, $y_{\mathrm{MgO}}=0.2$	$1673, 1773, 1873$
	$Al_2O_3-CaO-SiO_2$	$x_{\mathrm{Al_2O_3}}=0.0-0.33$, $x_{\mathrm{SiO_2}}=0.67$	$1673, 1873$
	$Al_2O_3-CaO-SiO_2$	$x_{\mathrm{Al_2O_3}}=0.0-0.25$, $x_{\mathrm{SiO_2}}=0.75$	$1673, 1873$
	$Al_2O_3-MgO-SiO_2$	$x_{\mathrm{Al_2O_3}}=0.0-0.50$, $x_{\mathrm{SiO_2}}=0.50$	$1673, 1873$
	$Al_2O_3-MgO-SiO_2$	$x_{\mathrm{Al_2O_3}}=0.0-0.33$, $x_{\mathrm{SiO_2}}=0.67$	$1673, 1873$
	$Al_2O_3-MgO-SiO_2$	$x_{\mathrm{Al_2O_3}}=0.0-0.25$, $x_{\mathrm{SiO_2}}=0.75$	$1673, 1873$
Quaternary	$Al_2O_3-CaO-MgO-SiO_2$	$y_{\mathrm{Al_2O_3}}=0.0-0.45$, $y_{\mathrm{SiO_2}}=0.5$, $y_{\mathrm{MgO}}=0.05$	1773
	$Al_2O_3-CaO-MgO-SiO_2$	$y_{\mathrm{Al_2O_3}}=0.0-0.35$, $y_{\mathrm{SiO_2}}=0.5$, $y_{\mathrm{MgO}}=0.15$	1773
	$Al_2O_3-CaO-MgO-SiO_2$	$y_{\mathrm{Al_2O_3}}=0.0-0.25$, $y_{\mathrm{SiO_2}}=0.5$, $y_{\mathrm{MgO}}=0.25$	1773

Fe-bearing systems validated by means of correlation plots;

1. $Al_2O_3-FeO-SiO_2$
2. $Fe_2O_3-FeO-SiO_2$
3. $Al_2O_3-CaO-FeO-SiO_2$
4. $FeO-MgO-SiO_2$
5. $CaO-Fe_2O_3-FeO-SiO_2$
6. $CaO-FeO-MgO-SiO_2$
7. $Al_2O_3-CaO-FeO-MgO-SiO_2$
8. $Al_2O_3-FeO-MgO-SiO_2$

See Figure 8.8.

Unary Systems

Figure 8.3 demonstrates the agreement between auxi-mpp and the literature model for unary systems, plotting the natural logarithm of viscosity against temperature.

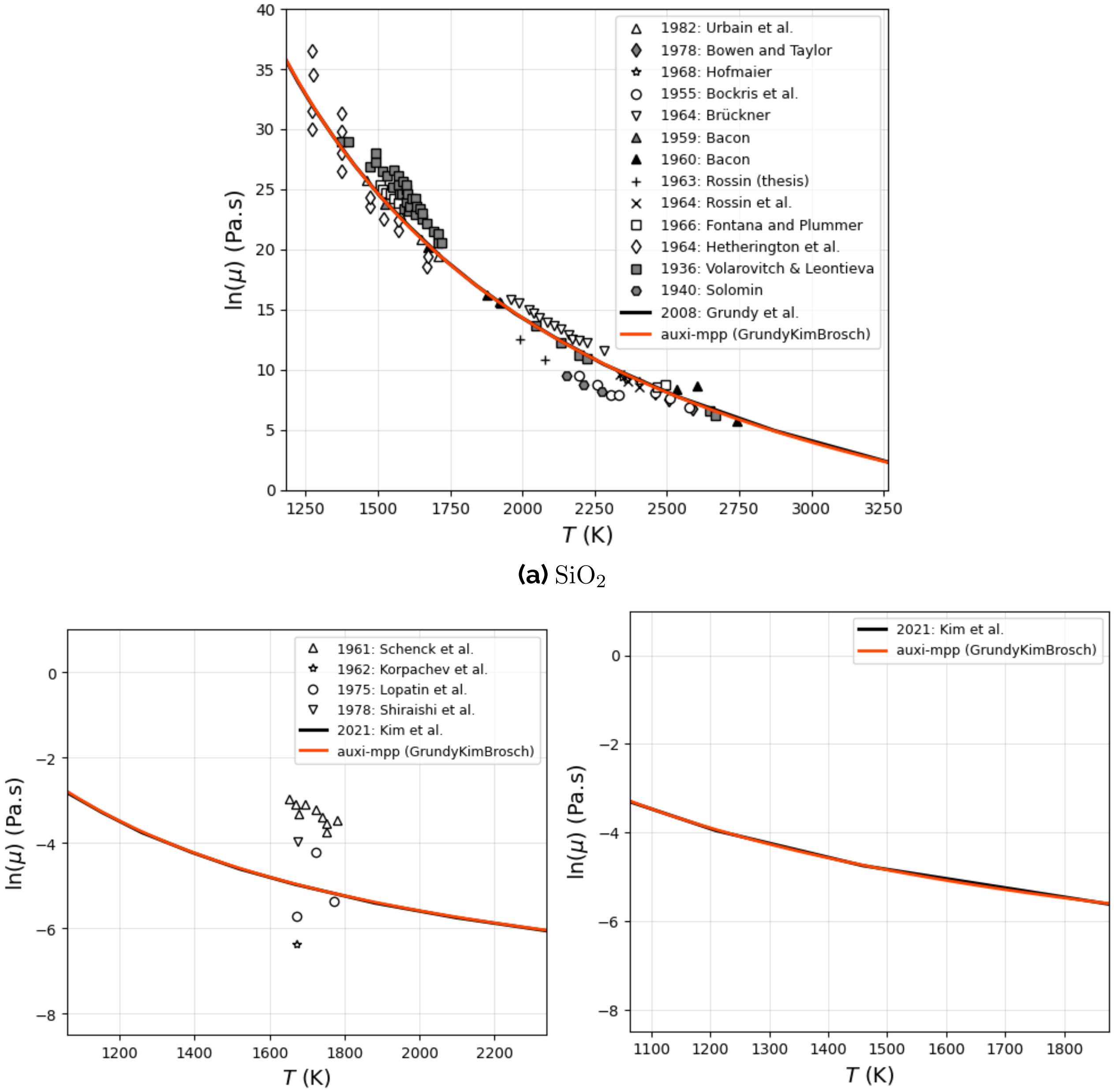

(a) SiO_2

(b) FeO

(c) Fe_2O_3

Figure 8.3: Viscosity model estimates and comparison for pure SiO_2, FeO and Fe_2O_3.

Binary Systems

Figure 8.4 illustrates the accuracy of the Grundy-Kim-Brosch model ("auxi-mpp GrundyKimBrosch") for estimating viscosities in binary $Al_2O_3-SiO_2$, $CaO-SiO_2$, and $MgO-SiO_2$ systems. Note that validations above 2200 K were intentionally omitted.

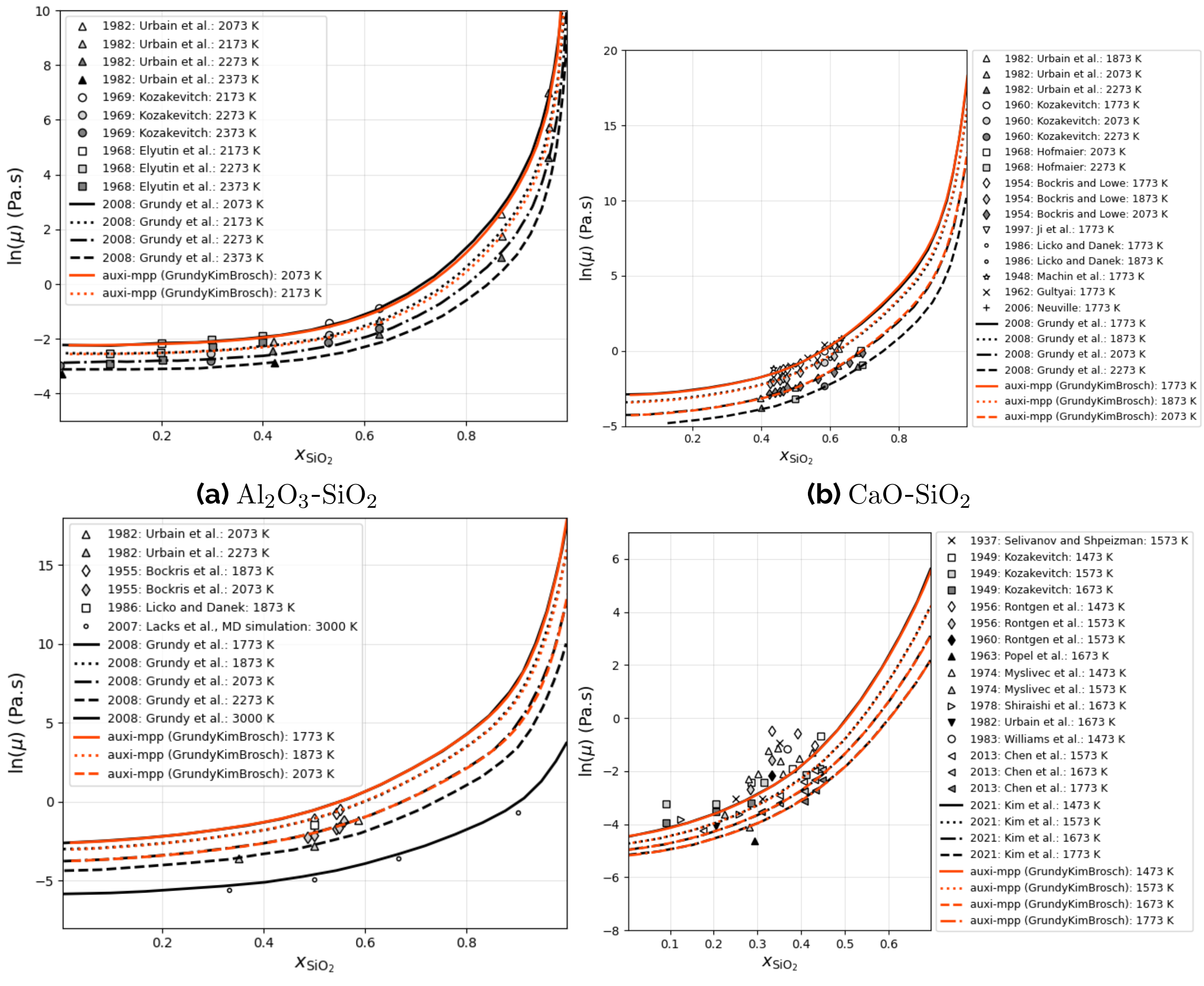

(a) Al_2O_3-SiO_2 **(b)** CaO-SiO_2 **(c)** MgO-SiO_2 **(d)** FeO-SiO_2

Figure 8.4: Viscosity model estimates and comparisons for binary slag systems.

Multicomponent Systems

Ternary systems without Al_2O_3 were validated initially, as the Grundy-Kim-Brosch model does not require consideration of the charge compensation effect of Al_2O_3 on slag viscosity (Kim 2011; Grundy et al. 2008a). Figure 8.5 demonstrates that viscosity estimates for systems of SiO_2 – MgO – CaO closely align with both model estimates and experimental data from the literature (Grundy et al. 2008a).

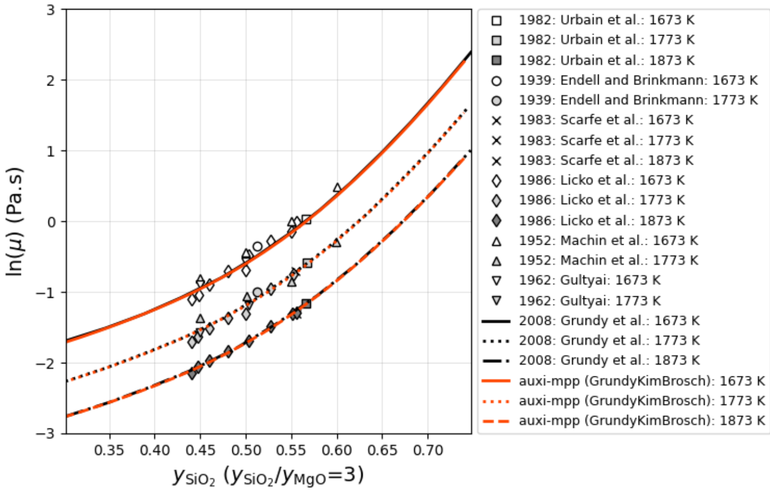

(a) $CaO - MgO - SiO_2$

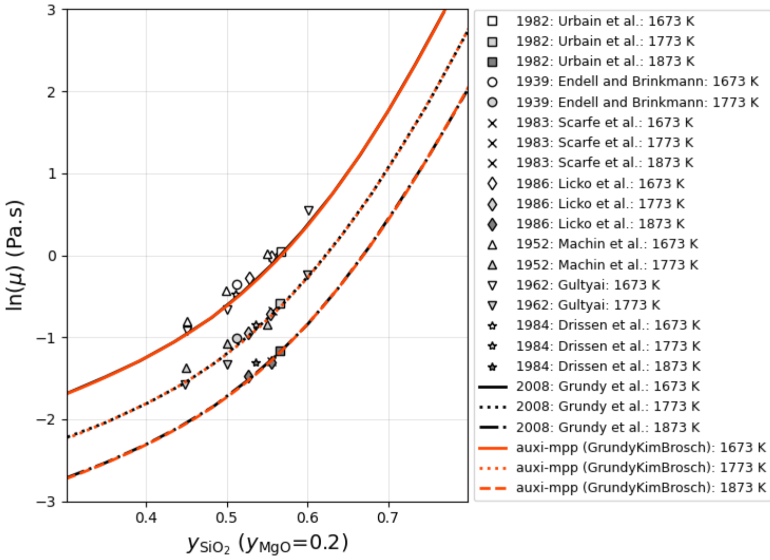

(b) $CaO - MgO - SiO_2$

Figure 8.5: Viscosity model estimates for ternary slag systems without alumina.

Some peculiar results were obtained when validating the model for systems containing Al_2O_3 as seen in Figure 8.6. In Figure 8.6a and Figure 8.6d we reason that the literature plots are incorrect. To support this, the results of FactSage 8.3 were added for comparison. In Figure 8.6d the auxi-mpp model follows the result of FactSage, confirming that the auxi-mpp implementation is correct. This was also applied to Figure 8.6a, however it seems like FactSage's model does not correctly estimate viscosity for systems containing CaO. At the extremes, the auxi-mpp model agrees with FactSage's model, however.

Another reason why these two literature figures are incorrect is that the auxi-mpp binary model, that were successfully validated for the relevant systems, agrees with the multi-component auxi-mpp model at $x_{\mathrm{Al_2O_3}} = 0.0$.

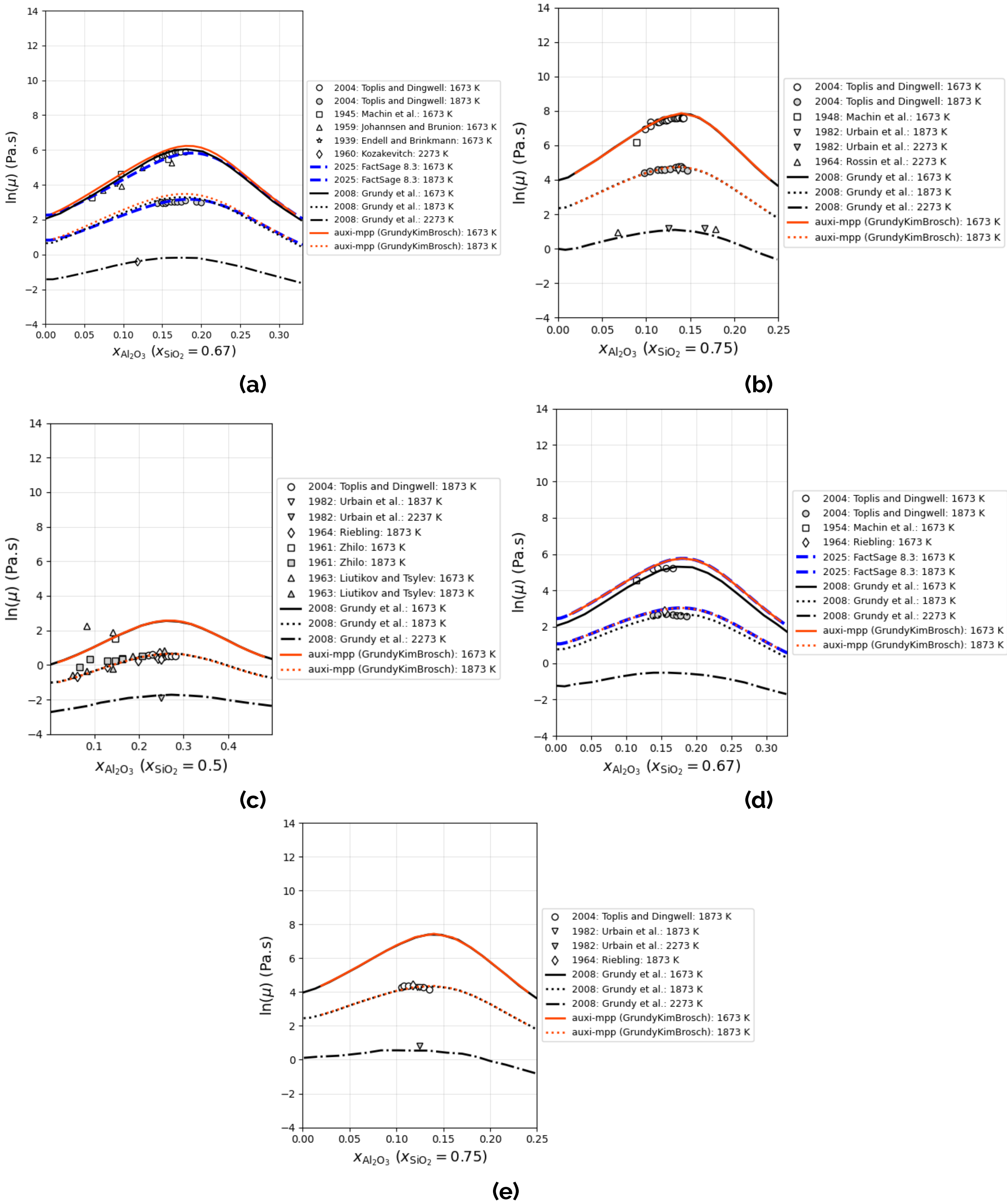

Figure 8.6: Viscosity model estimates for ternary slag systems containing alumina.

The multicomponent viscosity model was successfully validated for the $Al_2O_3 - CaO - MgO - SiO_2$ system for a range of compositions at 1773 K as shown in Figure 8.7.

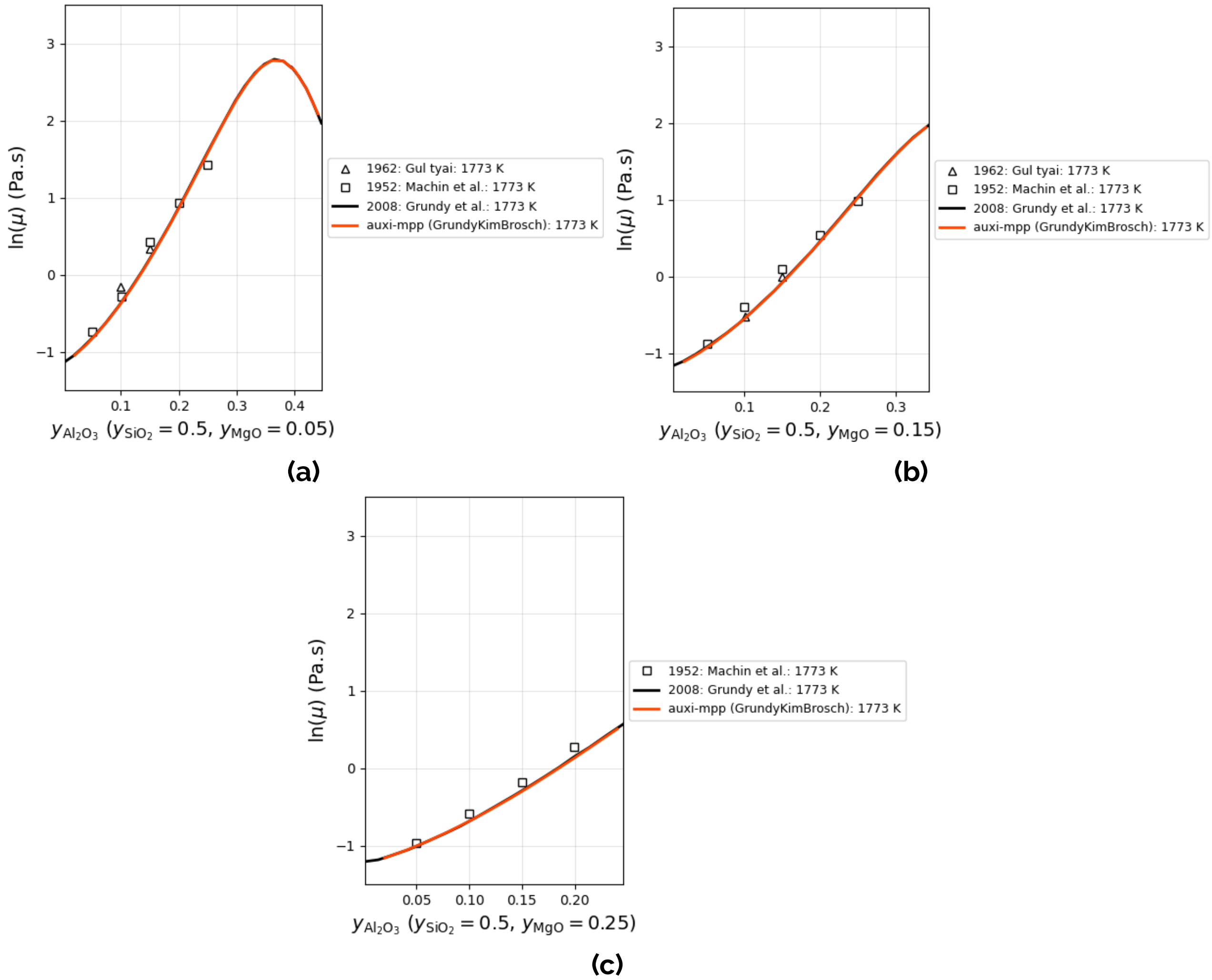

Figure 8.7: Viscosity model estimates for the $Al_2O_3 - CaO - MgO - SiO_2$ quaternary slag system at 1773 K.

Multicomponent Fe-bearing Systems

The available data for multi-component Fe-bearing systems often have abstract axes making it time-consuming to reproduce. These systems are therefore validated by means of correlation plots. Figure 8.8 shows how auxi-mpp performs, with systems containing either FeO or Fe_2O_3 or both, compared to Kim's model as presented in literature (Kim et al. 2021a; Kim et al. 2021b).

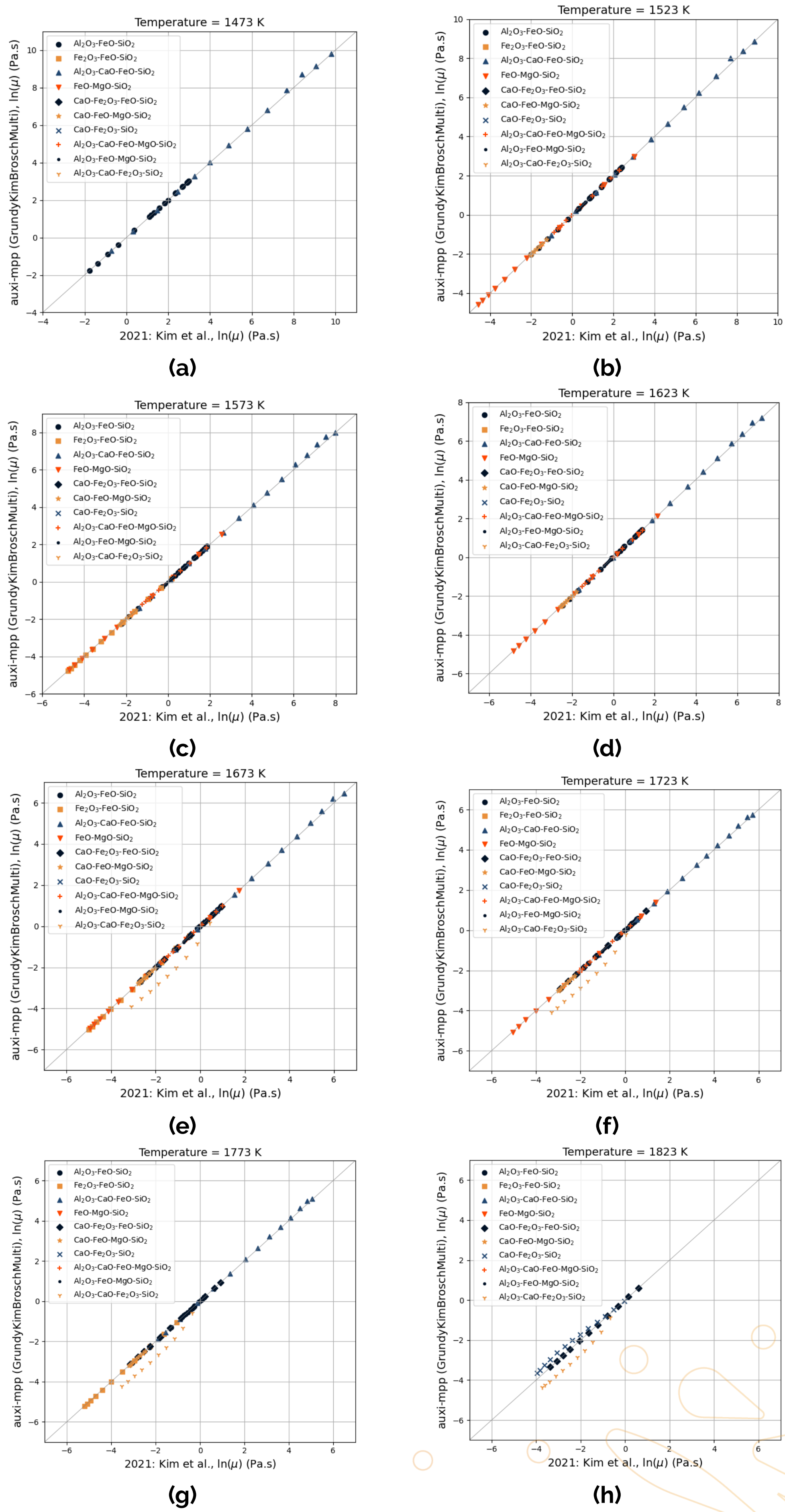

Figure 8.8: auxi-mpp vs Kim et al. (2021b) correlation plots.

For most systems auxi-mpp performs well. There are two systems for which there are visible deviation from literature, however. These are $CaO-Fe_2O_3-SiO_2$ and $Al_2O_3-CaO-Fe_2O_3-SiO_2$. For $CaO-Fe_2O_3-SiO_2$ the original figure were reproduced in Figure 8.9, adding the performance of FactSage 8.3's (2025) viscosity model. auxi-mpp plots close to but not exactly on top of FactSage, and both deviates significantly from literature. Whether this is an error in literature or if both auxi-mpp and FactSage are incorrect, is uncertain. It is also possible that this is caused by a parameter change in FactSage's FToxid database in the time period of 2021 to 2025.

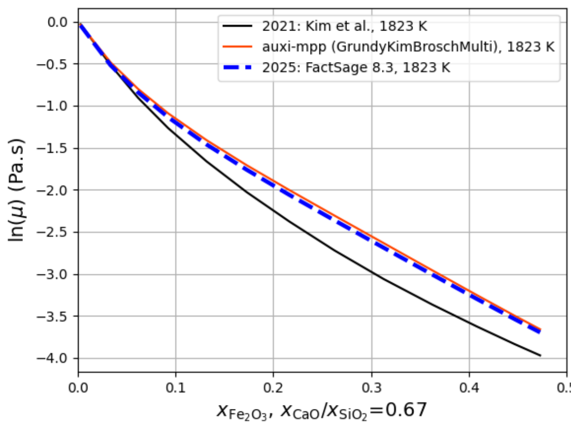

(a) $CaO-Fe_2O_3-SiO_2$

Figure 8.9: auxi-mpp vs FactSage 8.3 (2025) vs Kim et al. (2021b).

The issue with $Al_2O_3-CaO-Fe_2O_3-SiO_2$ is similar as auxi-mpp's results is close to FactSage 8.3, with both deviating significantly from literature.

Issues

Potential issue with the systems $CaO-Fe_2O_3-SiO_2$ and $Al_2O_3-CaO-Fe_2O_3-SiO_2$. See Figures 8.8 and 8.9.

Part III

Liquid Alloy Material Properties

Chapter 9

Background

In pyrometallurgical operations like the REF process, the formation of a liquid metal phase, or alloy, is the most important outcome. Liquid alloy is the primary product and a dynamic medium that interacts directly with the furnace lining and the overlying slag layer. Therefore, understanding the physical properties of molten alloy, not just the slag, is crucial for the successful and efficient operation of a REF process for the production of green steel.

The physical characteristics of the liquid alloy play a part in influencing process behaviour and outcomes. Density is fundamental to achieving effective gravitational separation between the valuable metal and the slag impurities. Viscosity governs the fluid dynamics within the furnace, influencing mixing, mass transfer rates within the alloy and at the interface between alloy and slag, and the ease of tapping the final product. Electrical and thermal conductivity are critical properties to understand in a furnace. Electrical conductivity directly impacts the energy efficiency of the furnace's heating systems, while thermal conductivity dictates heat distribution, which affects reaction kinetics and furnace wear.

Directly measuring these properties under the extreme temperatures and reactive conditions of a furnace is often impractical and expensive. Therefore, accurate and reliable physical property models are indispensable tools for process simulation, optimisation, and the development of new, more sustainable steelmaking technologies. This section of the manual details the theoretical foundations of the models implemented in auxi-mpp for estimating these key physical properties for liquid alloys, along with their validation against experimental data and literature models.

Chapter 10

Density

This chapter presents several models implemented in auxi-mpp to estimate the density of various liquid alloys. The models cover three distinct categories of alloy systems.

The primary approach, based on volumetric thermal expansion coefficients, is used to calculate the density of unary, binary, and multi-component liquid alloys that contain only metallic elements. For binary alloys that include non-metallic elements like carbon and sulfur, a set of distinct empirical models is provided. Lastly, the chapter details specific models for estimating the density of common multi-component commercial alloys, such as stainless steel and grey cast iron

10.1 Density by Volumetric Thermal Expansion

A density model based on volumetric thermal expansion coefficients.

10.1.1 Introduction

Extensive reference correlation data was discovered using the Nation Institute of Standards and Technology (NIST) Alloy Data web app to directly model density for a wide range of alloy systems ("Thermodynamics Research Center" 2009). Molar volume is then derived from the estimated densities.

10.1.2 Overview

Reference data for unary, binary and multi-component liquid alloy systems have been found in literature that employs volumetric thermal expansion coefficients to estimate the density of liquid alloys (Assael et al. 2006; Assael et al. 2010; Assael et al. 2012a; Assael et al. 2012b; Brillo et al. 2006; Brillo and Egry 2004; Brillo and Egry 2003). Density estimates for these unary, binary and multi-component systems only focus on alloys containing metallic elements. Systems containing non-metallic elements such as C, P and S are estimated with empirical models, which are described in Section 10.2.

10.1.3 Formulation

It is important to understand the relationship between molar volume and density. The following model formulation starts by first describing how molar volume can be determined followed by deriving density from it.

Molar volume for an ideal alloy system can be determined by applying Vegard's law, Equation (10.1), where x_i is the mole fraction of component i, V_i is the molar volume of component i, M_i is the molar mass of component i, and ρ_i is the density of component i.

$$V^{ideal} = \sum_i x_i V_i = \sum_i x_i \frac{M_i}{\rho_i} \tag{10.1}$$

For non-ideal systems where excess molar volume must be considered, Equation (10.2), the density of the system can be used to determine its molar volume, as shown in Equation (10.3). Here, $V^{non-ideal}$ is the non-ideal molar volume, M_i is the molar mass of component i, and ρ_{system} is the density of the system.

$$V^{non-ideal} = V_{ideal} + V_{excess} \tag{10.2}$$

$$V^{non-ideal} = \frac{\sum_i^{system} x_i M_i}{\rho_{system}} \tag{10.3}$$

The molar volume of molten alloy systems containing only metallic elements exhibits a linear temperature dependence that can be modelled using the volumetric thermal expansion coefficient, β, as shown in Equation (10.4), where $V_{T,melt}$ is the molar volume at the melting temperature and T is the temperature of the system.

$$V(T) = V_{T,melt}(1 + \beta(T - T_{melt})) \tag{10.4}$$

Similarly, this can be related to the density of pure liquid metals and alloys with Equation (10.5) and Equation (10.6) respectively, where $\rho_{T,melt}$ is the density at the melting temperature and $\rho_{T,liquidus}$ is the density at the liquidus temperature.

$$\rho(T) = \rho_{T,melt}(1 + \beta(T - T_{melt})) \tag{10.5}$$

$$\rho(T) = \rho_{T,liquidus}(1 + \beta(T - T_{liquidus})) \tag{10.6}$$

For modelling purposes using the density reference data found in literature, Equation (10.6) is rearranged to form Equation (10.7), where $\rho_T = \beta \cdot \rho_L$ is the thermal expansion coefficient, ρ_L is the density at the liquidus temperature, T_L is the liquidus temperature and T is the temperature of the system (Assael et al. 2006; Brillo and Egry 2004).

$$\rho(T) = \rho_L - \rho_T(T - T_L) \tag{10.7}$$

For each composition in a unary, binary, or multi-component system, the parameters ρ_L, ρ_T, and T_L are determined from experimental data and used in Equation (10.7) to estimate the density of the system at a given temperature. It is important to note that the parameters are only valid within a specific temperature range, which is also determined from the experimental data.

Unary Systems

For unary systems, the density of a pure liquid metal is estimated using Equation (10.7). The supported elements, along with their model parameters and valid temperature ranges, are listed in Table 10.1. It is important to note that the application of the model should be restricted to the temperature ranges for which the parameters have been validated. Using the model outside these ranges may lead to inaccurate density estimates.

Table 10.1: Supported elements, temperature limits and parameters for the unary density model.

Element	Symbol	Temp. Range (K)	ρ_L (kg/m^3)	ρ_T (kg/m$^3\cdot$ K)	T_{ref} (K)
Aluminum	Al	933 – 1190	2377.2	0.311	934
Antimony	Sb	900 – 1300	6467.0	0.608	899
Bismuth	Bi	545 – 1500	10028.0	1.213	545
Cadmium	Cd	594 – 833	8008.0	1.251	594
Chromium	Cr	2186 – 2503	6097.1	0.6536	2180
Cobalt	Co	1768 – 2500	7827.0	0.936	1768
Copper	Cu	1356 – 2500	7997.0	0.819	1358
Gallium	Ga	303 – 1500	6077.0	0.611	303
Hafnium	Hf	2500 – 4981	11902.6	0.6704	2500
Indium	In	430 – 1100	7022.0	0.762	430
Iron	Fe	1809 – 2480	7035.0	0.926	1811
Lead	Pb	601 – 2000	10656.0	1.239	601
Molybdenum	Mo	2896 – 5914	9062.6	0.3947	2896
Nickel	Ni	1728 – 2500	7861.0	0.988	1728
Niobium	Nb	2742 – 5848	7664.0	0.2943	2742
Silicon	Si	1687 – 2000	2550.0	0.264	1687
Silver	Ag	1235 – 1600	9294.0	0.877	1235
Tantalum	Ta	3293 – 7400	14977.5	0.6802	3293
Thallium	Tl	576 – 1200	11233.0	1.2	577
Tin	Sn	506 – 1950	6979.0	0.652	505
Titanium	Ti	1941 – 3520	4222.1	0.3952	1941
Tungsten	W	3695 – 5818	17146.4	0.6769	3695
Vanadium	V	2183 – 4500	5517.0	0.5895	2183
Zinc	Zn	692 – 910	6559.0	0.884	693
Zirconium	Zr	2128 – 4100	6100.0	0.242	2128

Binary Systems

Densities for binary alloy systems using Equation (10.7) can be estimated for the following compositions and temperature ranges found in Table 10.2. For compositions not explicitly listed, the required parameters (ρ_L, ρ_T, and T_L) are determined by linear interpolation between the two nearest compositions for which data is available. These interpolated parameters are then used in Equation (10.7). This approach is valid only for compositions that fall between the available data points and within their valid temperature ranges.

Table 10.2: Supported systems, compositions and parameters for the binary density model

System	Composition	Temp. Range (K)	ρ_L (kg/m^3)	ρ_T (kg/m$^3\cdot$ K)	T_{liquidus} (K)
Ag-Al	Ag0.10Al0.90	893 – 1193	2830.0	0.21	893
	Ag0.20Al0.80	864 – 1164	3830.0	0.42	864
	Ag0.40Al0.60	840 – 1140	5380.0	0.48	840
	Ag0.60Al0.40	979 – 1279	6810.0	1.05	979
	Ag0.79Al0.21	1049 – 1349	8070.0	0.68	1049
Ag-Au	Ag0.75Au0.25	1276 – 1576	11200.0	0.7	1276
	Ag0.50Au0.50	1306 – 1606	13300.0	0.6	1306
	Ag0.25Au0.75	1326 – 1626	15600.0	1.2	1326
Ag-Cu	Ag0.80Cu0.20	1135 – 1435	9000.0	0.6	1135
	Ag0.60Cu0.40	1053 – 1353	8900.0	0.7	1053
	Ag0.40Cu0.60	1132 – 1432	8600.0	0.6	1132
	Ag0.20Cu0.80	1225 – 1525	8400.0	1.2	1225
Al-Au	Al1.0Au0.0	934 – 1234	2291.0	0.251	934
	Al0.85Au0.15	835 – 1135	4425.0	0.327	835
	Al0.80Au0.20	847 – 1147	5275.0	0.59	847
	Al0.67Au0.33	895 – 1195	7231.0	0.685	895
	Al0.55Au0.45	1144 – 1444	9163.0	0.63	1144
	Al0.50Au0.50	1252 – 1552	10050.0	1.06	1252
	Al0.33Au0.67	1333 – 1633	12842.0	1.0	1333
	Al0.27Au0.73	1280 – 1580	13840.0	1.01	1280
	Al0.20Au0.80	1237 – 1537	15020.0	1.08	1237
	Al0.0Au1.0	1338 – 1638	17192.0	1.11	1338
Al-Cu	Al1.0Cu0.0	933 – 1233	2360.0	0.33	933
	Al0.80Cu0.20	835 – 1135	3320.0	0.53	835
	Al0.70Cu0.30	865 – 1165	3760.0	0.49	865
	Al0.60Cu0.40	900 – 1200	4440.0	0.54	900
	Al0.50Cu0.50	1087 – 1387	5050.0	0.61	1087
	Al0.40Cu0.60	1233 – 1533	5490.0	0.69	1233
	Al0.30Cu0.70	1314 – 1614	6170.0	0.85	1314
	Al0.20Cu0.80	1315 – 1615	6660.0	0.77	1315
	Al0.0Cu1.0	1358 – 1658	7920.0	0.76	1358
Al-Fe	Al0.90Fe0.10	1289 – 1589	950.0	0.48	1289
	Al0.80Fe0.20	1430 – 1730	1080.0	0.58	1430
	Al0.75Fe0.25	1433 – 1733	1080.0	0.37	1433
	Al0.71Fe0.29	1452 – 1752	1120.0	0.71	1452
	Al0.67Fe0.33	1457 – 1757	1160.0	0.44	1457
	Al0.60Fe0.40	1505 – 1805	1220.0	0.14	1505
Al-Ni	Al0.82Ni0.18	1221 – 1521	3310.0	0.48	1221
	Al0.75Ni0.25	1377 – 1677	3550.0	0.76	1377
	Al0.70Ni0.30	1565 – 1865	3800.0	0.94	1565
	Al0.60Ni0.40	1835 – 2135	4490.0	1.29	1835
	Al0.50Ni0.50	1913 – 2213	4460.0	1.92	1913
	Al0.25Ni0.75	1670 – 1970	6420.0	0.8	1670
Al-Si	Al0.8847Si0.1153	850 – 1700	2398.0	0.24	850
Al-Ti	Al0.90Ti0.10	843 – 1343	2500.0	0.306	843
	Al0.80Ti0.20	835 – 1335	2760.0	0.353	835
	Al0.70Ti0.30	1063 – 1563	3040.0	0.33	1063
	Al0.60Ti0.40	1410 – 1910	3300.0	0.401	1410
	Al0.50Ti0.50	1643 – 2143	3580.0	0.45	1643
	Al0.40Ti0.60	1750 – 2250	3740.0	0.42	1750
	Al0.30Ti0.70	1808 – 2308	3900.0	0.377	1808

Table 10.2 continued from previous page

System	Composition	Temp. Range (K)	ρ_L (kg/m^3)	ρ_T (kg/m^3· K)	T_{liquidus} (K)
	Al0.20Ti0.80	1883 – 2383	4000.0	0.368	1883
	Al0.10Ti0.90	1910 – 2410	4090.0	0.33	1910
Co-Cu	Co1.0Cu0.0	1768 – 2068	7810.0	0.885	1768
	Co0.85Cu0.15	1713 – 2013	7740.0	1.16	1713
	Co0.75Cu0.25	1687 – 1987	7750.0	0.94	1687
	Co0.50Cu0.50	1652 – 1952	7660.0	0.72	1652
	Co0.25Cu0.75	1628 – 1928	7690.0	0.72	1628
Co-Fe	Co1.0Fe0.0	1768 – 2068	7810.0	0.885	1768
	Co0.75Fe0.25	1752 – 2052	7580.0	0.954	1752
	Co0.50Fe0.50	1752 – 2052	7430.0	0.748	1752
	Co0.25Fe0.75	1767 – 2067	7210.0	0.332	1767
	Co0.0Fe1.0	1811 – 2111	7040.0	1.08	1811
Cr-Fe	Cr0.10Fe0.90	1805 – 2105	6980.0	0.54	1805
	Cr0.20Fe0.80	1800 – 2100	6900.0	0.862	1800
	Cr0.40Fe0.60	1798 – 2098	7911.0	0.792	1798
Cr-Ni	Cr0.10Ni0.90	1710 – 2010	7690.0	0.79	1710
	Cr0.20Ni0.80	1700 – 2000	7410.0	0.792	1700
	Cr0.40Ni0.60	1648 – 1948	8111.0	0.608	1648
	Cr0.0Ni1.0	1728 – 2028	7820.0	0.856	1728
Cu-Au	Cu1.0Au0.0	1357 – 1673	7900.0	0.77	1357
	Cu0.75Au0.25	1243 – 1673	11390.0	1.95	1243
	Cu0.50Au0.50	1193 – 1673	13500.0	1.26	1193
	Cu0.25Au0.75	1215 – 1673	15670.0	1.76	1215
	Cu0.0Au1.0	1337 – 1673	17390.0	1.1	1337
Cu-Fe	Cu0.0Fe1.0	1811 – 2111	7040.0	1.08	1811
	Cu0.70Fe0.30	1693 – 1993	7370.0	0.79	1693
	Cu0.80Fe0.20	1673 – 1973	7480.0	0.813	1673
	Cu0.90Fe0.10	1578 – 1878	7670.0	0.857	1578
	Cu1.0Fe0.0	1357 – 1657	7900.0	0.765	1357
Cu-Ni	Cu1.0Ni0.0	1357 – 1657	7900.0	0.765	1357
	Cu0.90Ni0.10	1409 – 1709	7970.0	0.795	1409
	Cu0.80Ni0.20	1473 – 1773	8090.0	0.957	1473
	Cu0.60Ni0.40	1553 – 1853	8130.0	1.03	1553
	Cu0.50Ni0.50	1593 – 1893	8100.0	0.772	1593
	Cu0.30Ni0.70	1653 – 1953	8060.0	0.911	1653
	Cu0.10Ni0.90	1706 – 2006	7960.0	0.926	1706
	Cu0.0Ni1.0	1727 – 2027	7920.0	1.01	1727
Cu-Si	Cu0.95Si0.05	1311 – 1611	7790.0	0.701	1311
	Cu0.90Si0.10	1246 – 1546	7590.0	0.631	1246
	Cu0.851Si0.149	1159 – 1459	7470.0	0.673	1159
	Cu0.84Si0.16	1125 – 1425	7380.0	0.673	1125
	Cu0.854Si0.166	1118 – 1418	7400.0	0.704	1118
	Cu0.80Si0.20	1094 – 1394	7210.0	0.695	1094
	Cu0.775Si0.225	1131 – 1431	7090.0	0.681	1131
	Cu0.76Si0.24	1132 – 1432	6800.0	0.573	1132
	Cu0.75Si0.25	1131 – 1431	6830.0	0.627	1131
	Cu0.725Si0.275	1114 – 1414	6700.0	0.514	1114
	Cu0.70Si0.30	1075 – 1375	6510.0	0.592	1075
	Cu0.65Si0.35	1164 – 1464	6070.0	0.55	1164
	Cu0.60Si0.40	1235 – 1535	5740.0	0.567	1235
	Cu0.50Si0.50	1363 – 1663	5260.0	0.54	1363
Cu-Ti	Cu1.0Ti0.0	1358 – 1758	7900.0	0.76	1358
	Cu0.9Ti0.1	1380 – 1850	7300.0	0.32	1293
	Cu0.8Ti0.2	1320 – 1850	6900.0	0.87	1204
	Cu0.7Ti0.3	1260 – 1633	6300.0	0.58	1190
	Cu0.6Ti0.4	1360 – 1576	6100.0	1.23	1238
	Cu0.5Ti0.5	1260 – 1510	5300.0	0.55	1254
	Cu0.4Ti0.6	1327 – 1516	5000.0	0.62	1253
	Cu0.3Ti0.7	1326 – 1492	4600.0	0.13	1415
	Cu0.2Ti0.8	1545 – 1766	4600.0	0.1	1641
	Cu0.1Ti0.9	1659 – 1805	4300.0	0.46	1807
	Cu0.0Ti1.0	1858 – 1982	4100.0	0.33	1941
Fe-Cr	Fe1.0Cr0.0	1808 – 2108	6990.0	0.555	1808
	Fe0.90Cr0.10	1748 – 2048	7090.0	0.604	1748

Table 10.2 continued from previous page

System	Composition	Temp. Range (K)	ρ_L (kg/m^3)	ρ_T (kg/m^3· K)	T_{liquidus} (K)
	Fe0.80Cr0.20	1710 – 2010	6890.0	0.939	1710
	Fe0.70Cr0.30	1723 – 2023	7882.0	0.627	1723
	Fe0.60Cr0.40	1635 – 1935	8064.0	0.747	1635
	Fe0.50Cr0.50	1640 – 1940	8011.0	0.634	1640
Fe-Ni	Fe1.0Ni0.0	1811 – 2111	7040.0	1.08	1811
	Fe0.80Ni0.20	1753 – 2053	7320.0	1.0	1753
	Fe0.60Ni0.40	1725 – 2025	7430.0	1.15	1725
	Fe0.50Ni0.50	1716 – 2016	7500.0	1.02	1716
	Fe0.40Ni0.60	1713 – 2013	7510.0	1.06	1713
	Fe0.20Ni0.80	1713 – 2013	7870.0	1.23	1713
	Fe0.0Ni1.0	1727 – 2027	7930.0	1.01	1727
Pb-Bi	Pb0.4375Bi0.5625	400 – 1200	10484.0	1.1	400
Pb-Sn	Pb0.261Sn0.739	400 – 1000	8148.0	0.81	400

Multi-Component Systems

The density of multi-component (specifically ternary) liquid alloys is estimated using the same linear temperature-dependent equation, Equation (10.7), as for unary and binary systems. The supported systems are listed in Table 10.3.

For compositions not explicitly listed, the required parameters (ρ_L, ρ_T, and T_L) are estimated via barycentric interpolation from known compositions within the ternary system. Barycentric interpolation is a method of estimating values between known data points by weighting the contributions of each point based on its distance to the target point. These parameters are then used in Equation (10.7) to calculate the density at a given temperature. To ensure accuracy, and prevent extrapolation errors, calculations must be performed within the composition and temperature ranges for which the parameters have been experimentally determined.

Table 10.3: Supported systems, compositions, and parameters for the multi-component density model.

System	Composition	Temp. Range (K)	ρ_L (kg/m^3)	ρ_T (kg/m^3· K)	T_{liquidus} (K)
Ag-Al-Cu	Ag0.10Al0.90Cu0.0	920 – 1220	2820.0	0.21	920
	Ag0.10Al0.80Cu0.10	890 – 1190	3480.0	0.54	890
	Ag0.10Al0.60Cu0.30	810 – 1110	4490.0	0.64	810
	Ag0.10Al0.50Cu0.40	840 – 1140	5480.0	0.98	840
	Ag0.10Al0.40Cu0.50	880 – 1180	6030.0	1.01	880
	Ag0.10Al0.20Cu0.70	1190 – 1490	6900.0	0.646	1190
	Ag0.10Al0.0Cu0.90	1310 – 1610	8120.0	1.05	1310
Al-Cu-Si	Al1.0Cu0.00Si0.00	933 – 1233	2420.0	0.3	933
	Al0.90Cu0.05Si0.05	870 – 1170	2690.0	0.48	870
	Al0.80Cu0.10Si0.10	837 – 1137	3070.0	0.55	837
	Al0.60Cu0.20Si0.20	1035 – 1335	3230.0	0.24	1035
	Al0.33Cu0.33Si0.33	1270 – 1570	3890.0	0.26	1270
	Al0.0Cu0.50Si0.50	1363 – 1663	5260.0	0.54	1363
	Al0.30Cu0.40Si0.30	1245 – 1545	4360.0	0.37	1245
	Al0.40Cu0.20Si0.40	1302 – 1602	3330.0	0.25	1302
Co-Cu-Fe	Co0.50Cu0.0Fe0.50	1752 – 2052	7430.0	0.748	1752
	Co0.40Cu0.20Fe0.40	1696 – 1996	7470.0	1.37	1696
	Co0.30Cu0.40Fe0.30	1675 – 1975	7480.0	1.03	1675
	Co0.20Cu0.60Fe0.20	1662 – 1962	7530.0	1.17	1662
	Co0.15Cu0.70Fe0.15	1656 – 1956	7570.0	1.15	1656
	Co0.10Cu0.80Fe0.10	1639 – 1939	7630.0	0.779	1639
	Co0.05Cu0.90Fe0.05	1558 – 1858	7710.0	0.499	1558
	Co0.0Cu1.0Fe0.0	1357 – 1657	7900.0	0.765	1357
	Co0.20Cu0.20Fe0.60	1711 – 2011	7260.0	0.839	1711

Table 10.3 continued from previous page

System	Composition	Temp. Range (K)	ρ_L (kg/m^3)	ρ_T (kg/m$^3\cdot$ K)	T_{liquidus} (K)
	Co0.20Cu0.40Fe0.40	1696 – 1996	7470.0	1.37	1696
	Co0.20Cu0.60Fe0.20	1693 – 1993	7610.0	1.05	1693
Co-Cu-Ni	Co0.80Cu0.0Ni0.20	1758 – 2058	8100.0	0.76	1758
	Co0.70Cu0.10Ni0.20	1721 – 2021	8250.0	1.17	1721
	Co0.50Cu0.30Ni0.20	1654 – 1954	8170.0	1.26	1654
	Co0.40Cu0.40Ni0.20	1621 – 1921	8220.0	0.81	1621
	Co0.30Cu0.50Ni0.20	1590 – 1890	8190.0	1.09	1590
	Co0.10Cu0.70Ni0.20	1508 – 1808	8210.0	0.8	1508
	Co0.0Cu0.80Ni0.20	1473 – 1773	8130.0	0.96	1473
	Co0.50Cu0.50Ni0.0	1650 – 1950	7660.0	0.72	1650
	Co0.35Cu0.35Ni0.30	1641 – 1941	8400.0	0.91	1641
	Co0.30Cu0.30Ni0.40	1642 – 1942	8220.0	1.67	1642
	Co0.20Cu0.20Ni0.60	1643 – 1943	8240.0	1.46	1643
	Co0.15Cu0.15Ni0.70	1685 – 1985	8130.0	0.87	1685
	Co0.10Cu0.10Ni0.80	1685 – 1985	8250.0	1.21	1685
	Co0.0Cu0.0Ni1.0	1728 – 2028	7930.0	1.01	1728
Cr-Fe-Ni	Cr0.10Fe0.18Ni0.72	1724 – 2024	7500.0	0.376	1724
	Cr0.10Fe0.36Ni0.54	1724 – 2024	7330.0	0.41	1724
	Cr0.10Fe0.54Ni0.36	1722 – 2022	7180.0	0.572	1722
	Cr0.10Fe0.63Ni0.27	1734 – 2034	7100.0	0.613	1734
	Cr0.10Fe0.72Ni0.18	1748 – 2048	7090.0	0.604	1748
	Cr0.20Fe0.16Ni0.64	1690 – 1990	7160.0	0.687	1690
	Cr0.20Fe0.32Ni0.48	1690 – 1990	7050.0	0.558	1690
	Cr0.20Fe0.48Ni0.32	1698 – 1998	6950.0	0.636	1698
	Cr0.20Fe0.56Ni0.24	1710 – 2010	6930.0	0.703	1710
	Cr0.20Fe0.64Ni0.16	1710 – 2010	6890.0	0.939	1710
	Cr0.40Fe0.12Ni0.48	1640 – 1940	8011.0	0.634	1640
Cu-Fe-Ni	Cu0.13Fe0.54Ni0.33	1692 – 1992	7110.0	0.28	1692
	Cu0.40Fe0.35Ni0.25	1610 – 1910	7140.0	0.79	1610
	Cu0.50Fe0.30Ni0.20	1591 – 1891	7200.0	0.36	1591
	Cu0.60Fe0.24Ni0.16	1580 – 1880	7530.0	1.96	1580
	Cu0.70Fe0.13Ni0.17	1546 – 1846	7760.0	1.16	1546
	Cu0.20Fe0.65Ni0.15	1701 – 2001	7160.0	1.43	1701
	Cu0.20Fe0.48Ni0.32	1669 – 1969	7400.0	1.7	1669
	Cu0.20Fe0.35Ni0.45	1663 – 1963	7420.0	1.04	1663
	Cu0.20Fe0.20Ni0.60	1668 – 1968	7560.0	0.83	1668
	Cu0.20Fe0.10Ni0.70	1673 – 1973	7790.0	0.86	1673

10.1.4 Model Validation

Due to time constraints and the extensive amount of data available for unary, binary, and multi-component liquid alloy systems, only a selection of the validation plots are presented. Additional validation plots will be made available in future releases of the manual as more systems with their respective parameters are validated against experimental data. **Therefore, users are cautioned that not all the model estimates may be accurate, especially those not explicitly validated here.**

Unary Systems

For the unary systems shown Figure 10.1, density estimates from auxi-mpp's EmpiricalUnary model are validated against recommended referenced data (Assael et al. 2006; Assael et al. 2010; Assael et al. 2012a; Assael et al. 2012b; Ntonti et al. 2024). Model estimates for each supported element show good agreement with the reference data over the recommended temperature ranges.

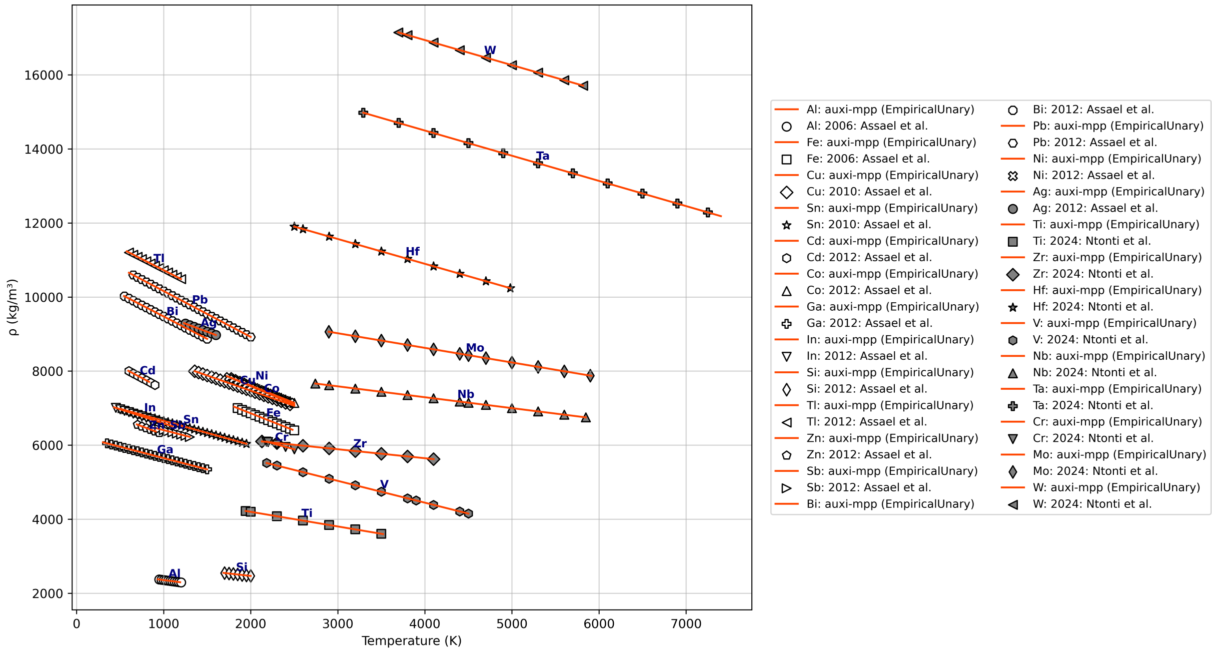

Figure 10.1: EmpiricalUnary model estimates versus recommended values for all supported liquid metals.

Binary Systems

For the binary systems, only the Fe – Ni system has been validated against experimental data, as shown in Figure 10.2. The model estimates from auxi-mpp's EmpiricalBinary model are plotted over the recommended temperature range where the alloy is fully liquid and show good agreement with the experimental data (Brillo and Egry 2004). It is evident in Figure 10.2 that some of the model estimate lines do not extend over the entire range of available experimental data. This is because some of these experimental data points are below the liquidus temperature and, therefore, fall outside the model's valid temperature range, making them invalid for comparison.

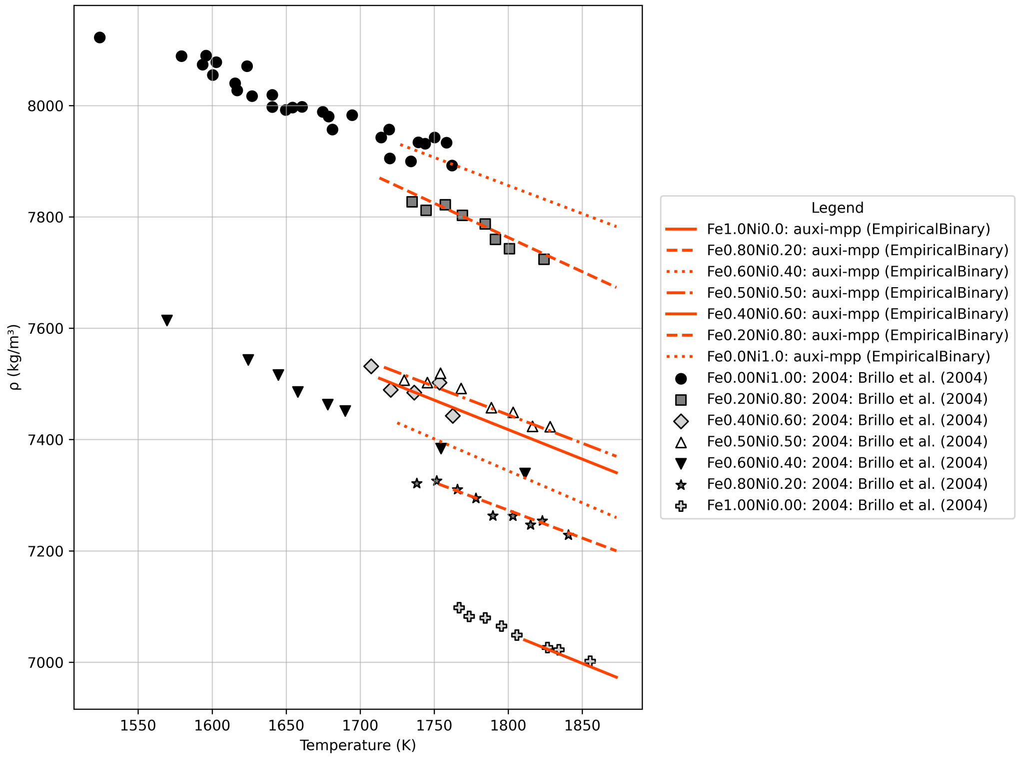

Figure 10.2: EmpiricalBinary model estimates for Fe – Ni at various compositions compared to experimental data (Brillo and Egry 2004).

Multi-Component Systems

Lastly, for the multi-component systems, only the Cu – Fe – Ni system has been validated against experimental data, as shown in Figure 10.3. Again, the model estimates from auxi-mpp's EmpiricalMultitiComponent model are plotted only over the recommended temperature range where the alloy is fully liquid and shows good agreement with the experimental data (Brillo et al. 2006).

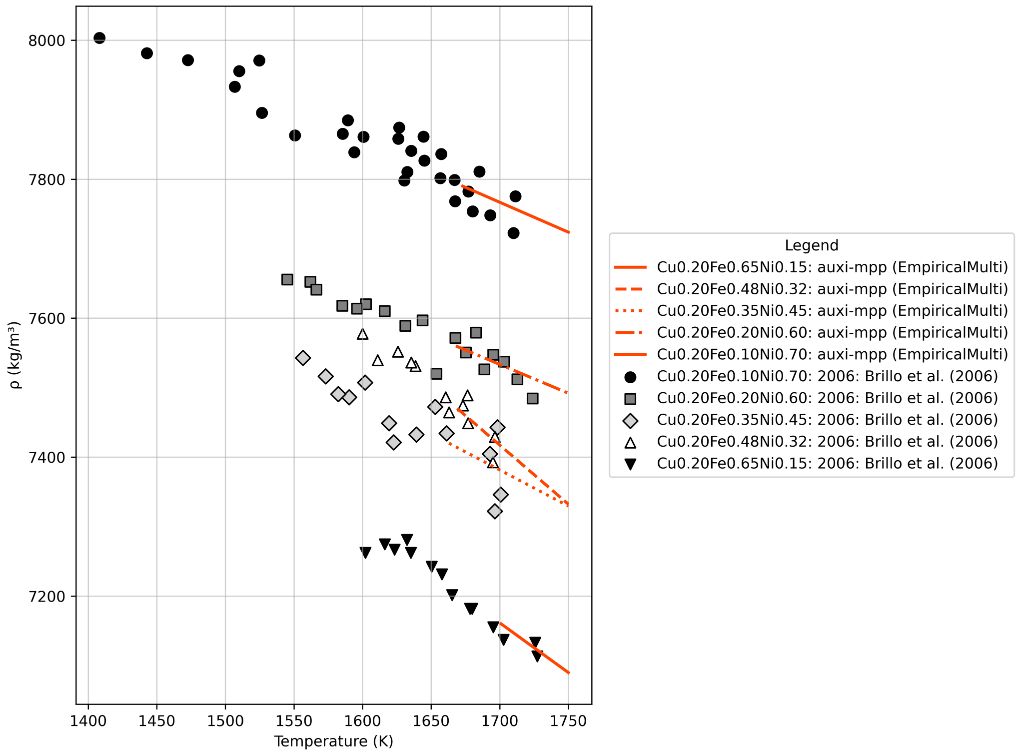

Figure 10.3: EmpiricalMulti model estimates for the Cu – Fe – Ni system at various compositions compared to experimental data (Brillo et al. 2006).

10.1.5 Issues

There are no known issues.

10.2 Binary Metallic Alloys with Non-Metallics

Simple empirical models have been implemented in auxi-mpp to help estimate the density of binary alloys containing non-metallic elements such as C and S.

10.2.1 Introduction

Empirical models for estimating the density for system of Fe – C, Fe – S, Cu – S and Ni – S have been found in literature (Tesfaye and Taskinen 2010). These models serve as a first approximation for estimating the density of binary alloys containing non-metallic elements.

10.2.2 Formulation

Fe-S System (Nagamori, 1968)

The density of a liquid Fe-S alloy system is estimated using an empirical model developed by Nagamori, which is based on experimental data at high temperatures. This model describes the properties as a function of sulfur content (Tesfaye and Taskinen 2010).

The density, ρ, of Fe-S melts at 1200°C is given by a quadratic function of the weight percent of sulfur (C_S) as shown in Equation (10.8):

$$\rho(C_S) = 6.957 - 7.523 \times 10^{-2} C_S - 2.997 \times 10^{-4} C_S^2 \quad (10.8)$$

The density composition range for which the model is valid is: 28-37 wt% S.

Ni-S System (Nagamori, 1969)

The density of Ni-S melts is calculated based on the density at a reference temperature of 1200 °C and a linear temperature correction as shown in Equation (10.9) (Tesfaye and Taskinen 2010).

$$\rho(T, C_S) = \rho_{1200} + \frac{d\rho}{dT}(T_C - 1200) \quad (10.9)$$

Here, ρ_{1200} is the density at 1200 °C and $\frac{d\rho}{dT}$ is the temperature coefficient. As shown in Equations (10.10) and (10.11), both are dependent on the weight percent of sulfur, C_S.

$$\rho_{1200} = c_0 - c_1 C_S - c_2 C_S^2 \quad (10.10)$$

$$\frac{d\rho}{dT} = d_0 + d_1 C_S \quad (10.11)$$

The resulting density is in g/cm^3 and is converted to kg/m^3 by multiplying by 1000.

Table 10.4: Parameters for the Ni-S Density Model

Parameter	Value	Unit
c_0	7.24	g/cm^3
c_1	2.254e-2	g/(cm^3 · wt%)
c_2	1.795e-3	g/(cm^3 · wt%^{2})
d_0	-2.4e-3	g/(cm^3·°C)
d_1	8.0e-5	g/(cm^3·°C · wt%)

The model is valid within the following ranges temperature range of 1000-1200 °C and a composition of 18-30 wt% S.

Cu-S System (Nagamori, 1969)

The density of molten Cu-S at a fixed temperature of 1200 °C (1473.15 K) is estimated using Equation (10.12). The model describes density as a linear function of the sulfur weight percent, C_S (Tesfaye and Taskinen 2010).

$$\rho(C_S) = c_0 - c_1 C_S \quad (10.12)$$

The resulting density is in g/cm^3 and is converted to kg/m^3 by multiplying by 1000.

The model is valid only within the composition range of 19.6-20.6 wt% S.

Table 10.5: Parameters for the Cu-S Density Model

Parameter	Value	Unit
c_0	7.9	g/cm^3
c_1	1.348e-1	g/(cm$^3 \cdot$ wt%)

Fe-C System (Jimbo and Cramb, 1993)

The density of liquid Fe-C alloys is modelled as a function of temperature and the weight percent of carbon, as shown in Equation (10.13), where T_K is the temperature in Kelvin and C_C is the weight percent of carbon (Jimbo and Cramb 1993).

$$\rho(T, C_C) = (a_0 - a_1 C_C) - (b_0 - b_1 C_C) \times 10^{-4} (T_K - 1823) \tag{10.13}$$

The resulting density is in g/cm^3 and is converted to kg/m^3 by multiplying by 1000.

Table 10.6: Parameters for the Fe-C Density Model

Parameter	Value	Unit
a_0	7.10	g/cm^3
a_1	0.0732	g/(cm$^3 \cdot$ wt%)
b_0	8.28	g·K/(cm^3)
b_1	0.874	g·K/(cm$^3 \cdot$ wt%)

The model is valid within the temperature range of 1250-1550°C and a composition range of 0-4 wt% C.

10.2.3 Model Validation

Due to time constraints, model validation for binary alloys with non-metallics was limited to the Fe-S and Fe-C systems. Estimates from the EmpiricalBinaryWithNonMetallics model in auxi-mpp, which incorporates the Fe-S and Fe-C submodels, show good agreement with experimental data (Tesfaye and Taskinen 2010; Jimbo and Cramb 1993). Validation for the Cu-S and Ni-S systems is planned for a future release.

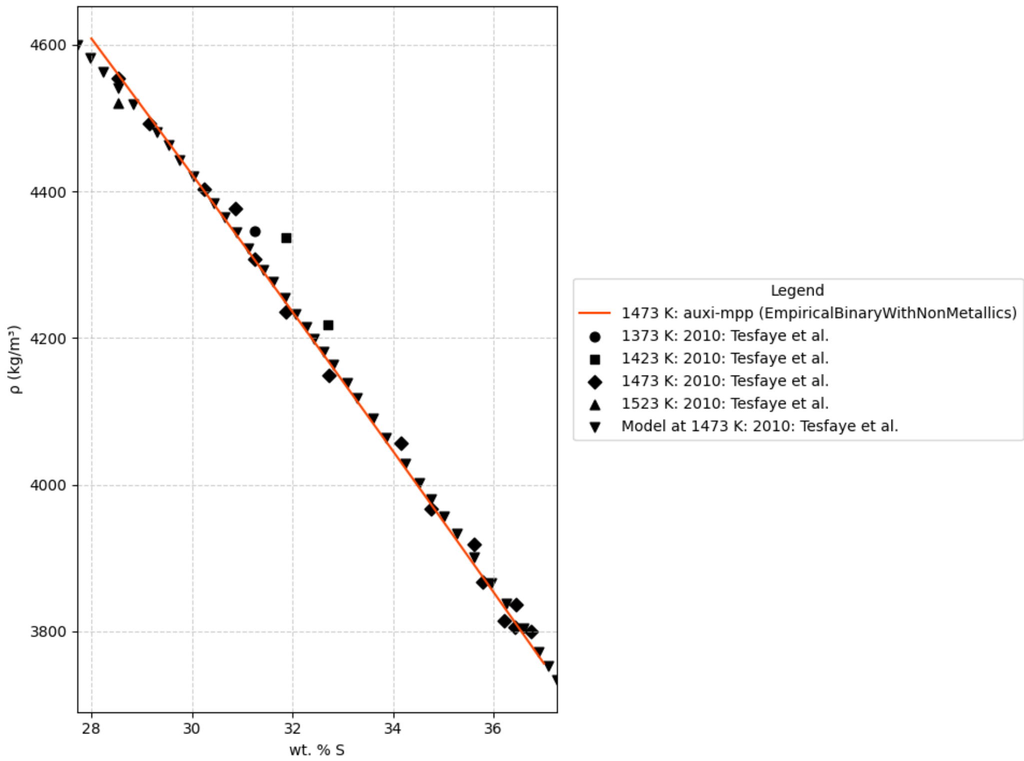

(a) Binary Fe – S system (Tesfaye and Taskinen 2010).

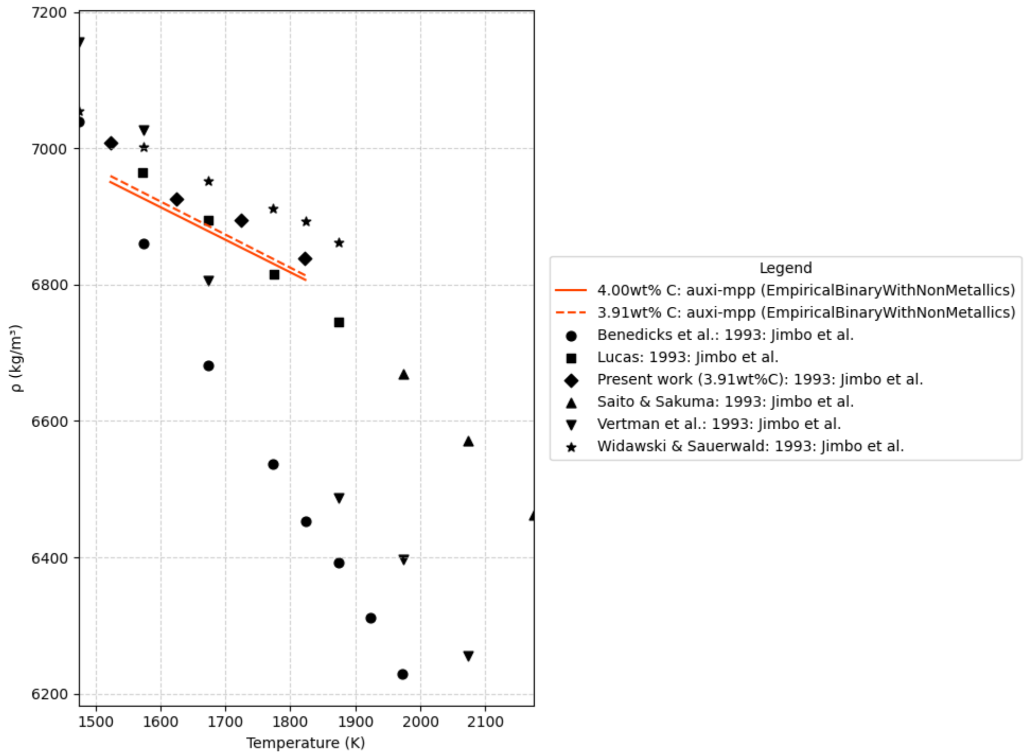

(b) Binary Fe – C system (Jimbo and Cramb 1993).

Figure 10.4: EmpiricalBinaryWithNonMetallics model estimates for binary alloys with non-metallic elements versus experimental data.

10.2.4 Issues

There are no known issues.

10.3 Density for Multi-Component Commercial Alloys

Liquid alloy density models for estimating the density of various commercial liquid alloys have been implemented in auxi-mpp.

10.3.1 Introduction

The work of Mills (2002) contains various commercial alloys of Al, Co, Cu, Fe, Mg, Ni, Si, Ti, and Zn with associated material property data and estimates. These alloys consist of unique multi-component compositions that include both metallic and non-metallic elements. As first an implementation into auxi-mpp, the liquid alloy density models for Fe based commercial alloys have been implemented.

10.3.2 Formulation

The density, ρ, of a commercial alloy is calculated as a function of temperature in Celsius (T_C). For some alloys, the density is also dependent on the weight percent of silicon (wt% Si). The general form of the equation is given by Equation (10.14).

$$\rho(T) = A - B(T_C - T_{\text{ref,C}}) - C_{\text{Si}}(\text{wt\% Si}) \tag{10.14}$$

where:

1. $\rho(T)$ is the density of the alloy in kg/m^3.
2. T_C is the temperature in degrees Celsius (°C).
3. A is an empirical density parameter in kg/m^3.
4. B is the empirical temperature coefficient of density in kg/m^3 ·° C.
5. $T_{\text{ref,C}}$ is a reference temperature in degrees Celsius (°C).
6. C_{Si} is the coefficient for the silicon content adjustment, in kg/m^3 · wt%. This term is only applicable for certain alloys, such as cast irons.
7. wt% Si is the weight percent of silicon in the alloy.

The model calculates the density for a specific set of supported commercial alloys based on fixed compositions and parameters. Table 10.7 details the supported alloys, their compositions, valid temperature ranges, and the specific parameters used in Equation (10.14).

Table 10.7: Supported Commercial Alloys and Model Parameters

Alloy Name	Parameter	Value	Unit
Grey Cast Iron	Temp. Range	1463 – 1773	K
	Composition	C: 3.72, Fe: 91.9, Si: 1.89, Cr: 0.95, Mn: 0.66, Mg: 0.002, Mo: 0.59, Ni: 0.19, P: 0.09, S: 0.03	wt%
	A	6829.0	kg/m^3
	B	0.50	kg/(m^3·°C)

Table 10.7 continued from previous page

Alloy Name	Parameter	Value	Unit
	$T_{\text{ref,C}}$	1550.0	°C
	C_{Si}	130.0	kg/(m^3· wt%)
Ductile Iron	Temp. Range	1451 – 1773	K
	Composition	C: 3.61, Fe: 92.4, Si: 2.91, Mn: 0.65, Mg: 0.002, Ni: 0.13, P: 0.12, Cr: 0.08, S: 0.076	wt%
	A	6836.0	kg/m^3
	B	0.513	kg/(m^3·°C)
	$T_{\text{ref,C}}$	1550.0	°C
	C_{Si}	130.0	kg/(m^3· wt%)
304 Stainless Steel	Temp. Range	1727 – 1873	K
	Composition	C: 0.08, Cr: 19.0, Fe: 69, Ni: 9.5, Mn: 2.0, Cu: 0.3	wt%
	A	6900.0	kg/m^3
	B	0.80	kg/(m^3·°C)
	$T_{\text{ref,C}}$	1454.0	°C
316 Stainless Steel	Temp. Range	1723 – 1873	K
	Composition	C: 0.08, Cr: 17.0, Fe: 65, Ni: 12.0, Mn: 2.0, Mo: 2.5, Si: 1.0, Cu: 0.3	wt%
	A	6881.0	kg/m^3
	B	0.77	kg/(m^3·°C)
	$T_{\text{ref,C}}$	1450.0	°C

10.3.3 Model Validation

Due to time constraints, this initial validation is limited to the liquid density of stainless steel 304. The model estimates from MillsCommericalhows good agreement with the experimental data, as shown in Figure 10.5 (Mills 2002). The other commercial alloys listed in Table 10.7 will be validated in future releases of the manual.

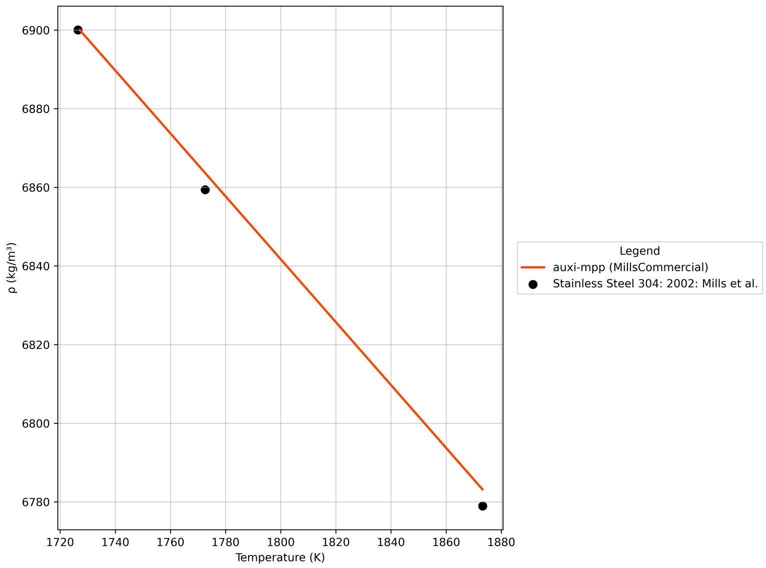

Figure 10.5: MillsCommerical model estimates over recommended temperature range for stainless steel 304 compared to experimental data points (Mills 2002).

10.3.4 Issues

There are no known issues.

10.3.5 Molar Volume

Once the density is known, the molar volume can be calculated. The molar volume can be calculated from density with Equation (10.15).

$$\bar{V}_{\text{alloy}} = \frac{\sum_i \bar{m}_{\text{i}} x_{\text{i}}}{\rho_{\text{alloy}}} \tag{10.15}$$

If the density model proofs to be accurate, accurate molar volume values can be calculated from it.

Chapter 11

Electrical Conductivity

Charge in liquids is transported in two ways – the movement of electrons and that of ions. The dominant mechanism for electrical conductivity in liquid alloys is the movement of electrons. While the ions in liquid metals are mobile and do diffuse, their contribution to electrical current is completely overshadowed by the flow of electrons.

The reason for this is the staggering difference in mass. An ion consists of a nucleus (protons and neutrons) and core electrons, making it thousands of times more massive than a single free electron. Under the influence of an electric field, electrons will accelerate orders of magnitudes faster than ions, establishing a current long before the ions have had a chance to diffuse in any meaningful way. Any model, attempting to estimate the electrical conductivity of liquid alloys from fundamental principles, will therefore have to describe the movement of electrons.

The Kubo-Greenwood formalism stands out as the most successful at this, deriving conductivity from fundamental quantum mechanics without empirical inputs. However, its reliance on computationally intensive ab initio molecular dynamics (MD) and density functional theory (DFT) calculations makes it prohibitively expensive for routine use. It is best employed as a computational experiment to generate high-fidelity benchmark data for validating more practical models.

As the more popular alternative, Ziman theory is a semi-empirical model that still offers valuable physical insights by linking resistivity to atomic structure and electron scattering. While effective for simple metals, it critically fails for alloys containing transition metals like iron, whose strong electron scattering violates the theory's core assumptions, leading to significant errors. Proposed enhancements involve using structural data from large-scale MD simulations and employing advanced scattering potentials (t-matrix formalism) for such elements. Finally, it should also be noted that Ziman theory is formally documented only up to binary alloys.

Besides these two techniques of estimating electrical conductivity, there are no physically rigorous ones available in literature.

11.1 Electrical Conductivity Polynomial Fit

Polynomial fits to measured liquid alloy electrical resistivity data.

11.1.1 Introduction

Due to the lack of readily available models to estimate electrical conductivity for liquid metals, polynomials were fitted to experimental measurements instead. The technicalities of the polynomials available in auxi-mpp are documented here.

11.1.2 Overview

Polynomials have been fitted to electrical resistivity measurements of liquid Fe, Fe – C, Fe – Si, Fe – Mn, Fe – Ni and Fe – C – Si. Electrical resistivity data was used instead of conductivity data for two reasons. Firstly, in literature almost exclusively resistivity measurement data are found and therefore there are no actual conductivity data available. This is likely because of the conductivity being very high for liquid alloys, and therefore difficult to measure accurately. Secondly, the fits have a slightly better R^2 value for resistivity data as these tend to scale linearly with temperature.

Before using these polynomial fits, the user is encouraged to first evaluate the range of data used to fit them before using. For this, see Section 11.1.4. This is because these are polynomial fits and are therefore not based on any physical principle. Their extrapolation accuracy should thus be assumed to be low, and it is recommended to use them within the range of the experimental measurements.

The alloy systems chosen are aimed at representing pig iron which roughly has a composition of 92% Fe, 4% C, 2% Si, 1% Mn, 0.3% P and 0.1% S. Unfortunately, no measurement data could be obtained for Fe – S and Fe – P liquid alloys.

The reason Fe – Ni was included, is that it is the only binary system for which thermal conductivity data was also found. We could therefore use this system to test first-hand how well the Wiedemann-Franz law can estimate the thermal conductivity from electrical conductivity values. See Chapter 13 for the comparison.

Finally, it should be noted that occasionally, conductivity and resistivity is used interchangably. If the performance of auxi-mpp is shown as resistivity, it simply means that the reciprocal of the output from auxi-mpp was taken.

11.1.3 Formulation

For pure Fe, a first and second degree polynomial was fitted, for the binaries a first, second and third degree and for Fe – C – Si a second, third and fourth degree polynomial was fitted. The polynomials were set up to take temperature and composition as inputs, assuming Fe will always be present in the binary and ternary systems. Below, the fitted polynomials are presented for each system. To see the R^2 values, see Section 11.1.4.

Unary Fe System

Equations (11.1) and (11.2) presents the first and second degree polynomial fitted to pure Fe resistivity measurements.

$$\rho_{\text{first}} = 93.6919 + 0.0240T \tag{11.1}$$

$$\rho_{\text{second}} = 72.2778 + 0.0410T - 3.1276 \times 10^{-6}T^2 \tag{11.2}$$

Unary Ni System

Equations (11.3) and (11.4) presents the first and second degree polynomial fitted to pure Ni resistivity measurements.

$$\rho_{\text{first}} = 59.36181 + 0.01575T \tag{11.3}$$

$$\rho_{\text{second}} = 63.73571 + 0.01203T + 7.3751 \times 10^{-7}T^2 \tag{11.4}$$

Unary Si System

Equations (11.5) and (11.6) presents the first and second degree polynomial fitted to pure Si resistivity measurements.

$$\rho_{\text{first}} = 72.92953 - 0.00069T \tag{11.5}$$

$$\rho_{\text{second}} = 146.44446 - 0.08317T + 2.3098 \times 10^{-5}T^2 \tag{11.6}$$

Binary Fe – C System

Equations (11.7) to (11.9) presents the first, second and third degree polynomial fitted to the Fe – C resistivity measurements. Assuming that Fe makes up the rest of the composition, only the mole fraction of the second component should be provided.

$$\rho_{\text{first}} = 92.9871 + 0.0243T + 112.5398x_{\text{C}} \tag{11.7}$$

$$\rho_{\text{second}} = 75.3933 + 0.0387T + 8.2111x_{\text{C}} - 2.7378 \times 10^{-6}T^2 + 0.0435Tx_{\text{C}} + 264.2014x_{\text{C}}^2 \tag{11.8}$$

$$\begin{aligned}\rho_{\text{third}} = {} & 133.9585 - 0.0295T + 297.2871x_{\text{C}} + 2.2889 \times 10^{-5}T^2 - 0.3647Tx_{\text{C}} \\ & + 92.7134x_{\text{C}}^2 - 3.0932 \times 10^{-5}T^3 + 0.0001T^2x_{\text{C}} + 0.1280Tx_{\text{C}}^2 + 31.8100x_{\text{C}}^3\end{aligned} \tag{11.9}$$

Binary Fe – Si System

Equations (11.10) to (11.12) presents the first, second and third degree polynomial fitted to the Fe – Si resistivity measurements.

$$\rho_{\text{first}} = 145.16895 + 0.00355T - 52.44309x_{\text{Si}} \tag{11.10}$$

$$\begin{aligned}\rho_{\text{second}} = {} & 1.07524 + 0.09575T + 419.23624x_{\text{Si}} \\ & - 1.2854 \times 10^{-5}T^2 - 0.13748Tx_{\text{Si}} - 231.77971x_{\text{Si}}^2\end{aligned} \tag{11.11}$$

$$\begin{aligned}\rho_{\text{third}} = {} & 201.38264 - 0.10332T + 864.82400x_{\text{Si}} \\ & + 4.8753 \times 10^{-5}T^2 - 1.16402Tx_{\text{Si}} + 653.88877x_{\text{Si}}^2 \\ & - 6.0184 \times 10^{-9}T^3 + 0.00040T^2x_{\text{Si}} - 0.28473Tx_{\text{Si}}^2 - 263.35838x_{\text{Si}}^3\end{aligned} \tag{11.12}$$

Binary Fe – Mn System

Equations (11.13) to (11.15) presents the first, second and third degree polynomial fitted to the Fe – Mn resistivity measurements.

$$\rho_{\text{first}} = 94.4813 + 0.0238T + 227.6563x_{\text{Mn}} \tag{11.13}$$

$$\rho_{\text{second}} = 74.6696 + 0.0393T + 177.9867x_{\text{Mn}} - 2.8329 \times 10^{-6}T^2 + 0.0667Tx_{\text{Mn}} - 660.5977x_{\text{Mn}}^2 \tag{11.14}$$

$$\begin{aligned}\rho_{\text{third}} = {} & 133.3610 - 0.0289T + 0.0002x_{\text{Mn}} + 2.2645 \times 10^{-5}T^2 + 0.1703Tx_{\text{Mn}} \\ & - 0.0002x_{\text{Mn}}^2 - 3.0650 \times 10^{-9}T^3 - 6.5907 \times 10^{-6}T^2x_{\text{Mn}} - 0.3341Tx_{\text{Mn}}^2 - 3.3852 \times 10^{-5}x_{\text{Mn}}^3\end{aligned} \tag{11.15}$$

Binary Fe – Ni System

Equations (11.16) to (11.18) presents the first, second and third degree polynomial fitted to the Fe – Ni resistivity measurements.

$$\rho_{\text{first}} = 132.32556 + 0.00816T - 41.28897x_{\text{Ni}} \tag{11.16}$$

$$\begin{aligned}\rho_{\text{second}} = {} & 93.20065 + 0.02342T + 116.51028x_{\text{Ni}} \\ & + 2.3049 \times 10^{-7}T^2 - 0.01233Tx_{\text{Ni}} - 138.91424x_{\text{Ni}}^2\end{aligned} \tag{11.17}$$

$$\begin{aligned}\rho_{\text{third}} = {} & 142.95516 - 0.03978T - 189.69026x_{\text{Ni}} \\ & + 2.6654 \times 10^{-5}T^2 + 0.05863Tx_{\text{Ni}} + 421.13095x_{\text{Ni}}^2 \\ & - 3.5400 \times 10^{-9}T^3 + 4.6242 \times 10^{-6}T^2x_{\text{Ni}} - 0.09280Tx_{\text{Ni}}^2 - 231.85544x_{\text{Ni}}^3\end{aligned} \tag{11.18}$$

Ternary Fe – C – Si System

Equations (11.19) and (11.20) presents the second and third degree polynomial fitted to the Fe – C – Si resistivity measurements. For this ternary system, a fourth degree polynomial have also been fitted, however due to its complexity, it is not shown here. The coefficients for its terms can be found in the source code of auxi-mpp, however.

$$\begin{aligned}\rho_{\text{second}} = {} & 13.12644 + 0.08669T + 315.76813x_{\text{C}} + 408.54928x_{\text{Si}} \\ & - 1.1268 \times 10^{-5}T^2 - 0.08207Tx_{\text{C}} - 0.13297Tx_{\text{Si}} - 158.67827x_{\text{C}}^2 \\ & - 745.16858x_{\text{C}}x_{\text{Si}} - 230.08561x_{\text{Si}}^2\end{aligned} \tag{11.19}$$

$$\rho_{\text{third}} = 251.74375 - 0.15978T - 3.09670x_{\text{C}} + 779.52392x_{\text{Si}} + 6.9083 \times 10^{-5}T^2 - 0.18232Tx_{\text{C}} - 1.08060Tx_{\text{Si}} + 5.30280x_{\text{C}}^2 - 7.68851x_{\text{C}}x_{\text{Si}} + 660.19505x_{\text{Si}}^2 - 8.3788 \times 10^{-9}T^3 + 0.00011T^2x_{\text{C}} + 0.00038T^2x_{\text{Si}} + 0.25701Tx_{\text{C}}^2 + 0.36579Tx_{\text{C}}x_{\text{Si}} - 0.29099Tx_{\text{Si}}^2 + 0.25065x_{\text{C}}^3 + 1.70881x_{\text{C}}^2x_{\text{Si}} - 5.66292x_{\text{C}}x_{\text{Si}}^2 - 258.92131x_{\text{Si}}^3 \quad (11.20)$$

11.1.4 Model Validation

Table 11.1 summarises the temperature and composition ranges for which liquid alloy electrical resistivity data could be collected. These data points was used to fit the polynomials to. Note that when fitting a polynomial to the binary system data, the unary Fe data was included. Similarly, fitting a polynomial to the Fe – C – Si data, the relevant binary and unary data were also included to make the fit.

Table 11.1: Temperature and composition ranges for which liquid metal or alloy electrical resistivity data was captured.

System (c1-c2-c3)	T (K)	x_{c1} (mol mol^{-1})	x_{c2} (mol mol^{-1})	x_{c3} (mol mol^{-1})	# of data points
Fe	1824 – 3950	1.0	-	-	96
Ni	1722 – 3704	1.0	-	-	91
Si	1685 – 1899	1.0	-	-	31
Fe – C	1448 – 1873	0.830 – 0.999	0.001 – 0.170	-	53
Fe – Si	1473 – 1849	0.197 – 0.911	0.089 – 0.803	-	67
Fe – Mn	1753 – 2053	0.867 – 0.961	0.039 – 0.133	-	50
Fe – Ni	1714 – 1908	0.000 – 0.988	0.012 – 1.000	-	163
Fe – C – Si	1497 – 1846	0.784 – 0.918	0.041 – 0.124	0.035 – 0.175	41

Below the polynomials are validated by plotting them against the experimental data.

Unary Model Validation

In Figure 11.1, the performance of auxi-mpp is compared to measured data for pure iron. The data points were obtained from Ono et al. (1976), Zytveld (1980), and Hixson et al. (1990).

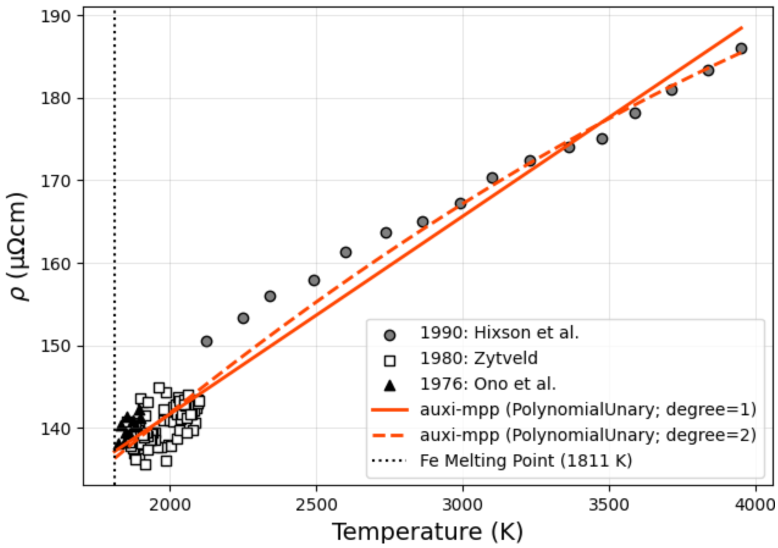

Figure 11.1: Validating auxi-mpp PolynomialUnary for pure Fe. Degree $= 1$ R^2 : 0.957. Degree $= 2$ R^2 : 0.960.

In Figure 11.2, the performance of auxi-mpp is compared to measured data for pure nickel. The data points were obtained from Kita et al. (1978), Seydel and Fucke (1977), Hixson et al. (1990), and Cagran et al. (2007). Surprisingly, the second degree fit has an R^2 of only 0.0005

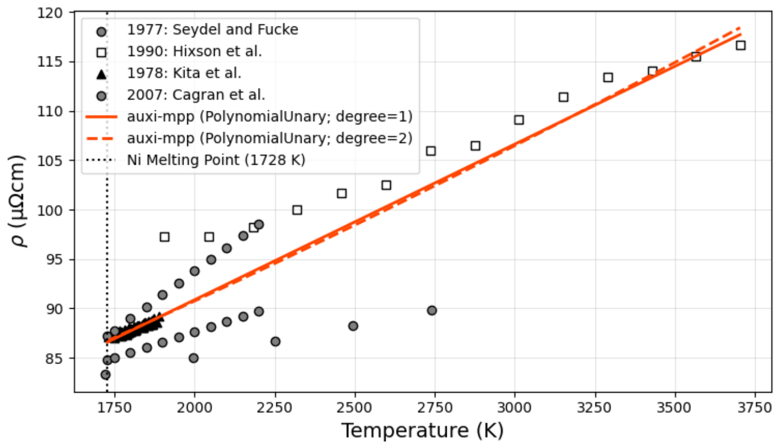

Figure 11.2: Validating auxi-mpp PolynomialUnary for pure Ni. Degree $= 1$ R^2 : 0.846. Degree $= 2$ R^2 : 0.846.

In Figure 11.3, the performance of auxi-mpp is compared to measured data for pure silicon. The data points were obtained from Sasaki et al. (1995).

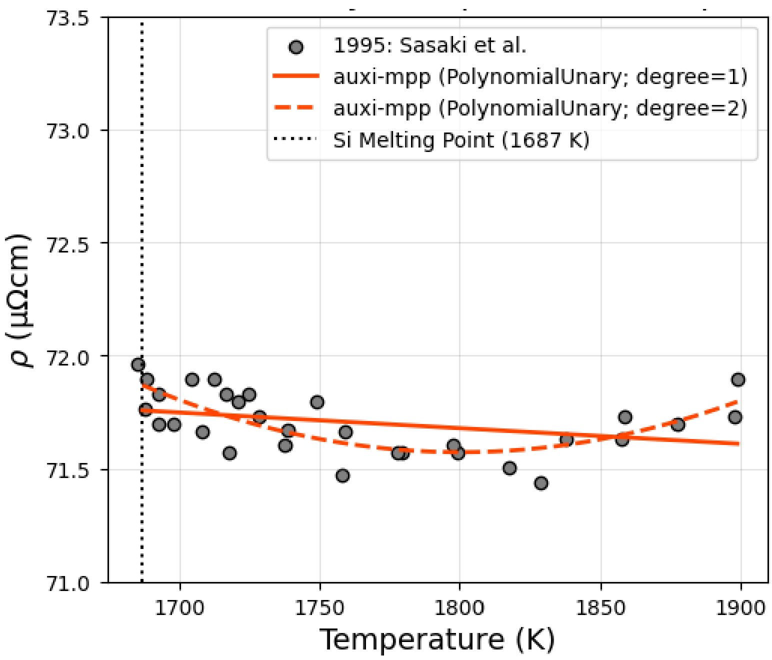

Figure 11.3: Validating auxi-mpp PolynomialUnary for pure Si. Degree $= 1$ R^2 : 0.117. Degree $= 2$ R^2 : 0.530.

For these we regard the second degree fit to be the best.

Binary Model Validation

In Figures 11.4, 11.5, 11.7 and 11.8, the performance of the first, second and third degree polynomials are presented with experimental data of the Fe – C, Fe – Si, Fe – Mn and Fe – Ni systems, respectively. In all cases, we regard the second degree fit to be the best, despite higher R^2 values for third degree fits. The apparent better fits to the data by third degree polynomials, brings about unnecessary complexities and extremities (see Figures 11.5c and 11.8c), rendering them not suitable for reliable interpolations. The first degree fits are also not suitable as the linear dependence of resistivity on temperature changes with composition.

The data points were obtained from Baum et al. (1971), Ono and Yagi (1972), Ono et al. (1976), Zytveld (1980), Kita and Morita (1984), Hixson et al. (1990), and Chikova et al. (2021).

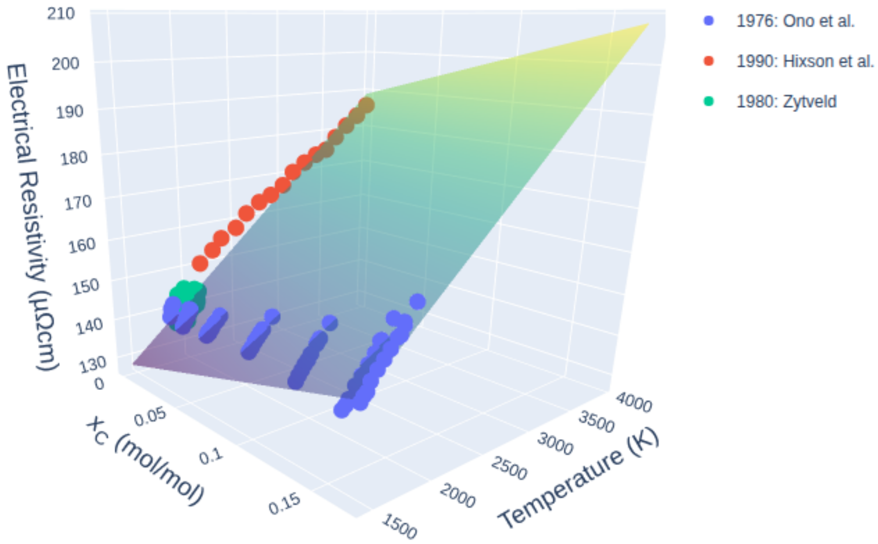

(a) Degree $= 1$. $R^2 = 0.950$

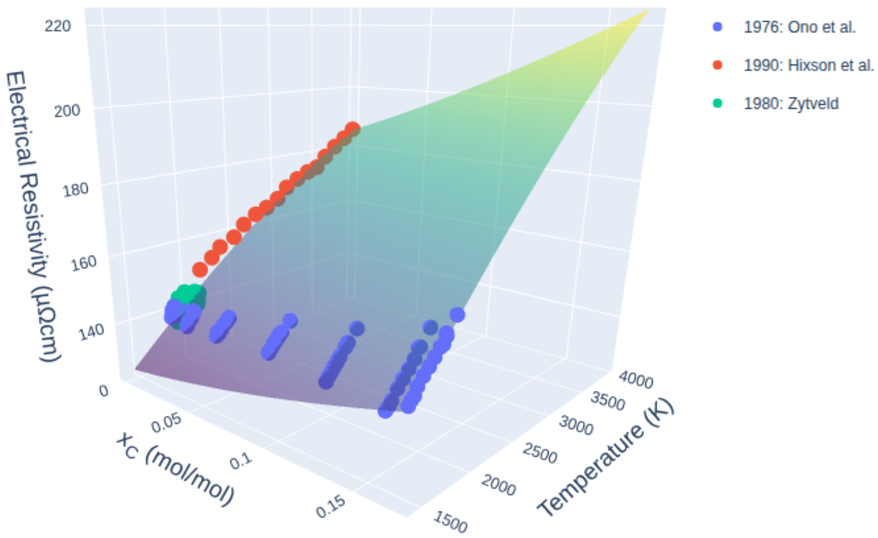

(b) Degree $= 2$. $R^2 = 0.959$

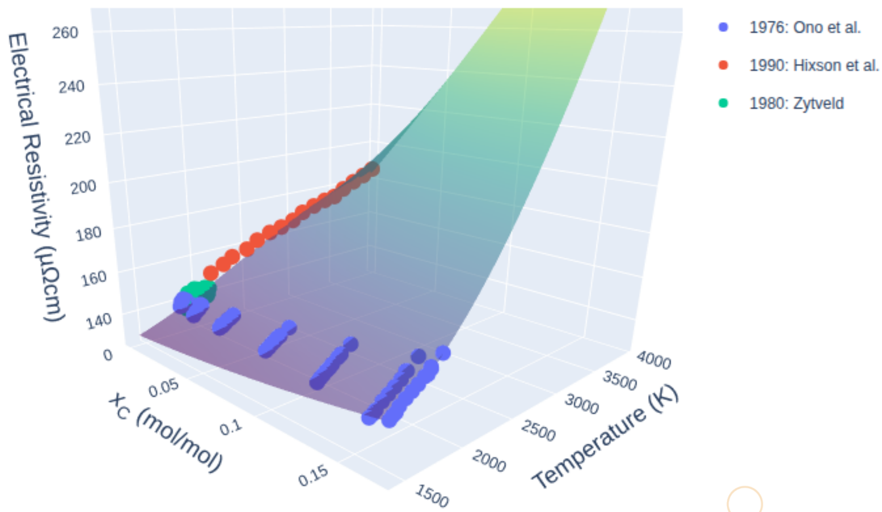

(c) Degree $= 3$. $R^2 = 0.961$

Figure 11.4: Polynomial fits to Fe – C electrical resistivity measurement data.

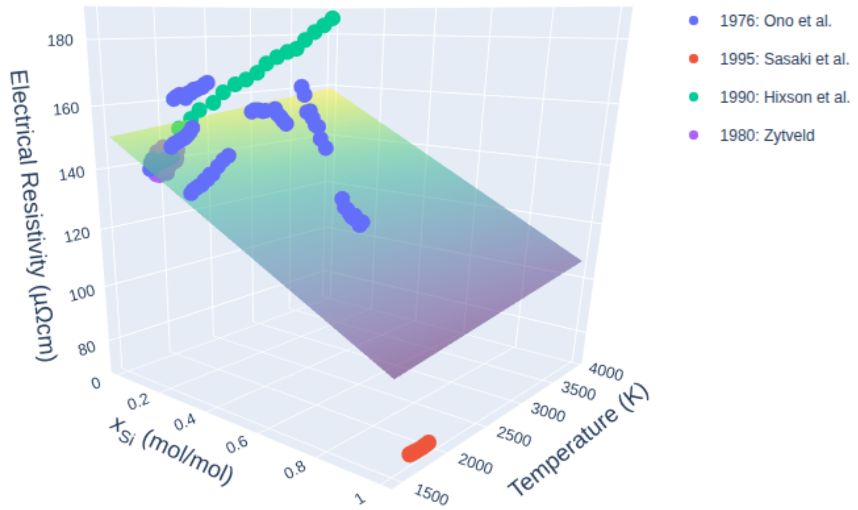

(a) Degree $= 1$. $R^2 = 0.474$

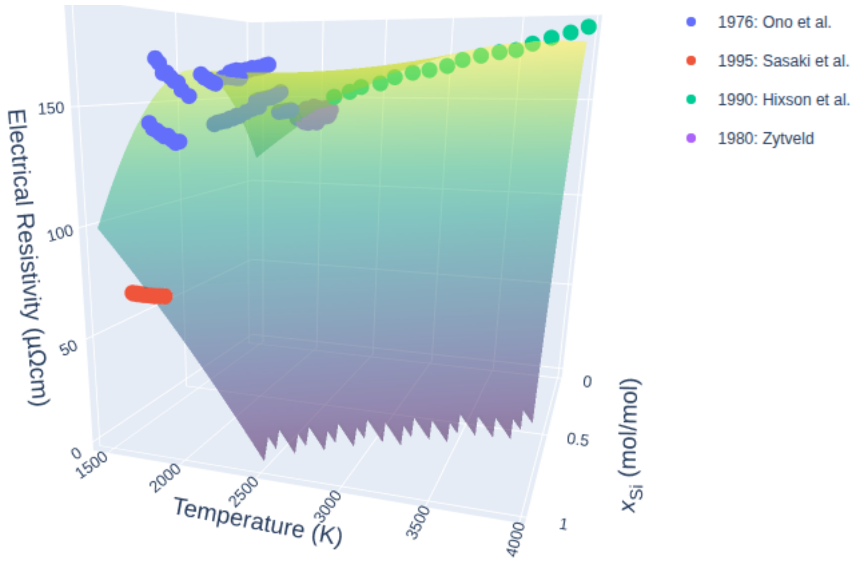

(b) Degree $= 2$. $R^2 = 0.935$

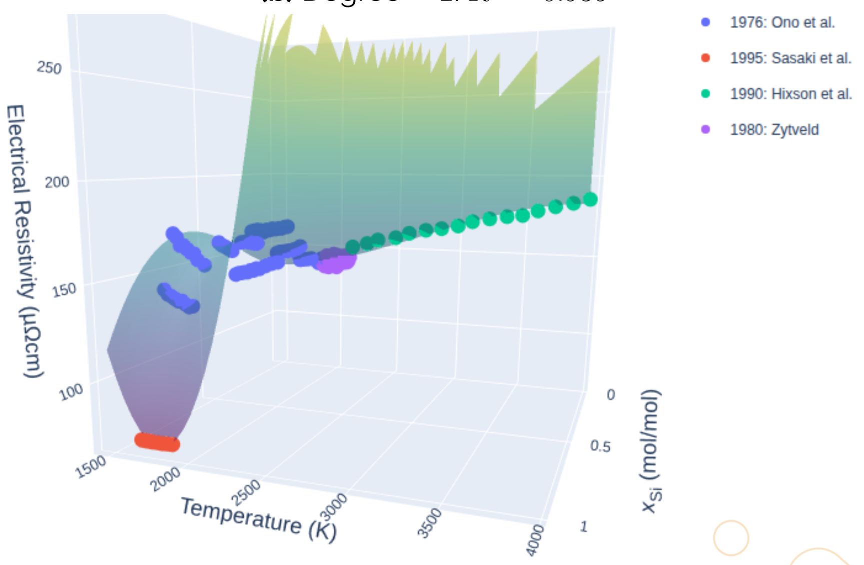

(c) Degree $= 3$. $R^2 = 0.964$

Figure 11.5: Polynomial fits to Fe – Si electrical resistivity measurement data.

To have a better view of the data in Figure 11.5, the second and third degree plots were plotted in 2D in Figure 11.6.

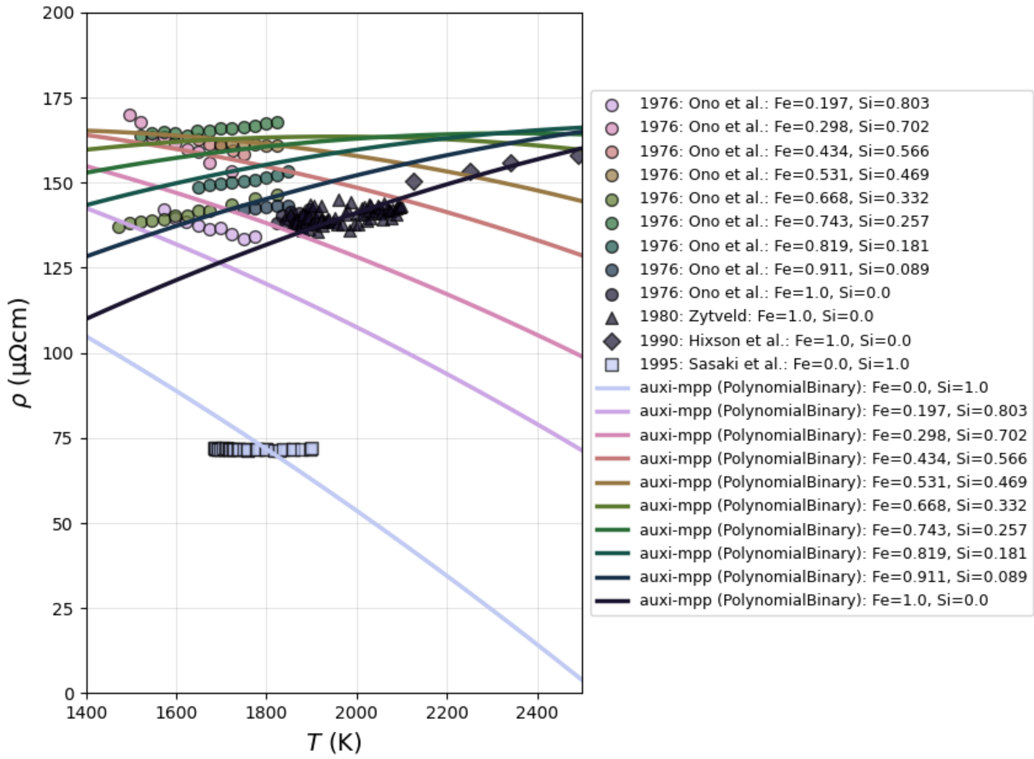

(a) Degree $= 2$. $R^2 = 0.935$

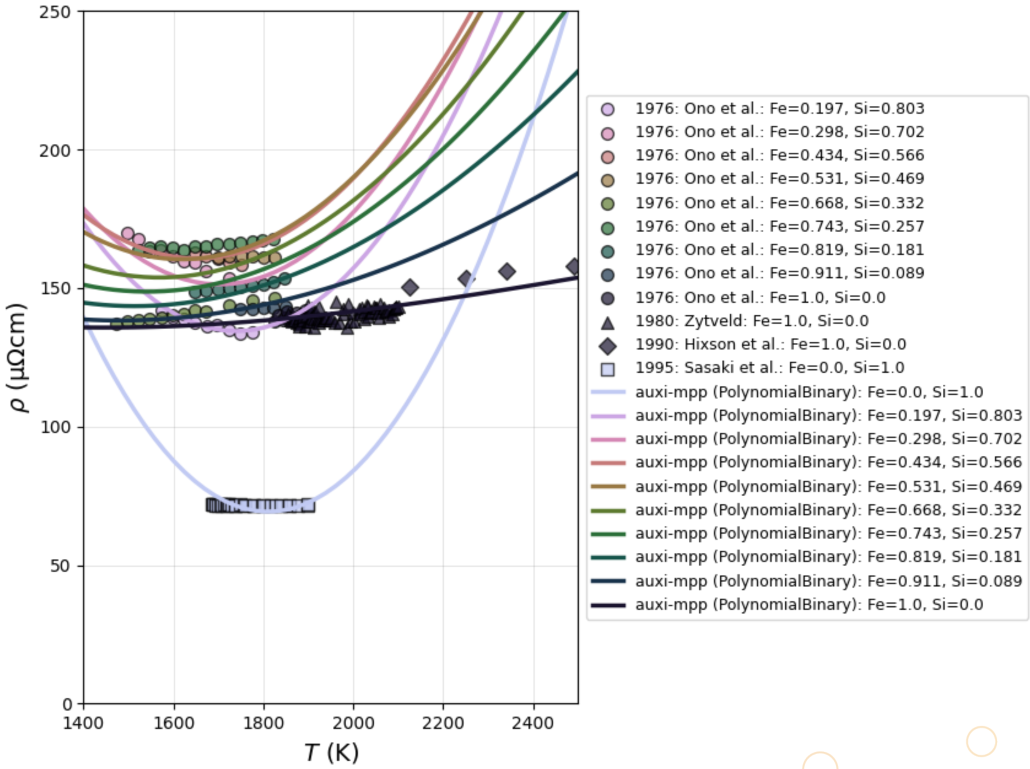

(b) Degree $= 3$. $R^2 = 0.964$

Figure 11.6: A 2D view of the second and third order polynomial fits to Fe – Si electrical resistivity measurement data.

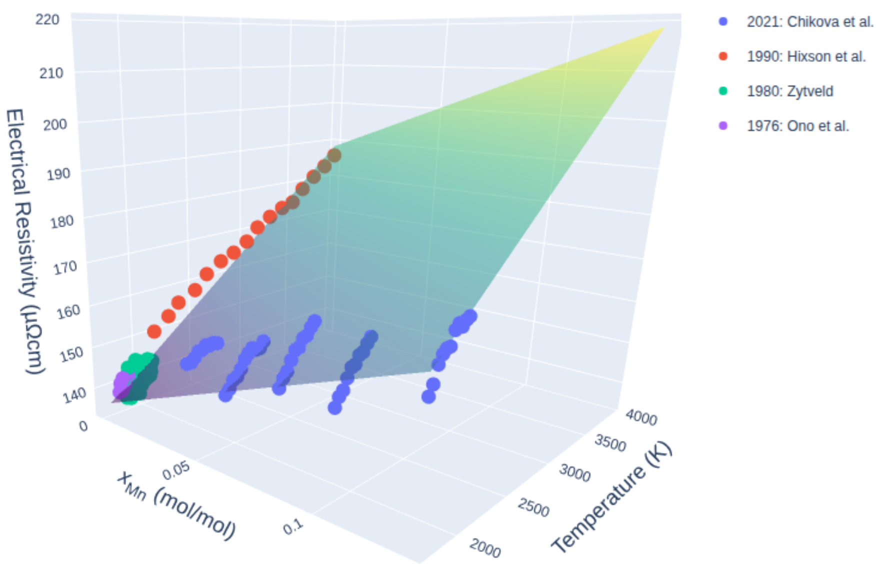

(a) Degree $= 1.$ $R^2 = 0.957$

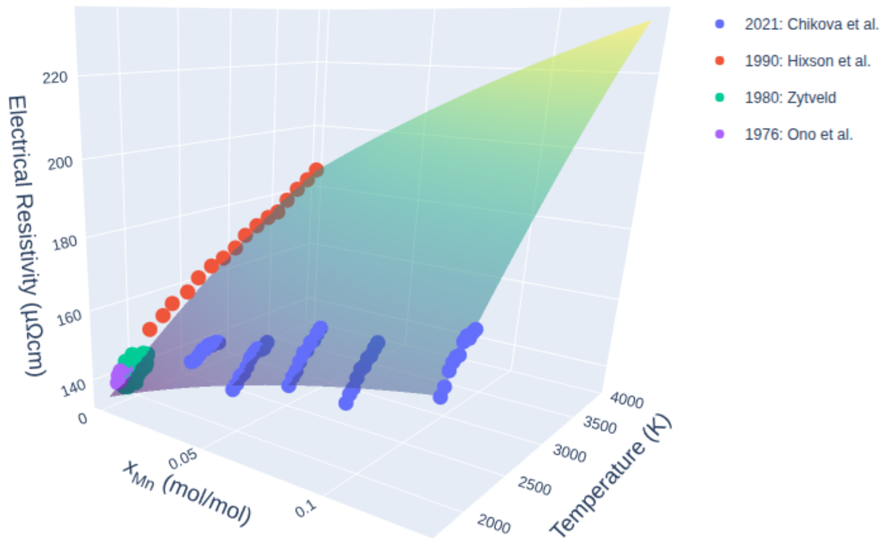

(b) Degree $= 2.$ $R^2 = 0.966$

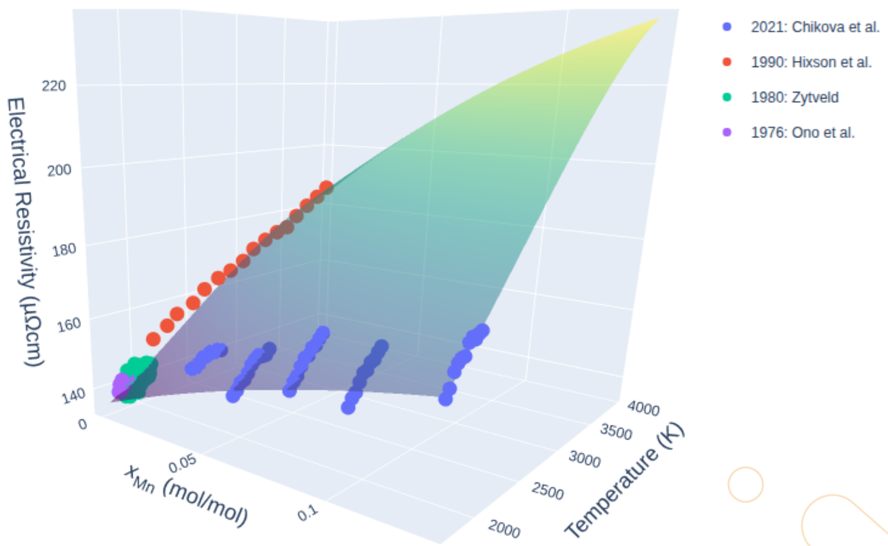

(c) Degree $= 3.$ $R^2 = 0.967$

Figure 11.7: Polynomial fits to Fe – Mn electrical resistivity measurement data.

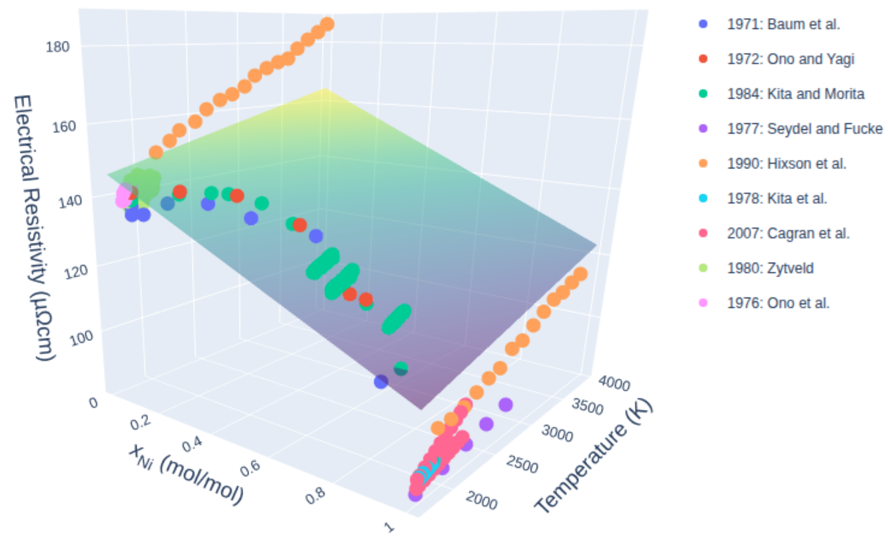

(a) Degree $= 1$. $R^2 = 0.634$

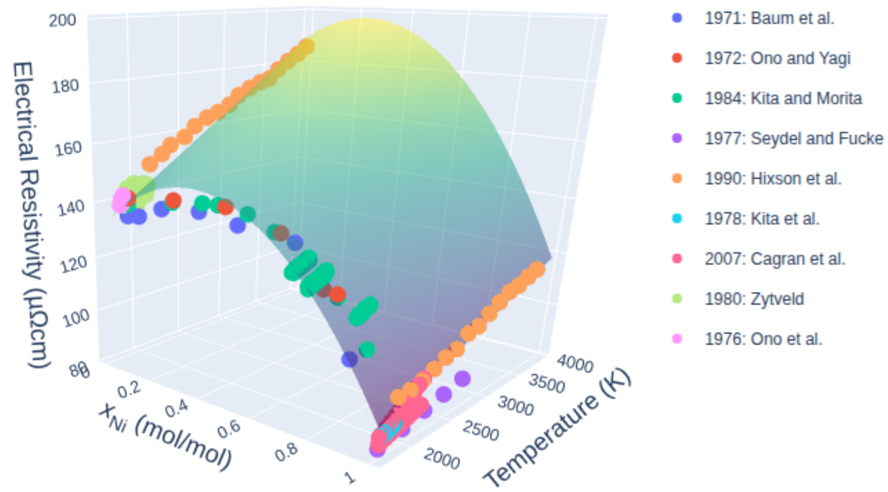

(b) Degree $= 2$. $R^2 = 0.943$

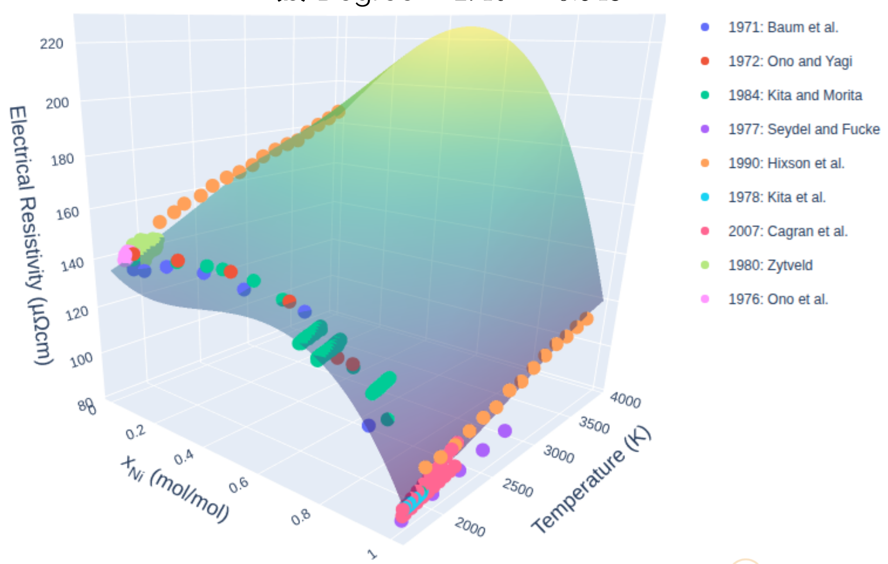

(c) Degree $= 3$. $R^2 = 0.963$

Figure 11.8: Polynomial fits to Fe – Ni electrical resistivity measurement data.

Multi-Component Model Validation

Currently, Fe – C – Si is the only multi-component system available for liquid alloys in auxi-mpp. To the available experimental data, a second, third and fourth degree polynomial have been fitted. The data used is the combination of pure Fe, Fe – C, Fe – Si and Fe – C – Si data. The performance of these polynomials can be analysed in Table 11.2 and Figure 11.9.

Table 11.2: Comparing the electrical conductivity calculated from second, third, and fourth-degree polynomial fits, with the measured values (Ono et al. 1976).

T (K)	x_{Fe}	x_C	x_{Si}	$\sigma_{measured}$ (S m^{-1})	$\Delta\sigma_{second}$	$\Delta\sigma_{third}$	$\Delta\sigma_{fourth}$
1473	0.78	0.04	0.18	660455	-10969	-10585	-6686
1497	0.78	0.04	0.18	660290	-8288	-11136	-7751
1522	0.78	0.04	0.18	655547	-10140	-15725	-12919
1548	0.78	0.04	0.18	651666	-11020	-18812	-16652
1573	0.84	0.12	0.04	725003	38954	40502	40884
1574	0.79	0.12	0.09	684150	15368	21154	21529
1574	0.78	0.04	0.18	649225	-10696	-19901	-18355
1598	0.78	0.04	0.18	644122	-13221	-23165	-22190
1598	0.84	0.12	0.04	717683	35855	36220	36420
1599	0.79	0.12	0.09	677723	12238	18165	18143
1623	0.79	0.12	0.09	670854	8444	14936	14585
1623	0.78	0.04	0.18	641651	-13171	-23260	-22818
1623	0.84	0.12	0.04	710613	32850	32446	32500
1646	0.87	0.04	0.09	670124	-18297	-21213	-21821
1647	0.84	0.12	0.04	702655	28645	27869	27819
1647	0.79	0.12	0.09	666879	7486	14959	14333
1647	0.78	0.04	0.18	638014	-14438	-24106	-24124
1671	0.84	0.12	0.04	699716	29548	28741	28622
1671	0.87	0.04	0.09	667820	-16613	-20774	-21569
1671	0.78	0.04	0.18	635338	-14768	-23455	-23866
1671	0.79	0.12	0.09	661587	5159	14026	13189
1696	0.87	0.04	0.09	662969	-17699	-22604	-23525
1696	0.84	0.12	0.04	691602	25223	24745	24603
1696	0.79	0.12	0.09	655041	1556	12246	11271
1697	0.78	0.04	0.18	631608	-16106	-23178	-23901
1723	0.78	0.04	0.18	631293	-14115	-19004	-19918
1723	0.84	0.12	0.04	687283	24802	25052	24936
1723	0.79	0.12	0.09	652310	1849	14885	13856
1723	0.87	0.04	0.09	661078	-15519	-20734	-21717
1723	0.92	0.04	0.04	702816	-3350	1406	139
1748	0.92	0.04	0.04	702324	1057	3695	2643
1749	0.87	0.04	0.09	657667	-15198	-20224	-21183
1749	0.84	0.12	0.04	687400	28621	29940	29908
1749	0.78	0.04	0.18	624358	-18766	-20854	-21822
1773	0.92	0.04	0.04	699997	3401	4342	3534
1774	0.87	0.04	0.09	654469	-14880	-19293	-20145
1774	0.84	0.12	0.04	679760	24490	27174	27278
1774	0.78	0.04	0.18	625914	-15084	-13957	-14827
1797	0.92	0.04	0.04	700524	8278	7935	7394
1821	0.92	0.04	0.04	695689	7739	6420	6183
1846	0.92	0.04	0.04	695206	11600	9600	9721
				Standard Deviation	**17943**	**21232**	**21162**

Considering only the Fe – C – Si data, the second degree polynomial results in a standard deviation of about 2.5% of the average of the measured data.

A correlation plot of the performance of auxi-mpp are presented in Figure 11.9.

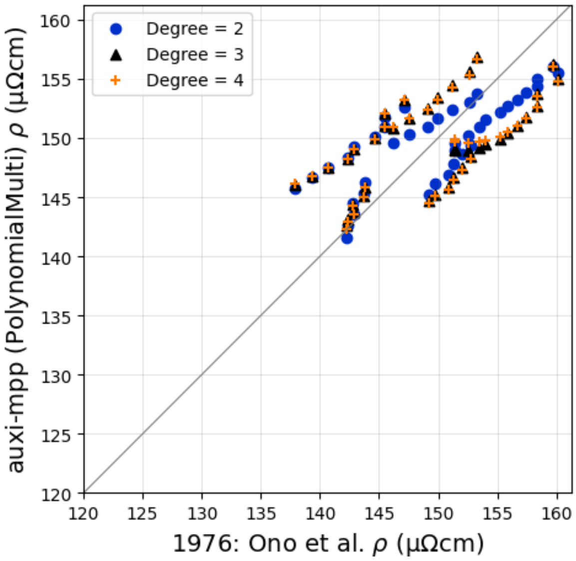

Figure 11.9: Correlation plot for the Fe – C – Si data of auxi-mpp vs experimental data measured by Ono et al. (1976). Degree $= 2$ $R^2 : 0.935$. Degree $= 3$ $R^2 : 0.960$. Degree $= 4$ $R^2 : 0.959$.

The reason for the larger standard deviation for the third and fourth degree polynomial, compared to the second degree, is likely because the data shown in Table 11.2 is only the Fe – C – Si data and thus not all data points used to fit the polynomials.

11.1.5 Issues

There are no known issues.

Chapter 12

Viscosity

This chapter details the models implemented in auxi-mpp for estimating the viscosity of different liquid alloy systems. This chapter details the models implemented in the auxi-mpp for estimating the viscosity of different liquid alloy systems. Two primary approaches are presented.

The first is a model for unary liquid alloys, which estimates viscosity as a function of temperature using an Andrade-type equation. The second approach is an empirical, linear model developed by (Deng et al. 2018) for calculating the viscosity of binary and multi-component iron-based alloys.

12.1 Viscosity with Andrade Type Equation

A viscosity model to estimate the viscosity of unary liquid alloys is described in this section.

12.1.1 Introduction

The viscosity of pure liquid metals is modelled as a function of temperature using an Andrade-type equation, shown in Equation (12.1). The parameters of this equation were fitted to reference experimental data for various elements (Assael et al. 2006; Assael et al. 2010; Assael et al. 2012a; Assael et al. 2012b). The resulting models for each element are implemented in auxi-mpp to provide viscosity estimates for unary liquid systems.

$$\log(\mu(T)) = -a_1 + \frac{a_2}{T} \tag{12.1}$$

12.1.2 Formulation

The viscosity of a unary liquid metal system, μ, is estimated as a function of the absolute temperature, T, using the further developed Andrade-type equation shown in Equation (12.2).

$$\mu(T) = \frac{10^{(-a_1+a_2/T)}}{1000} \tag{12.2}$$

where:

1. $\mu(T)$ is the dynamic viscosity of the liquid metal in Pascal-seconds (Pa·s).
2. T is the absolute temperature of the system in Kelvin (K).
3. a_1 is a dimensionless empirical parameter.
4. a_2 is an empirical parameter related to the activation energy for viscous flow, in Kelvin (K).

The parameters a_1 and a_2 are specific to each element. The equation is formulated to calculate viscosity in millipascal-seconds (mPa·s), which is then divided by 1000 to convert to the standard SI unit of Pa·s.

This model is applicable to a specific set of elements, each within a defined temperature range. Table 12.1 lists the supported elements, their valid temperature ranges, and the corresponding model parameters derived from experimental data. Using the model outside of the recommended temperature limits may result in inaccuracies.

Table 12.1: Supported Elements, Temperature Limits, and Parameters for the Unary Viscosity Model

Element Name	Symbol	Temp. Range (K)	a_1 (dimensionless)	a_2 (K)
Aluminum	Al	933 – 1270	0.7324	803.49
Antimony	Sb	900 – 1300	0.637	712.5
Bismuth	Bi	545 – 1000	0.345	321.4
Cadmium	Cd	600 – 900	0.4239	513.89
Cobalt	Co	1768 – 2100	0.9030	2808.7
Copper	Cu	1356 – 1970	0.4220	1393.4
Gallium	Ga	304 – 800	0.4465	204.03
Indium	In	429 – 1000	0.3621	272.06
Iron	Fe	1809 – 2480	0.7209	2694.95
Lead	Pb	601 – 1400	0.295	427.1
Nickel	Ni	1728 – 2100	0.505	2108.2
Silicon	Si	1685 – 1900	1.0881	1478.7
Silver	Ag	1235 – 1500	0.258	1081.8
Thallium	Tl	577 – 800	0.3017	412.84
Tin	Sn	506 – 1280	0.408	343.4
Zinc	Zn	695 – 1100	0.3291	631.12

12.1.3 Model Validation

The unary viscosity model implemented in auxi-mpp is validated against recommended reference viscosity data for various pure liquid metals (Assael et al. 2010; Assael et al. 2012a; Assael et al. 2012b). The MillsCommercial model implemented in auxi-mpp is validated against recommended reference viscosity data for various pure liquid metals (Assael et al. 2010; Assael et al. 2012a; Assael et al. 2012b).

All supported unary liquid metal systems show good agreement between the model estimates and the reference data, as illustrated in Figure 12.1.

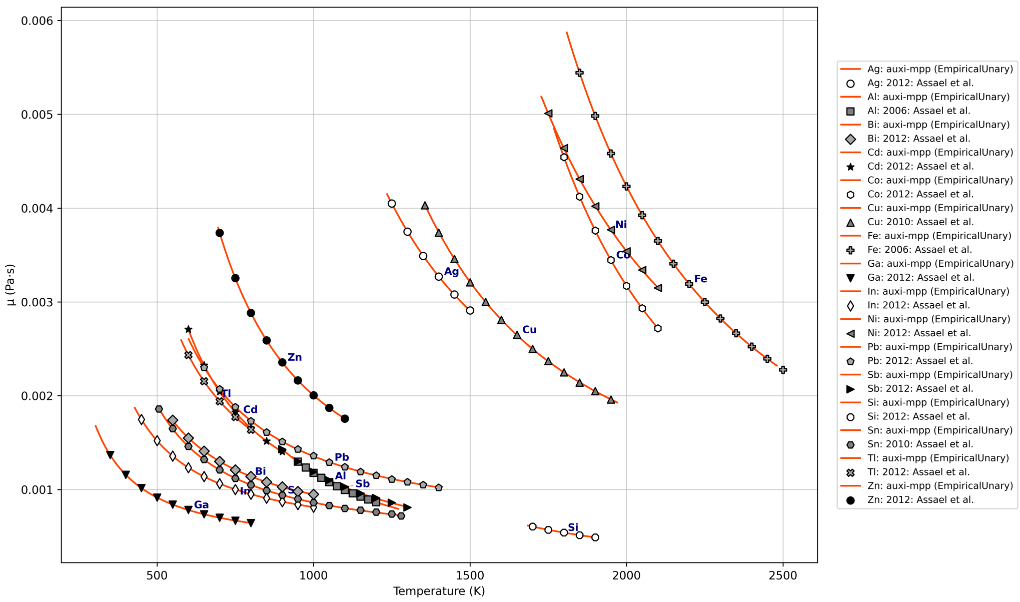

Figure 12.1: MillsCommercial model estimates for unary liquid metals versus recommended reference data (Assael et al. 2010; Assael et al. 2012a; Assael et al. 2012b).

12.1.4 Issues

There are no known issues.

12.2 Deng Viscosity Model

A viscosity model based on the work by Deng et al. (2018) is implemented for binary and multi-component liquid alloys of iron.

12.2.1 Introduction

Based on experimental data, Deng et al. (2018) developed a quantitative, linear model for estimating the viscosity of multi-component liquid iron-based alloys. This empirical equation calculates the alloy's viscosity by considering its temperature and the weight percentage of several alloying elements.

12.2.2 Formulation

The model calculates the viscosity of liquid ferrous alloys by starting with a temperature-dependent base viscosity for pure iron and then adding the contributions from various alloying elements. This approach is applicable to binary Fe – C and multi-component Fe – C – X systems, where X can be Si, Mn, P, S, or Ti. The model is valid for a temperature range of 1463 K to 1723 K and requires a carbon content between 3.0 and 4.5 wt%.

Fe-C System

The viscosity of the Fe-C system, μ, is calculated based on the contributions of the base element (Fe) and the alloying element (C) of the system, as shown in Equation (12.3). Table 12.2 lists the parameters used in the model for the Fe-C system.

$$\mu(T, \text{wt\%}_C) = \frac{(\text{A}_{\text{Fe}} + k_T T) + (k_C \cdot \text{wt\%}_C)}{1000} \tag{12.3}$$

where:

1. $\mu(T, \text{wt\%}_C)$ is the dynamic viscosity in Pascal-seconds (Pa·s).
2. T is the absolute temperature in Kelvin (K).
3. $\text{wt\%}_C$ is the weight percent of carbon in the alloy.
4. A_{Fe} is the constant term for pure iron's viscosity.
5. k_T is the temperature coefficient for iron's viscosity.
6. k_C is the coefficient for the effect of carbon on viscosity.

The calculation is performed in millipascal-seconds (mPa·s) and then converted to Pa·s.

Table 12.2: Parameters for the Fe-C Viscosity Model

Component	Parameter	Value	Unit
Fe	A_{Fe}	34.42973	mPa·s
	k_T	-0.01514	mPa·s/K
C	k_C	-0.00349	mPa·s / wt%

Multi-Component

For multi-component systems, the viscosity is calculated by summing the contributions from all alloying elements present in the alloy, as shown in Equation (12.4).

$$\mu(T, \text{wt\%}_i) = \frac{(\text{A}_{\text{Fe}} + k_T T) + \sum_i (k_i \cdot \text{wt\%}_i)}{1000} \tag{12.4}$$

where the additional terms are defined as:

1. k_i is the coefficient for the effect of alloying element i on viscosity.
2. $\text{wt\%}_i$ is the weight percent of the alloying element i.

The summation is performed over all alloying elements present in the system (excluding Fe). The calculation gives a result in millipascal-seconds (mPa·s), which is then converted to Pa·s.

The model is validated for several Fe-based ternary systems (Deng et al. 2018). Each alloying element has a specific coefficient and a valid composition range.

Table 12.3: Parameters for the Multi-Component Viscosity Model

Component	Parameter	Value	Composition Range (wt%)
Fe	A_{Fe}	34.42973	-
	k_T	-0.01514	-
C	k_C	-0.00349	3.0 – 4.5
Si	k_{Si}	0.76756	0.2 – 0.6
Mn	k_{Mn}	-2.35139	0.1 – 0.5
P	k_P	-3.63856	0.1 – 0.3
S	k_S	-6.91921	0.02 – 0.08
Ti	k_{Ti}	5.91118	0.05 – 0.2

12.2.3 Model Validation

The DengBinary and DengMulti models, implemented in auxi-mpp, show good agreement with experimental data for the Fe – C and multi-component liquid iron-based alloy systems, as illustrated in Figures 12.2 to 12.7.

Fe-C System

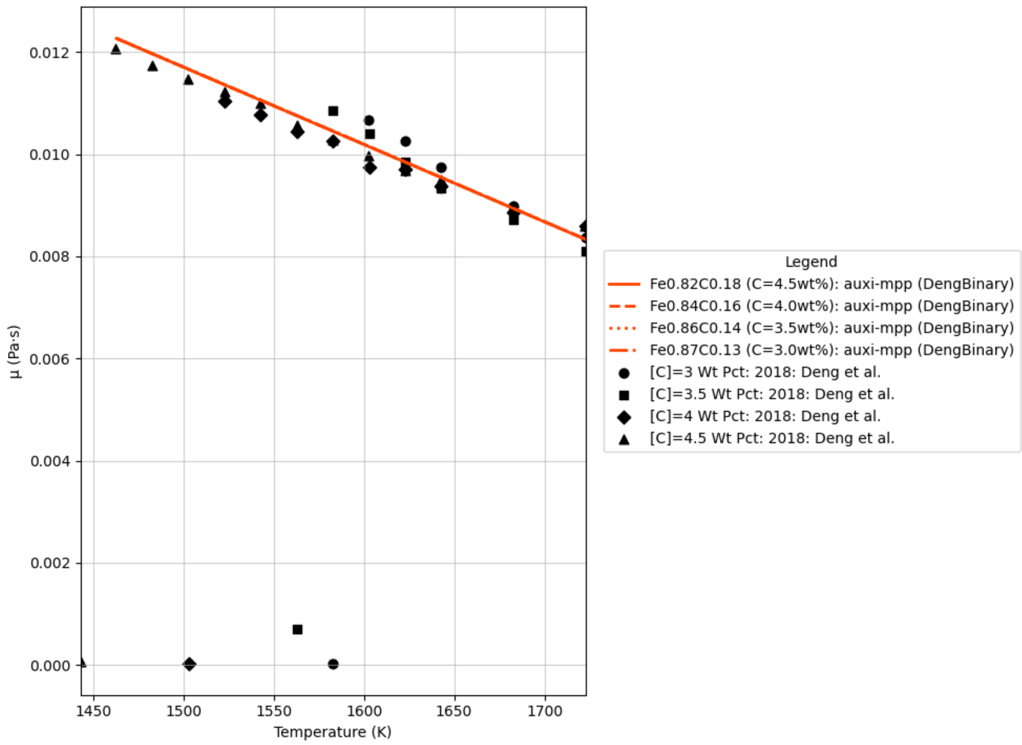

Figure 12.2: DengBinary model estimates for the binary Fe – C system versus experimental data (Deng et al. 2018).

Multi-Component Systems

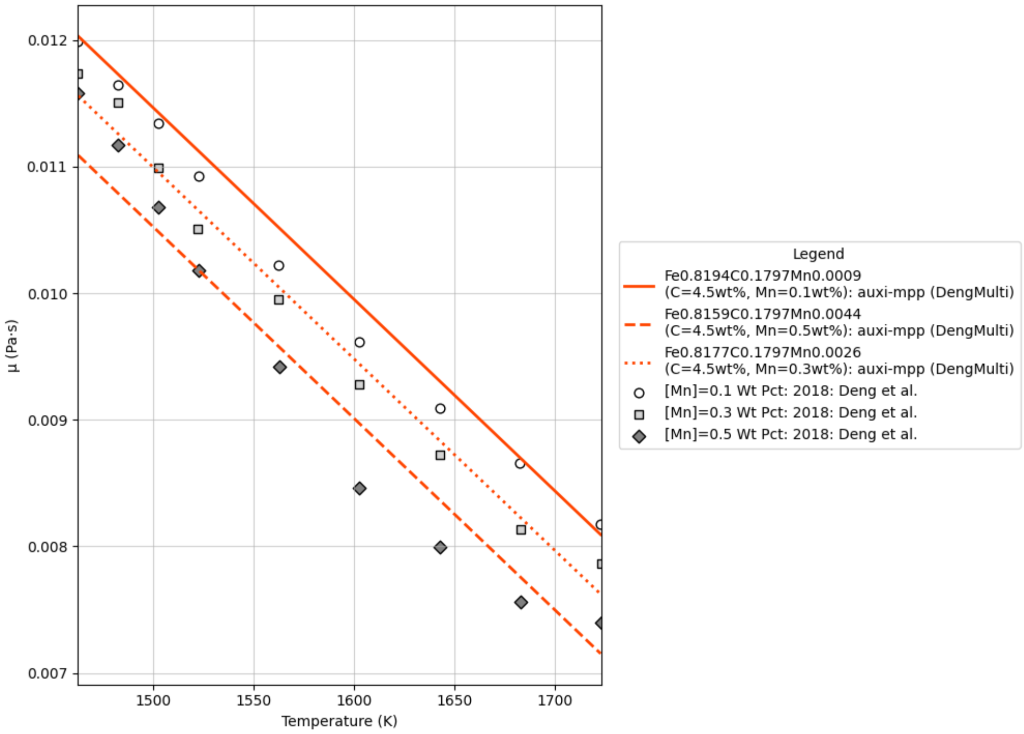

Figure 12.3: DengMulti model estimates for Fe – C – Mn system versus experimental data (Deng et al. 2018).

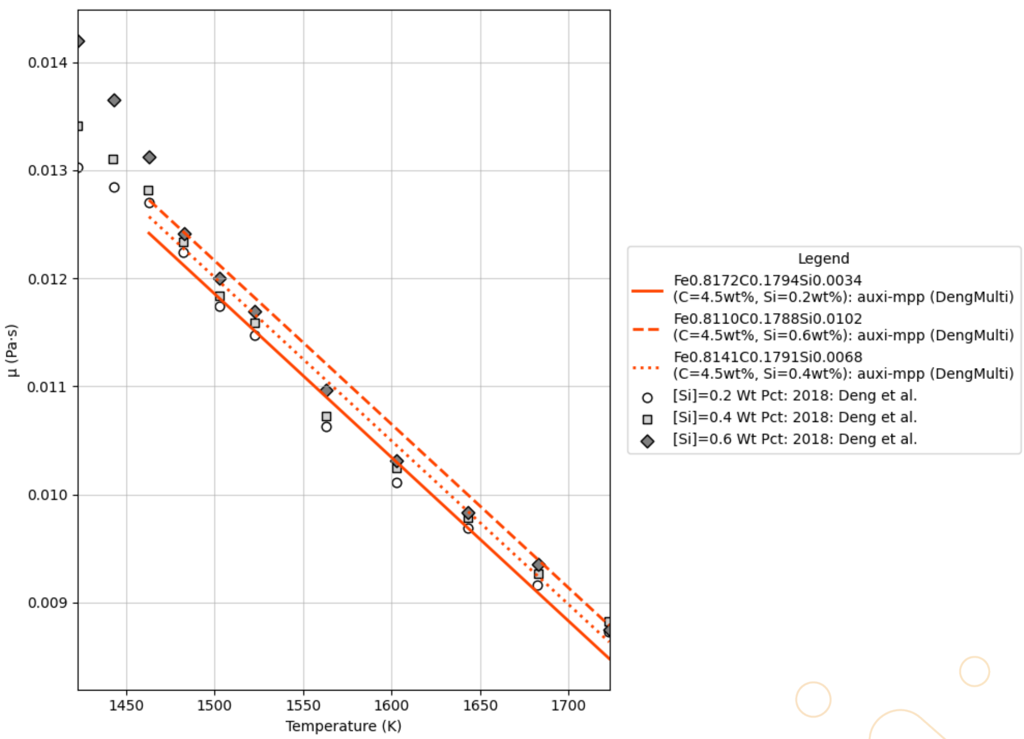

Figure 12.4: DengMulti model estimates for Fe – C – Si system versus experimental data (Deng et al. 2018).

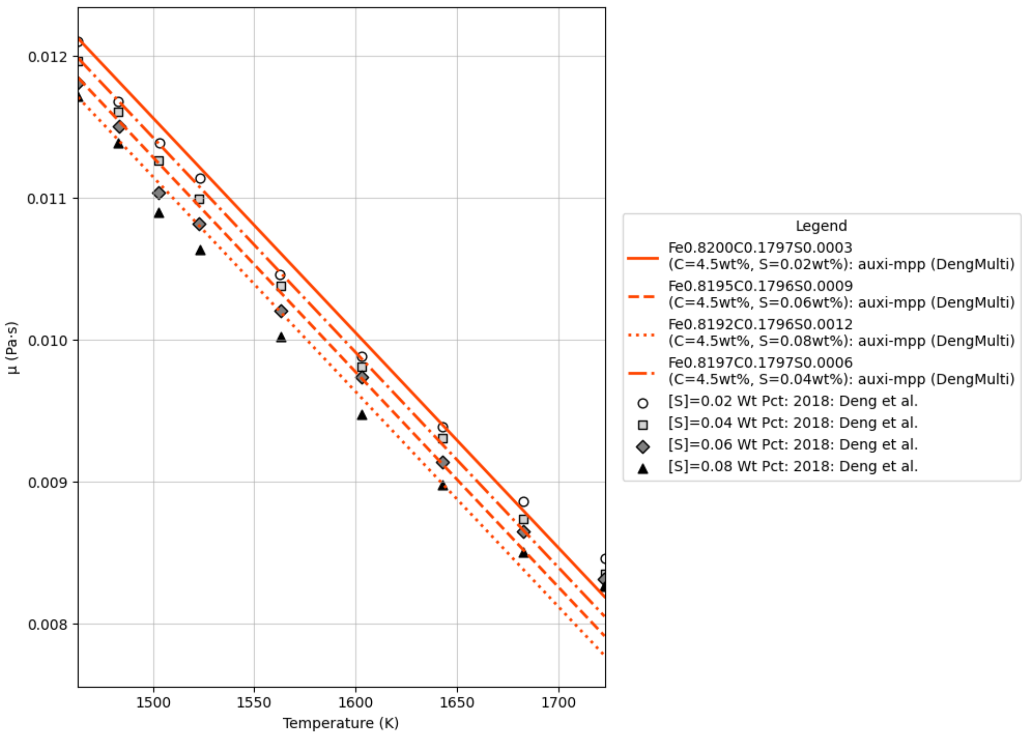

Figure 12.5: DengMulti model estimates for Fe – C – S system versus experimental data (Deng et al. 2018).

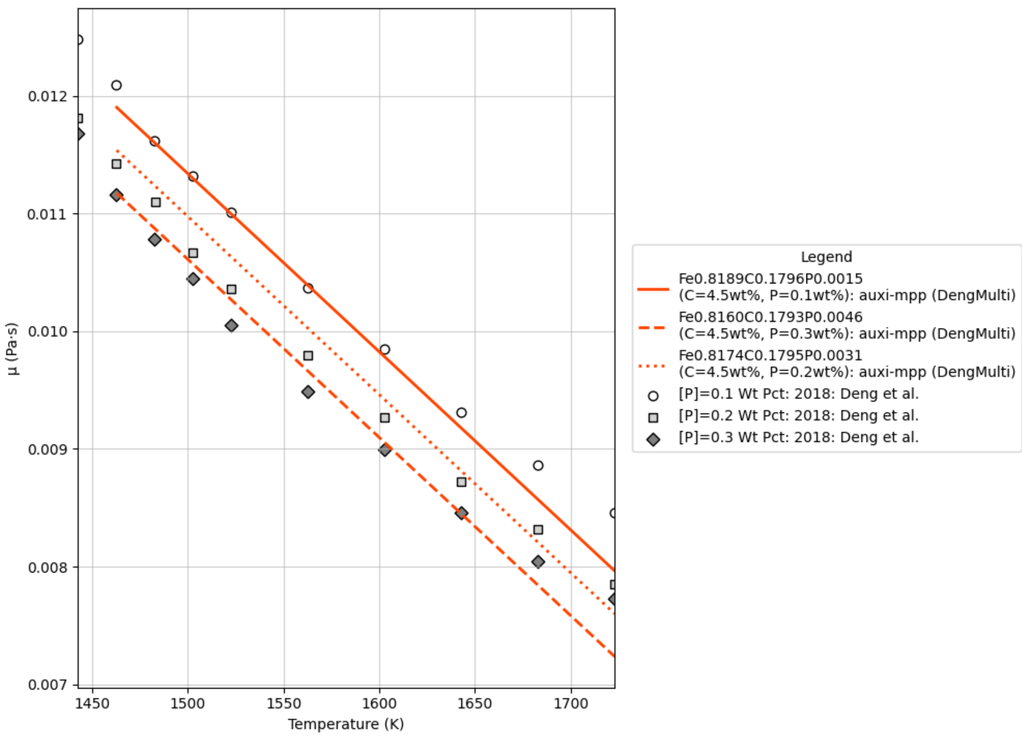

Figure 12.6: DengMulti model estimates for Fe – C – P system versus experimental data (Deng et al. 2018).

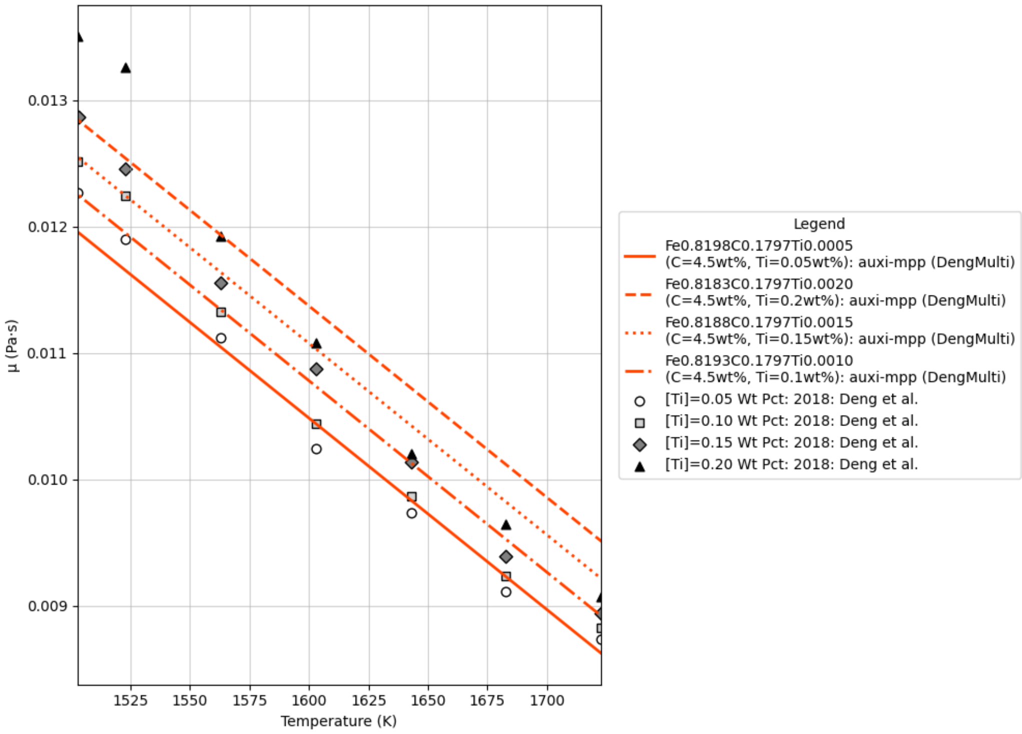

Figure 12.7: DengMulti model estimates for Fe – C – Ti system versus experimental data (Deng et al. 2018).

12.2.4 Issues

There are no known issues.

Chapter 13

Thermal Conductivity

There are two mechanisms for transferring thermal energy in liquid alloys. These are transfer by phonons, which are quantized lattice vibrations, and transfer by free electons. The dominant mechanism in liquid alloys is the transfer of thermal energy by the movement of free electrons. In high temperature liquids, phonons are scattered significantly more than in crystalline solids. Consequently, the phonon contribution to thermal conductivity becomes minor – about 1 % of total heat transfer (Ziman 2001).

The state-of-the-art ab initio workflow for calculating the transport properties, including thermal conductivity, of liquid metals involves a multi-step computational process that combines quantum molecular dynamics with the Kubo-Greenwood linear response theory. The major drawback for this method is its prohibitive computational cost.

The dominance of electrons in both thermal and electrical conduction in metals leads to a powerful and elegant relationship between the two properties known as the Wiedemann-Franz (W-F) Law. First proposed empirically by Gustav Wiedemann and Rudolph Franz in 1853 and later given a theoretical basis by Ludvig Lorenz, the law states that the ratio of the electronic thermal conductivity (κ_e) to the electrical conductivity (σ) for a metal is directly proportional to the absolute temperature (T). Note that the W-F law only accounts for the electronic contribution to the thermal conductivity of the melt.

The W-F law effectively transforms the problem of estimating the thermal conductivity of a liquid alloy – a property that is extremely difficult to measure directly – into the much more manageable problem of estimating its electrical conductivity. We can therefore invest in a proper description of the electrical conductivity and simply derive the thermal conductivity from that using the W-F law.

The scarcity of experimental data for the thermal conductivity of liquid metals and alloys remains a critical challenge for validating the W-F law, however.

13.1 Thermal Conductivity by Wiedemann-Franz

A thermal conductivity model by applying the Wiedemann-Franz law to electrical conductivity estimations.

13.1.1 Introduction

Due to the lack of readily available models to estimate thermal conductivity for liquid metals, the W-F law were applied to the available electrical conductivity models instead. Applying the W-F law is documented here.

13.1.2 Overview

To estimate thermal conductivity, the W-F law is applied to all models available to estimate electrical conductivity. For an overview of the electrical conductivity polynomials, see Section 11.1.2.

It should be noted that the W-F law makes assumptions that, strictly speaking, disqualify using it on pig iron melts. The models available should therefore be used with caution, and the user is encouraged to ponder the listed assumptions and the presented validation before using them.

The validation of the W-F law was performed on the Fe – Ni system, as this is the only one for which data on both thermal and electrical conductivity could be obtained. To give the user a general idea of the performance of the W-F law, we cite a few use cases found in the literature.

Literature on Applying the W-F Law

Mills et al. (1996) and Giordanengo et al. (1999) reported that the W-F law is valid for most pure metals at their melting points.

According to Zhao and Garay (2023), the Lorenz number varies with pressure, temperature and metal composition. They state that the real L does not exactly equal L_0 for liquid metals, so the W-F law has to be applied with caution when measuring thermal conductivity directly from electrical conductivity measurements. Nevertheless, they do report that the law provides a reasonable approximation of thermal conductivity from electron transport.

Watanabe et al. (2019) reported a higher measured thermal conductivity than that estimated by the W-F law for Fe and Ni systems. From this, they deduced that atomic thermal vibration (phonons) also contributes significantly to the thermal conductivity in Fe and Ni and their alloys.

Secco (2017) have shown that the Lorenz number can vary between $1L_0$ and $3L_0$ for Fe – Si alloys in the solid state. That leaves the question of whether this is also the case for liquid Fe – Si melts.

Yamasue et al. (2003) have shown that around the melting point, the measured thermal conductivity values for liquid Sn and Pb are in good agreement with the values obtained using the W-F law. They put this forward as evidence that liquid metals indeed have a free-electron structure.

Another study indicates that Sn-based alloys deviate from the W-F law (Mizuno et al. 2020) – one of the few studies not confirming the W-F law.

To conclude, the majority of the literature confirms the validity of the W-F law; however, it should indeed be applied with caution.

13.1.3 Formulation

Applying the Wiedemann-Franz law is straight forward and is captured in Equation (13.1).

$$\kappa_e = \sigma L_0 T \tag{13.1}$$

Here, $L_0 = 2.445 \times 10^{-8}$, and σ is the electrical conductivity of the system at the particular temperature. Equation (13.1) was applied to all electrical conductivity estimations of the unary, binary and multi-component polynomial fits described in Section 11.1.3.

13.1.4 Assumptions

To apply the universal Lorenz number (see Equation (13.1)), which gives the W-F law its estimating power, the following assumptions are made.

1. **Electron scattering is elastic scattering**. Inelastic scattering events can transport charge without proportional transport of heat and will therefore deviate from the W-F law.
2. **The alloy's electronic structure has a low complexity.** Significant deviation can be expected for complex alloys.
3. **No transition metals are present.** The d-orbitals of transition metals can lead to different scattering behaviour for electrons. First principles calculations have shown that for binary iron-based alloys, the Lorenz number can deviate by more than 25%.
4. **The alloy is made up of only metal atoms.** There is evidence that alloys containing semi-metals like Sn, Bi and Si exhibit complex eletronic interactions, causing significant deviations from the W-F law.

The last two assumptions are particularly problematic for the pig iron alloys we are interested in. Pig iron contain substantian amounts of Fe, a transition metal, as well as small amounts of C and Si, which are not metals. The user should therefore be aware that some of the core assumptions of the W-F law are violated when applying it to pig iron melts.

13.1.5 Model Validation

To validate the W-F law we test its performance against experimental measurements. We therefore require the systems to have measurements for both electrical resistivity and thermal conductivity. We then need to fit polynomials to the measured resistivity data, apply the W-F to the polynomials to get thermal conductivity, and then finally plot the resulting functions against measured thermal conductivity data. Due to the scarcity of measured thermal conductivity data, the only binary system for which we could find both electrical resistivity and thermal conductivity measurements is the Fe – Ni system. This system is therefore the only one we can use to validate the W-F law.

The Fe – Ni System

In Figure 13.1, a surface of the W-F law, applied to the second degree polynomial fit for electrical resistivity data, were plotted against measured thermal conductivity data.

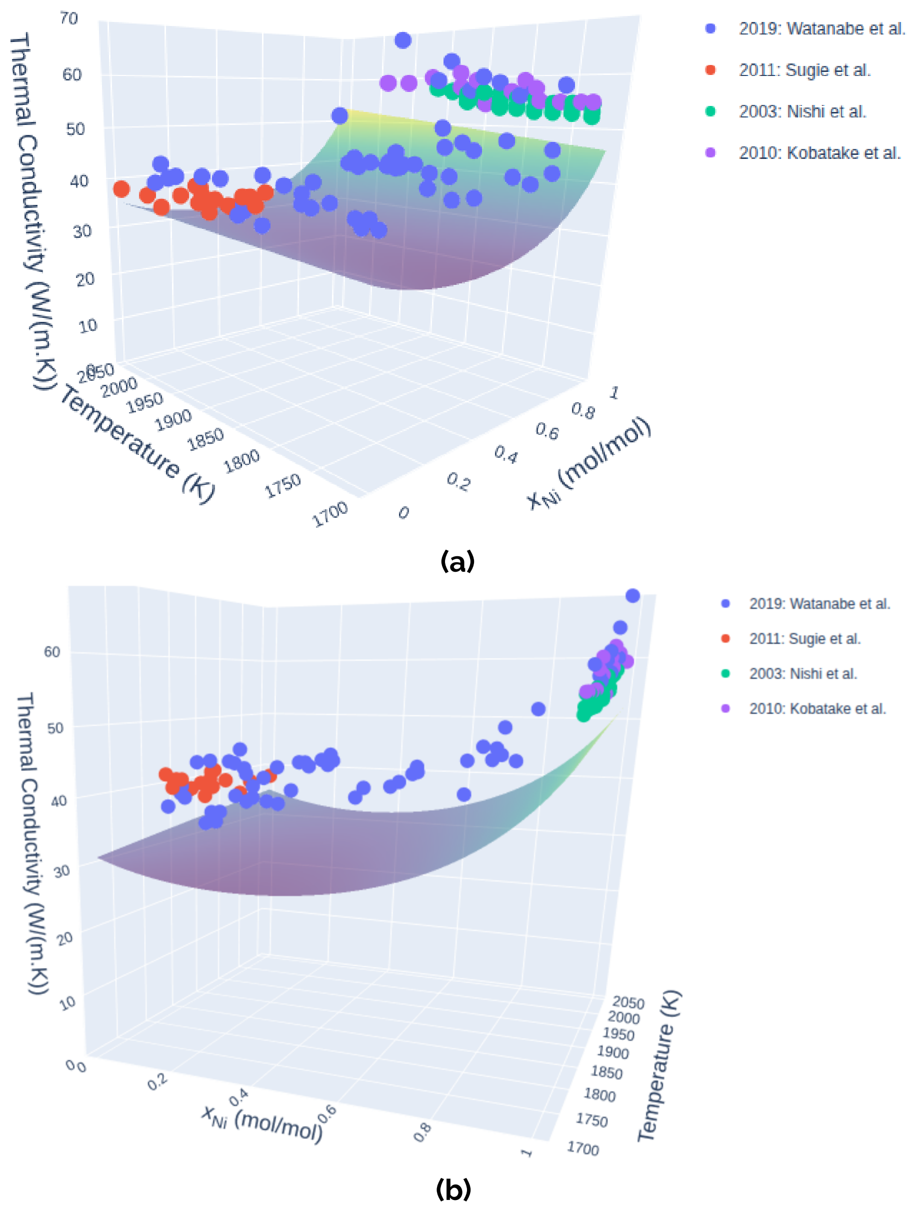

Figure 13.1: Testing the performance of the Wiedemann-Franz law against experimental measurements. Surface: auxi-mpp (WiedemannFranzBinary, degree=2).

Figure 13.2 shows Figure 13.1 in 2D slices.

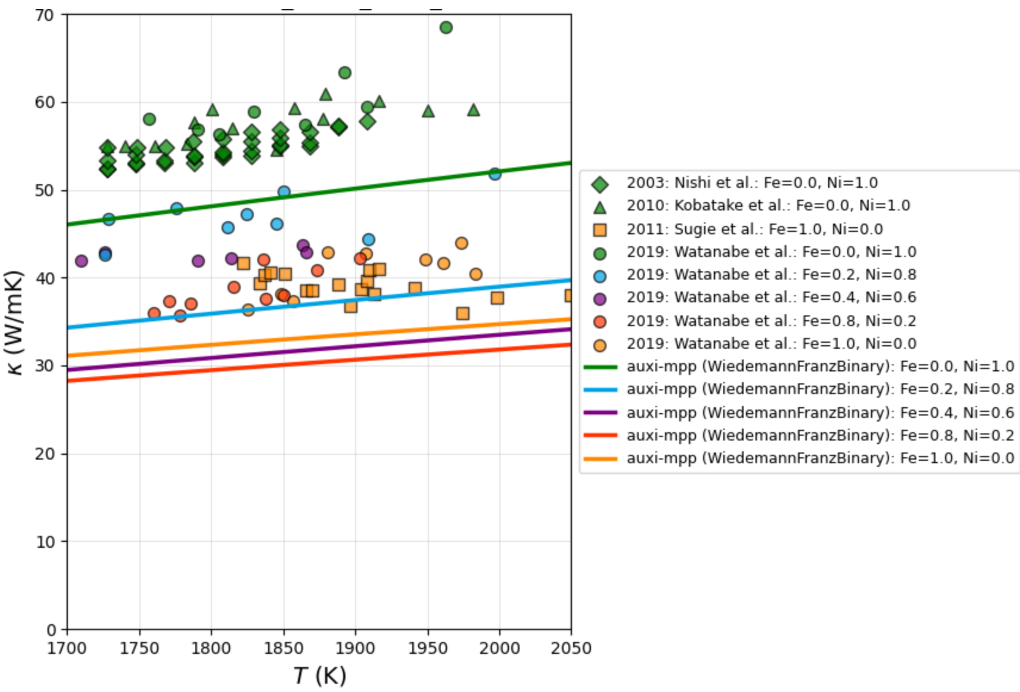

Figure 13.2: Testing auxi-mpp (WiedemannFranzBinary, degree=2) against experimental measurements.

As confirmed by Watanabe et al. (2019), the W-F law underestimates the thermal conductivity by roughly 10 $\mathrm{W\,m^{-1}\,K^{-1}}$ for the pure substances and roughly 15 $\mathrm{W\,m^{-1}\,K^{-1}}$ for a 1:1 Fe – Ni ratio. This amounts to an underestimation of roughly 20% to 38%. Interestingly, Watanabe et al. (2019) comments on this underestimation and suggests that thermal vibration of atoms contributed to the thermal conductivities of Fe – Ni alloys, not attributing it to violating the core assumptions of the W-F law.

Performance for Pig Iron Binaries

For reference, in Figure 13.3 we present the performance of the W-F law over realistic composition ranges for binary systems representing pig iron melts over the temperature range 1000 to 2500 K.

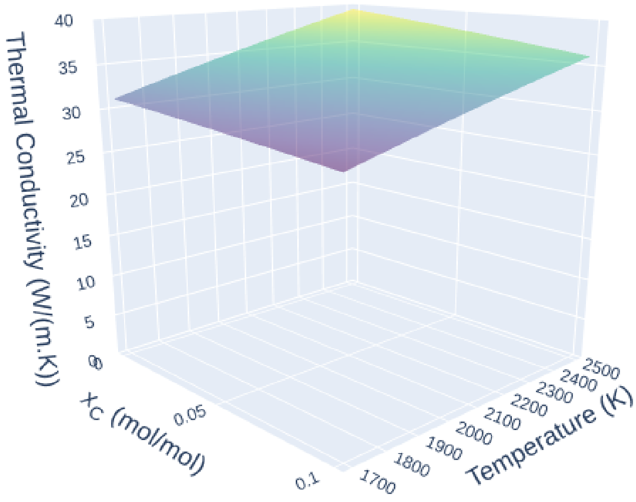

(a) Fe – C

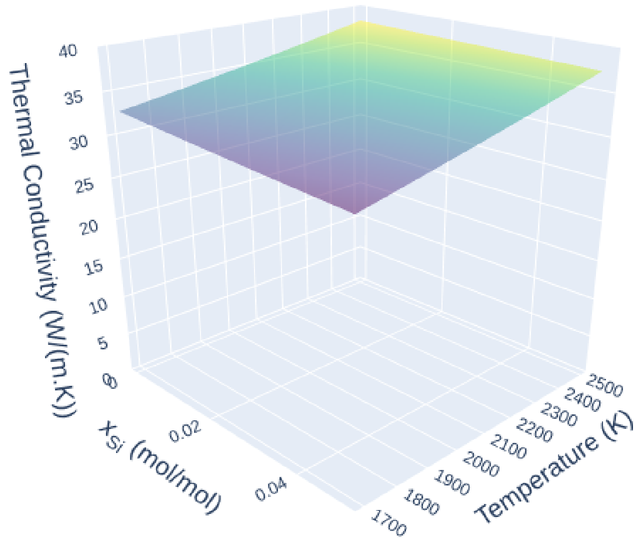

(b) Fe – Si

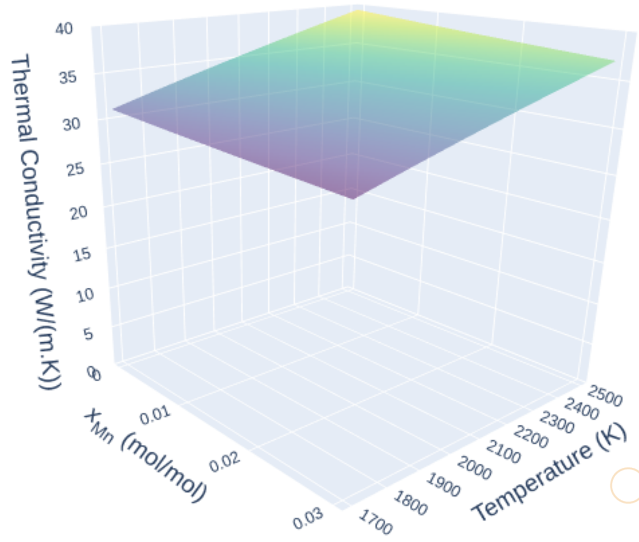

(c) Fe – Mn

Figure 13.3: Thermal conductivity estimates by auxi-mpp (WiedemannFranzBinary; degree=2) for pig iron representing binaries.

Figure 13.4 compares the sensitivity of thermal conductivity to either carbon, silicon or manganese.

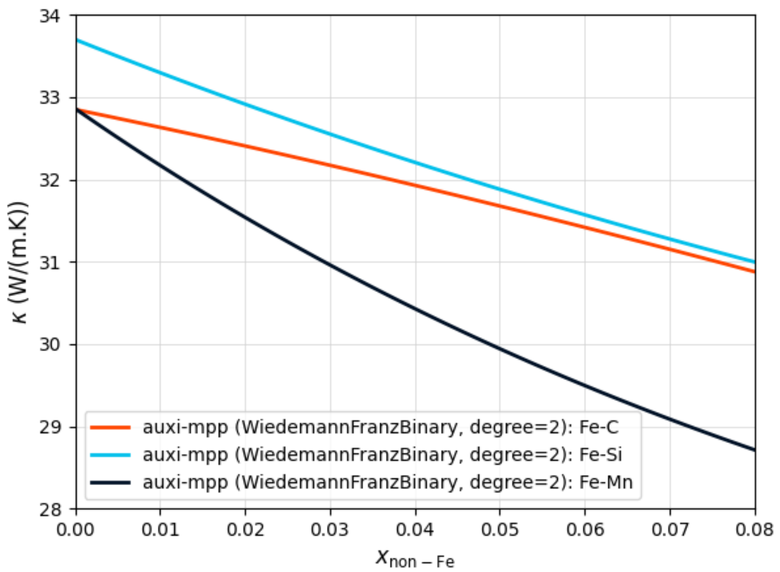

Figure 13.4: Sensitivity of thermal conductivity to carbon, silicon or manganese at the 1850 K isotherm.

Here, the effect of the rapidly changing electrical resistivity data for the Fe – Si system, as seen in Figure 11.5b, can be seen as the polynomial used for the W-F law deviates from pure iron thermal conductivity compared to Fe – C and Fe – Mn.

13.1.6 Issues

The performance of the W-F law could not be validated against experimental measurements for pig iron related melts, due to a lack of data. The models should therefore be used with caution.

Part IV

Gas Material Properties

Chapter 14

Background

The gas phase in smelting processes acts as the primary medium for convective heat transfer, the delivery of gaseous reductants, and the removal of volatile reaction products. The physical properties of this phase are governed fundamentally by the Kinetic Theory of Gases, which treats the gas as a collection of discrete molecules in constant, random motion. Consequently, the macroscopic properties are determined by intermolecular forces, molecular weight, and collision mechanics, which are strongly dependent on temperature and pressure.

Under these kinetic principles, transport properties exhibit distinct temperature dependencies. Viscosity increases with rising temperature, as higher thermal energy results in more frequent and energetic molecular collisions, increasing internal friction. Similarly, thermal conductivity typically rises with temperature due to the increased velocity of the molecules facilitating energy transfer. The density is generally described by equations of state, such as the Ideal Gas Law, where density decreases significantly as temperature rises, driving buoyancy forces within the furnace. The models presented here provide the constitutive equations for these properties, enabling the calculation of heat transfer coefficients, viscosities, and diffusion rates, etc..

Chapter 15

Density

Molar volume and density are essential physical properties for characterising gas behaviour under varying temperature and pressure conditions. In engineering, these properties are essential for calculating gas flows through systems like furnace freeboards and secondary processes, and for verifying overall mass and energy balances.

The models in this chapter calculate molar volume and density for pure gases and mixtures based on the ideal gas law. This fundamental equation of state provides sufficient accuracy for many industrial applications, particularly at the high temperatures and low to moderate pressures found in processes like smelting furnace freeboards.

This chapter presents an overview of the Clapeyron models, their formulation, and validation against reference data.

15.1 Clapeyron Density Model

The ideal gas law was used to model the molar volume and density of pure gases and gas mixtures composed of CO, CO_2, N_2, Ar, H_2, H_2O, and O_2. The models implemented and discussed in this section are named after Benoît Paul Émile Clapeyron, who is credited with first formulating the ideal gas law (Clapeyron 1834).

The models that fall under this section include the following molar volume and density models:

1. `ClapeyronUnary`
2. `ClapeyronBinary`
3. `ClapeyronMulti`
4. `ClapeyronDensityUnary`
5. `ClapeyronDensityBinary`
6. `ClapeyronDensityMulti`

15.1.1 Model Overview

The ideal gas law is a fundamental relationship in physics and chemistry, represented by Equation (15.1).

$$PV = nRT \tag{15.1}$$

This relationship, also referred to as the *simple gas law*, was historically formulated by combining several empirical gas laws. It integrates the work of Robert Boyle, who described the inverse relationship between pressure and volume, with the findings of Jacques Charles, who established the direct proportionality between temperature and volume, and Joseph Louis Gay-Lussac, who established the direct proportionality between temperature and pressure. The formulation was completed by incorporating Avogadro's hypothesis, which relates the volume of a gas to the number of molecules (Clapeyron 1834; Poling et al. 2001).

The ideal gas law is generally useful at low to modest pressures and increasing temperatures, where gases tend to behave more ideally. For practical engineering applications, such as relating mass and volumetric flow rates of gases in a furnace freeboard, it is justified to use Equation (15.1).

However, at higher pressures or lower temperatures, deviations from the ideal gas law can become significant. These deviations are linked to the fundamental nature of molecules, which have a finite volume and experience intermolecular forces. More advanced equations of state, such as the van der Waals equation (Equation (15.2)), were developed to account for these deviations by introducing parameters for molecular volume (b) and intermolecular attraction (a) (Poling et al. 2001).

$$\left(P + \frac{a}{V^2}\right)(V - b) = RT \tag{15.2}$$

Another approach to account for non-ideal behaviour is to use compressibility factors (Z), as shown in Equation (15.3), which modify the ideal gas law to better reflect real gas behaviour. Additional equations, such as virial equations of state, can be used to estimate Z; however, this is left for the reader to explore further (Poling et al. 2001).

$$Z = \frac{PV}{RT} \tag{15.3}$$

15.1.2 Model Formulation

The Clapeyron models, as initially stated, is based on the ideal gas law, Equation (15.1), and to calculate the molar volume (V_m) the ideal gas equation, as shown in Equation (15.4) is used where $V_m = V/n$.

$$V_m = \frac{RT}{P} \tag{15.4}$$

Here, T is the system temperature in Kelvin (K), P is the system pressure in Pascals (Pa), and R is the universal gas constant (8.314 46 m Pa^3 K^{-1} mol^{-1}). Since this equation is independent of gas composition, it applies to both pure components and multi-component mixtures.

Density (ρ) can be derived from molar volume through the relationship outlined below. Density is defined as mass (m) per unit volume (V), while molar mass (M) is mass per mole (n), and molar volume (V_m) is volume per mole. By substituting the expressions for mass ($m = Mn$) and volume ($V = V_m n$) into the definition of density, the relationship between density, molar mass, and molar volume is obtained, as shown in Equation (15.5).

$$\rho = \frac{m}{V} = \frac{Mn}{V_m n} = \frac{M}{V_m} \tag{15.5}$$

Combining Equation (15.5) with Equation (15.4) yields the ideal gas density equation for pure components, as shown in Equation (15.6).

$$\rho = \frac{PM}{RT} \tag{15.6}$$

For gas mixtures, the density is calculated using Equation (15.7).

$$\rho = \frac{PM_{mix}}{RT} \tag{15.7}$$

This calculation requires the average molar mass of the gas mixture (M_{mix}), which is determined using Equation (15.8).

$$M_{mix} = \sum_{i=1}^{N} x_i M_i \tag{15.8}$$

In this equation, x_i represents the mole fraction of component i, and M_i is its molar mass in kg mol^{-1}.

15.1.3 Assumptions

The models implemented are based on the ideal gas law. The following assumptions are made when applying this law to estimate gas density:

1. Gas particles have negligible volume compared to the volume of the container they occupy.
2. There are no intermolecular forces between gas particles; they do not attract or repel each other.
3. Gas particles are in constant, random motion and collide elastically with each other and the walls of the container.

15.1.4 Model Validation

Pure Component Validation

For pure components, density (ρ) is plotted against temperature (T) at a fixed pressure. This allows for a direct comparison of the `ClapeyronDensityUnary` model against NIST reference data (Linstrom and Mallard 2001). Table 15.1 summarises the specific model validated, the respective temperature range, and the reference data sources. The original source of the reference data is also provided.

Importantly, if the validation of the density model (`ClapeyronDensityUnary`) was successful, it implies that the corresponding molar volume model (`ClapeyronUnary`) is also validated, as density is directly derived from molar volume.

Table 15.1: Model validation ranges for unary gas density model.

Gas	Specific Model	Temperture Range (K)	Pressure (Pa)	Reference Data Source	Reference
N_2	`ClapeyronUnary`, `ClapeyronDensityUnary`	77–2000	101325	NIST Chemistry WebBook	(Span et al. 2000)
CO	`ClapeyronUnary`, `ClapeyronDensityUnary`	81–500	101325	NIST Chemistry WebBook	(Lemmon and Span 2006)
O_2	`ClapeyronUnary`, `ClapeyronDensityUnary`	90–2000	101325	NIST Chemistry WebBook	(Schmidt and Wagner 1985)
Ar	`ClapeyronUnary`, `ClapeyronDensityUnary`	87–2000	101325	NIST Chemistry WebBook	(Tegeler et al. 1999)
H_2O	`ClapeyronUnary`, `ClapeyronDensityUnary`	250–2500	101325	NIST Chemistry WebBook	(Wagner and Pruß 2002)
CO_2	`ClapeyronUnary`, `ClapeyronDensityUnary`	150–2000	101325	NIST Chemistry WebBook	(Span and Wagner 1996)
H_2	`ClapeyronUnary`, `ClapeyronDensityUnary`	20–1000	101325	NIST Chemistry WebBook	(Leachman et al. 2009)

Pure component validation plots for H_2, O_2, N_2, CO, CO_2, Ar, and H_2O are provided as follows with Figures 15.1 to 15.7 respectively.

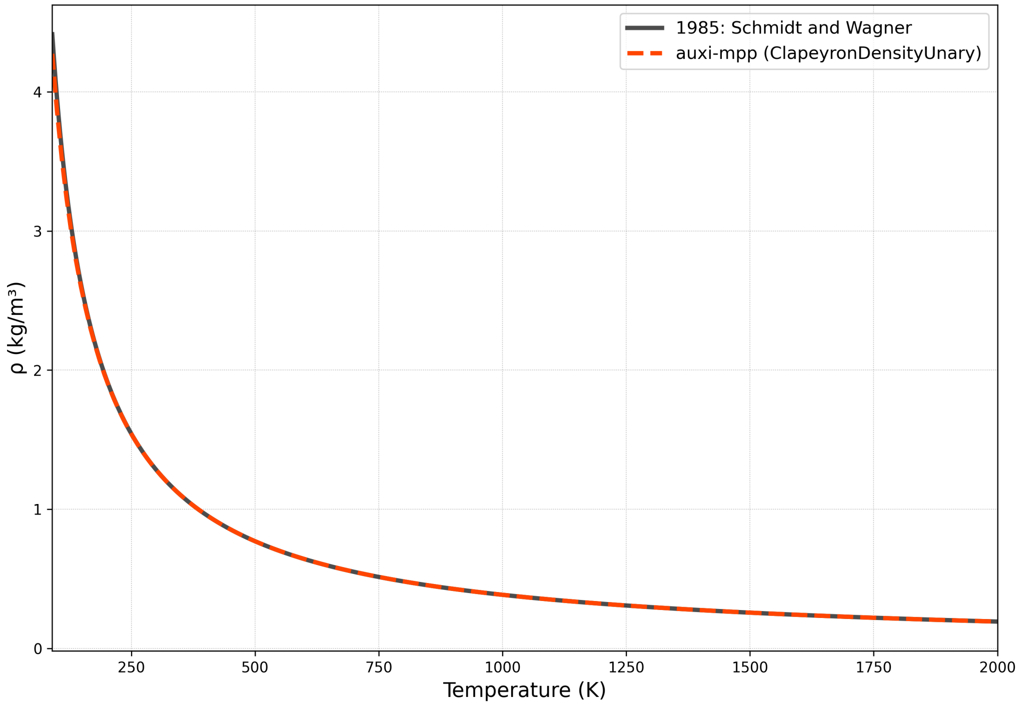

Figure 15.1: Clapeyron unary density model estimates compared to reference data for O_2.

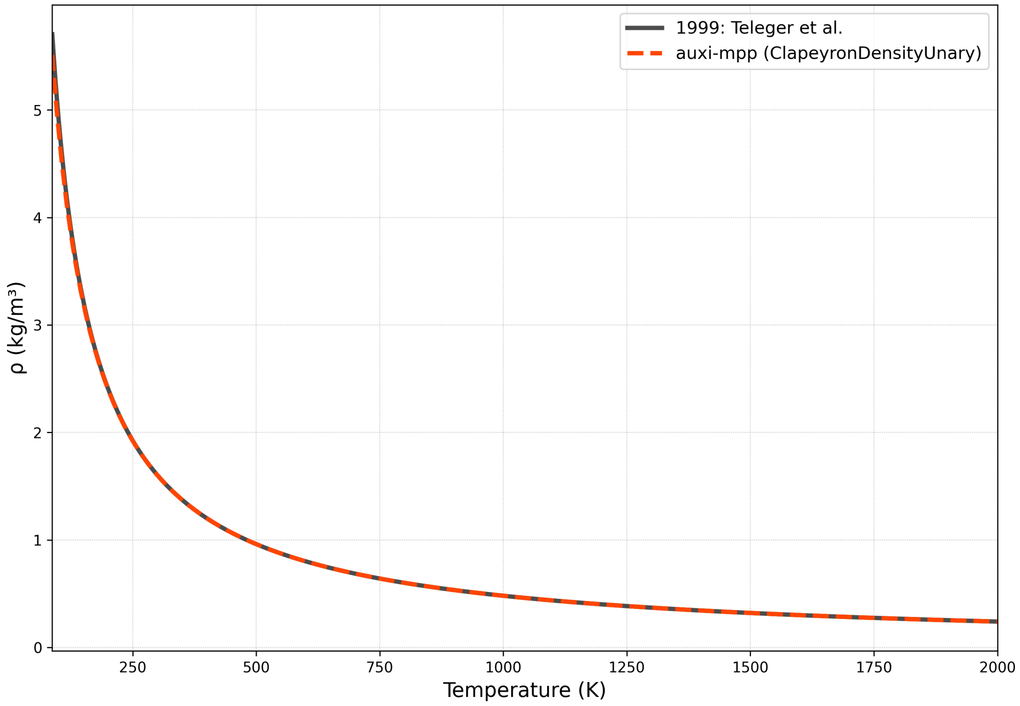

Figure 15.2: Clapeyron unary density model estimates compared to reference data for Ar.

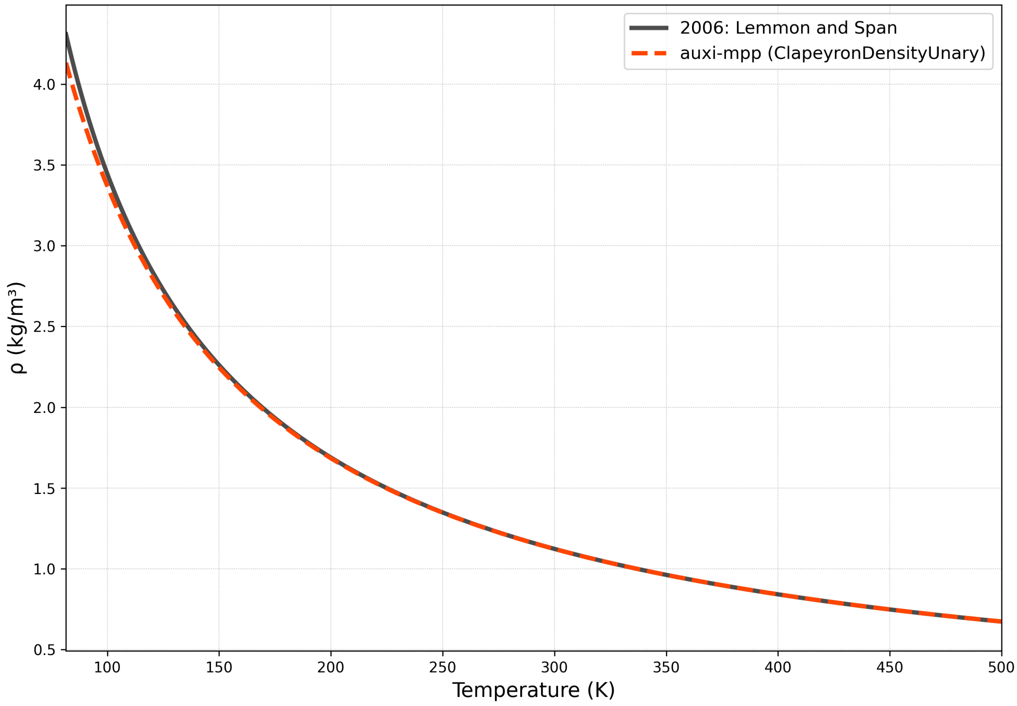

Figure 15.3: Clapeyron unary density model estimates compared to reference data for CO.

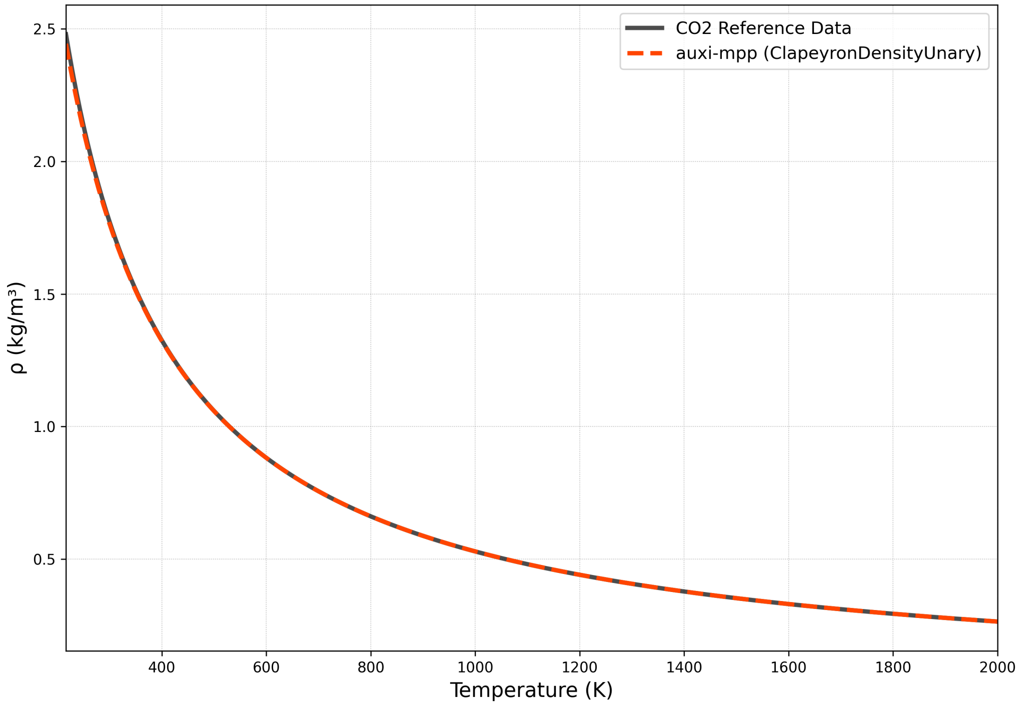

Figure 15.4: Clapeyron unary density model estimates compared to reference data for CO_2.

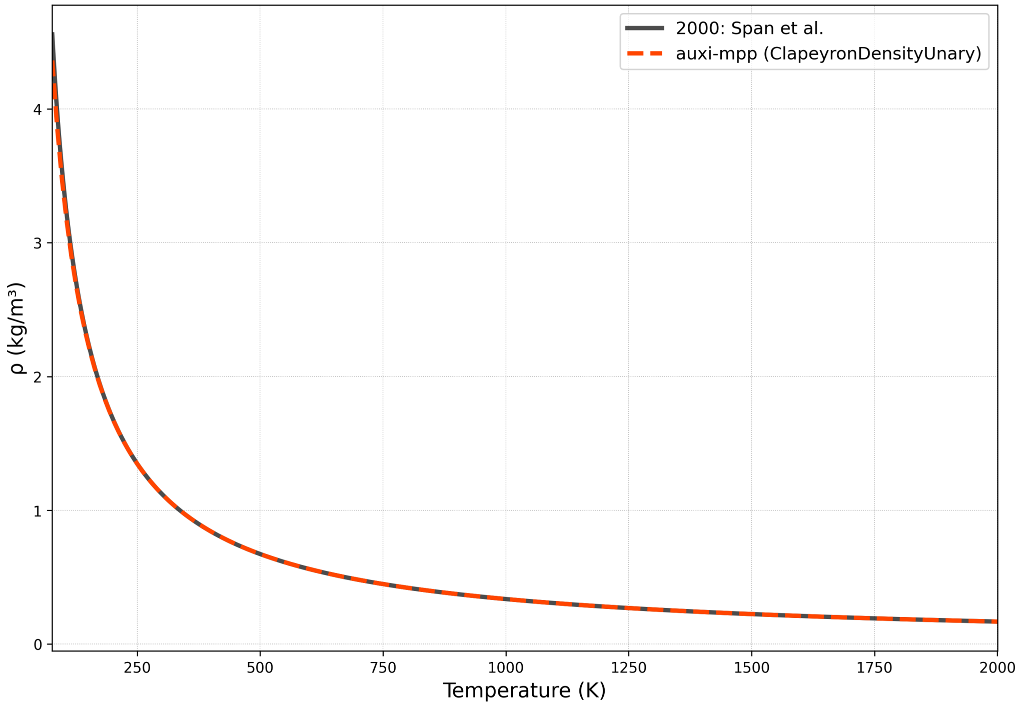

Figure 15.5: Clapeyron unary density model estimates compared to reference data for N_2.

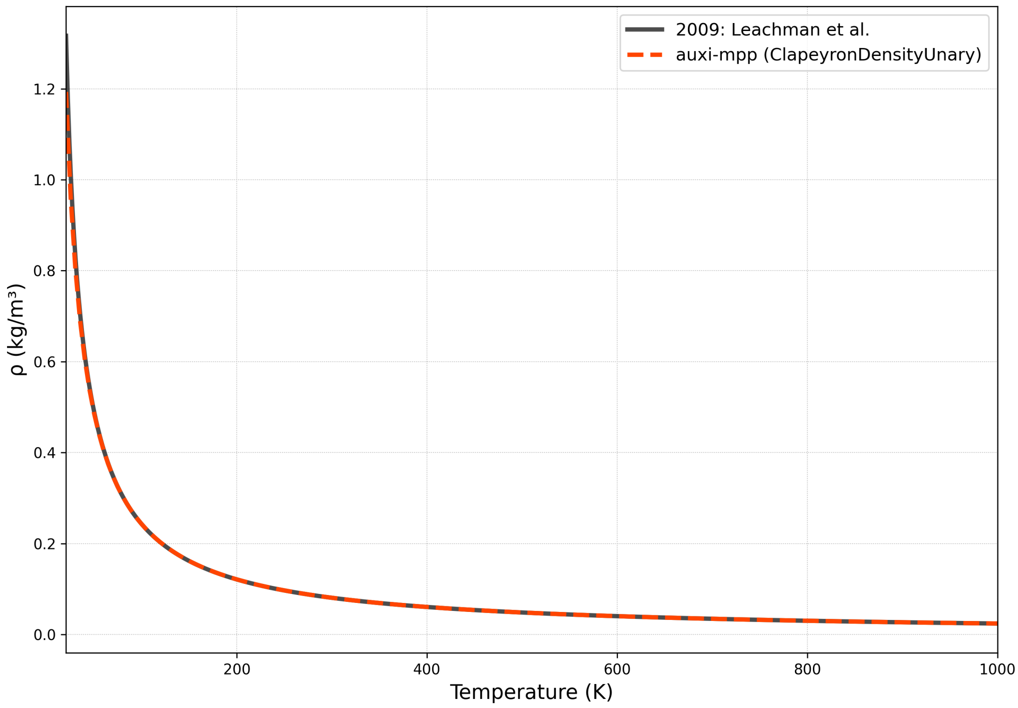

Figure 15.6: Clapeyron unary density model estimates compared to reference data for H_2.

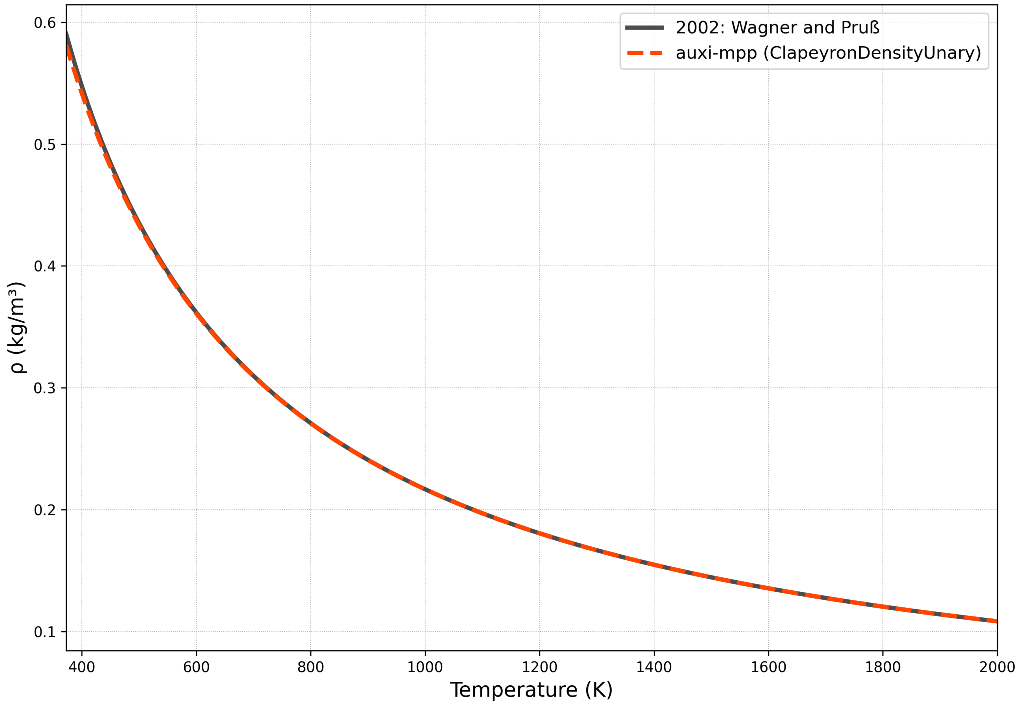

Figure 15.7: Clapeyron unary density model estimates compared to reference data for H_2O.

The model estimations show good agreement with the reference data across the validated temperature ranges for all pure components. Minor deviations are observed at low temperatures, particularly for CO_2 and H_2O.

Further validation at higher temperatures is recommended for CO and H_2, as their models are currently validated only up to 500 K and 1000 K, respectively. While extrapolation beyond these ranges is possible because gas behaviour approaches ideality at higher temperatures, users should proceed with caution.

Overall, the `ClapeyronDensityUnary` model and therefore the `ClapeyronUnary` model demonstrates reliable performance for estimating the density of pure gases.

Binary Mixture Validation

A unique approach was taken to validate the binary mixture models (`ClapeyronBinary` and `ClapeyronDensityBinary`). Reference data from diffusivity studies conducted by Hellmann (2019a), Hellmann (2019b), and Hellmann (2024) and Crusius et al. (2018) were utilised.

Reference data in the form of molar density (ρ_m) combined with binary diffusion coefficients (D) were presented in tables in these studies. This data was used and combined with the `HellmannBinary` model, discussed in the Diffusivity chapter, to back-calculate density data to validate the `ClapeyronDensityBinary` model against.

Table 15.2 summarises the validation ranges for which back-calculated density data was generated and used to validate the `ClapeyronDensityBinary` model.

Again, if the density model validation is successful, it implies that the corresponding molar volume model is also validated.

Table 15.2: Model validation for binary gas mixtures using the `ClapeyronDensityBinary` model.

Binary Mixture	Model	Temperature Range (K)	Pressure (Pa)	Reference Data Source	Reference
$N_2 - CO_2$	`ClapeyronBinary`, `ClapeyronDensityBinary`	150–2000	101325	Supplementary data	(Crusius et al. 2018)
$H_2O - Ar$	`ClapeyronBinary`, `ClapeyronDensityBinary`	250–2000	101325	Table 3	(Hellmann 2024)
$H_2O - N_2$	`ClapeyronBinary`, `ClapeyronDensityBinary`	250–2000	101325	Table 3	(Hellmann 2019b)
$H_2O - CO_2$	`ClapeyronBinary`, `ClapeyronDensityBinary`	250–2000	101325	Table 2	(Hellmann 2019a)

Validation isotherms for $N_2 - CO_2$, $H_2O - Ar$, $H_2O - N_2$, $H_2O - O_2$ and $H_2O - CO_2$ are provided as follows with Figures 15.8 to 15.12 respectively.

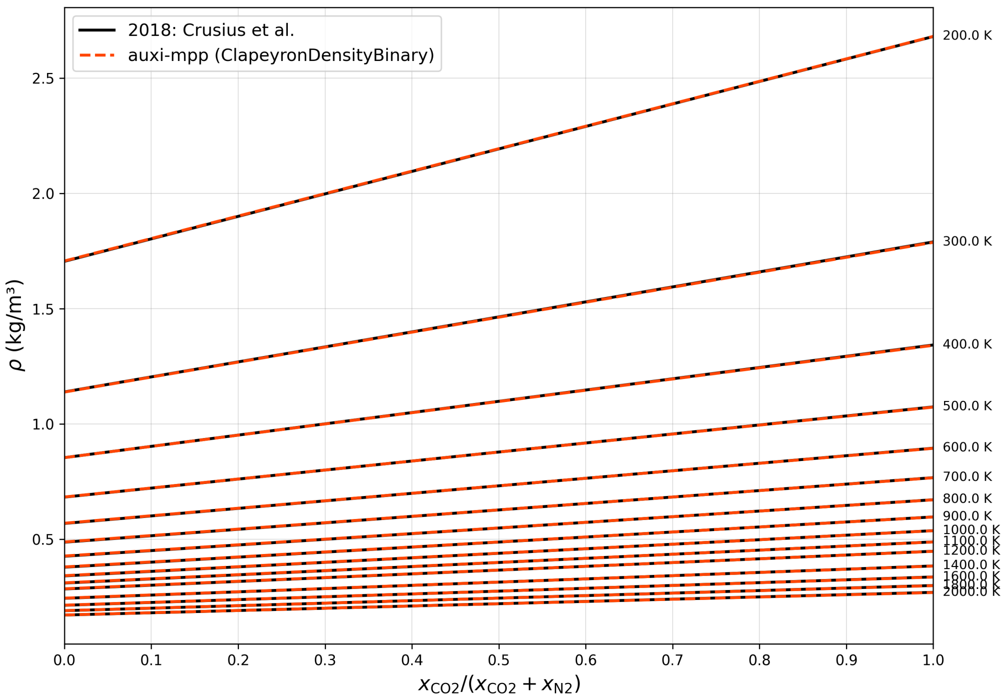

Figure 15.8: Clapeyron binary density model estimates compared to reference data for $N_2 - CO_2$ binary mixture.

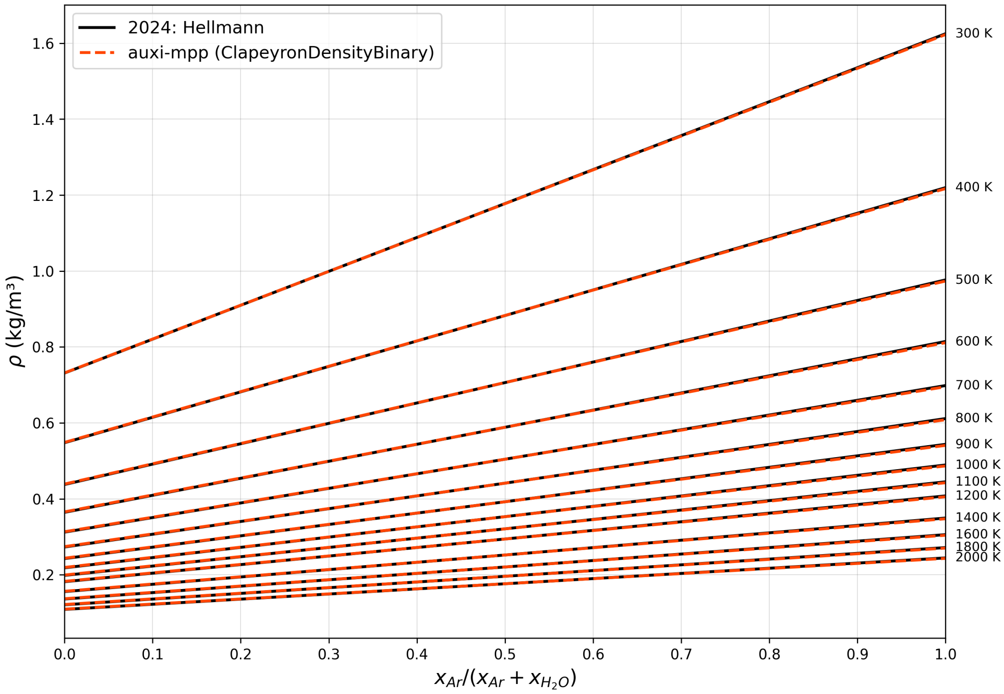

Figure 15.9: Clapeyron binary density model estimates compared to reference data for H_2O – Ar binary mixture.

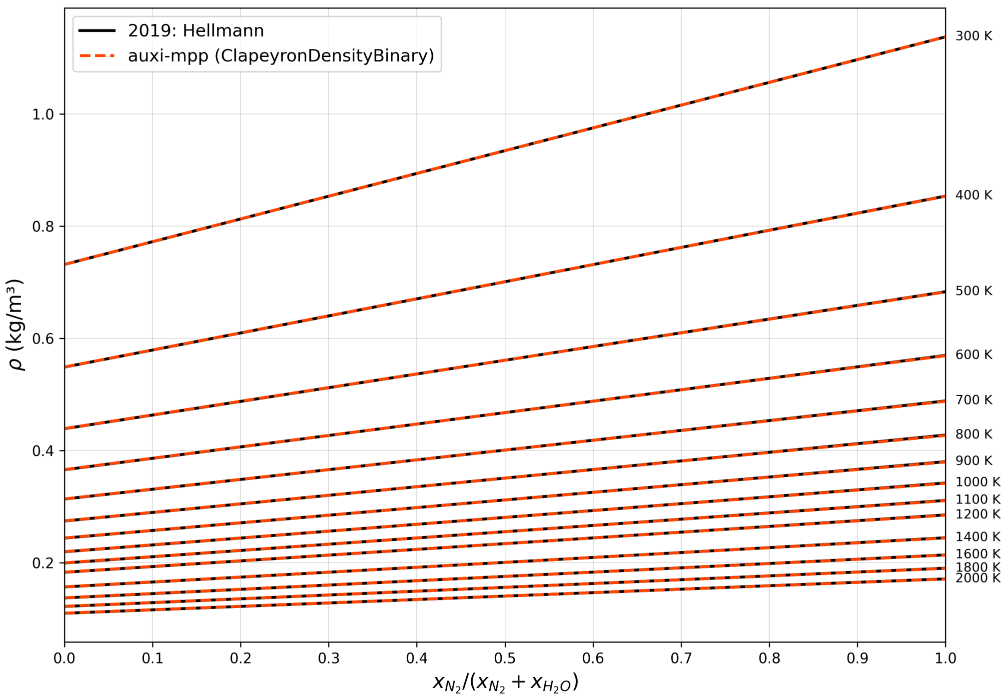

Figure 15.10: Clapeyron binary density model estimates compared to reference data for H_2O – N_2 binary mixture.

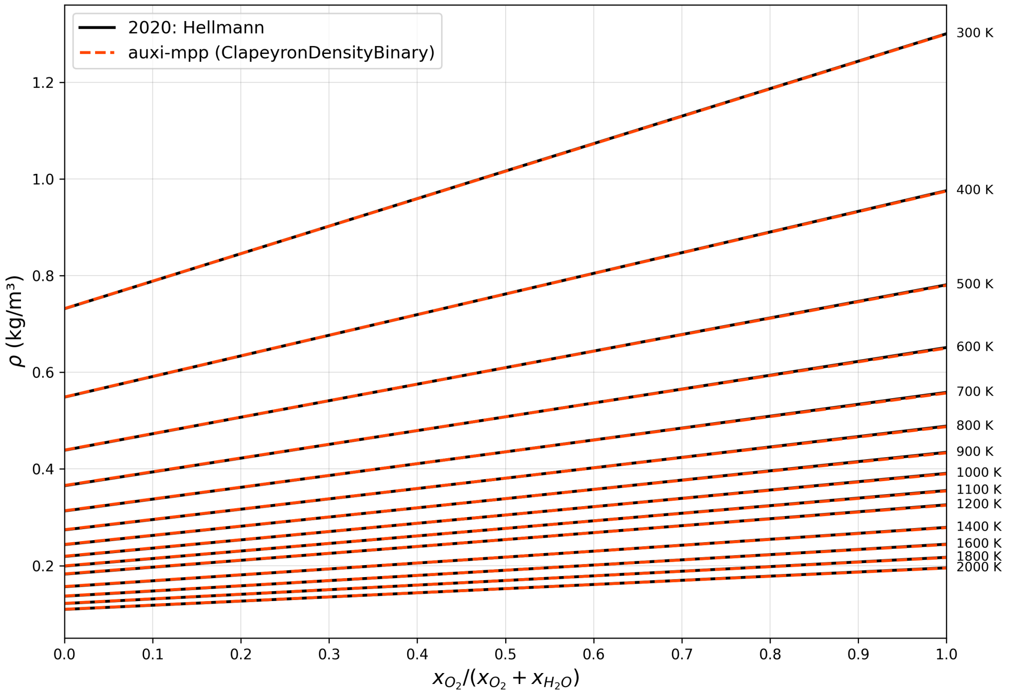

Figure 15.11: Clapeyron binary density model estimates compared to reference data for $H_2O - O_2$ binary mixture.

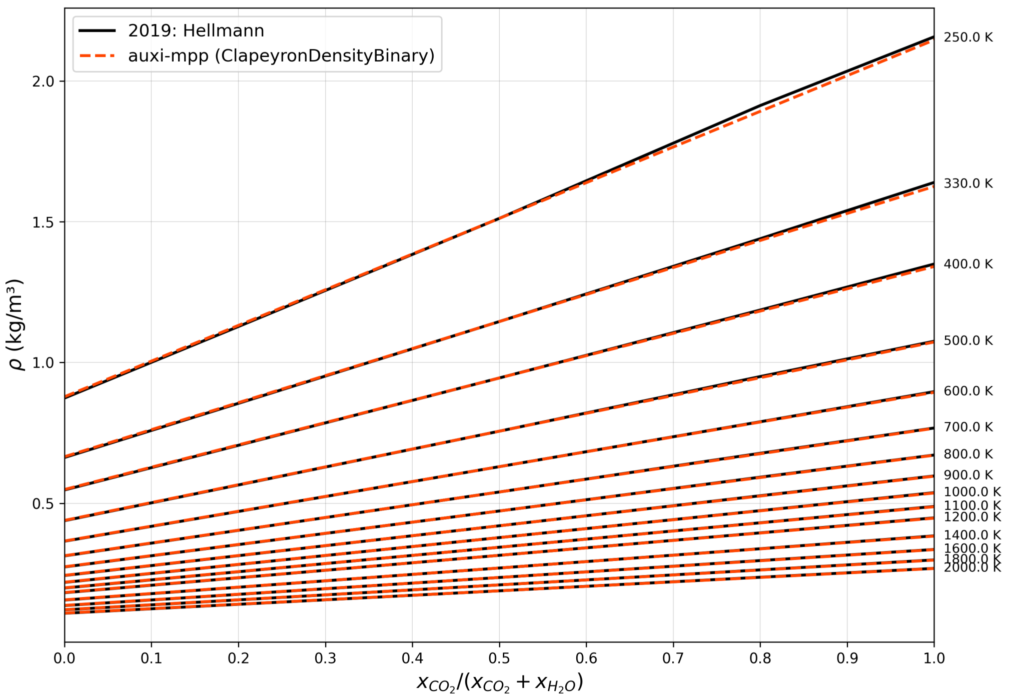

Figure 15.12: Clapeyron binary density model estimates compared to reference data for $H_2O - CO_2$ binary mixture.

All binary mixture validation plots demonstrate good agreement between the `ClapeyronDensityBinary` model estimations and the back-calculated reference data across the shown temperature ranges. The $H_2O - CO_2$ mixture, Figure 15.12, is the only one that shows some minor deviations at lower temperatures, but overall the model estimates density values well for all the binary mixtures.

Overall, the `ClapeyronDensityBinary` model and therefore the `ClapeyronBinary` model demonstrates reliable performance for estimating the density of binary gas mixtures.

Multi Component Mixture Validation

In Section 15.1, the `ClapeyronMulti` and `ClapeyronDensityMulti` models were introduced for multi-component gas mixtures. However, no specific validation has been performed for these models, but it is planned for future work. Given that these models are functionally the same as the unary and binary models—applying the ideal gas law and differing only in the number of components handled—it is reasonable to infer that their performance is similar, particularly within the validated temperature and pressure ranges. Users should still exercise caution and use their judgment when applying these models to multi-component mixtures.

Chapter 16

Viscosity

Viscosity is a fundamental transport property of gases, quantifying its resistance to flow is important for understanding and estimating fluid flow within the freeboard of a furnace.

Viscosity is also particularly important for understanding the entrainment of dust and fine particles. If the gas is sufficiently viscous, these particles may not settle back into the melt. This dust entrainment can lead to several problems, including the loss of valuable material, reduced efficiency of downstream equipment like cyclones and scrubbers, and the formation of accretions in off-gas systems.

This chapter presents the framework for calculating the viscosity of individual gas species and their binary mixtures at high temperatures.

For pure (unary) gases, a composite model is presented, combining the work of various researchers into a single unified approach. This model is applicable to several common gases found in industrial processes, namely CO, CO_2, N_2, Ar, H_2, H_2O, and O_2.

For binary gas mixtures, the Wilke model is employed. This model uses the pure component viscosities calculated from the unary model and applies a mixing rule to determine the viscosity.

16.1 Lemmon, Hellmann, Laesecke and Muzny Viscosity Model

The Lemmon-Hellmann-Laesecke-Muzny (LHLM) model combines individual models from different references to provide a comprehensive approach for calculating the viscosity of the unary gases CO, CO_2, N_2, Ar, H_2, H_2O, and O_2 (Lemmon and Jacobsen 2004; Hellmann and Vogel 2015; Laesecke and Muzny 2017; Muzny et al. 2013).

16.1.1 Model Overview

The combined unary gas model integrates the following individual models:

1. **Hellmann-Vogel Model**: for H_2O
2. **Laesecke-Muzny Model**: for CO_2

3. **Lemmon-Jacobsen Model**: for N_2, O_2, Ar, and CO
4. **Muzny Model**: for H_2

The LHLM model consolidates these models, providing a unified interface for calculating the viscosity of the supported gas species.

16.1.2 Model Formulation

All the implemented unary gas viscosity models share a common characteristic: they are setup to calculate the zero-density limit (or dilute gas) viscosity, which is appropriate for gases at low pressures (atmospheric pressure of 101325 Pa for this implementation) (Hellmann 2014; Poling et al. 2001).

In the zero-density limit, the viscosity of a pure gas is governed solely by binary collisions between its molecules (Hellmann 2014; Poling et al. 2001). This concept is explained further below in the context of the total viscosity.

The total viscosity μ, Equation (16.1), is typically formulated as the sum of three distinct terms, reflecting the influence of density (ρ) and temperature (T):

$$\mu(\rho, T) = \mu_0(T) + \Delta\mu_{\mathrm{r}}(\rho, T) + \Delta\mu_{\mathrm{c}}(\rho, T) \tag{16.1}$$

where:

1. $\mu_0(T)$: This term is the zero-density (or dilute-gas) contribution to viscosity. It is a function of temperature only and is the viscosity limit where molecular interactions are governed solely by binary interactions (Hellmann 2014; Poling et al. 2001).
2. $\Delta\mu_{\mathrm{r}}(\rho, T)$: This is the residual contribution (sometimes called the excess contribution) (Huber 2018a; Huber et al. 2009). It accounts for contributions to viscosity arising from elevated densities (Muzny et al. 2013), including many-body collisions, molecular-velocity correlations, and collisional transfer (Poling et al. 2001; Huber 2018a).
3. $\Delta\mu_{\mathrm{c}}(\rho, T)$: This is the critical enhancement term. It represents the contribution to viscosity arising from long-range interaction fluctuations that occur near the critical point (Muzny et al. 2013; Laesecke and Muzny 2017). This term contributes to a weak divergence of the viscosity at the critical point (Muzny et al. 2013).

A zero-density limit is achieved when the fluid is in a highly dilute gaseous state (low pressure, low density). In this state, the total viscosity simplifies significantly because the contributions dependent on density are negligible (Hellmann 2014; Muzny et al. 2013).

The total viscosity equation in the zero-density limit (μ_0), is approximated by Equation (16.2).

$$\mu(T) \approx \mu_0(T) + \cancel{\Delta\mu_{\mathrm{r}}(\rho, T)} + \cancel{\Delta\mu_{\mathrm{c}}(\rho, T)} \tag{16.2}$$

The zero-density viscosity, $\mu_0(T)$ (or simply $\mu(T)$), is calculated using a specific formulation for each of the models that constitute the LHLM model:

Hellmann-Vogel Model for H_2O

This model is based on the classical kinetic theory of molecular gases with a highly accurate *ab initio* potential for the H_2O – H_2O molecule pair to calculate reference viscosity values. These calculated values were subsequently scaled by a factor of 1.001 to align with experimental data and obtain the final reference values used for fitting (Hellmann and Vogel 2015).

The correlation, Equation (16.3), for the zero-density limit (μ_0 in μPa s) is a function of the reduced temperature ($\bar{T}$)

$$\mu_0 = \frac{\bar{T}^{1/2}}{\sum_{i=0}^{7} a_i \bar{T}^{-i/2}} \tag{16.3}$$

where $\bar{T} = T/T_c$ and the critical temperature used for scaling is $T_c = 647.096$ K. Coefficients a_0 to a_7 are provided in Table 16.2.

Laesecke-Muzny Model for CO_2

The zero density viscosity (μ_0) of this model is also rooted in the kinetic theory of gases and uses a novel functional form obtained via symbolic regression, scaled by 1.0055 to match high-accuracy data (Laesecke and Muzny 2017).

The correlation, Equation (16.4), for the zero-density limit (μ_0 in mPa s) is given as:

$$\mu_0(T) = \frac{1.0055\sqrt{T}}{\left(a_0 + a_1 T^{1/6} + a_2 \exp\left(a_3 T^{1/3}\right) + \frac{a_4 + a_5 T^{1/3}}{\exp\left(T^{1/3}\right)} + a_6\sqrt{T}\right)} \tag{16.4}$$

where T is in K and coefficients a_0 to a_6 are provided in Table 16.2.

Lemmon-Jacobsen Model for N_2, O_2, Ar, and CO

The model for N_2, O_2, and Ar is based on the Chapman-Enskog theory (Lemmon and Jacobsen 2004). The zero-density viscosity, given in Equation (16.5), is calculated using a collision integral, Ω (Equation (16.6)), that was fitted to experimental data. Due to its physical similarities to N_2 (e.g., molar mass, triple bond, bond length, and bond energy), CO is also described by this model, using the same parameters as N_2 (Poling et al. 2001).

$$\mu_0(T) = 0.0266958 \frac{\sqrt{MT}}{\sigma^2 \Omega(T^*)} \tag{16.5}$$

M is molar mass in g mol^{-1}, T in K, σ is the Lennard-Jones size parameter in nm.

$$\Omega(T^*) = \exp\left(\sum_{i=0}^{4} a_i (\ln(T^*))^i\right) \tag{16.6}$$

where the reduced temperature is $T^* = T/(\epsilon/k)$ and ϵ/k is the Lennard-Jones energy parameter. Coefficients a_0 to a_4 are provided in Table 16.1.

Muzny Model for H_2

The zero-density viscosity(μ_0), Equation (16.7), relies on the kinetic theory of gases (Chapman-Enskog) and specific scaling parameters based on accurate *ab initio* and experimental data (Muzny et al. 2013).

$$\mu_0(T) = 0.021357\frac{\sqrt{MT}}{\sigma^2\Omega^*(T^*)} \tag{16.7}$$

M is molar mass in g mol^{-1} and σ is length scaling parameter in nm. Ω^*, Equation (16.8), is a reduced effective cross section (collision integral) where the reduced temperature is $T^* = k_B T/\epsilon$ and ϵ/k_B is an energy scaling parameter in K.

$$\Omega^*(T^*) = \exp\left(\sum_{i=0}^{4} a_i(\ln(T^*))^i\right) \tag{16.8}$$

Coefficients a_0 to a_4 are provided in Table 16.2.

16.1.3 Variable Declarations

Table 16.1: Model parameters and coefficients for Lemmon-Jacobsen viscosity model.

Parameters and Coefficients	Ar	N_2	O_2	CO
ϵ/k (K)	143.2	98.94	118.5	98.94
σ (nm)	0.335	0.3656	0.3428	0.3656
a_0	0.431	0.431	0.431	0.431
a_1	-0.4623	-0.4623	-0.4623	-0.4623
a_2	0.08406	0.08406	0.08406	0.08406
a_3	0.005341	0.005341	0.005341	0.005341
a_4	-0.00331	-0.00331	-0.00331	-0.00331
Reference	(Lemmon and Jacobsen 2004)			

Table 16.2: Model parameters and coefficients for Hellmann-Vogel, Laesecke-Muzny, and Muzny viscosity models.

Parameter	H_2	CO_2	H_2O
ϵ/k (K)	30.41	–	–
σ (nm)	0.297	–	–
a_0	2.09630$\times 10^{-1}$	1749.354893188350	3.933738$\times 10^{-2}$
a_1	-4.55274$\times 10^{-1}$	-369.069300007128	-2.361739$\times 10^{-1}$
a_2	1.43602$\times 10^{-1}$	5423856.34887691	1.059696
a_3	-3.35325$\times 10^{-2}$	-2.21283852168356	-2.300709
a_4	2.76981$\times 10^{-3}$	-269503.247933569	2.786190
a_5	–	73145.021531826	-1.852813
a_6	–	5.34368649509278	6.352538$\times 10^{-1}$
a_7	–	–	-8.803352$\times 10^{-2}$
Reference	(Muzny et al. 2013)	(Laesecke and Muzny 2017)	(Hellmann and Vogel 2015)

16.1.4 Assumptions

The models implement the following base assumptions:

1. Kinetic theory application: The zero-density viscosity is calculated using the framework of classical kinetic theory, specifically the Chapman-Enskog theory, which is the theoretical model used for the dilute gas component of viscosity correlations (Muzny et al. 2013).
2. Two-body interactions: By definition, the zero-density limit assumes that only two-body molecular interactions occur (Muzny et al. 2013).
3. Mean free path limitation: Derived equations for the Lemmon-Jacobsen model are not valid when the mean free path of the gas is comparable to the dimensions of the confining medium (Lemmon and Jacobsen 2004).

16.1.5 Model Validation

The Lemmon-Hellmann-Laesecke-Muzny (LHLM) unary model was validated against reference data for several gas species. Table 16.3 summarises the specific models validated, their respective temperature range, pressure, and the reference data sources. For data taken from secondary sources, such as the NIST Chemistry WebBook, the original reference is also provided (Linstrom and Mallard 2001).

Table 16.3: Model validation ranges for unary gas viscosity models.

Gas	Specific Model	Temperture Range (K)	Pressure (Pa)	Reference Data Source	Reference
N_2	Lemmon-Jacobsen	77–2000	101325	NIST Chemistry WebBook	(Lemmon and Jacobsen 2004)
CO	Lemmon-Jacobsen	81–500	101325	NIST Chemistry WebBook	(Huber 2018a)
O_2	Lemmon-Jacobsen	90–2000	101325	NIST Chemistry WebBook	(Lemmon and Jacobsen 2004)
Ar	Lemmon-Jacobsen	87–2000	101325	NIST Chemistry WebBook	(Lemmon and Jacobsen 2004)
H_2O	Hellmann-Vogel	250–2500	101325	NIST Chemistry WebBook Table 2	(Huber et al. 2009) (Hellmann and Vogel 2015)
CO_2	Laesecke-Muzny	150–2000	101325	NIST Chemistry WebBook Supplementary Data	(Laesecke and Muzny 2017) (Hellmann 2014)
H_2	Muzny	20–1000	101325	NIST Chemistry WebBook	(Muzny et al. 2013)

Validation plots for Ar, N_2, O_2, CO, CO_2, H_2, and H_2O are shown in Figures 16.1 to 16.7, respectively. The model as implemented in auxi-mpp is shown as LemmonHellmannLaeseckeMuznyUnary in the plots.

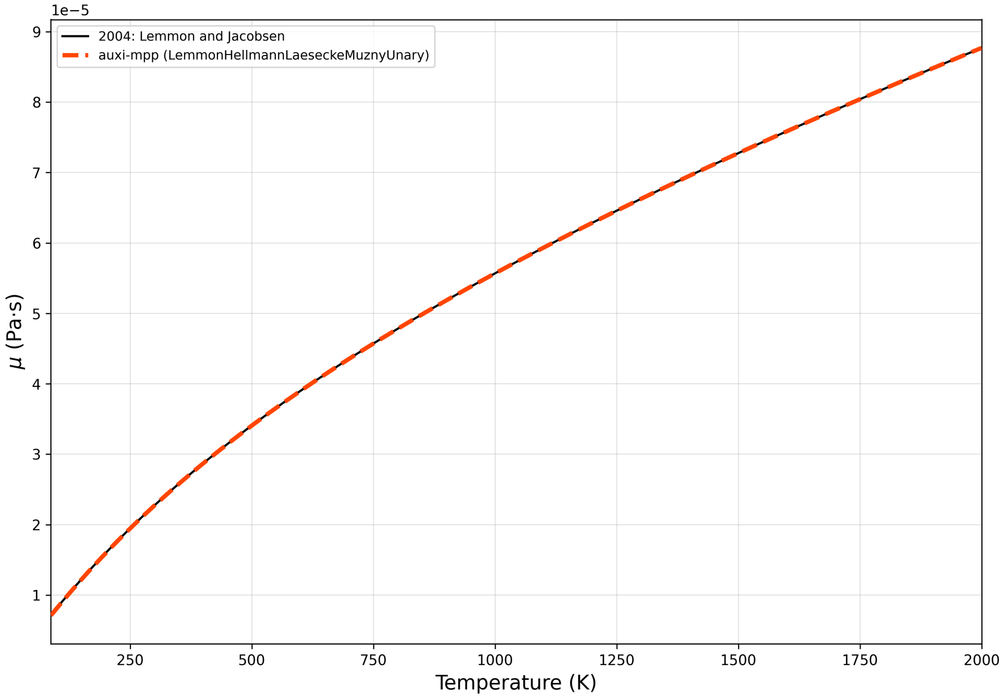

Figure 16.1: Lemmon-Hellmann-Laesecke-Muzny unary viscosity model estimates compared to reference data for Ar.

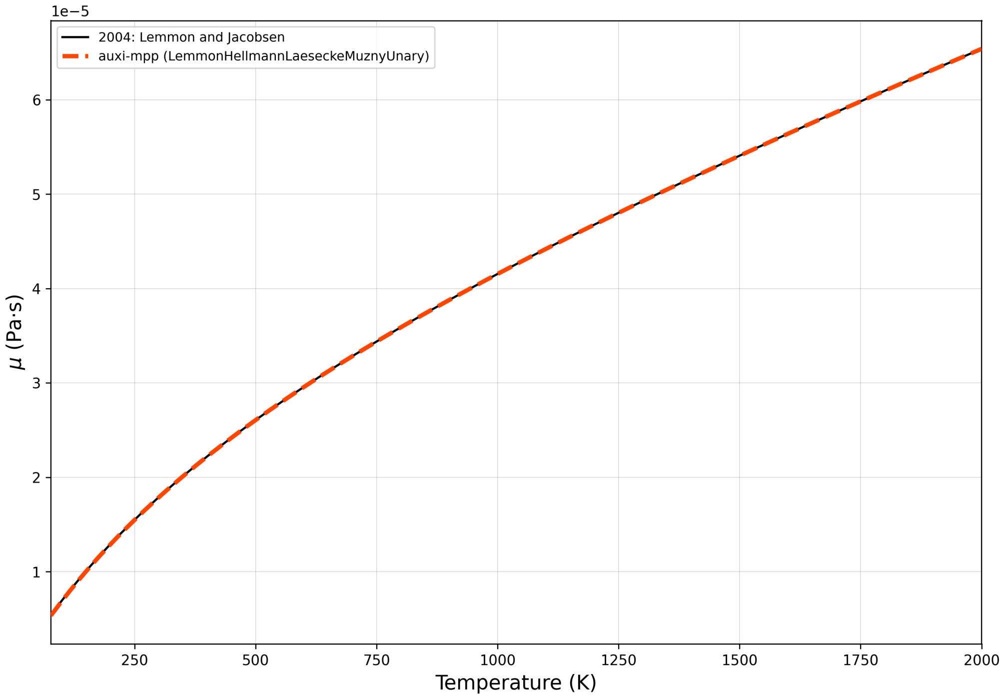

Figure 16.2: Lemmon-Hellmann-Laesecke-Muzny unary viscosity viscosity model estimates compared to reference data for N_2.

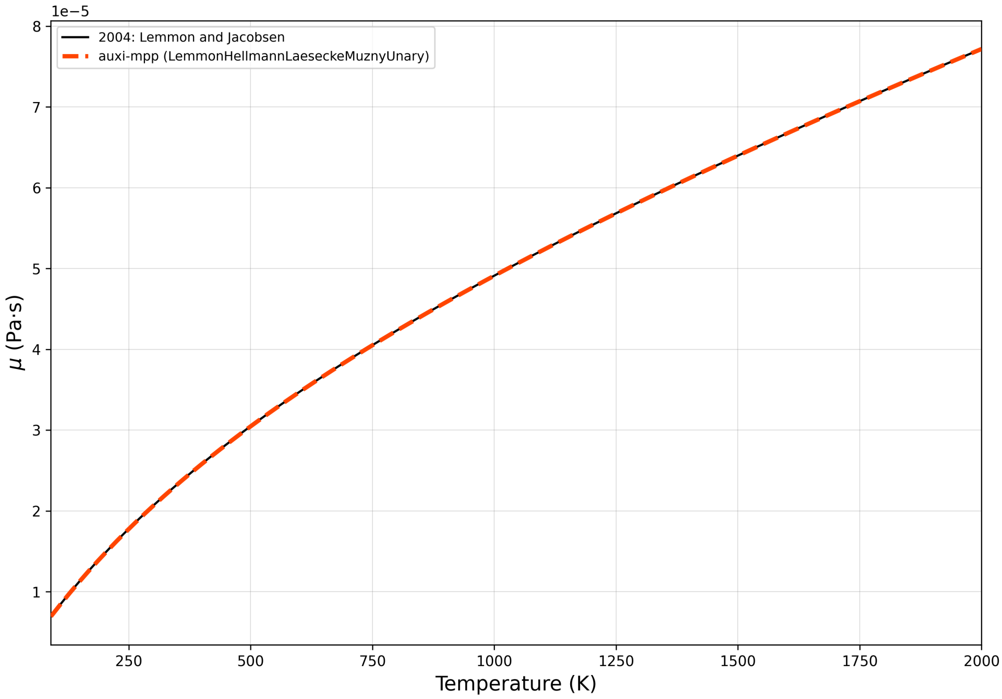

Figure 16.3: Lemmon-Hellmann-Laesecke-Muzny unary viscosity viscosity model estimates compared to reference data for O_2.

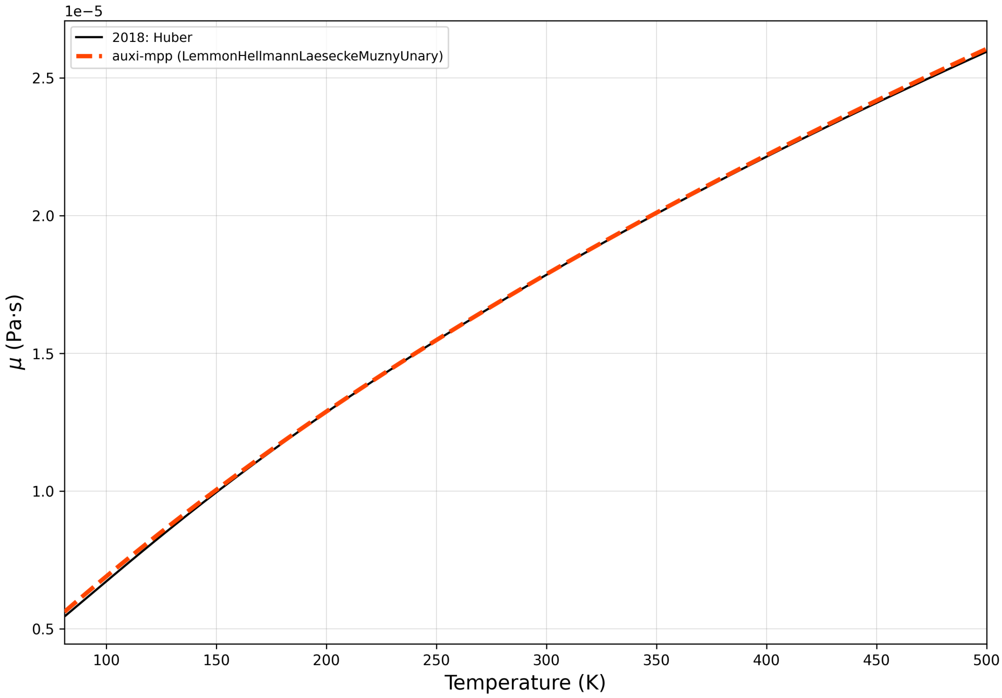

Figure 16.4: Lemmon-Hellmann-Laesecke-Muzny unary viscosity model estimates compared to reference data for CO.

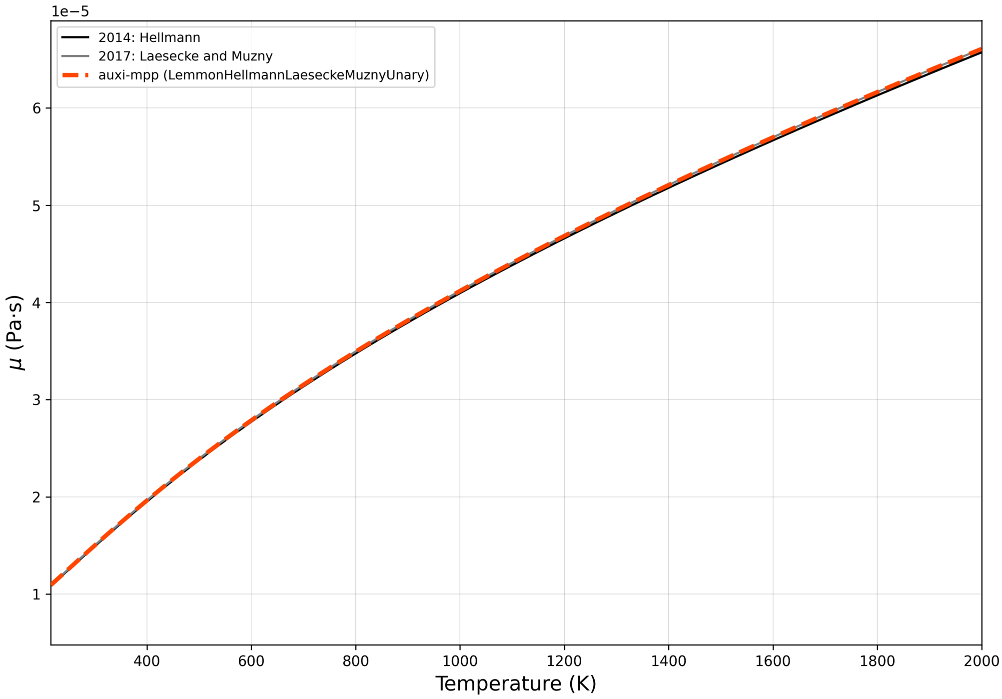

Figure 16.5: Lemmon-Hellmann-Laesecke-Muzny unary viscosity model estimates compared to reference data for CO_2.

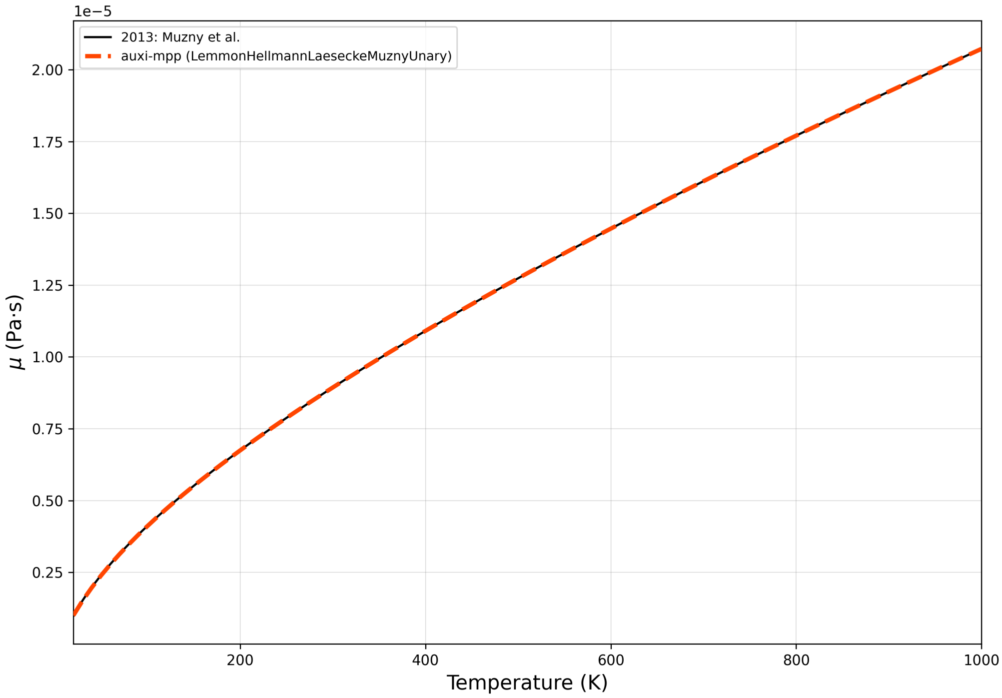

Figure 16.6: Lemmon-Hellmann-Laesecke-Muzny unary viscosity model estimates compared to reference data for H_2.

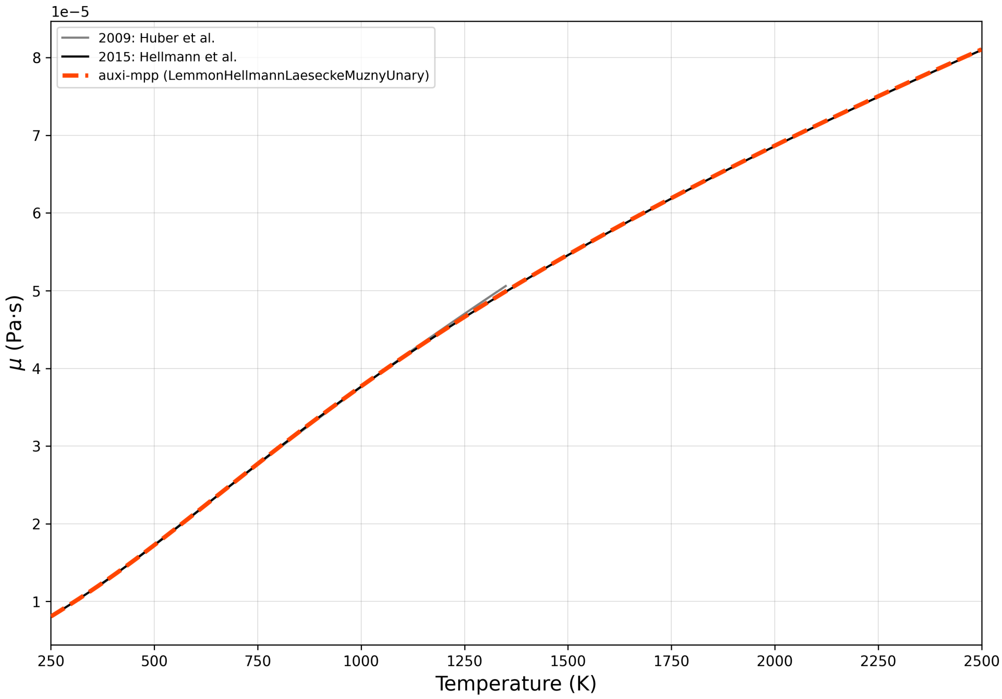

Figure 16.7: Lemmon-Hellmann-Laesecke-Muzny unary viscosity model estimates compared to reference data for H_2O.

The model estimations for all the plots show good agreement with the reference data across the validated temperature ranges for each gas. The use of N_2 parameters for CO in the Lemmon-Jacobsen model,Figure 16.4, only shows small deviations at very low temperatures and temperatures nearing 500 K.

It was recommended that the CO_2 reference data from Hellmann (2014) be adjusted by a scaling factor of 1.005. This was not done for the validation plot shown in Figure 16.5 and shows a slight deviation from Laesecke and Muzny (2017) NIST reference data which the model aligns with more closely.

The reference data for H_2O from Huber et al. (2009) also shows a slight deviation at end of its data range near 1350 K in Figure 16.7 when compared to the data from Hellmann and Vogel (2015) which the Hellmann-Vogel model aligns accurately with.

Overall, the deviations as seen as minor and the LHLM unary viscosity model provides reliable estimates for the viscosities of the gases considered within the specified temperature range and pressure.

The only recommendation is that the models for CO and H_2 be validated for a wider temperature range (up to 2000 K) in future work to ensure accuracy beyond their current limits.

Muzny et al. (2013) does mention that the model for H_2 extrapolates in a physically reasonable manner to 2000 K. Similarly, extrapolation of the model for CO to 2000 K is expected to be reasonable due to its similarities to N_2; however, there may be over estimations at higher temperatures based on observed fit of the model to the reference data in Figure 16.4. Any extrapolations should be treated with caution until further validation can be performed.

16.2 Wilke Viscosity Model

A model developed by Wilke (1950) for estimating the viscosity of gas mixtures is implemented in this section.

16.2.1 Model Overview

The Wilke model uses the models of CO, CO_2, N_2, Ar, H_2, H_2O, and O_2 from Section 16.1 and combines them with a mixing rule to estimate the viscosity of binary gas mixtures (Poling et al. 2001; Lemmon and Jacobsen 2004; Hellmann and Vogel 2015; Laesecke and Muzny 2017; Muzny et al. 2013).

16.2.2 Model Formulation

The viscosity of a gas mixture, μ_m, is estimated using the Wilke mixing rule, as shown in Equation (16.9).

$$\mu_m(T) = \sum_{i=1}^{n} \frac{x_i \mu_i(T)}{\sum_{j=1}^{n} x_j \Phi_{ij}} \tag{16.9}$$

where x_i and μ_i are the mole fraction and viscosity of pure component i, respectively, and Φ_{ij} is an interaction parameter that is calculated as shown in eq. (16.10).

$$\Phi_{ij} = \frac{1}{\sqrt{8}} \left(1 + \frac{M_i}{M_j}\right)^{-1/2} \left[1 + \left(\frac{\mu_i}{\mu_j}\right)^{1/2} \left(\frac{M_j}{M_i}\right)^{1/4}\right]^2 \tag{16.10}$$

In this equation, M_i and M_j represent the molar masses of components i and j. The pure component viscosities, μ_i, are obtained from the unary models described in Section 16.1 model section.

16.2.3 Assumptions

The Wilke model for estimating the viscosity of gas mixtures is based on the following key assumptions:

1. The model is a semi-empirical simplification of the rigorous kinetic theory of gases.
2. The method is applicable to gas mixtures at low pressures, where the gas is dilute enough that only binary molecular collisions are significant.
3. The binary interaction parameters, Ψ_{ij}, are estimated using only the viscosities and molar masses of the pure components. This avoids the need for intermolecular potential energy parameters required by more rigorous theories (Poling et al. 2001).

16.2.4 Model Validation

The Wilke binary model was validated against reference data for the following mixtures as shown in Table 16.4.

Table 16.4: Model validation for binary gas mixtures using the Wilke model.

Binary Mixture	Model	Temperature Range (K)	Pressure (Pa)	Reference Data Source	Reference
$N_2 - CO_2$	Wilke	150–2000	101325	Supplementary data	(Crusius et al. 2018)
$H_2O - Ar$	Wilke	250–2000	101325	Table 3	(Hellmann 2024)
$H_2O - N_2$	Wilke	250–2000	101325	Table 3	(Hellmann 2019b)
$H_2O - CO_2$	Wilke	250–2000	101325	Table 2	(Hellmann 2019a)

Validation isotherms in increments of 100 K for the different binary mixtures are shown in Figures 16.8 to 16.11. The model as implemented in auxi-mpp is shown as WilkeBinary in the plots.

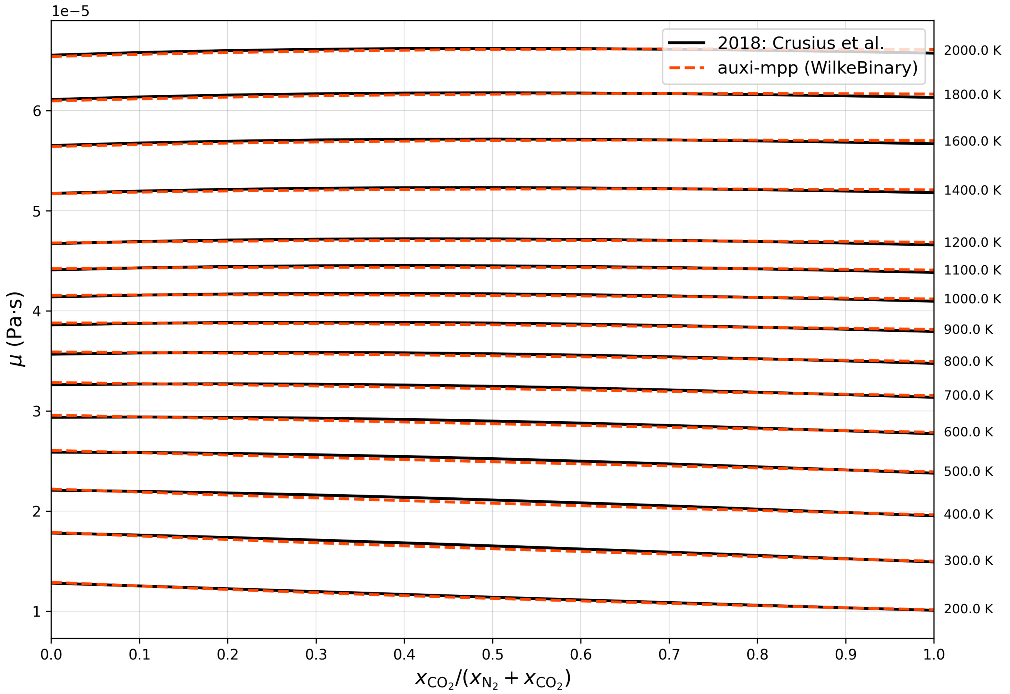

Figure 16.8: Wilke viscosity model estimates compared to supplementary reference data for the $N_2 - CO_2$ binary mixture.

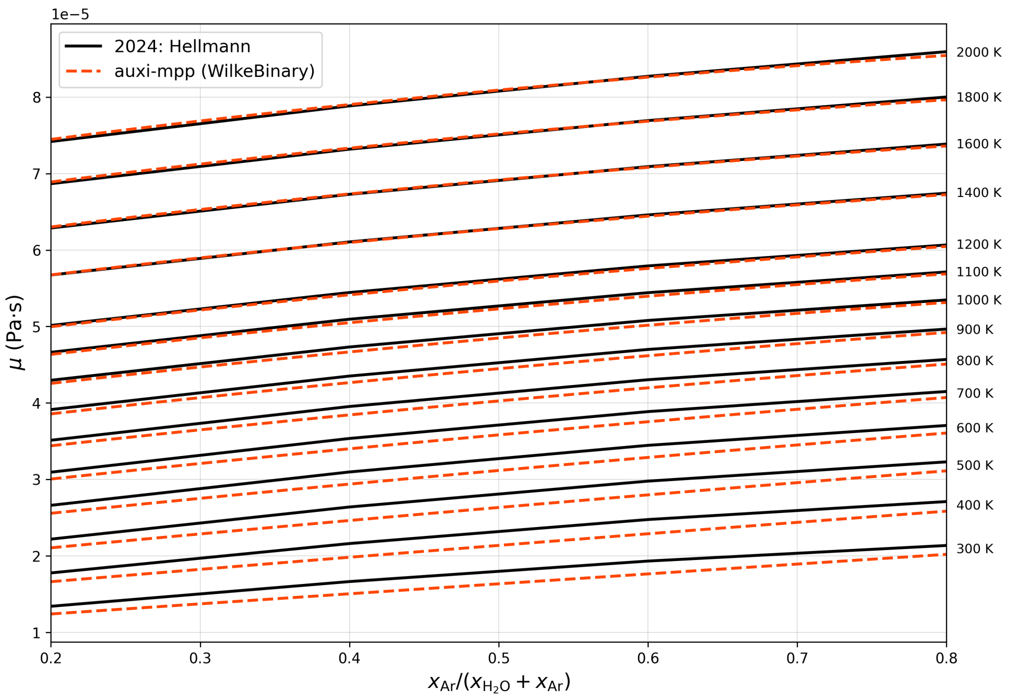

Figure 16.9: Wilke viscosity model estimates compared to reference data for the $H_2O - Ar$ binary mixture.

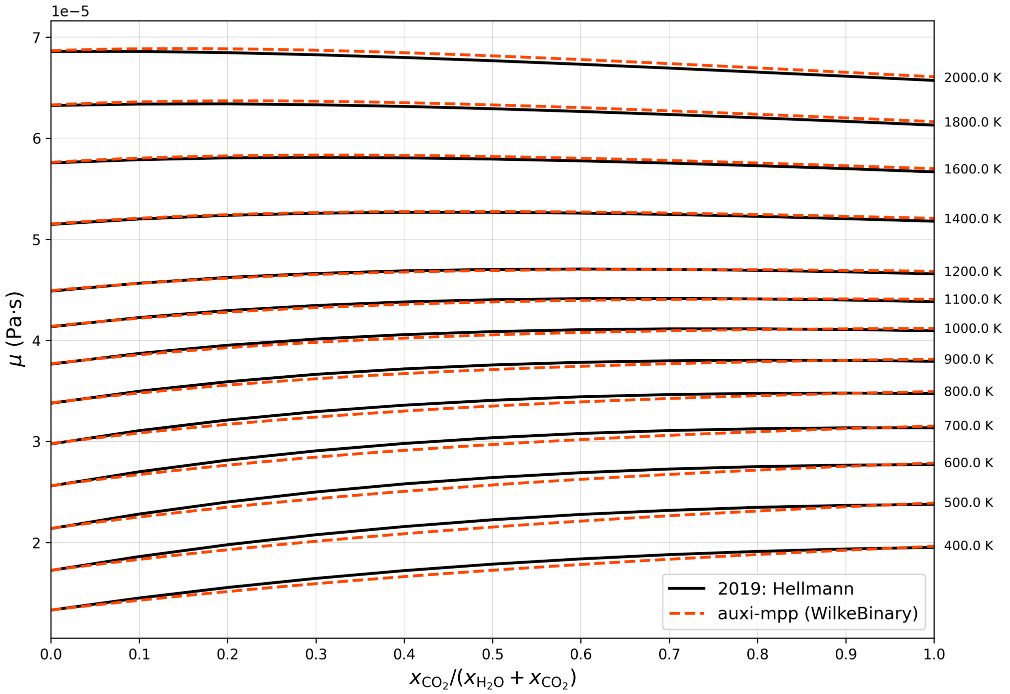

Figure 16.10: Wilke viscosity model estimates compared to reference data for the H_2O-CO_2 binary mixture.

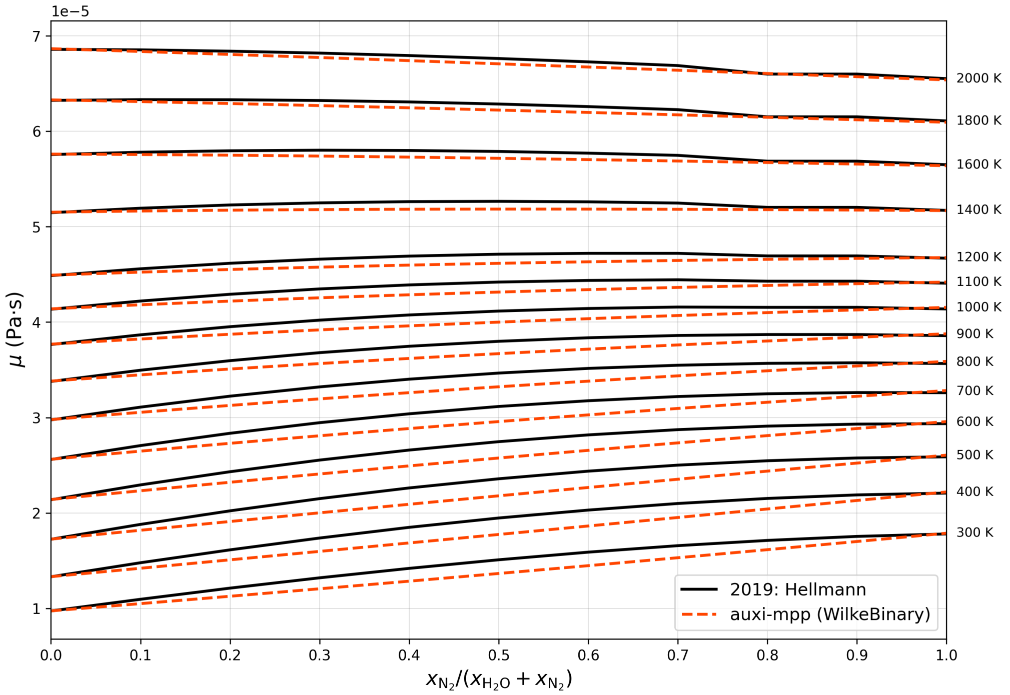

Figure 16.11: Wilke viscosity model estimates compared to reference data for the H_2O-N_2 binary mixture.

The agreement between the Wilke model and the reference data varies among the mixtures. The best agreement is observed for the N_2-CO_2 mixture, as shown in Figure 16.8. For the H_2O-Ar mixture (Figure 16.9), deviations become more visible at temperatures below 1200 K. The $H_2O - CO_2$ mixture (Figure 16.10) shows good agreement in the 1200 to 1400 K range, with slight deviations at lower and higher temperatures. In contrast, the $H_2O - N_2$ mixture (Figure 16.11) exhibits deviations across the entire temperature range, which are more pronounced at equimolar compositions.

Despite these deviations, the Wilke model consistently tracks the trend of the reference data for all mixtures. The estimated viscosities increase with temperature, which aligns with the expected physical behaviour of gas mixtures.

Overall, the Wilke binary viscosity model provides reasonable estimates for the viscosities of the validated gas mixtures within the specified temperature ranges.

Recommendations for future work include validating the model against additional binary gas mixtures and higher order mixtures to further assess the model's applicability and accuracy.

Chapter 17

Diffusivity

Diffusion coefficients are relevant to the kinetics of the reduction process where gases, such as CO or H_2, react with metal ores. The overall speed of this reaction can be partially dependent on the rate at which these gases diffuse through stagnant boundary layers or into the ore's porous structure. While chemical kinetics often drive the process, diffusion limitations can occur, potentially affecting the reaction rate if the gas transport is slow. Consequently, knowing the diffusion coefficients helps estimate the mass transfer rates of reactants to the surface and the removal of gaseous products like CO_2 and H_2O, which contributes to calculations regarding furnace sizing and residence time.

17.1 Burgess Model

This is a model by Burgess Jr. (2024) to estimate self-diffusion coefficients of pure gases.

17.1.1 Model Overview

This model is designed to predict self-diffusion coefficients at slightly higher temperatures, up to about 450 K. While simpler methods might assume a straightforward relationship where diffusion increases with temperature based on a single activation barrier, this approach recognises that the change is more complex as the temperature rises. To capture this, the model combines three distinct components: a constant baseline value, a primary term that accounts for the energy required for movement (activation barrier), and a logarithmic correction factor.

17.1.2 Model Formulation

This model captured by Equation (17.1).

$$\ln(D) = A + B/T + C \cdot \ln(T) \tag{17.1}$$

Here, D is the self-diffusion coefficient given in cm^2 s^{-1} and A, B and C are parameters specific to the pure gas. These parameters are captured in Table 17.1. Note that in auxi-mpp, the self-diffusion coefficient is returned in SI units; m^2 s^{-1}.

The B/T term in Equation (17.1) acts as the activation barrier, and the $C \cdot \ln(T)$ term ensures that the model remains accurate at higher temperatures.

The model is currently limited in temperature range of roughly between 233 to 422 K except for O_2 where model parameters were calibrated from 55 K to 2000 K.

17.1.3 Variable Declarations

Besides the interaction parameters, Table 17.1 also shows the temperature ranges for which the parameters are valid.

Table 17.1: Valid Temperature ranges and Interaction Parameters.

System	T Range (K)	Parameters		
		A	B	C
Ar	235–418	-11.097	-45.486	1.676
CO	233–422	-10.132	-64.216	1.545
CO_2	233–363	0.015	-637.089	0.0
H_2	115–295	-9.309	-8.028	1.686
N_2	233–422	-10.397	-52.566	1.581
O_2	55–2000	-10.787	-44.220	1.649

The parameters for Ar, CO, CO_2, H_2 and N_2 was obtained from Suárez-Iglesias et al. (2015). That for O_2 was obtained from Hellmann (2023).

17.1.4 Assumptions

This model assumes standard atmospheric pressure (101325 Pa).

17.1.5 Model Validation

The validation ranges of the model by Burgess Jr. (2024) are summarised in Table 17.2.

Table 17.2: Self-diffusion coefficent model validation ranges.

Model	Systems	Composition	Temperature (K)	Pressure (Pa)
Unary	Ar	pure	$70 - 420$	101325
	CO	pure	$190 - 420$	101325
	CO_2	pure	$200 - 420$	101325
	H_2	pure	$20 - 350$	101325
	N_2	pure	$75 - 420$	101325
	O_2	pure	$75 - 360$	101325

Figures 17.1 to 17.6 tests the performance of the Burgess Jr. (2024) model implemented in auxi-mpp against experimental data for Ar, CO, CO_2, H_2, N_2, and O_2. All model estimates show good agreement with experimental data within the valid temperature ranges.

The deviation seen in Figure 17.3 is well above the reported valid temperature range and is therefore not unexpected. This serves as a prime example of how significant the deviation can be outside of the calibrated temperature ranges.

Most experimental data used for validation here was taken from Suárez-Iglesias et al. (2015).

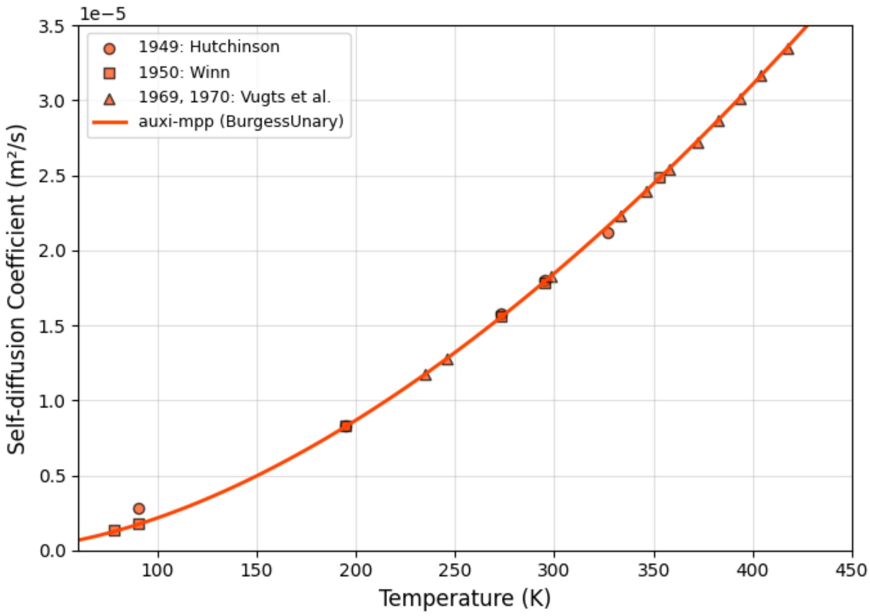

Figure 17.1: Testing the implemented model against experimental data for Ar.

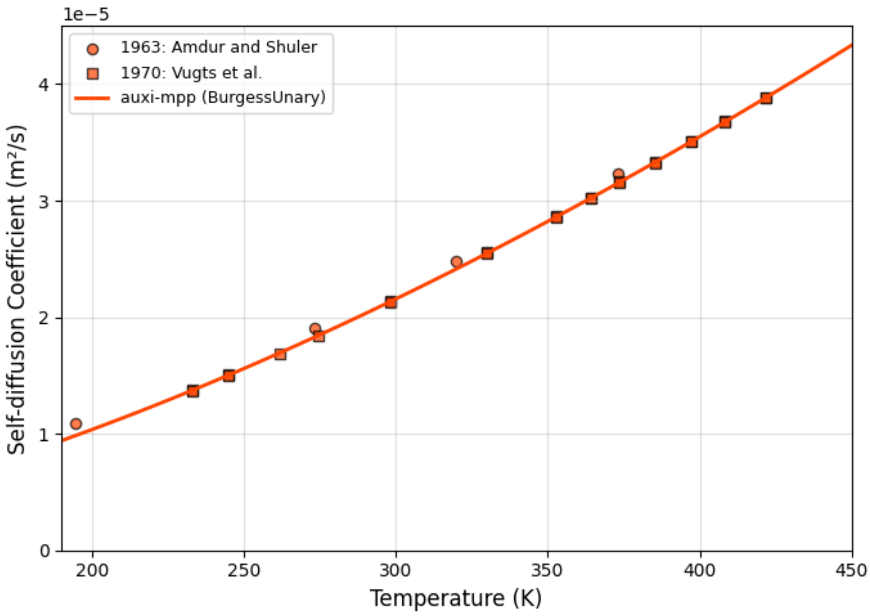

Figure 17.2: Testing the implemented model against experimental data for CO.

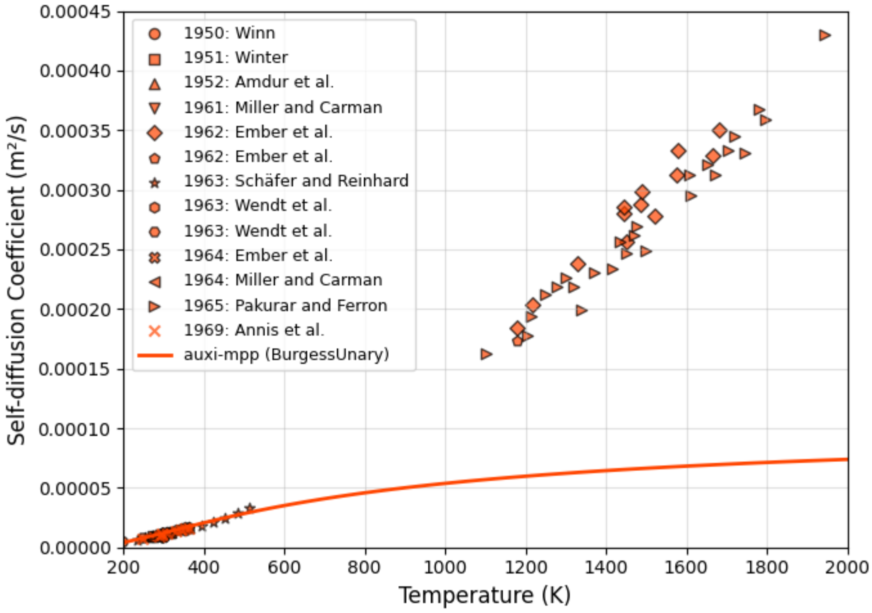

Figure 17.3: Testing the implemented model against experimental data for CO_2.

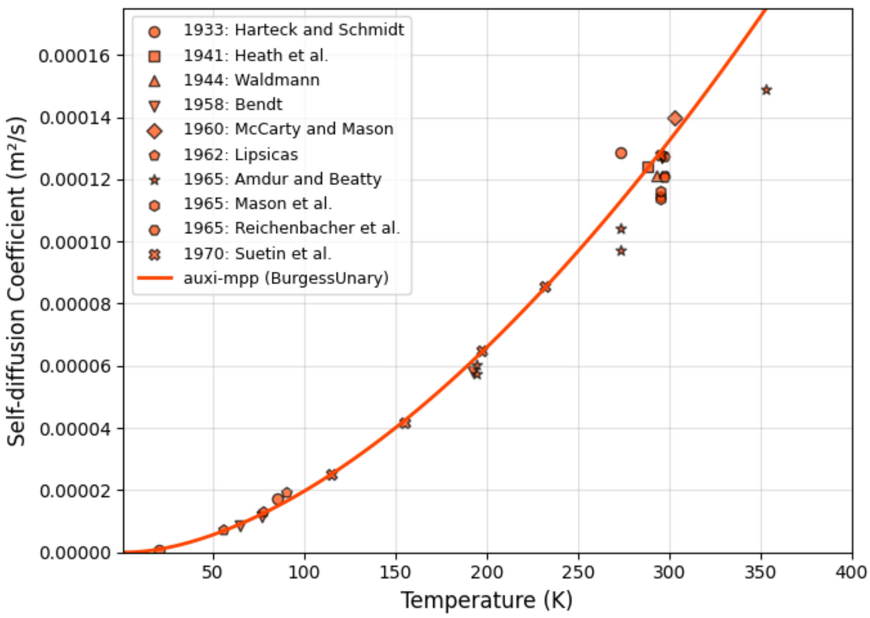

Figure 17.4: Testing the implemented model against experimental data for H_2.

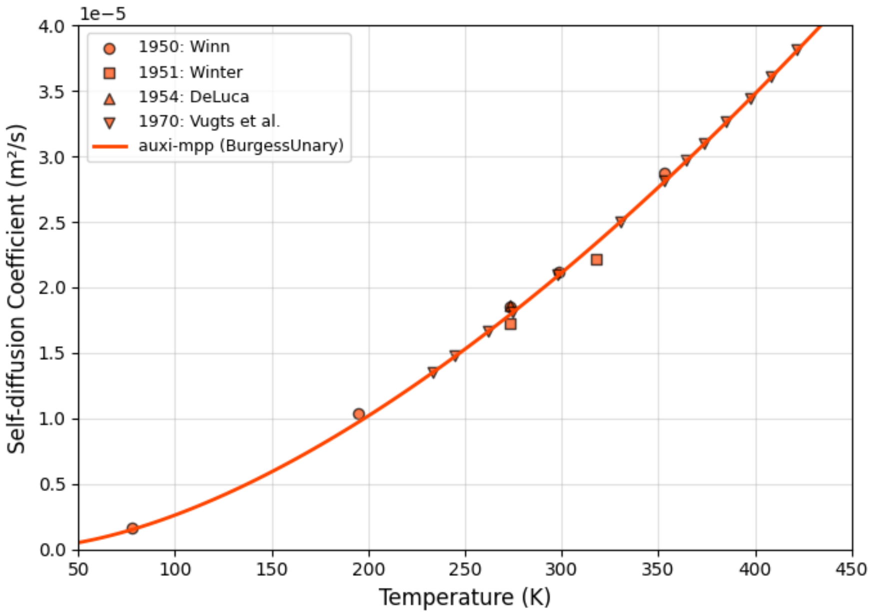

Figure 17.5: Testing the implemented model against experimental data for N_2.

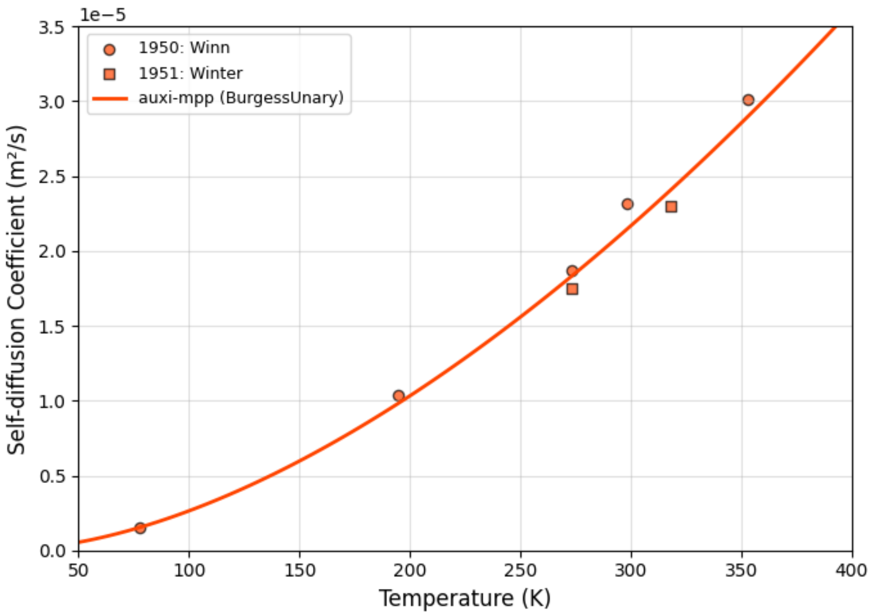

Figure 17.6: Testing the implemented model against experimental data for O_2.

Unfortunately, despite the broad valid temperature range for O_2, we could only validate the model for a limited temperature range of 40 to 350 K.

To summarise, the model could be validated, and is therefore regarded as credible, within the valid temperature ranges for all available gases, except O_2. For O_2 we recommend only using it within the range we could validat it for here.

Issues

The main issue with this model is that its temperature ranges are very narrow, as it is not usable for temperatures above 500 K. Secondly, the self-diffusion coefficient of H_2O

vapour cannot be estimated due to the lack of available parameters. These issue will have to be addressed in a future update.

17.2 Hellmann Model

This model was taken from Hellmann (2019a), Hellmann (2020a), Hellmann (2020b), Hellmann (2024), and Crusius et al. (2018) for estimating the binary diffusion coefficients of binary gas mixtures.

17.2.1 Model Overview

This model is grounded in the kinetic theory of gases, utilising the relationship between diffusion that is enhanced by thermal energy and resisted by intermolecular collisions. In other words, the binary diffusion coefficent is estimated based on the ratio between the molecular velocities and the effective collision surface area of the molecules.

Physically, the collision surface area must shrink as temperatures increase, because high-energy molecules are less susceptible to being pulled off course by attractive forces. The model captures this behaviour to ensure the results remain physically realistic across all temperature ranges. To increase accuracy, the curve for the collision cross-section was derived from rigorous quantum-chemical simulations rather than experimental data.

For engineering applications, the model simplifies the final correlation by ignoring the negligible effect of mixture concentration, treating the diffusion coefficient as a property dependent solely on the temperature and the specific pair of gases involved.

17.2.2 Model Formulation

In auxi-mpp, the binary diffusion coefficients are obtained from Equation (17.2).

$$\rho_{\mathrm{m}} D = \frac{\overline{T}^{1/2}}{10^4 \times S(\overline{T})} \tag{17.2}$$

Here, $\overline{T} = T/1\mathrm{K}$, which simply results in $\overline{T} = T$ since T is in Kelvin, and ρ_{m} is the molar density in units of $\mathrm{mol\,m^{-3}}$. The correlation function $S(\overline{T})$ is defined differently for most binary pairs as shown in Equations (17.3) to (17.6).

$S(\overline{T})$ for $CO_2 - H_2O$ and $Ar - H_2O$ from Hellmann (2019a) and Hellmann (2024) is defined as follows:

$$S(\overline{T}) = d_1 + d_2\overline{T}^{-1/6} + d_3\overline{T}^{1/3}\exp\left(-\overline{T}^{1/3}\right) + d_4\exp\left(-2\overline{T}^{1/3}\right) + d_5\exp\left(-3\overline{T}^{1/3}\right) \tag{17.3}$$

For $H_2O - N_2$ from Hellmann (2020a) it is defined as:

$$S(\overline{T}) = d_1 + d_2\overline{T}^{-1/6} + d_3\exp\left(-\overline{T}^{1/3}\right) \tag{17.4}$$

For $H_2O - O_2$ from Hellmann (2020b):

$$S(\overline{T}) = d_1 + \overline{T}^{1/6}\left[d_2 \exp\left(-\overline{T}^{1/6}\right) + d_3 \exp\left(-\overline{T}^{1/3}\right)\right] \tag{17.5}$$

And for $CO_2 - N_2$ from Crusius et al. (2018) it is defined as:

$$S(\overline{T}) = d_1 + d_2\overline{T}^{-1/6} + d_3\overline{T}^{1/6} \exp\left(-\overline{T}^{1/3}\right) \tag{17.6}$$

The parameters of these functions were fitted using first-principles calculations of the intermolecular potential energy surfaces (PES) for a given binary system. The parameters were calibrated for a temperature range of 250 to 2500 K, and are presented in Table 17.3.

To isolate the diffusion coefficient, the molar density is calculated using the gas density model in auxi-mpp, and is divided through Equation (17.2).

The system scope of the this model is limited by the availablity of binary pair parameters. The systems for which parameters could be obtained are $Ar - H_2O$, $CO_2 - H_2O$, $H_2O - N_2$, $H_2O - O_2$ and $CO_2 - N_2$.

17.2.3 Variable Declarations

The interaction parameters required in Equation (17.3) is provided in Table 17.3.

Table 17.3: Interaction parameters for binary gases.

Pair	d_1	d_2	d_3	d_4	d_5
$CO_2 - H_2O$	-0.09647	4.8695	103.70	-40400.0	2176400.0
$Ar - H_2O$	-0.22758	4.5498	21.056	0.0	0.0
$H_2O - N_2$	-0.17076	4.2835	148.37	0.0	0.0
$H_2O - O_2$	0.56998	4.3982	51.149	0.0	0.0
$CO_2 - N_2$	0.10261	5.5239	94.161	0.0	0.0

The parameters for $CO_2 - H_2O$, $Ar - H_2O$, $H_2O - N_2$ and $H_2O - O_2$ was obtained from Hellmann (2019a), Hellmann (2024), Hellmann (2019b) and Hellmann (2020b), respectively. Parameters for $CO_2 - N_2$ were obtained from Crusius et al. (2018).

17.2.4 Assumptions

In this model the following assumptions are made:

1. It assumes the dilute gas limit and therefore only considers two-body collisions between the gas molecules.
2. The molecules are treated as rigid rotors, meaning their internal bond lengths and angles are fixed at specific values and do not distort or vibrate during collisions.
3. The mathematical correlation assumes that the binary diffusion coefficient is entirely independent of the mixture's composition.

17.2.5 Model Validation

The validation ranges of the model by Hellmann (2019a) are summarised in Table 17.4.

Table 17.4: Binary diffusion coefficent model validation ranges.

Model	Systems	Composition	Temperature (K)	Pressure (Pa)
Binary	$Ar-H_2O$	$x_{Ar} = 0.5$	$300 - 2000$	101325
	H_2O-O_2	$x_{O_2} = 0.5$	$300 - 2000$	101325
	CO_2-H_2O	$x_{CO_2} = 0.2, 0.5, 0.8$	$300 - 2000$	101325
	H_2O-N_2	$x_{N_2} = 0.2, 0.5, 0.8$	$300 - 2000$	101325
	CO_2-N_2	$x_{CO_2} = 0.1 - 0.9$	$300 - 2000$	101325

The model by Hellmann (2019a) are validated in Figures 17.7 to 17.11.

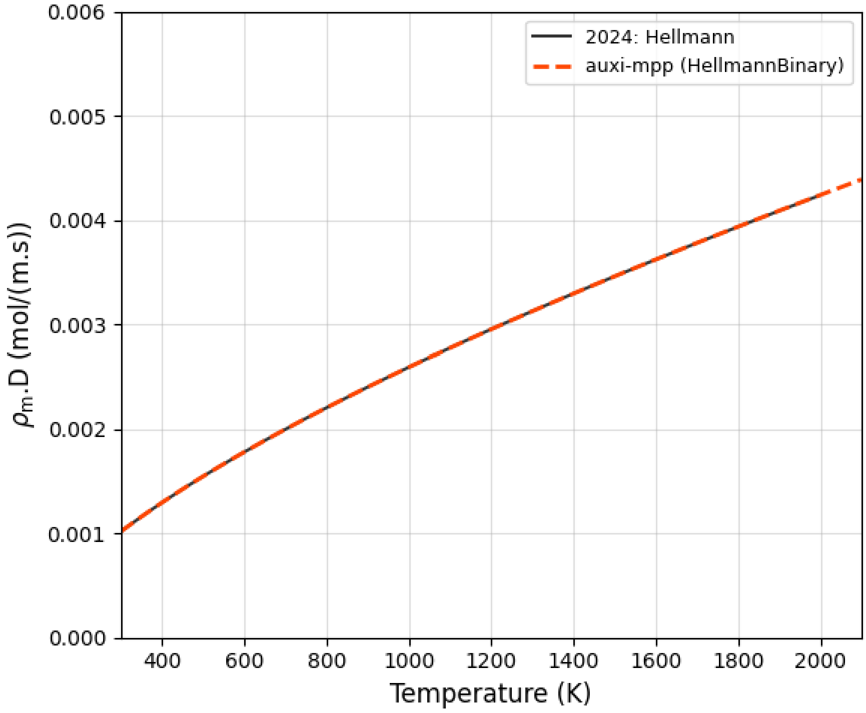

Figure 17.7: Testing the implemented model against reference data for $Ar-H_2O$: $x_{Ar} = 0.5$.

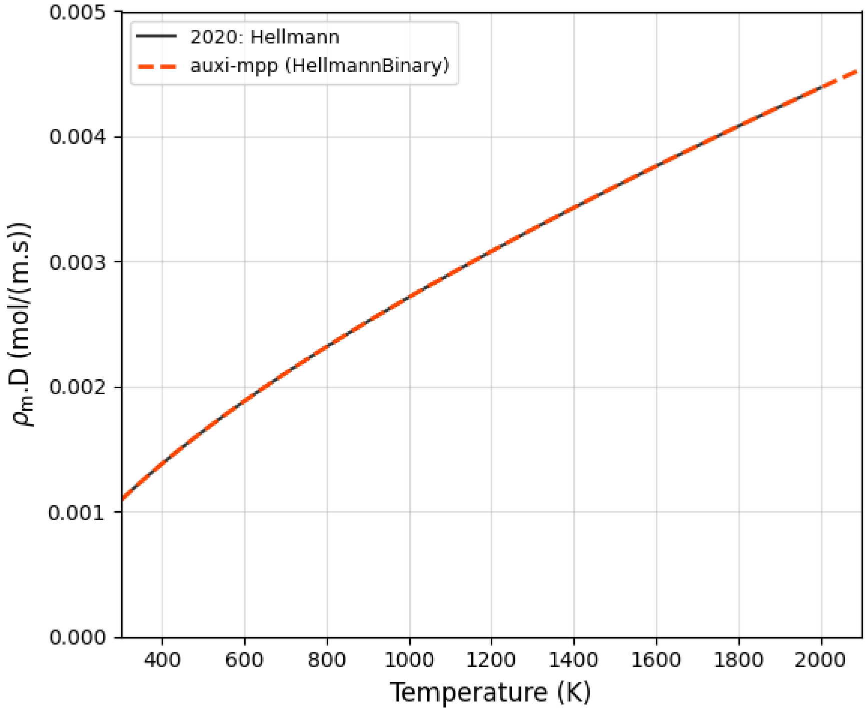

Figure 17.8: Testing the implemented model against reference data for H_2O-O_2: $x_{O_2} = 0.5$.

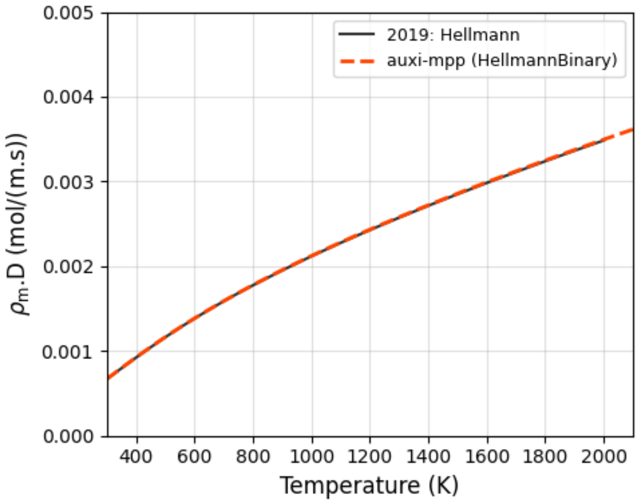

(a) $x_{\mathrm{CO_2}} = 0.2$

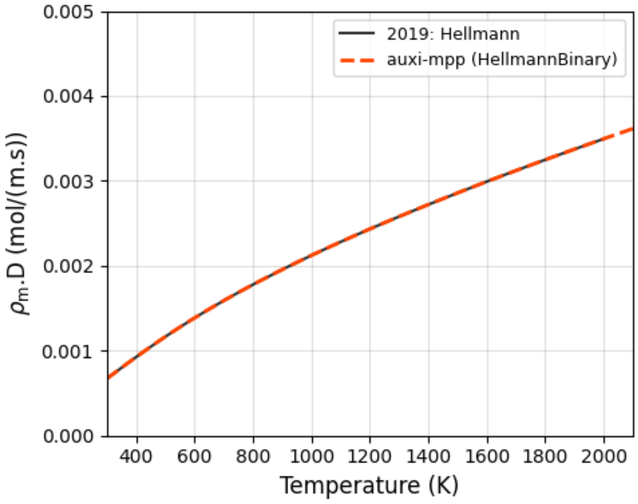

(b) $x_{\mathrm{CO_2}} = 0.5$

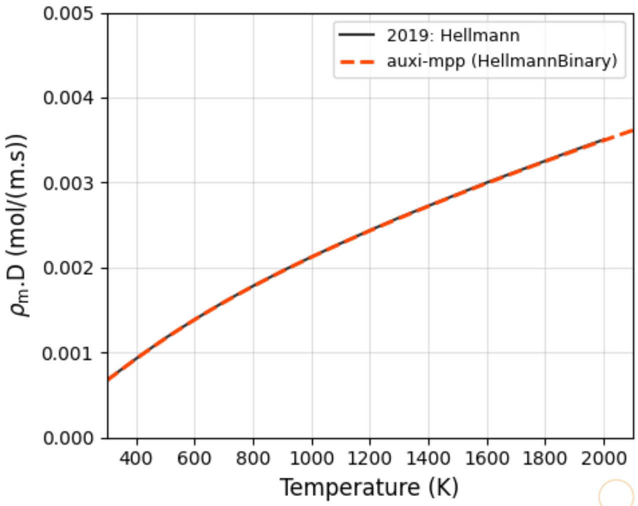

(c) $x_{\mathrm{CO_2}} = 0.8$

Figure 17.9: Testing the implemented model against reference data for $CO_2 - H_2O$.

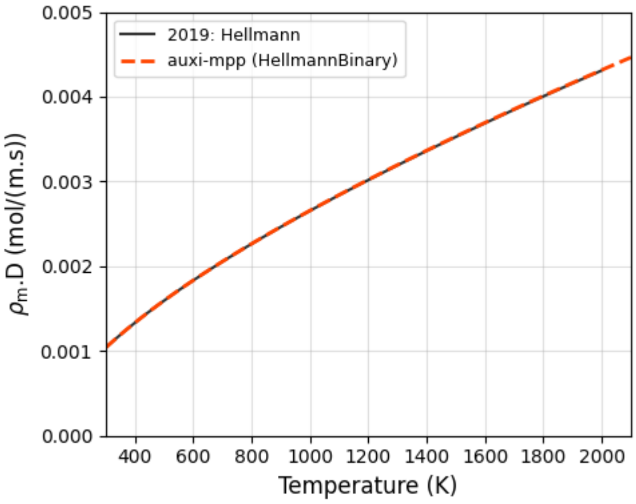

(a) $x_{\mathrm{N_2}} = 0.2$

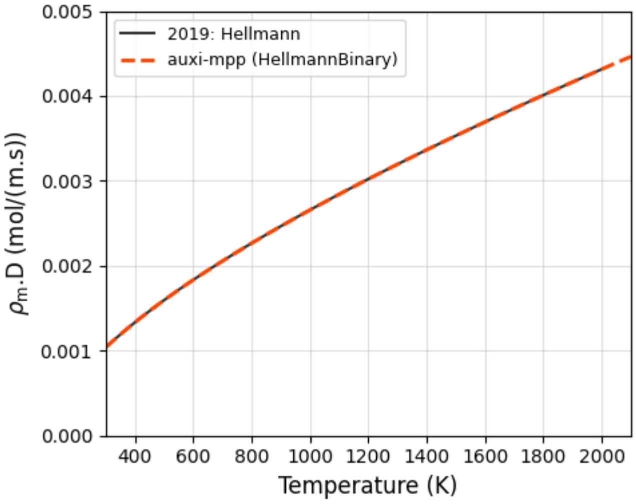

(b) $x_{\mathrm{N_2}} = 0.5$

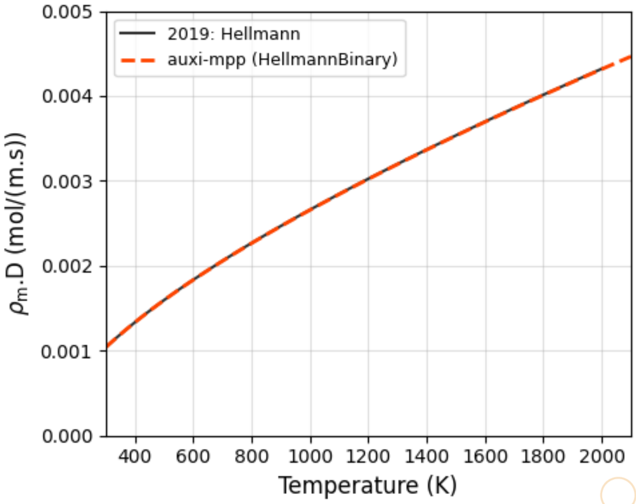

(c) $x_{\mathrm{N_2}} = 0.8$

Figure 17.10: Testing the implemented model against reference data for H_2O – N_2.

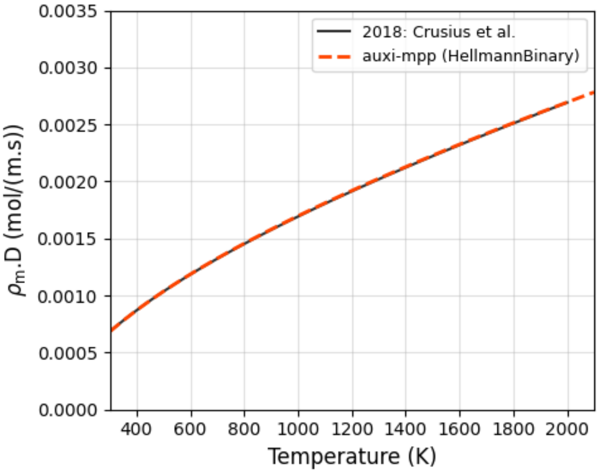

(a) $x_{\mathrm{CO_2}} = 0.1$

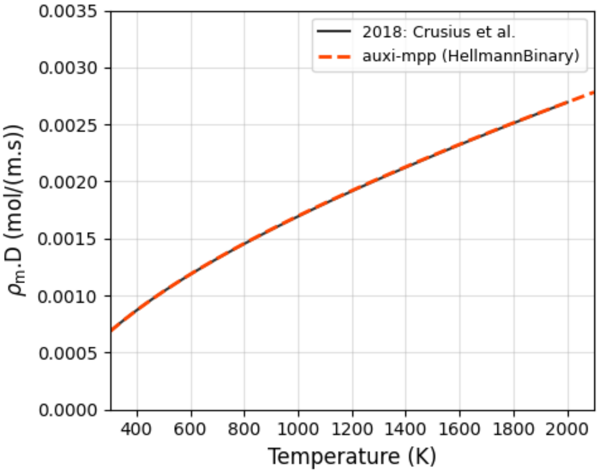

(b) $x_{\mathrm{CO_2}} = 0.2$

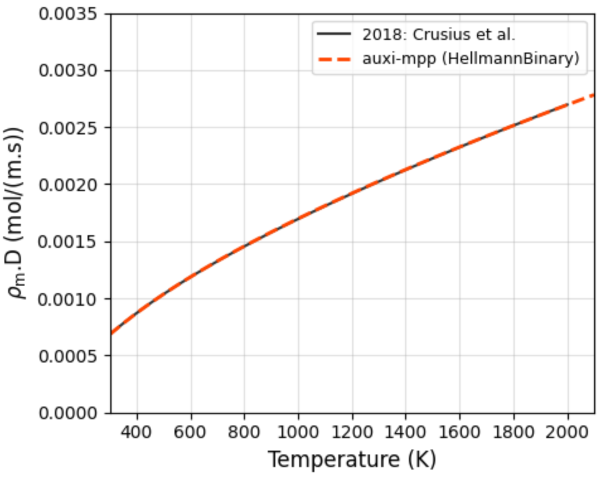

(c) $x_{\mathrm{CO_2}} = 0.4$

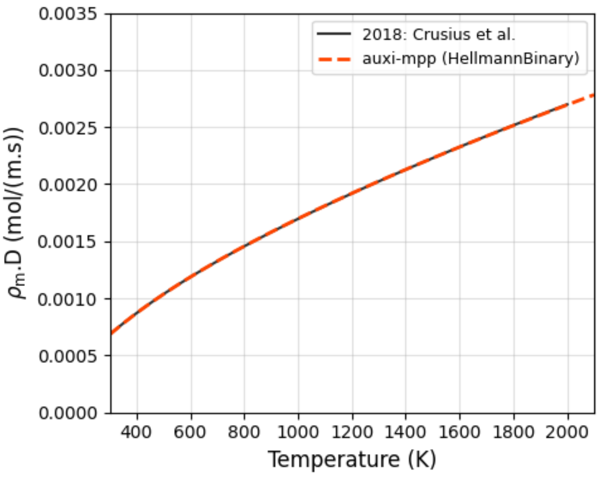

(d) $x_{\mathrm{CO_2}} = 0.6$

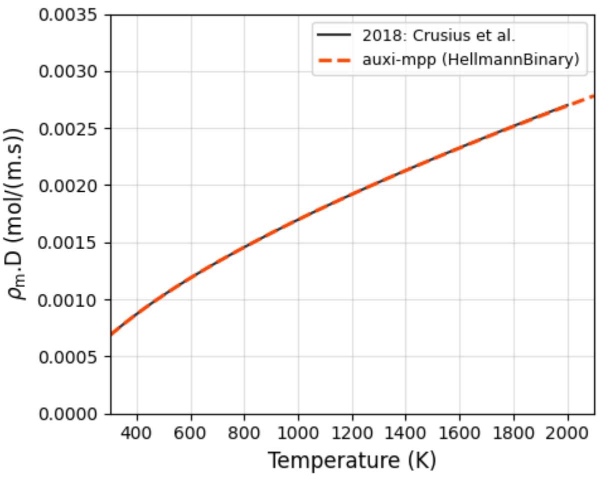

(e) $x_{\mathrm{CO_2}} = 0.8$

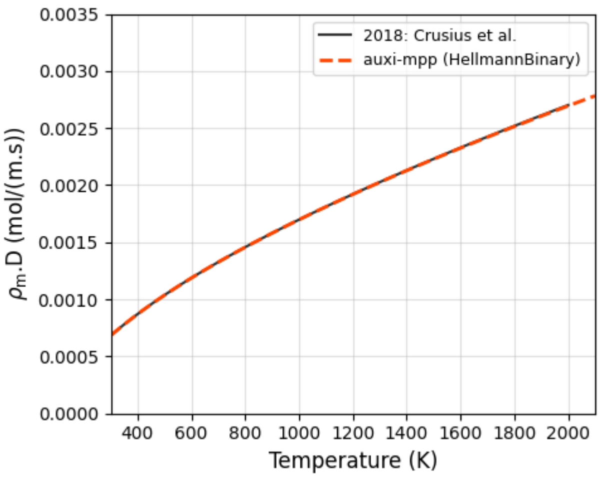

(f) $x_{\mathrm{CO_2}} = 0.9$

Figure 17.11: Testing the implemented model against reference data for CO_2 – N_2.

From Figures 17.9 to 17.11 it is clear that the mixture composition has indeed a negligible effect on $\rho_{\mathrm{m}} D$.

From the figures presented here we regard the validation to be succesfull and we therefore see this model as credible.

Issues

The model is limited to a small number of binary gas mixtures. This will have to be addressed in a future update.

Chapter 18

Thermal Conductivity

Gas thermal conductivity is the primary mechanism for heat transfer across the stagnant gas layers that form adjacent to the containers' walls. It is therefore important to complete the energy balance for the freeboard gas inside the furnace, as well as for designing off-gas systems for gases at very high temperatures.

Thermal conductivity in a gas arises from atomic or molecular collisions transferring kinetic energy from one molecule to another. According to the kinetic theory of gases, as molecules move and collide, they transfer energy associated with their translational, rotational, and vibrational modes. Because the efficiency of this transfer depends on molecular weight, collision cross-sections, and intermolecular forces, every gas species exhibits a distinct conductivity profile that varies non-linearly with temperature.

For practical engineering simulations, treating conductivity as a constant is insufficient due to the wide temperature ranges and evolving chemical compositions inherent to furnace operations. Instead, for use in computational models, the gas thermal conductivity should be computed dynamically. This chapter unpacks the models implemented in auxi-mpp to approximate these values.

The callable modules implemented in auxi-mpp to estimate the thermal conductivity of a gas mixture are composed of pure component correlations from various authors and a mixture rule by Mason and Saxena (1958). As the best performing pure gas correlation was selected for each pure gas, the final unary model is a combination of models from different authors, hence the name `ChungLemmonHuberAssaelUnary`.

It should be noted that the `MasonSaxenaMulti` model could not be validated due to a lack of experimental data. However, since `MasonSaxenaBinary`, which is based on the same logic, could be validated successfully, the multi-component model is considered to be credible and therefore added to auxi-mpp.

18.1 Chung et al. Thermal Conductivity Model

This is a model developed by Chung et al. (1988) for calculating the thermal conductivity of a pure polyatomic gas. In auxi-mpp this model was implemented only for CO and CO_2.

18.1.1 Model Overview

This model relies on a modified Eucken relation that links thermal conductivity directly to viscosity and heat capacity. This captures how heat is transported, both by the physical movement of molecules (translation) and by the energy stored within their internal structures (rotation and vibration).

18.1.2 Model Formulation

The model is captured by Equation (18.1).

$$\kappa_i = \frac{3.75\mu_i \Psi_i R}{M_i} \tag{18.1}$$

Here, μ_i is the viscosity of the pure gas of species i, R is the gas constant, M_i is the molecular weight (kg mol^{-1}) and Ψ_i is a factor accounting for the heat capacity and molecular structure and is given by Equation (18.2).

$$\Psi_i = 1 + \alpha_i \frac{0.215 + 0.28288\alpha_i - 1.061\beta_i + 0.26665 Z_i}{0.6366 + \beta_i Z_i + 1.061\alpha_i \beta_i} \tag{18.2}$$

Equations (18.3) to (18.5) gives α_i, β_i and Z_i.

$$\alpha_i = (C_{vi}/R) - 3/2 \tag{18.3}$$

$$\beta_i = 0.7862 - 0.7109\omega_i + 1.3168\omega_i^2 \tag{18.4}$$

$$Z_i = 2.0 + 10.5 T_{ri}^2 \tag{18.5}$$

ω_i is the Pitzer acentric factor of the compound, and $T_{ri} = T/T_{ci}$ is the reduced temperature. ω_i and T_{ci} are given in Table 18.1.

To obtain the viscosity needed in Equation (18.1), the viscosity model implemented in auxi-mpp is deployed.

18.1.3 Variable Declaration

Despite the model by Chung et al. (1988) only being implemented for CO and CO_2 in auxi-mpp, parameters for O_2, H_2O, H_2 and N_2 are also provided in Table 18.1 for reference. The Chung et al. (1984) model was not implemented for the latter four gases, as better performing models were found for estimating their thermal conductivity.

Table 18.1: Acentric factors and critical temperatures according to NIST Chemistry Webbook (Linstrom and Mallard 2001).

Species i	Pitzer Acentric Factors (ω_i [-])	Critical Temperature (T_{ci} [K])
CO	0.0497	132.86
CO_2	0.22394	304.1282
O_2	0.0222	154.581
H_2O	0.3443	647.096
H_2	-0.219	33.145
N_2	0.0372	126.192

18.1.4 Assumptions

The following is assumed in this model.

1. The gas is sufficiently dilute such that only two-body collisions occur.
2. The modified Eucken relation is valid; (1) The thermal conductivity is directly proportional to the viscosity and inversely proportional to molecular weight. (2) Heat transfer can be decoupled into translational energy and internal energy.
3. The actual volume that the molecules occupy are negligible compared to the total volume.

18.1.5 Model Validation

In Figure 18.1, the model by Chung et al. (1988) was validated for CO and CO_2. Unfortunately, the validation for CO is limited to a range of only 298 to 500 K. The validation ranges are captured in Table 18.2.

Table 18.2: Thermal Conductivity model by Chung et al. (1988) Validation Ranges

Model	Systems	Composition	Temperature (K)	Pressure (Pa)
Unary	CO	pure	$298 - 500$	101325
	CO_2	pure	$298 - 2000$	101325

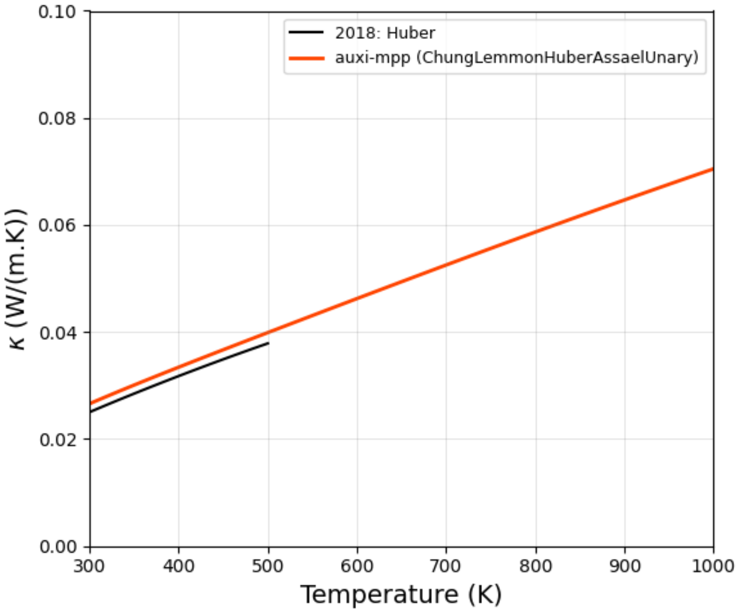

(a) CO

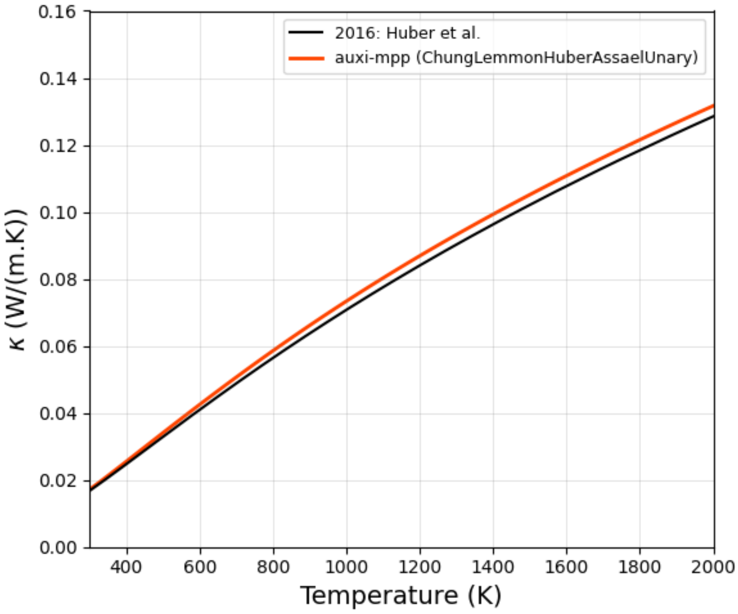

(b) CO_2

Figure 18.1: Testing auxi-mpp's implemented Chung et al. (1988) model against data from Huber et al. (2016) and Huber (2018b) as presented by NIST Chemistry WebBook 2025.

There are slight deviations from the performance of the Huber models as presented by NIST Chemistry WebBook (Linstrom and Mallard 2001). However, these deviations are not seen as significant enough to render the model inadequate; we therefore regard the model as credible within the temperature ranges for which we have literature data, as summarised in Table 18.2.

Issues

The model could only be validated for CO over a very limited temperature range. Due to time constraints we were unable to collect more data, so a full validation was postponed to a future update.

18.2 Lemmon and Jacobsen Model

This is a model developed by Lemmon and Jacobsen (2004) to estimate the thermal conductivity of N_2, O_2 and Ar.

18.2.1 Model Overview

In the dilute gas limit, which was implemented in auxi-mpp, the model by Lemmon and Jacobsen (2004) determines thermal conductivity solely as a function of temperature, utilising the Chapman-Enskog kinetic theory solution. The authors used a physically robust formulation based on collision integrals, which allows for accurate extrapolation to high temperatures where experimental data is often unavailable.

The model distinguishes between the simple translational energy transfer and the more complex internal rotational and vibrational contributions required for polyatomic molecules. By fitting coefficients to the most reliable low-density experimental measurements, this approach establishes a high-precision baseline that isolates intrinsic molecular heat transfer mechanisms independent of the density-driven effects found in high-pressure regimes.

The model operates at standard pressure and no pressure dependence was built in.

18.2.2 Model Formulation

The dilute gas limit as determined by Lemmon and Jacobsen (2004) is defined in Equation (18.6).

$$\kappa^0 = N_1 \left[\frac{\mu^0(T)}{1\ \mu\text{Pa} \cdot \text{s}} \right] + N_2 \tau^{t_2} + N_3 \tau^{t_3}, \tag{18.6}$$

Here, $\tau = T_c/T$ and the viscosity, $\mu^0(T)$, is in units of µPa s. The parameters used are provided in Table 18.3.

18.2.3 Variable Declaration

The parameters to be used in Equation (18.6) is summarised in Table 18.3.

Table 18.3: Parameters for N_2, O_2 and Ar

	N_2 ($T_c = 126.2$)		O_2 ($T_c = 154.6$)		Ar ($T_c = 150.7$)	
i	N_i	t_i	N_i	t_i	N_i	t_i
1	1.511	—	1.036	—	0.8158	—
2	2.117	-1.0	6.283	-0.9	-0.4320	-0.77
3	-3.332	-0.7	-4.262	-0.6	0.0	-1.0

18.2.4 Assumptions

The following is assumed in this model.

1. The gas is sufficiently dilute such that only two-body collisions occur.
2. It is assumed that N_2 and O_2 are spherical so that the collision integrals could be derived from the more simple spherical potentials.
3. It assumes that thermal conductivity can be separated into two independent contributions; translational and internal energy.

18.2.5 Model Validation

The model by Lemmon and Jacobsen (2004) was validated in Figure 18.2, and the validation ranges are summarised in Table 18.4.

Table 18.4: Thermal Conductivity model by Lemmon and Jacobsen (2004) Validation Ranges

Model	Systems	Composition	Temperature (K)	Pressure (Pa)
Unary	Ar	pure	$298 - 2000$	101325
	N_2	pure	$298 - 2000$	101325
	O_2	pure	$298 - 2000$	101325

From Figure 18.2, we regard this model as successfully validated.

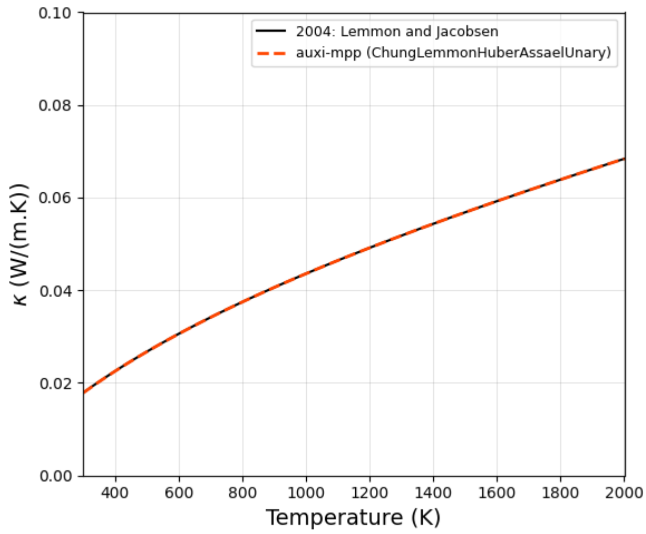

(a) Ar

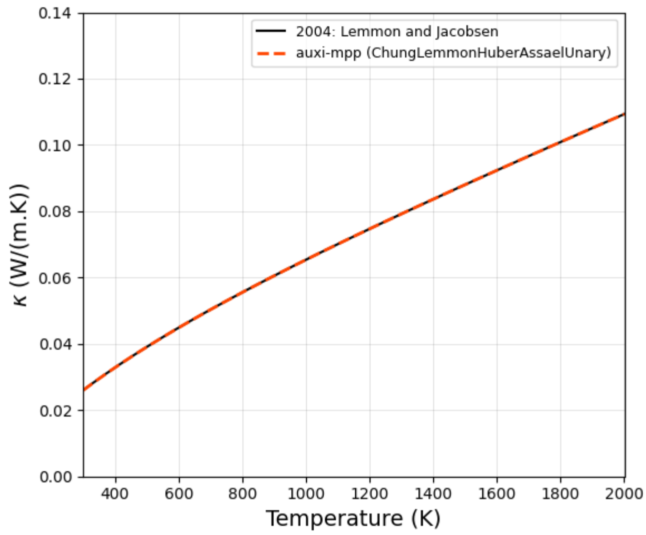

(b) N_2

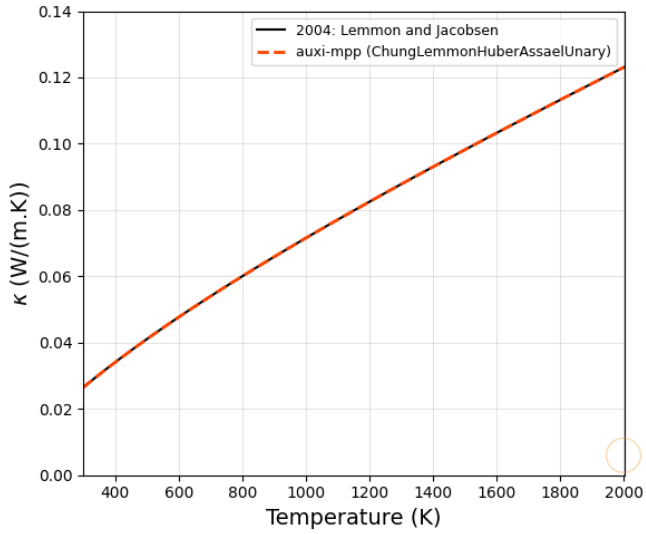

(c) O_2

Figure 18.2: Testing auxi-mpp's implemented Lemmon and Jacobsen (2004) model against its performance as presented by NIST Chemistry WebBook 2025.

18.3 Huber et al. Thermal Conductivity Model

This model by Huber et al. (2012) was specifically developed for H_2O vapour.

18.3.1 Model Overview

In the dilute gas limit, which was implemented here, the Huber et al. (2012) model calculates thermal conductivity purely as a function of temperature. This formulation implicitly incorporates the significant contributions of rotational energy and the strong dipole-dipole interactions characteristic of the water molecule.

To achieve high accuracy, the authors abandoned purely theoretical collision integrals in favour of an interpolating equation fitted to a rigorously screened set of experimental data and high-level theoretical calculations. This creates a baseline conductivity curve that scales with temperature, representing molecular velocity, modified by a polynomial expansion to capture the temperature dependence of the molecule's effective cross-section.

The model operates at standard pressure and no pressure dependence was built in.

18.3.2 Model Formulation

This model is described by Equation (18.7).

$$\kappa_0 = \frac{\sqrt{T_r}}{\sum_{k=0}^{4} \frac{L_k}{T_r^k}} \tag{18.7}$$

Here, $T_r = T/T_c$, where T_c is the critical temperature, and the polynomial coefficients, L_k, are given in Table 18.5.

18.3.3 Variable Declaration

Table 18.5: Coefficients in Equation (18.7).

k	L_k
0	$2.443\,221 \times 10^{-3}$
1	$1.323\,095 \times 10^{-2}$
2	$6.770\,357 \times 10^{-3}$
3	$-3.454\,586 \times 10^{-3}$
4	$4.096\,266 \times 10^{-4}$

18.3.4 Assumptions

The following is assumed in this model.

1. The gas is sufficiently dilute such that only two-body collisions occur.

2. It is assumed that the structural and polarity effects of water are sufficiently captured by fitting a polynomial to data.
3. Since experimental data is scarce above 1000 K, it is assumed that thermal conductivity values derived from theoretical calculations are an accurate proxy for high-temperature regions.
4. It assumes that the effect of dissociating H_2O molecules at very high temperatures is negligible.

18.3.5 Model Validation

The model by Huber et al. (2012) was validated in Figure 18.3, and the validation ranges are summarised in Table 18.6.

Table 18.6: Thermal Conductivity model by Huber et al. (2012) Validation Range

Model	Systems	Composition	Temperature (K)	Pressure (Pa)
Unary	H_2O	pure	$373 - 1350$	101325

From Figure 18.3 we regard this model as successfully validated. It should be noted, however, that the validation only extends up to 1350 K.

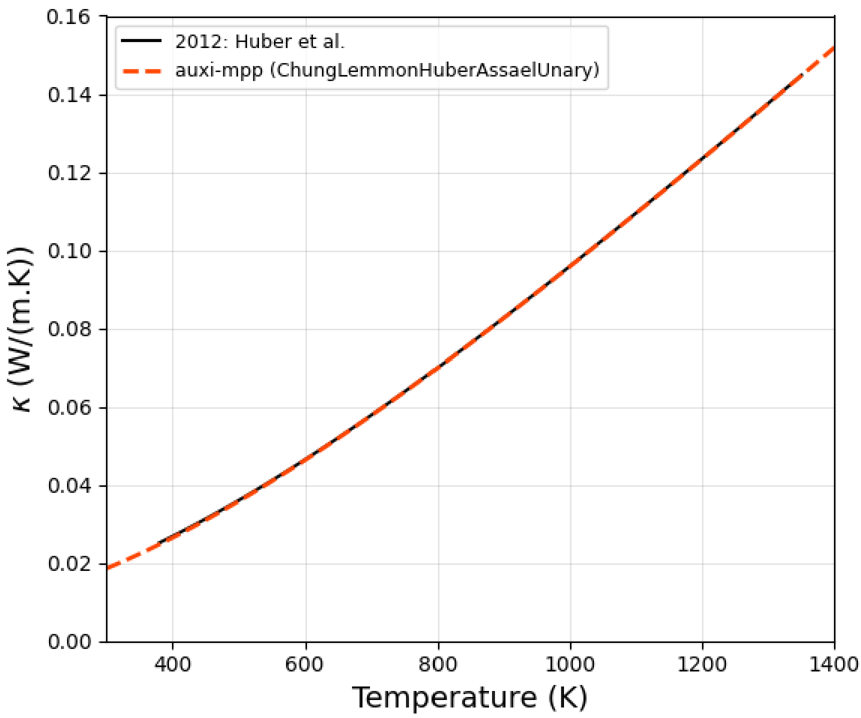

(a) H_2O

Figure 18.3: Testing auxi-mpp's implemented Huber et al. (2012) model against its performance as presented by NIST Chemistry WebBook 2025.

18.4 Assael et al. Thermal Conductivity Model

This model by Assael et al. (2011) was developed specifically to estimate the thermal conductivity of H_2 gas.

18.4.1 Model Overview

Only the dilute gas limit was implemented here as well. In this limit, the model determines thermal conductivity strictly as a function of temperature by fitting a polynomial equation to high-accuracy theoretical data. Rather than relying solely on experimental measurements, the authors adopted values calculated by a full quantum-mechanical formalism and a spherical intermolecular potential. To make these complex theoretical results usable for engineering applications, Assael et al. (2011) represented them using a functional form consisting of polynomials.

The model operates at standard pressure and no pressure dependence was built in.

18.4.2 Model Formulation

The model is described by eq. (18.8).

$$\kappa_0 = \frac{\sum_{i=0}^{m} A_{1,i}(T/T_c)^i}{\sum_{i=0}^{n} A_{2,i}(T/T_c)^i} \tag{18.8}$$

18.4.3 Variable Declaration

The $A_{n,i}$ coefficients are given in Table 18.7.

Table 18.7: Coefficients of Equation (18.8) for hydrogen.

i	$A_{1,i}$	$A_{2,i}$
0	$-3.409\,76 \times 10^{-1}$	$1.384\,97 \times 10^{2}$
1	$4.588\,20 \times 10^{0}$	$-2.218\,78 \times 10^{1}$
2	$-1.450\,80 \times 10^{0}$	$4.571\,51 \times 10^{0}$
3	$3.263\,94 \times 10^{-1}$	$1.000\,00 \times 10^{0}$
4	$3.169\,39 \times 10^{-3}$	
5	$1.905\,92 \times 10^{-4}$	
6	$-1.139\,00 \times 10^{-6}$	

18.4.4 Assumptions

The following is assumed in this model.

1. The gas is sufficiently dilute such that only two-body collisions occur.

2. It assumes that theoretical values derived from a full quantum-mechanical formalism provide a more accurate basis for the correlation than the scarce experimental data available at extreme temperatures.

18.4.5 Model Validation

The model by Assael et al. (2011) was validated in Figure 18.4, and the validation ranges are summarised in Table 18.8. Unfortunately, the validation range only extends up to 1000 K.

Table 18.8: Validation Ranges for the Thermal Conductivity model by Assael et al. (2011)

Model	Systems	Composition	Temperature (K)	Pressure (Pa)
Unary	H_2	pure	$298 - 1000$	101325

From Figure 18.4, we regard this model as successfully validated for the specified temperature range.

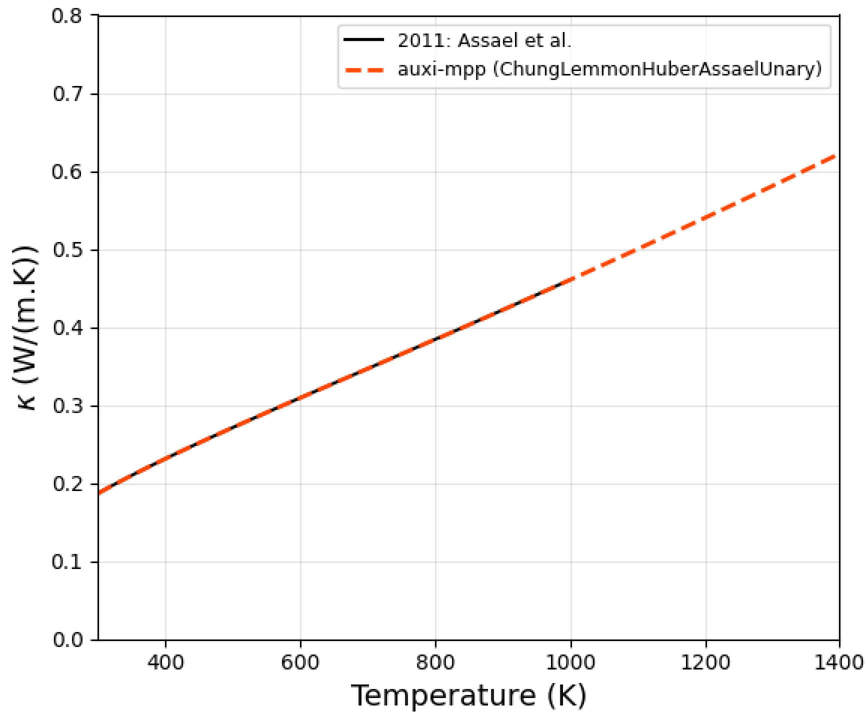

(a) H_2

Figure 18.4: Testing auxi-mpp's implemented Assael et al. (2011) model against its performance as presented by NIST Chemistry WebBook 2025.

18.5 Mason and Saxena Mixture Rule

A mixture rule developed by Mason and Saxena (1958) to estimate the thermal conductivity of gas mixtures from that of the mixture components in their pure form.

18.5.1 Model Overview

This mixing rule estimates the thermal conductivity of a gas mixture by treating it as a weighted sum of that of the pure components, correcting for how different molecules interfere with each other's heat transfer. Rather than taking the average, the model calculates a specific interaction factor (G_{ik}) for every pair of gases in the mixture. This factor determines how the presence of one gas impacts the ability of another to conduct heat, effectively modelling the physical dynamics of collisions in the mixture.

To calculate this interaction, the model relies on the ratio of the *frozen* thermal conductivities of the components. The *frozen* thermal conductivity is a theoretical value representing how well the gas would conduct heat if its molecules only had translational energy without rotations or vibrations. By comparing the *frozen* conductivities of the two species in each pair, as well as their molecular weights, the model isolates the fundamental translational energy transfer between the colliding pair.

18.5.2 Model Formulation

The mixing rule developed by Mason and Saxena (1958) is given in Equation (18.9).

$$\kappa_{\text{mix}} = \sum_{i=1}^{n} \kappa_i \left[1 + \sum_{\substack{k=1 \\ k \neq i}}^{n} G_{ik} \frac{x_k}{x_i} \right]^{-1} \tag{18.9}$$

Here, n is the number of species in the gas mixture and the interaction parameter between species i and k is given by Equation (18.10).

$$G_{ik} = \frac{1.065}{2\sqrt{2}} \left(1 + \frac{M_i}{M_k} \right)^{-\frac{1}{2}} \left[1 + \left(\frac{\kappa_i^\circ}{\kappa_k^\circ} \right)^{\frac{1}{2}} \left(\frac{M_i}{M_k} \right)^{\frac{1}{4}} \right]^2 \tag{18.10}$$

κ° is the so-called *frozen* thermal conductivity, which is the thermal conductivity where all rotational and vibrational modes of storing and transferring energy are ignored. How to calculate it is described in Equations (18.11) and (18.12).

$$\kappa_i^\circ = \kappa_i / E_i \tag{18.11}$$

$$E_i = 0.115 + 0.354(C_{pi}/R) \tag{18.12}$$

κ_i is the thermal conductivity of the mixture component in its pure form. For estimating this the unary models described earlier are deployed.

18.5.3 Variable Declaration

There are no model specific parameters to declare.

18.5.4 Assumptions

The following is assumed in this model.

1. The model assumes that the rigorous kinetic theory of multi-component gas mixtures, as formulated by Hirschfelder (1957), provides the correct theoretical basis for deriving the simplified expressions.
2. The formulation assumes that the complex ratio of collision integrals can be replaced by a single universal empirical constant of 1.065 to correct for expansion errors across different gas pairs.
3. It assumes that thermal conductivity can be separated into two independent energy contributions; translational and internal energy.

18.5.5 Model Validation

The mixing rule by Mason and Saxena (1958) was validated in Figures 18.5 to 18.9. These validation ranges are summarised in Table 18.9.

Table 18.9: Thermal Conductivity Mixing Rule by Mason and Saxena (1958) Validation Ranges

Model	Systems	Composition	Temperature (K)	Pressure (Pa)
Binary	$CO_2 - N_2$	$x_{CO_2} = 0.1 - 0.9$	$300 - 2000$	101325
	$CO_2 - N_2$	$x_{CO_2} = 0 - 1$	$323 - 961$	101325
	$CO_2 - N_2$	$x_{CO_2} = 0.25, 0.5, 0.75$	$300 - 1100$	101325
	$H_2 - N_2$	$x_{N_2} = 0 - 1$	273	101325
	$O_2 - N_2$	$x_{O_2} = 0 - 1$	295	101325
	$H_2O - O_2$	$x_{H_2O} = 0.25, 0.5$	$400 - 1000$	101325

Unfortunately, this mixture rule could not be validated for all binary combinations of CO, CO_2, H_2O, O_2, H_2, N_2 and Ar.

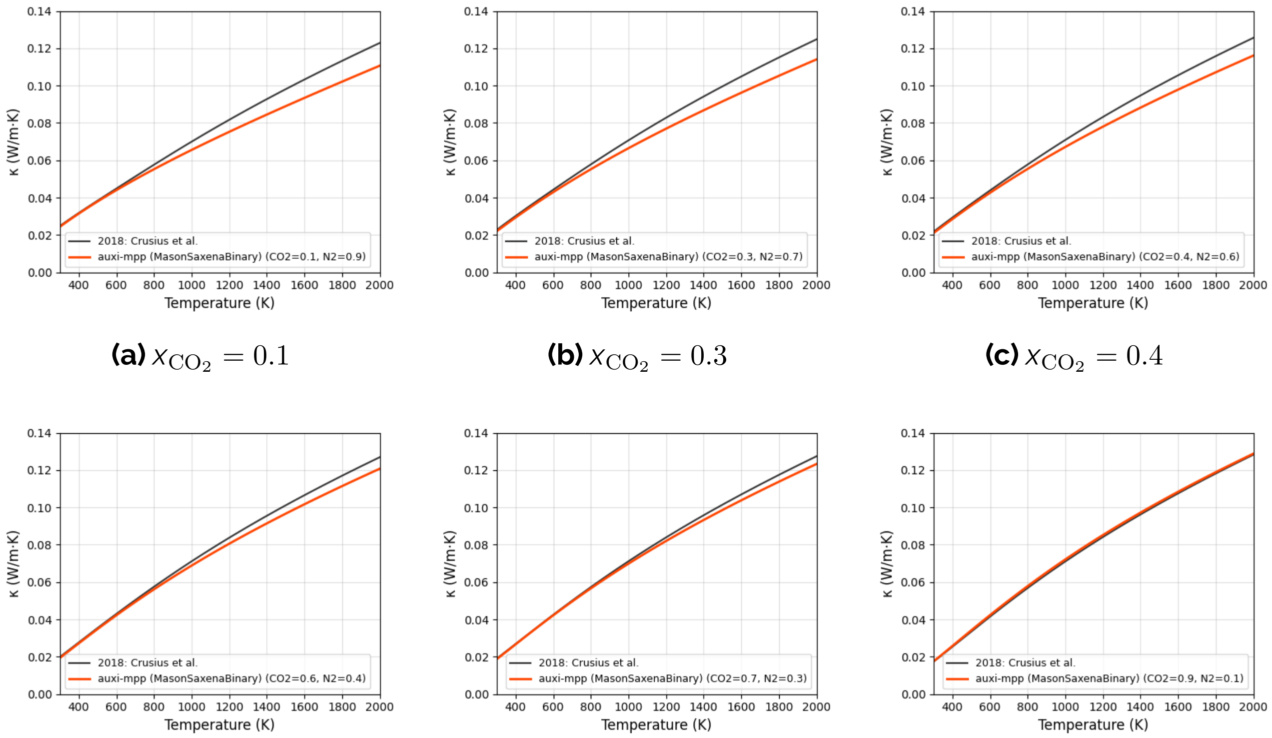

(a) $x_{\mathrm{CO_2}} = 0.1$ **(b)** $x_{\mathrm{CO_2}} = 0.3$ **(c)** $x_{\mathrm{CO_2}} = 0.4$

(d) $x_{\mathrm{CO_2}} = 0.6$ **(e)** $x_{\mathrm{CO_2}} = 0.7$ **(f)** $x_{\mathrm{CO_2}} = 0.9$

Figure 18.5: Testing auxi-mpp's implemented Mason and Saxena (1958) mixing rule against theoretically calculated data from Crusius et al. (2018).

To the data from Crusius et al. (2018) used in Figure 18.5, the recommended correction described in Equation (18.13) was made.

$$\kappa(T, x_{\mathrm{CO_2}}) = \kappa_{calc(T,x_{\mathrm{CO_2}})} \times (1.011 x_{\mathrm{CO_2}} + (1 - x_{\mathrm{CO_2}})) \tag{18.13}$$

From Figure 18.5, it seems like the mixing rule fails at high $x_{\mathrm{N_2}}$. However, comparing Figure 18.5a to Figure 18.2b, we see that the performance does approach that of the unary system as the fraction of N_2 approaches unity. The deviations here can therefore be attributed to different theories used to estimate pure component thermal conductivities, and not to the mixing rule itself. The data from Crusius et al. (2018) were calculated from fundamental theory, while the pure component thermal conductivity for N_2 and CO_2 were estimated using the models by Lemmon and Jacobsen (2004) and that of Chung et al. (1984), respectively.

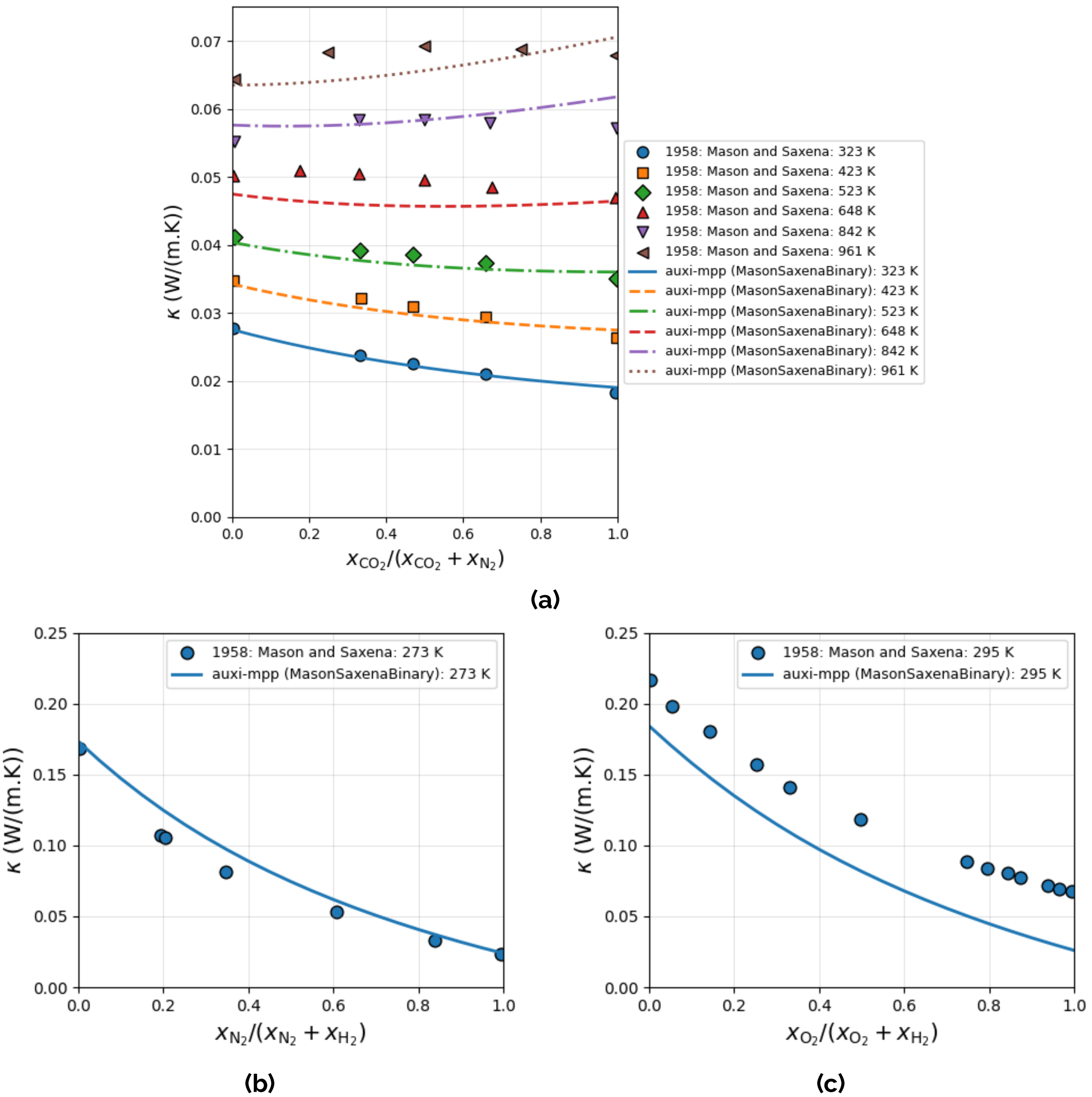

Figure 18.6: Testing auxi-mpp's implemented Mason and Saxena (1958) mixing rule against experimental data presented in the same article but from different authors.

As seen in Figures 18.6a and 18.6b, the mixing rule performs reasonably well for the binary $CO_2 - N_2$ and $H_2 - N_2$ systems. For the $CO_2 - N_2$ system, a thermal conductivity maximum arises for ~50% mixtures at high temperatures, which the mixing rule fails to account for, however.

In Figure 18.6c there is a poor match between model and data. However, comparing Figure 18.6c to Figures 18.2c and 18.4, we see that at the extremes, where $x_{O_2} = 0$ and 1, the performance corresponds to the validated unary models' performance. We therefore hypothesise that the data from Mason and Saxena (1958) is of poor quality. In short; this provides no evidence that the mixing rule is failing.

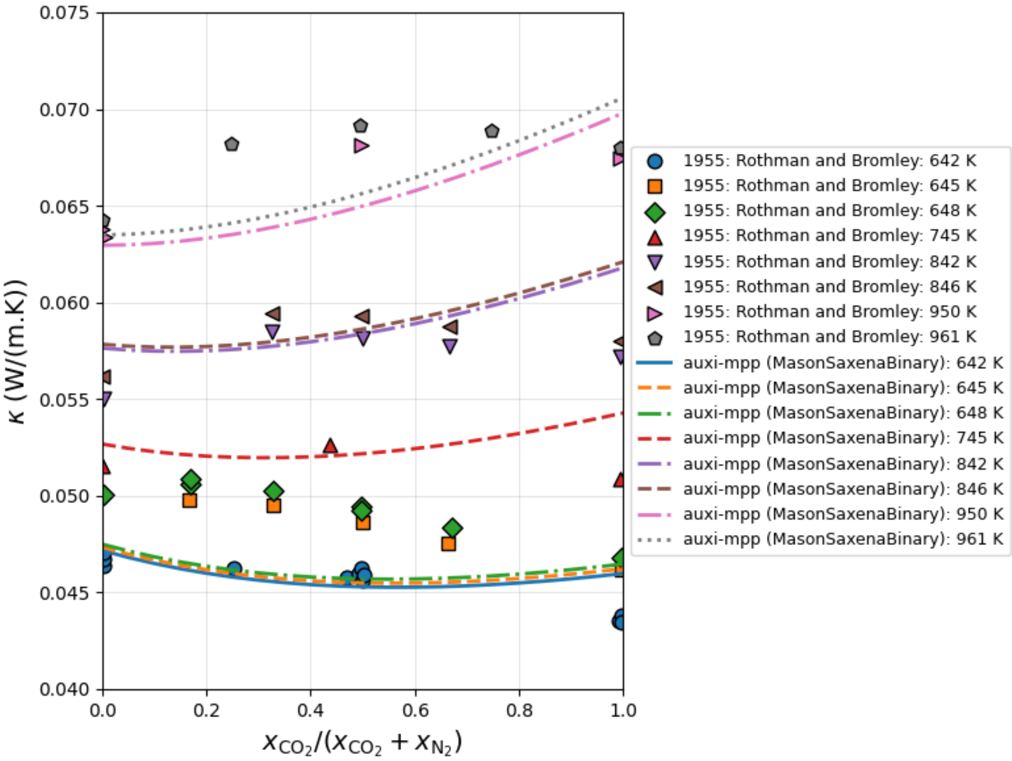

Figure 18.7: Testing auxi-mpp's implemented Mason and Saxena (1958) mixing rule against data from Rothman and Bromley (1955)

From Figure 18.7, we again observe a maximum at ∼50% mixtures of $CO_2 - N_2$. Here it is not only present at higher temperatures but also at the lower temperatures. The mixing rule by Mason and Saxena (1958) fails to capture this effect. Nevertheless, the experimental data in this figure is questionable, as there is a disproportionally large deviation between the data of 642 and 648 K. We therefore cannot draw strong conclusions from this comparison.

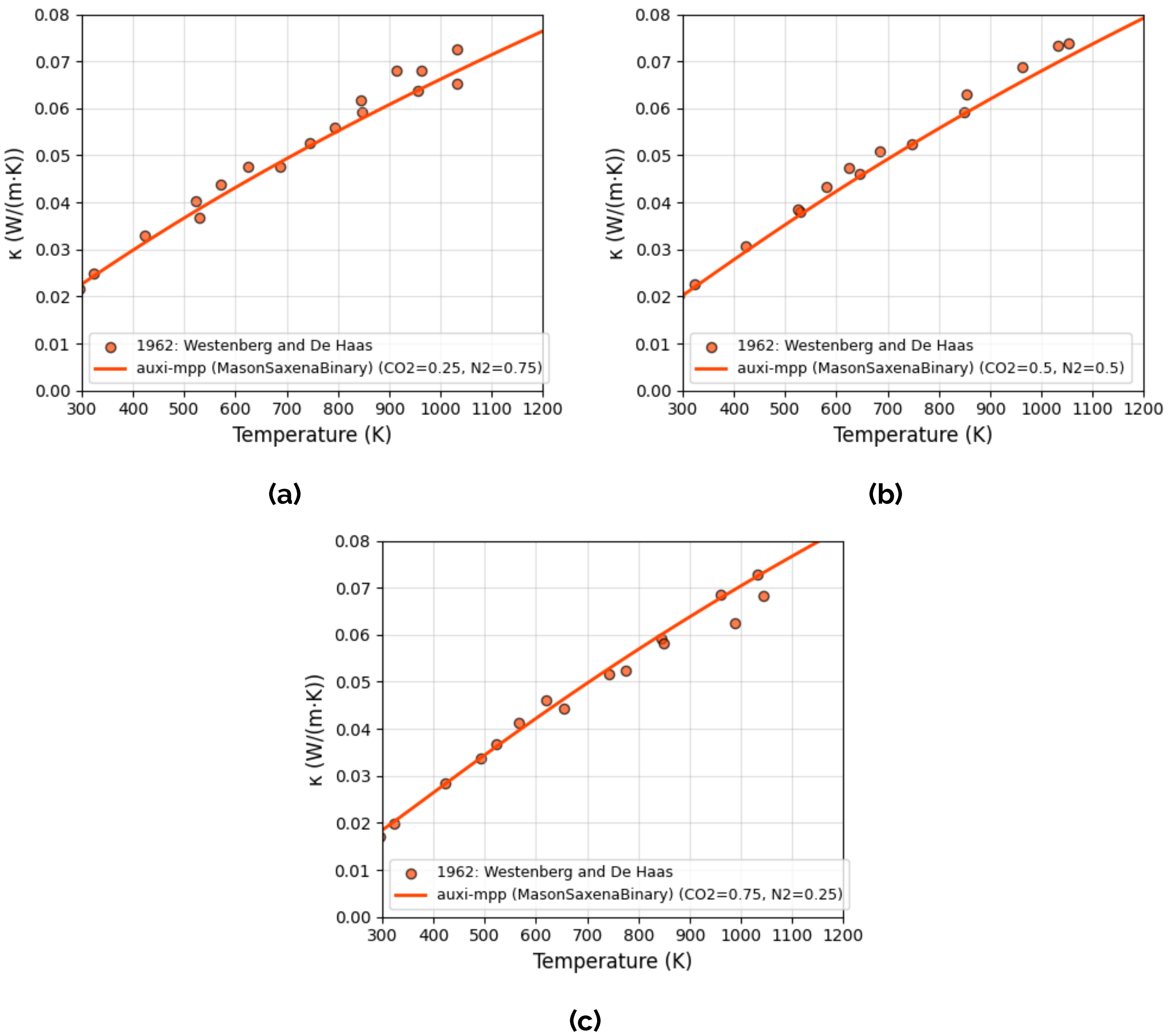

Figure 18.8: Testing auxi-mpp's implemented Mason and Saxena (1958) mixing rule against experimental data from Westenberg and DeHaas (1962).

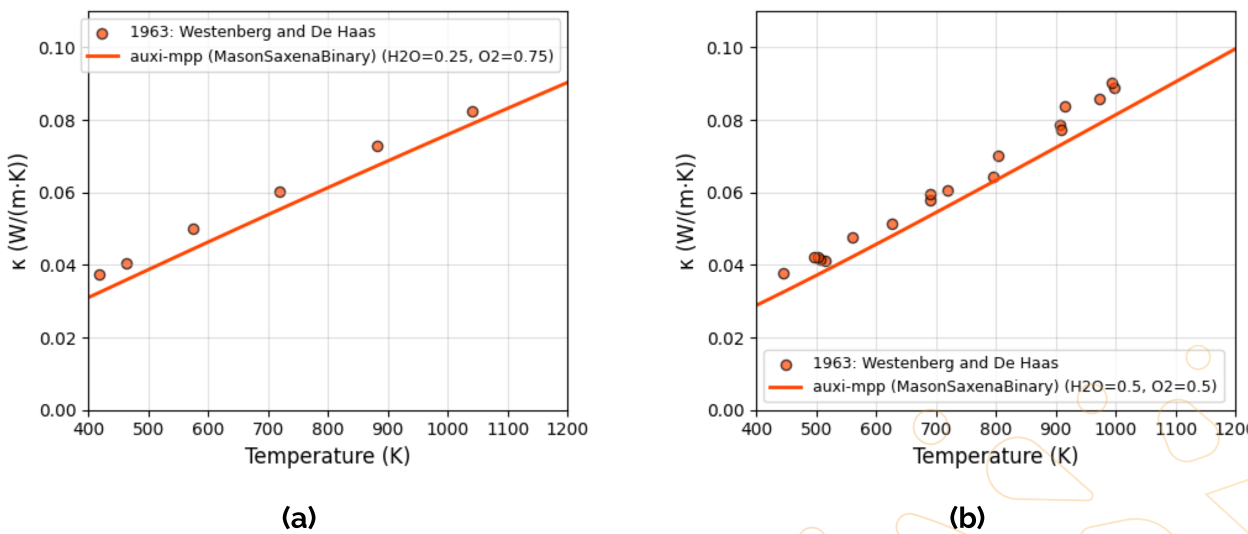

Figure 18.9: Testing auxi-mpp's implemented Mason and Saxena (1958) mixing rule against experimental data from Westenberg and De Haas (1963).

When comparing the model against the data from Westenberg and DeHaas (1962), the mixing rule does adequately estimate the thermal conductivity of a 50% CO_2 – N_2 mixture at higher temperatures. Figures 18.8 and 18.9 are compelling evidence that this mixture model does indeed perform well.

Based on all data presented, we regard this mixture model as successfully validated for at least binary systems.

Issues

Due to time constraints, the mixing rule could not be validated for all combinations of binary gas mixtures. And due to a lack of data, the mixture rule could not be validated for ternary (multi-component) mixtures. This will have to be revisited in the future.

Chapter 19

Total Emissivity

In the simulation of high-temperature processes within auxi-mpp, radiative heat transfer is governed by a material's emissivity. While idealised physics utilises the concept of a "blackbody"—a perfect emitter across all wavelengths—real-world materials, especially gases, exhibit complex, non-ideal behaviour. Thermal radiation arises from the transition of atoms and molecules between discrete energy states as dictated by quantum mechanics. Because every chemical compound possesses a unique molecular structure, each has a unique set of quantum transitions it can undergo. This results in a unique "spectral fingerprint" for every material, where radiation is emitted predominantly within specific wavelength regions known as spectral bands, rather than continuously across the spectrum. A spectral band, in turn, is composed of a multitude of spectral lines, each line representing an allowed quantum transition.

For practical engineering simulations, computing radiative exchange at every spectral line is often computationally prohibitive. Instead, the dimensionless total emissivity is used—an aggregate value that describes the overall efficiency of a surface's radiation compared to a blackbody. Mathematically, this is the integral of the material's spectral emissivity, which defines the emissivity at every spectral line, weighted by the Planck blackbody distribution function. This chapter unpacks the models implemented in auxi-mpp to approximate this integral.

The callable modules implemented in auxi-mpp to estimate the total emissivity of a gas are composed of two types of models. These are the Exponential Wide Band model by Edwards and Menard (1964) and Felske and Tien (1974) and a correlation chart model by Leckner (1972).

To simplify, the gases H_2, N_2 and O_2 are regarded as transparent. auxi-mpp therefore only includes total emissivity models for CO, CO_2 and H_2O vapour.

19.1 Exponential Wide Band Model

An Exponential Wide Band (EWB) model originally developed by Edwards and Menard (1964) and later improved by Felske and Tien (1974).

19.1.1 Model Overview

In this model the total emissivity is calculated from combining the emissivity of individual bands identified to be dominant for the species (also called wide bands or major absorbance bands). The emissivities of the wide bands are calculated from a set of predefined parameters which are based on experimental data.

It was found that for pure CO_2 and H_2O, this model deviates more from experimental data than the chart model by Leckner (1972), which is developed specifically for CO_2 and H_2O. This model is therefore only implemented for CO, however, all parameters for CO_2 and H_2O are still documented here.

19.1.2 Model Formulation

The basic idea is to calculate the optical thickness, τ_0, and the line overlap parameter, β, for every major absorbance band of the gas, as in Equation (19.1) and Equation (19.2). From these we calculate the total band absorptance, A, as in Equation (19.3) and Equation (19.4). To get the total emissivity of the gas, take the sum of the total absorptance of all major bands, each weighted by the black body intensity function, as shown in Equation (19.5).

$$\tau_0 = \frac{\alpha X}{\omega} \tag{19.1}$$

$$\beta = \beta_0^* \sqrt{\frac{T_0}{T}} \frac{\Phi}{\Phi_0} P_e \tag{19.2}$$

$$\begin{aligned} A^* = 2E_1\left(\sqrt{\frac{\tau_0\beta}{1+\beta/\tau_0}}\right) + E_1\left(\frac{1}{2}\sqrt{\frac{\tau_0/\beta}{1+\beta/\tau_0}}\right) \\ - E_1\left(\frac{1+2\beta}{2}\sqrt{\frac{\tau_0/\beta}{1+\beta/\tau_0}}\right) + ln\left(\frac{\tau_0\beta}{(1+\beta/\tau_0)(1+2\beta)}\right) + 2\gamma_E s \end{aligned} \tag{19.3}$$

$$A = A^*\omega \tag{19.4}$$

$$\epsilon = \sum_{i=1}^{N} \left(\frac{\pi I_{b\eta 0}}{\sigma T^4}\right)_i A_i \tag{19.5}$$

All parameters needed to calculate τ_0 and β are given in the equations below, as well as in Table 19.1.

Calculate the Optical Thickness

To calculate τ_0 in Equation (19.1), use Equation (19.6), Equation (19.11) and Equation (19.13).

$$\alpha = \alpha_0 \frac{\Psi}{\Psi_0} \tag{19.6}$$

where

$$\Psi(T) = \left(1 - \exp\left(-\sum_{k=1}^{m} u_k(T)\delta_k\right)\right) \frac{\prod_{k=1}^{m} \sum_{v_k=v_{0,k}}^{\infty} \frac{(v_k+g_k+|\delta_k|-1)!}{(g_k-1)!v_k!} e^{-u_k(T)v_k}}{\prod_{k=1}^{m} \sum_{v_k=0}^{\infty} \frac{(v_k+g_k-1)!}{(g_k-1)!v_k!} e^{-u_k(T)v_k}} \tag{19.7}$$

$$\Psi_0 = \Psi(T_0) \tag{19.8}$$

$$v_{0,k} = \{0 \text{ for } \delta_k \geq 0, |\delta_k| \text{ for } \delta_k \leq 0 \tag{19.9}$$

$$u_k(T) = hc\eta_k/kT \tag{19.10}$$

and

$$X = \rho_a s \tag{19.11}$$

where

$$\rho_a = \frac{Mp_a}{RT} \tag{19.12}$$

and

$$\omega = \omega_0 \sqrt{\frac{T}{T_0}} \tag{19.13}$$

α_0, δ_k, η_k, g_k, m and ω_0 are obtained from Table 19.1, where v_k are the vibrational quantum numbers, δ_k is the change in vibrational quantum number during transition, and g_k are statistical weights (degeneracy, i.e. the number of ways the transition can occur) for the transition. $T_0 = 100$ K and s is the optical path length.

To ensure the code for Equations (19.7) and (19.15) remain numerically stable, the mathematical shortcut in Equation (19.14) was substituted into those equations.

$$\sum_{v_k=0}^{\infty} \frac{(v_k + g_k - 1)!}{(g_k - 1)!v_k!} e^{-u_k(T)v_k} = (1 - e^{-u_k(T)})^{-g_k} \tag{19.14}$$

Calculate the Overlap Parameter

To calculate β in Equation (19.2), use Equation (19.15) and Equation (19.17).

$$\Phi(T) = \frac{\left\{\prod_{k=1}^{m} \sum_{v_k=v_{0,k}}^{\infty} \sqrt{\frac{(v_k+g_k+|\delta_k|-1)!}{(g_k-1)!v_k!} e^{-u_k(T)v_k}}\right\}^2}{\prod_{k=1}^{m} \sum_{v_k=v_{0,k}}^{\infty} \frac{(v_k+g_k+|\delta_k|-1)!}{(g_k-1)!v_k!} e^{-u_k(T)v_k}} \tag{19.15}$$

where the parameters required are the same as for Equation (19.15), and where

$$\Phi_0 = \Phi(T_0) \tag{19.16}$$

and

$$P_e = \left[\frac{p}{p_0}\left(1 + (b-1)\frac{p_a}{p}\right)\right]^n \tag{19.17}$$

P_e is the effective pressure which provides the pressure dependence of the line broadening due to collisions between absorbing and non-absorbing particles.

β_0^* (required in Equation (19.2)), b and n can be obtained from Table 19.1, $p_0 = 101325$ Pa and p_a is the partial pressure of the gas.

Calculate the Total Band Absorptance

To calculate A^* from Equation (19.3), use E_1 as defined in Equation (19.18).

$$E_1(x) = \int_0^1 \frac{e^{-x/u}}{u}\, du \tag{19.18}$$

Calculate the Total Emissivity

To calculate the total emissivity with Equation (19.5), use Equation (19.19) for the black-body intensity function.

$$I_{b\eta 0} = \frac{2hc_0^2\eta^3}{n^2[e^{hc_0\eta/nkT} - 1]} \tag{19.19}$$

Here, η is is also obtained from Table 19.1, and the refractive index n is set to unity.

19.1.3 Variable Declarations

Table 19.1: EWB model correlation parameters for CO, CO_2 and H_2O.

Band Location λ [μm]	η_c [cm^{-1}]	Vibr. Quantum Step (δ_k)	Pressure Parameters n	Pressure Parameters b	Correlation Parameters α_0 [cm^{-1}/(g/m^2)]	Correlation Parameters β_0^*	Correlation Parameters ω_0 [cm^{-1}]
H_2O $m = 3, \eta_1 = 3652\,\text{cm}^{-1}, \eta_2 = 1595\,\text{cm}^{-1}, \eta_3 = 3756\,\text{cm}^{-1}, g_k = (1,1,1)$							
71 μm	$\eta_c = 140\,\text{cm}^{-1}$	$(0,0,0)$	1	$8.6\sqrt{\frac{T_0}{T}} + 0.5$	5.455	0.143	69.3
6.3 μm	$\eta_c = 1600\,\text{cm}^{-1}$	$(0,1,0)$	1	$8.6\sqrt{\frac{T_0}{T}} + 0.5$	41.2	0.094	56.4
2.7 μm	$\eta_c = 3760\,\text{cm}^{-1}$	$(0,2,0)$ $(1,0,0)$ $(0,0,1)$	1	$8.6\sqrt{\frac{T_0}{T}} + 0.5$	0.2 2.3 23.4	0.132	60.0
1.87 μm	$\eta_c = 5350\,\text{cm}^{-1}$	$(0,1,1)$	1	$8.6\sqrt{\frac{T_0}{T}} + 0.5$	3.0	0.082	43.1
1.38 μm	$\eta_c = 7250\,\text{cm}^{-1}$	$(1,0,1)$	1	$8.6\sqrt{\frac{T_0}{T}} + 0.5$	2.5	0.116	32.0
CO_2 $m = 3, \eta_1 = 1351\,\text{cm}^{-1}, \eta_2 = 666\,\text{cm}^{-1}, \eta_3 = 2396\,\text{cm}^{-1}, g_k = (1,2,1)$							
15 μm	$\eta_c = 667\,\text{cm}^{-1}$	$(0,1,0)$	0.7	1.3	19.0	0.062	12.7
10.4 μm^d	$\eta_c = 960\,\text{cm}^{-1}$	$(-1,0,1)$	0.8	1.3	2.47×10^{-9}	0.040	13.4
9.4 μm^d	$\eta_c = 1060\,\text{cm}^{-1}$	$(0,-2,1)$	0.8	1.3	2.48×10^{-9}	0.119	10.1
4.3 μm	$\eta_c = 2410\,\text{cm}^{-1}$	$(0,0,1)$	0.8	1.3	110.0	0.247	11.2
2.7 μm	$\eta_c = 3660\,\text{cm}^{-1}$	$(1,0,1)$	0.65	1.3	4.0	0.133	23.5
2.0 μm	$\eta_c = 5200\,\text{cm}^{-1}$	$(2,0,1)$	0.65	1.3	0.060	0.393	34.5
CO $m = 1, \eta_1 = 2143\,\text{cm}^{-1}, g_1 = 1$							
4.7 μm	$\eta_c = 2143\,\text{cm}^{-1}$	(1)	0.8	1.1	20.9	0.075	25.5
2.35 μm	$\eta_c = 4260\,\text{cm}^{-1}$	(2)	0.8	1.0	0.14	0.168	20.0

19.1.4 Assumptions

The EWB model by Edwards and Menard (1964) and Felske and Tien (1974) assumes the following.

1. It is assumed that the real spectral lines of the molecules are not equally spaced and not of equal strength, but rather that they are randomly spaced and of random strength.

2. It is assumed that the gas is enclosed in an enclosure that have perfectly black walls and that there are no scattering particles present.
3. The spectral band decrease exponentially at the sides, hence the name 'Exponential Wide Band Model'.

19.1.5 Model Validation

The model is only used and therefore validated for CO. Gas mixtures will be considered in Section 19.2.

The EWB model implemented in auxi-mpp was validated for the range shown in Table 19.2.

Table 19.2: EWB model by Edwards and Menard (1964) and Felske and Tien (1974) Validation Ranges

Model	Systems	Composition	Temperature (K)	Pressure (Pa)	Pressure Path Length (Pa m)
Unary	CO	zero partial pressure	$298 - 3000$	100000	$843 - 375300$

In Figure 19.1 the model by Edwards and Menard (1964) and Felske and Tien (1974) presented here are tested against standard total emissivities provided by Alberti et al. (2018). Since the literature data is not said to be produced by the same model that we are testing here, we should not expect an exact match.

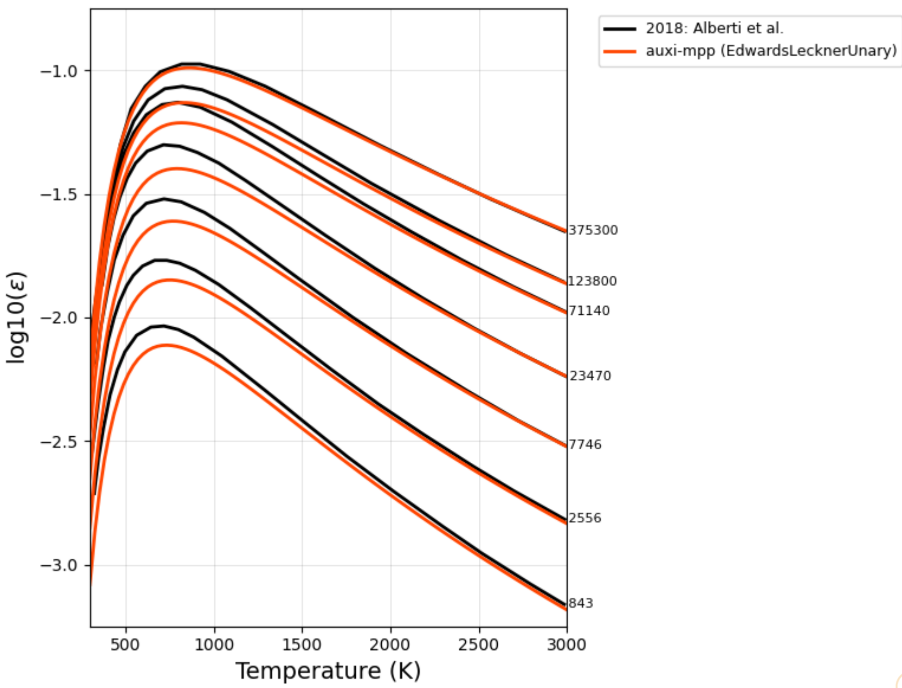

Figure 19.1: Standard total emissivity of CO at 100 000 Pa. Pressure length indicated on the graph are in units of Pa m

Issues

There is a significant amount of deviation from the literature values in the region of 300 to 1300 K. The reason for this deviation is suspected to be due to a different model used by Alberti et al. (2018) to generate the literature data, than we implemented here.

19.2 Chart Model

A correlation chart model developed by Leckner (1972).

19.2.1 Model Overview

This model is a correlation chart model, where a polynomial was fitted to integrated experimental spectral data. Emissivities are therefore not computed for individual bands, as with wide band models. This model have only been developed for H_2O and CO_2 gas mixtures. And it should also be noted that Leckner (1972) developed this chart model only for temperatures above 400 K.

19.2.2 Model Formulation

To get the total emissivity of species i, the zero-partial-pressure emissivity, ϵ_{0i}, is scaled as in Equation (19.20)

$$\epsilon_i = \epsilon_{0i} \left(\frac{\epsilon}{\epsilon_0} \right)_i \tag{19.20}$$

where ϵ_{0i} is given by Equation (19.21);

$$\epsilon_0 = \exp\left[\sum_{i=0}^{M} \sum_{j=0}^{N} c_{ji} \left(\frac{T}{T_0} \right)^j \left(\log_{10} \frac{p_a L}{(p_a L)_0} \right)^i \right] \tag{19.21}$$

and the scaling factor is given by Equation (19.22);

$$\left(\frac{\epsilon}{\epsilon_0} \right)_i = 1 - \frac{(a-1)(1-P_E)}{a+b-1+P_E} \exp\left[-c \left[\log_{10} \frac{(p_a L)_m}{p_a L} \right]^2 \right] \tag{19.22}$$

When estimating the total emissivity of a $CO_2 - H_2O$ gas mixture, the contributions of the individual gases are summed together and overlap between spectral bands of the two species is subtracted as in Equation (19.23).

$$\epsilon_{\mathrm{CO_2+H_2O}} = \epsilon_{\mathrm{CO_2}} + \epsilon_{\mathrm{H_2O}} - \Delta\epsilon_{\mathrm{CO_2\text{-}H_2O}} \tag{19.23}$$

The amount of overlap is estimated with Equation (19.24).

$$\Delta\epsilon_{\mathrm{CO_2\text{-}H_2O}} = \left[\frac{\zeta}{10.7 + 101\zeta} - 0.0089\zeta^{10.4} \right] \left(\log_{10} \frac{(p_{\mathrm{H_2O}} + p_{\mathrm{CO_2}})L}{(p_a L)_0} \right)^{2.76} \tag{19.24}$$

where

$$\zeta = \frac{p_{H_2O}}{p_{H_2O} + p_{CO_2}} \tag{19.25}$$

19.2.3 Variable Declarations

Table 19.3: Chart model correlation parameters for H_2O and CO_2.

Gas	H_2O			CO_2			
M, N	$2, 2$			$2, 3$			
$c_{00} \quad \cdots \quad c_{N0}$	-2.2118	-1.1987	0.035596	-3.9893	2.7669	-2.1081	0.39163
$\vdots \quad \vdots \quad \vdots$	0.85667	0.93048	-0.14391	1.2710	-1.1090	1.0195	-0.21897
$c_{0M} \quad \cdots \quad c_{NM}$	-0.10838	-0.17156	0.045915	-0.23678	0.19731	-0.19544	0.044644
P_E	$(p + 2.56 p_a/\sqrt{t})/p_0$			$(p + 0.28 p_a)/p_0$			
$(p_a L)_m/(p_a L)_0$	$13.2t^2$			$\begin{cases} 0.054/t^2, & t < 0.7 \\ 0.225t^2, & t > 0.7 \end{cases}$			
a	$\begin{cases} 2.144, & t < 0.75 \\ 1.888 - 2.053\log_{10} t, & t > 0.75 \end{cases}$			$1 + 0.1/t^{1.45}$			
b	$1.10/t^{1.4}$			0.23			
c	0.5			1.47			
$T_0 = 1000$ K, $p_0 = 100000$ Pa, $t = T/T_0$, $(p_a L)_0 = 1000$ Pa m							

19.2.4 Model Validation

In this section, we present validation figures for the Leckner (1972) chart model as well as that for mixtures of CO, CO_2 and H_2O. In such mixtures, the EWB model is used for the contribution of CO, and the chart model is used for that of CO_2 and H_2O.

The systems tested are summarised in Table 19.4

Table 19.4: Systems for which the total emissivity models are validated in this section.

Model	Systems	Composition	Temperature (K)	Pressure (Pa)	Pressure Path Length (Pa m)
Unary	CO_2	zero partial pressure	$298 - 2500$	100000	$50 - 100000$
	H_2O	zero partial pressure	$298 - 2500$	100000	$500 - 400000$
Binary	$CO_2 - H_2O$	$x_{CO_2} = 0.3, x_{H_2O} = 0.4$	$298 - 3000$	101325	$100 - 1000000$
	$CO_2 - H_2O$	$x_{CO_2} = 0.3, x_{H_2O} = 0.4$	$298 - 3000$	40×101325	$100 - 1000000$
Ternary	$CO - CO_2 - H_2O$	$x_{CO} = 0.3, x_{CO_2} = 0.3, x_{H_2O} = 0.3$	$298 - 2500$	100000	$500 - 500000$

Leckner Chart Model

The literature data obtained from Leckner (1972) shown in Figures 19.2 and 19.3 (black lines) are spectrally integrated emissivities calculated by Leckner. It should be noted that this data is not the performance of Leckner's correlation chart model. Instead, as reported by Modest (2013), Leckner's model has a maximum error of 5% for H_2O and 10% for CO_2 when compared to these spectral integrations.

With that said, Leckner's correlation chart model implemented in auxi-mpp performs as expected for the zero partial pressure limits shown in Figures 19.2 and 19.3, showing a closer correlation for H_2O than for CO_2. Since Leckner only developed his model for temperatures above 400 K, we only show the validation figures from there and upwards.

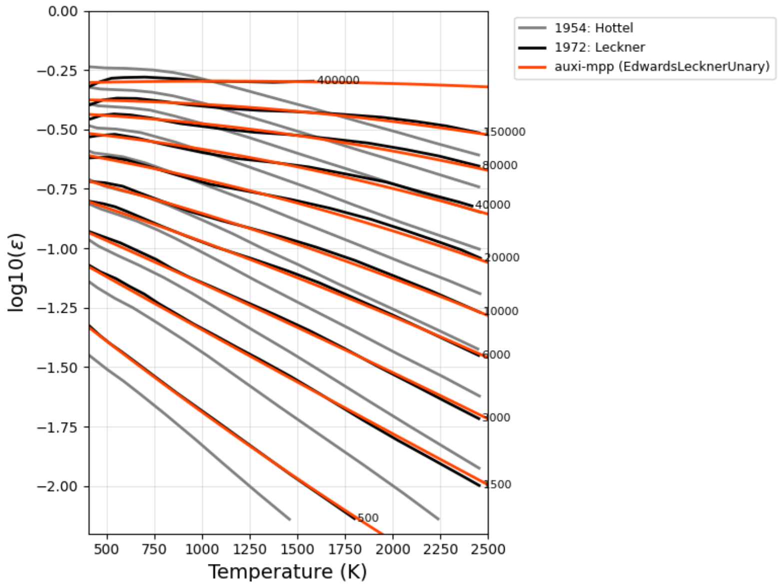

Figure 19.2: Standard total emissivity of H_2O at 100 000 Pa. Pressure length indicated on the graph are in units of Pa m

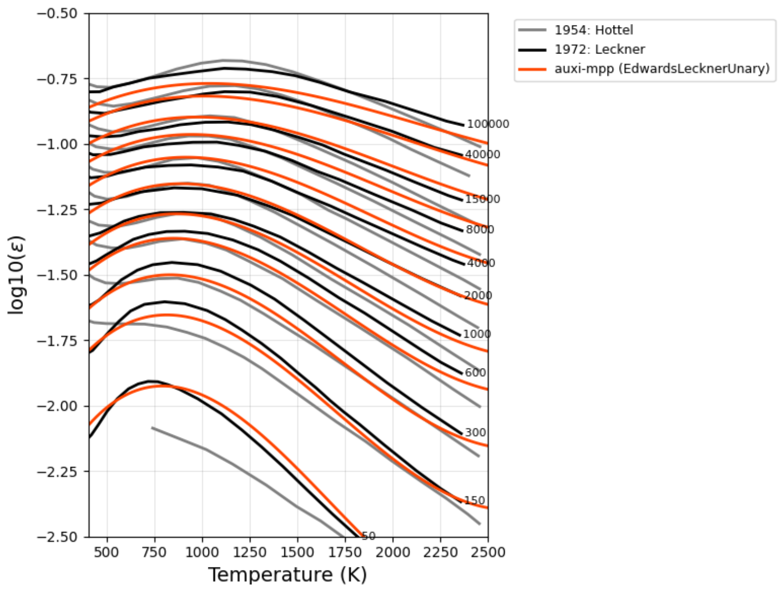

Figure 19.3: Standard total emissivity of CO_2 at 100 000 Pa. Pressure length indicated on the graph are in units of Pa m

For $CO_2 - H_2O$ mixtures, our implementation of Leckner's correlation chart is compared to line-by-line calculations (gray lines) and Leckner's model, both as presented by Alberti et al. (2018), in Figure 19.4. As the performance of Leckner's polynomial, presumably the same one we implemented, are shown here, we expect to see a very close correlation. This is not the case, however. There does seem to be a better correlation at higher pressure, though.

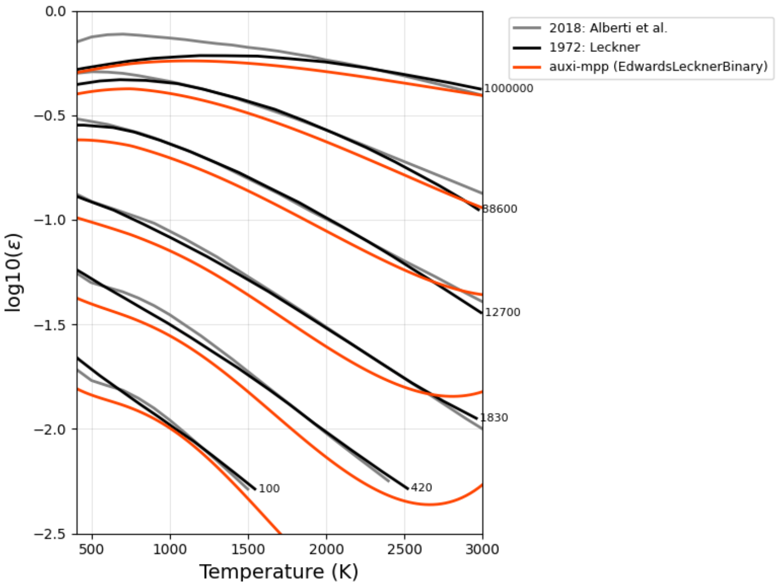

(a) $p = 1$ atm

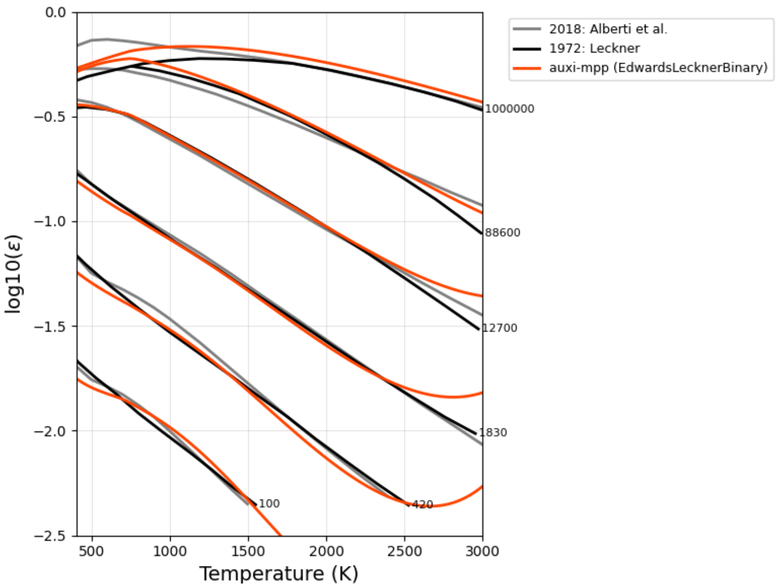

(b) $p = 40$ atm

Figure 19.4: Total emissivity for a 40% mole H_2O, 30% CO_2 gas mixture. Pressure length indicated on the graph are in units of Pa m

Issues

Our implementation of Leckner's chart model does not correspond exactly to the same model's performance presented by Alberti et al. (2018) and we could therefore not validate the model. The reason for this is not clear and will have to be investigated in a future update.

CO, CO_2 and H_2O Mixtures

To estimate emissivities for these mixtures, it is assumed that there is no overlap between CO and either CO_2 or H_2O. If both CO_2 and H_2O are present, Leckner's chart model is used to account for their overlap. The essence of how auxi-mpp handles these mixtures is captured in Equation (19.26).

$$\epsilon_{total} = \epsilon_{\text{CO}}^{\text{EdwardsFelskeTien}} + \epsilon_{\text{CO}_2}^{\text{Leckner}} + \epsilon_{\text{H}_2\text{O}}^{\text{Leckner}} - \Delta\epsilon_{\text{CO}_2\text{-H}_2\text{O}}^{\text{Leckner}} \tag{19.26}$$

Our implementation was compared to the performance of the EXCEL sheet provided by Alberti et al. (2018), which is closely correlated to line-by-line calculations. Overall our model performs adequately for this first iteration, but sees deviations at low as well as at very high temperatures, depending on the pressure path length used.

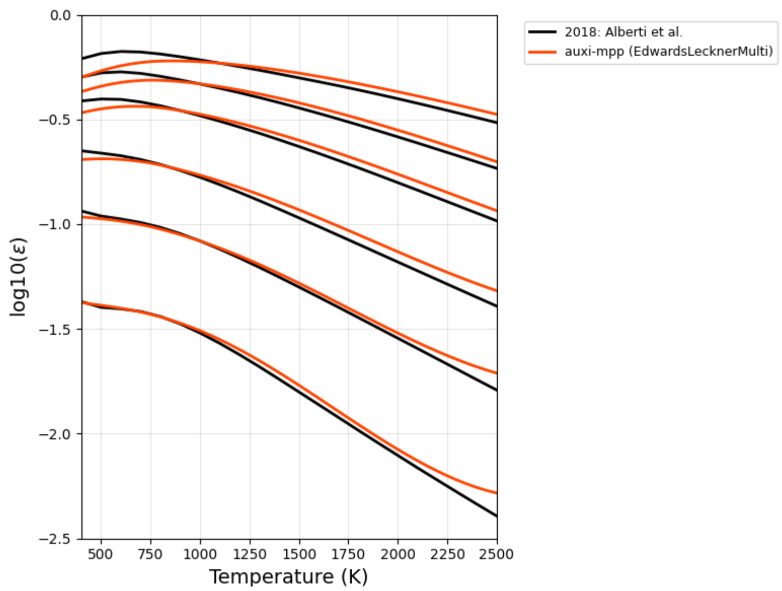

Figure 19.5: Total emissivity vs temperature for a 30% mole CO, 30% CO_2, 30% H_2O gas mixture at 100 000 Pa. Pressure length indicated on the graph are in units of Pa m

Issues

At low temperature and high pressure path length as well as at very high temperatures, our implementation deviate substantially from the EXCEL interpolations provided by Alberti et al. (2018). This will need to be addressed in a future update.

Part V

Appendices

Appendix A

Definitions

The following definitions apply to manual.

EM-MPPF means the Ex Mente Material Physical Property Framework.

EM-MPP-STK means the Ex Mente Material Physical Property Simulation Toolkit, which is a Python package.

EM-AMDF refers to the Ex Mente Accelerated Material Description Framework.

The Slag Sub-package means a sub-package of EM-MPP-STK that contains slag physical property models and their parameters and the necessary documentation.

REF processes means Reducing Electric Furnace processes.

REF-MPP means Reducing Electric Furnace Material Physical Property.

MQM means Modified Quasichemical Model

ChemApp for Python means the ChemApp for Python package for computational thermochemistry owned by GTT-Technologies.

FactSage means the FactSage suite for computational thermochemistry owned by GTT-Technologies.

auxi-mpp is the python package containing all material pysical property models, where 'auxi' means help, and 'mpp' means material physical properties.

References

Alberti, M., R. Weber, and M. Mancini (Jan. 1, 2018). “Overlap Corrections for Emissivity Calculations of H2O“CO2“CO“N2 Mixtures”. In: *Journal of Quantitative Spectroscopy and Radiative Transfer* 205, pp. 230–240. ISSN: 0022-4073. DOI: 10.1016/j.jqsrt.2017.10.005. URL: https://www.sciencedirect.com/science/article/pii/S002240731730609X (visited on 11/19/2025).

Assael, M. J., J.-A. M. Assael, M. L. Huber, R. A. Perkins, and Y. Takata (July 26, 2011). “Correlation of the Thermal Conductivity of Normal and Parahydrogen from the Triple Point to 1000 K and up to 100 MPaa)”. In: *Journal of Physical and Chemical Reference Data* 40.3, p. 033101. ISSN: 0047-2689. DOI: 10.1063/1.3606499. URL: https://doi.org/10.1063/1.3606499 (visited on 09/30/2025).

Assael, M. J., I. J. Armyra, J. Brillo, S. V. Stankus, J. Wu, and W. A. Wakeham (July 2012a). “Reference Data for the Density and Viscosity of Liquid Cadmium, Cobalt, Gallium, Indium, Mercury, Silicon, Thallium, and Zinc”. In: *Journal of Physical and Chemical Reference Data* 41.3, p. 033101. ISSN: 0047-2689. DOI: 10.1063/1.4729873. (Visited on 08/05/2025).

Assael, M. J., K. Kakosimos, R. M. Banish, J. Brillo, I. Egry, R. Brooks, P. N. Quested, K. C. Mills, A. Nagashima, Y. Sato, and W. A. Wakeham (Mar. 2006). “Reference Data for the Density and Viscosity of Liquid Aluminum and Liquid Iron”. In: *Journal of Physical and Chemical Reference Data* 35.1, pp. 285–300. ISSN: 0047-2689, 1529-7845. DOI: 10.1063/1.2149380. (Visited on 07/30/2025).

Assael, M. J., A. E. Kalyva, K. D. Antonia, R. M. Banish, I. Egry, J. Wu, E. Kaschnitz, and W. A. Wakeham (Aug. 2012b). “Reference Data for the Density and Viscosity of Liquid Antimony, Bismuth, Lead, Nickel and Silver.” In: *High Temperatures - High Pressures* 41.3, pp. 161–184. ISSN: 0018-1544. (Visited on 08/05/2025).

Assael, M. J., A. E. Kalyva, K. D. Antoniadis, R. Michael Banish, I. Egry, J. Wu, E. Kaschnitz, and W. A. Wakeham (Sept. 2010). “Reference Data for the Density and Viscosity of Liquid Copper and Liquid Tin”. In: *Journal of Physical and Chemical Reference Data* 39.3, p. 033105. ISSN: 0047-2689, 1529-7845. DOI: 10.1063/1.3467496. (Visited on 08/05/2025).

Brillo, J. and I. Egry (July 2003). “Density Determination of Liquid Copper, Nickel, and Their Alloys”. In: *International Journal of Thermophysics* 24.4, pp. 1155–1170. ISSN: 1572-9567. DOI: 10.1023/A:1025021521945. (Visited on 07/07/2025).

Brillo, J., I. Egry, and T. Matsushita (Nov. 2006). "Density and Surface Tension of Liquid Ternary Ni–Cu–Fe Alloys". In: *International Journal of Thermophysics* 27.6, pp. 1778–1791. ISSN: 1572-9567. DOI: 10.1007/s10765-006-0121-7. (Visited on 07/10/2025).

Brillo, J. and I. Egry (Aug. 2004). "Density and Excess Volume of Liquid Copper, Nickel, Iron, and Their Binary Alloys". In: *International Journal of Materials Research* 95.8, pp. 691–697. ISSN: 2195-8556. DOI: 10.1515/ijmr-2004-0128. (Visited on 07/07/2025).

Brosh, E., A. Pelton, and S. Decterov (May 2012). "A Model to Calculate the Viscosity of Silicate Melts. Part IV: Borosilicate Melts Containing Alkali Metals". In: *International Journal of Materials Research (formerly Zeitschrift fuer Metallkunde)* 103, p. 537. DOI: 10.3139/146.110639.

Burgess Jr., D. R. (Feb. 2024). *Self-Diffusion and Binary-Diffusion Coefficients in Gases*. Tech. rep. NIST TN 2279. Gaithersburg, MD: National Institute of Standards and Technology (U.S.), NIST TN 2279. DOI: 10.6028/NIST.TN.2279. (Visited on 10/06/2025).

Cagran, C., T. HÃ¼pf, G. Pottlacher, and G. LohÃ¶fer (Dec. 1, 2007). "High-Temperature Metallic Melts " Resistivity Intercomparison for Space Applications". In: *International Journal of Thermophysics* 28.6, pp. 2176–2187. ISSN: 1572-9567. DOI: 10.1007/s10765-007-0245-4. URL: https://doi.org/10.1007/s10765-007-0245-4 (visited on 08/11/2025).

Chikova, O. A., N. I. Sinitsin, and V. V. V™yukhin (Oct. 1, 2021). "Electrical Resistivity of Liquid Fe"Mn Alloys". In: *Russian Physics Journal* 64.6 (6), pp. 1039–1046. ISSN: 1573-9228. DOI: 10.1007/s11182-021-02426-y. URL: https://link.springer.com/article/10.1007/s11182-021-02426-y (visited on 08/05/2025).

Chung, T. H., M. Ajlan, L. L. Lee, and K. E. Starling (1988). *Generalized Multiparameter Correlation for Nonpolar and Polar Fluid Transport Properties*. ACS Publications. DOI: 10.1021/ie00076a024. URL: https://pubs.acs.org/doi/pdf/10.1021/ie00076a024 (visited on 10/08/2025).

Chung, T. H., L. L. Lee, and K. E. Starling (1984). *Applications of Kinetic Gas Theories and Multiparameter Correlation for Prediction of Dilute Gas Viscosity and Thermal Conductivity*. ACS Publications. DOI: 10.1021/i100013a002. URL: https://pubs.acs.org/doi/pdf/10.1021/i100013a002 (visited on 10/08/2025).

Clapeyron, É. (1834). *Mémoire Sur La Puissance Motrice de La Chaleur*. (Visited on 12/10/2025).

Crusius, J.-P., R. Hellmann, J. C. Castro-Palacio, and V. Vesovic (June 2018). "*Ab Initio* Intermolecular Potential Energy Surface for the CO2—N2 System and Related Thermophysical Properties". In: *The Journal of Chemical Physics* 148.21, p. 214306. ISSN: 0021-9606, 1089-7690. DOI: 10.1063/1.5034347. (Visited on 09/25/2025).

Deng, Y., J. Zhang, and K. Jiao (Sept. 2018). "Viscosity Measurement and Prediction Model of Molten Iron". In: *Ironmaking & Steelmaking* 45.8, pp. 773–777. ISSN: 0301-9233. DOI: 10.1080/03019233.2018.1491171. (Visited on 07/30/2025).

Edwards, D. K. and W. A. Menard (May 1, 1964). "Comparison of Models for Correlation of Total Band Absorption". In: *Applied Optics* 3.5, pp. 621–625. ISSN: 2155-3165. DOI: 10.1364/AO.3.000621. URL: https://opg.optica.org/ao/abstract.cfm?uri=ao-3-5-621 (visited on 11/26/2025).

Felske, J. D. and C. L. Tien (Jan. 1, 1974). "A Theoretical Closed Form Expression for the Total Band Absorptance of Infrared-Radiating Gases". In: *International Journal of Heat and Mass Transfer* 17.1, pp. 155–158. ISSN: 0017-9310. DOI: 10.1016/0017-9310(74)90049-0. URL: https://www.sciencedirect.com/science/article/pii/0017931074900490 (visited on 10/22/2025).

Giordanengo, B., N. Benazzi, J. Vinckel, J.-G. Gasser, and L. Roubi (Aug. 1, 1999). "Thermal Conductivity of Liquid Metals and Metallic Alloys". In: *Journal of Non-Crystalline Solids* s 250–252, pp. 377–383. DOI: 10.1016/S0022-3093(99)00268-9.

Grundy, A. N., I.-H. Jung, A. D. Pelton, and S. A. Decterov (2008a). "A Model to Calculate the Viscosity of Silicate Melts. Part II: The NaO0.5–MgO–CaO–AlO1.5–SiO2 System". In: *International Journal of Materials Research* 99.11, pp. 1195–1209. DOI: doi:10.3139/146.101753. (Visited on 08/22/2023).

Grundy, A. N., H. Liu, I.-H. Jung, S. A. Decterov, and A. D. Pelton (2008b). "A Model to Calculate the Viscosity of Silicate Melts. Part I: Viscosity of Binary SiO2–MeOx Systems (Me = Na, K, ca, Mg, Al)". In: *International Journal of Materials Research* 99.11, pp. 1185–1194. DOI: doi:10.3139/146.101752. (Visited on 08/22/2023).

Hellmann, R. (2014). "Ab initio potential energy surface for the carbon dioxide molecule pair and thermophysical properties of dilute carbon dioxide gas". In: *Chemical Physics Letters* 613. -, pp. 133–138. DOI: 10.1016/j.cplett.2014.08.057.

Hellmann, R. (Apr. 2019a). "Cross Second Virial Coefficient and Dilute Gas Transport Properties of the (H2O + CO2) System from First-Principles Calculations". In: *Fluid Phase Equilibria* 485, pp. 251–263. ISSN: 0378-3812. DOI: 10.1016/j.fluid.2018.11.033. (Visited on 09/22/2025).

Hellmann, R. (Dec. 2019b). "First-Principles Calculation of the Cross Second Virial Coefficient and the Dilute Gas Shear Viscosity, Thermal Conductivity, and Binary Diffusion Coefficient of the (H2O + N2) System". In: *Journal of Chemical & Engineering Data* 64.12, pp. 5959–5973. ISSN: 0021-9568. DOI: 10.1021/acs.jced.9b00822. (Visited on 09/25/2025).

Hellmann, R. (Apr. 2020a). "Correction to "First-Principles Calculation of the Cross Second Virial Coefficient and the Dilute Gas Shear Viscosity, Thermal Conductivity, and Binary Diffusion Coefficient of the (H_2O + N_2) System"". In: *Journal of Chemical & Engineering Data* 65.4, pp. 2251–2252. ISSN: 0021-9568, 1520-5134. DOI: 10.1021/acs.jced.0c00248. (Visited on 09/22/2025).

Hellmann, R. (Aug. 2020b). "Reference Values for the Cross Second Virial Coefficients and Dilute Gas Binary Diffusion Coefficients of the Systems (H_2O + O_2) and (H_2O + Air) from

First Principles". In: *Journal of Chemical & Engineering Data* 65.8, pp. 4130–4141. ISSN: 0021-9568, 1520-5134. DOI: 10.1021/acs.jced.0c00465. (Visited on 09/22/2025).

Hellmann, R. (Sept. 2023). "*Ab Initio* Potential Energy Surfaces for the O2–O2 System and Derived Thermophysical Properties". In: *The Journal of Chemical Physics* 159.10, p. 104303. ISSN: 0021-9606, 1089-7690. DOI: 10.1063/5.0166781. (Visited on 09/25/2025).

Hellmann, R. (Mar. 2024). "Cross Second and Third Virial Coefficients and Dilute Gas Transport Properties of the (H_2O + Ar) System from First-Principles Calculations". In: *Journal of Chemical & Engineering Data* 69.3, pp. 942–957. ISSN: 0021-9568, 1520-5134. DOI: 10.1021/acs.jced.3c00677. (Visited on 09/22/2025).

Hellmann, R. and E. Vogel (2015). "The Viscosity of Dilute Water Vapor Revisited: New Reference Values from Experiment and Theory for Temperatures between (250 and 2500) K". In: *Journal of Chemical & Engineering Data* 60.12. -, pp. 3600–3605. DOI: 10.1021/acs.jced.5b00599.

Hirschfelder, J. O. (Feb. 1, 1957). "Heat Conductivity in Polyatomic or Electronically Excited Gases. II". In: *The Journal of Chemical Physics* 26.2, pp. 282–285. ISSN: 0021-9606. DOI: 10.1063/1.1743285. URL: https://doi.org/10.1063/1.1743285 (visited on 10/08/2025).

Hixson, R. S., M. A. Winkler, and M. L. Hodgdon (Oct. 1, 1990). "Sound Speed and Thermophysical Properties of Liquid Iron and Nickel". In: *Physical Review B* 42.10, pp. 6485–6491. DOI: 10.1103/PhysRevB.42.6485. URL: https://link.aps.org/doi/10.1103/PhysRevB.42.6485 (visited on 07/31/2025).

Huber, M. L., R. A. Perkins, D. G. Friend, J. V. Sengers, M. J. Assael, I. N. Metaxa, K. Miyagawa, R. Hellmann, and E. Vogel (Aug. 23, 2012). "New International Formulation for the Thermal Conductivity of H2O". In: *Journal of Physical and Chemical Reference Data* 41.3, p. 033102. ISSN: 0047-2689. DOI: 10.1063/1.4738955. URL: https://doi.org/10.1063/1.4738955 (visited on 09/30/2025).

Huber, M. L., R. A. Perkins, A. Laesecke, D. G. Friend, J. V. Sengers, M. J. Assael, I. N. Metaxa, E. Vogel, R. Mareš, and K. Miyagawa (2009). "New International Formulation for the Viscosity of H2O". In: *Journal of Physical and Chemical Reference Data* 38.2, pp. 101–125.

Huber, M. L., E. A. Sykioti, M. J. Assael, and R. A. Perkins (Feb. 25, 2016). "Reference Correlation of the Thermal Conductivity of Carbon Dioxide from the Triple Point to 1100 K and up to 200 MPa". In: *Journal of Physical and Chemical Reference Data* 45.1, p. 013102. ISSN: 0047-2689. DOI: 10.1063/1.4940892. URL: https://doi.org/10.1063/1.4940892 (visited on 09/30/2025).

Huber, M. L. (2018a). *Models for Viscosity, Thermal Conductivity, and Surface Tension of Selected Pure Fluids as Implemented in REFPROP v10.0*. Interagency/Internal Report (NISTIR). -.

Huber, M. L. (Aug. 20, 2018b). "Models for Viscosity, Thermal Conductivity, and Surface Tension of Selected Pure Fluids as Implemented in REFPROP V10.0". In: *NIST*. URL: https://www.nist.gov/publications/models-viscosity-thermal-conductivity-and-surface-tension-selected-pure-fluids (visited on 11/05/2025).

Hundermark, R. (2003). "The Electrical Conductivity of Melter Type Slags". Master of Engineering, MEng. Cape Town, South Africa: University of Cape Town.

Jimbo, I. and A. W. Cramb (Feb. 1993). "The Density of Liquid Iron-Carbon Alloys". In: *Metallurgical Transactions B* 24.1, pp. 5–10. ISSN: 0360-2141, 1543-1916. DOI: 10.1007/BF02657866. (Visited on 04/12/2023).

Kim, W. Y. (Aug. 2011). "Modeling Viscosity of Molten Slags and Glasses". PhD thesis. École Polytechnique de Montréal. (Visited on 09/11/2024).

Kim, W.-Y., P. Hudon, and I.-H. Jung (Mar. 1, 2021a). "Modeling the viscosity of silicate melts containing Fe oxide: Fe saturation condition". In: *Calphad* 72, p. 102242. ISSN: 0364-5916. DOI: 10.1016/j.calphad.2020.102242. URL: https://www.sciencedirect.com/science/article/pii/S0364591620305058 (visited on 10/18/2024).

Kim, W.-Y., P. Hudon, and I.-H. Jung (Mar. 1, 2021b). "Modeling the viscosity of silicate melts containing Fe oxide: FeO/Fe2O3 containing system". In: *Calphad* 72, p. 102244. ISSN: 0364-5916. DOI: 10.1016/j.calphad.2020.102244. URL: https://www.sciencedirect.com/science/article/pii/S0364591620305071 (visited on 08/22/2023).

Kim, W.-Y., A. D. Pelton, and S. A. Decterov (2012a). "A Model to Calculate the Viscosity of Silicate Melts. Part III: Modification for Melts Containing Alkali Oxides". In: *International Journal of Materials Research* 103.3, pp. 313–328. DOI: doi:10.3139/146.110637. (Visited on 08/22/2023).

Kim, W.-Y., A. D. Pelton, and S. A. Decterov (2012b). "A Model to Calculate the Viscosity of Silicate Melts. Part III: Modification for Melts Containing Alkali Oxides". In: *International Journal of Materials Research* 103.3, pp. 313–328. DOI: doi:10.3139/146.110637. (Visited on 08/22/2023).

Kita, Y. and Z.-i. Morita (Jan. 1, 1984). "The Electrical Resistivity of Liquid Fe-Ni, Fe-Co and Ni-Co Alloys". In: *Journal of Non-Crystalline Solids* 61–62, pp. 1079–1084. ISSN: 0022-3093. DOI: 10.1016/0022-3093(84)90684-7. URL: https://www.sciencedirect.com/science/article/pii/0022309384906847 (visited on 07/07/2025).

Laesecke, A. and C. D. Muzny (2017). "Reference Correlation for the Viscosity of Carbon Dioxide". In: *Journal of Physical and Chemical Reference Data* 46.1. -, p. 013107. DOI: 10.1063/1.4977429.

Leachman, J. W., R. T Jacobsen, S. G. Penoncello, and E. W. Lemmon (Sept. 2009). "Fundamental Equations of State for Parahydrogen, Normal Hydrogen, and Orthohydrogen". In: *Journal of Physical and Chemical Reference Data* 38.3, pp. 721–748. ISSN: 0047-2689, 1529-7845. DOI: 10.1063/1.3160306. (Visited on 11/03/2025).

Leckner, B. (Aug. 1, 1972). "Spectral and Total Emissivity of Water Vapor and Carbon Dioxide". In: *Combustion and Flame* 19.1, pp. 33–48. ISSN: 0010-2180. DOI: 10.1016/S0010-2180(72)80084-1. URL: https://www.sciencedirect.com/science/article/pii/S0010218072800841 (visited on 10/08/2025).

Lemmon, E. W. and R. T. Jacobsen (Jan. 1, 2004). "Viscosity and Thermal Conductivity Equations for Nitrogen, Oxygen, Argon, and Air". In: *International Journal of Thermophysics* 25.1, pp. 21–69. ISSN: 1572-9567. DOI: 10.1023/B:IJOT.0000022327.04529.f3. URL: https://doi.org/10.1023/B:IJOT.0000022327.04529.f3 (visited on 09/30/2025).

Lemmon, E. W. and R. Span (May 2006). "Short Fundamental Equations of State for 20 Industrial Fluids". In: *Journal of Chemical & Engineering Data* 51.3, pp. 785–850. ISSN: 0021-9568, 1520-5134. DOI: 10.1021/je050186n. (Visited on 11/03/2025).

Linstrom, P. J. and W. G. Mallard (Sept. 2001). "The NIST Chemistry WebBook: A Chemical Data Resource on the Internet". In: *NIST* 46.No. 5, pp. 1059–1063. (Visited on 12/09/2025).

Mason, E. A. and S. C. Saxena (Sept. 1, 1958). "Approximate Formula for the Thermal Conductivity of Gas Mixtures". In: *The Physics of Fluids* 1.5, pp. 361–369. ISSN: 0031-9171. DOI: 10.1063/1.1724352. URL: https://doi.org/10.1063/1.1724352 (visited on 10/08/2025).

Mills, K. C., B. J. Monaghan, and B. J. Keene (Jan. 1, 1996). "Thermal Conductivities of Molten Metals: Part 1 Pure Metals". In: *International Materials Reviews* 41.6, pp. 209–242. ISSN: 0950-6608. DOI: 10.1179/imr.1996.41.6.209. URL: https://doi.org/10.1179/imr.1996.41.6.209 (visited on 07/10/2025).

Mills, K. C. (2002). *Recommended Values of Thermophysical Properties for Selected Commercial Alloys*. 1. publ. Cambridge: Woodhead. ISBN: 978-1-85573-569-9 978-0-87170-753-6.

Mizuno, N., S. Kosai, and E. Yamasue (2020). "Applicability of Wiedemann-Franz Law to Thermal Conductivity of Molten Field™s Metal". In: *Materials Science Forum* 985, pp. 1–9. ISSN: 1662-9752. DOI: 10.4028/www.scientific.net/MSF.985.1. URL: https://www.scientific.net/MSF.985.1 (visited on 08/13/2025).

Modest, M. F. (Feb. 1, 2013). *Radiative Heat Transfer*. 3rd. ISBN: 978-0-12-386944-9. URL: https://shop.elsevier.com/books/radiative-heat-transfer/modest/978-0-12-386944-9 (visited on 10/21/2025).

Muzny, C. D., M. L. Huber, and A. F. Kazakov (2013). "Correlation for the Viscosity of Normal Hydrogen Obtained from Symbolic Regression". In: *Journal of Chemical & Engineering Data* 58.4. -, pp. 969–979. DOI: 10.1021/je301273j.

Mysen, B. and P. Richet (2019). *Silicate Glasses and Melts - 2nd Edition*. 2nd. Elsevier. ISBN: 978-0-444-63709-3. URL: https://shop.elsevier.com/books/silicate-glasses-and-melts/mysen/978-0-444-63708-6 (visited on 10/03/2023).

Ntonti, E., S. Sotiriadou, M. J. Assael, M. L. Huber, B. Wilthan, and M. Watanabe (Jan. 2024). "Reference Correlations for the Density and Thermal Conductivity, and Review of the Viscosity Measurements, of Liquid Titanium, Zirconium, Hafnium, Vanadium, Niobium, Tantalum, Chromium, Molybdenum, and Tungsten". In: *International Journal of Thermophysics* 45.2, p. 18. ISSN: 1572-9567. DOI: 10.1007/s10765-023-03305-z. (Visited on 08/05/2025).

Ono, Y., K. Hirayama, and K. Furukawa (1976). "Electric Resistivity of Molten Fe-C, Fe-Si and Fe-C-Si Alloys". In: *Transactions of the Iron and Steel Institute of Japan* 16.3, pp. 153–160. DOI: 10.2355/isijinternational1966.16.153.

Ono, Y. and T. Yagi (1972). "Electric Resistivity of Molten Fe-Ni and Fe-Co Alloys". In: *Transactions of the Iron and Steel Institute of Japan* 12.4, pp. 314–316. DOI: 10.2355/isijinternational1966.12.314.

Poling, B. E., J. M. Prausnitz, and J. P. O'Connell (2001). *The Properties of Gases and Liquids, Fifth Edition*. -. McGraw-Hill.

Rothman, A. J. and L. A. Bromley (1955). *High Temperature Thermal Conductivity of Gases*. ACS Publications. DOI: 10.1021/ie50545a015. URL: https://pubs.acs.org/doi/pdf/10.1021/ie50545a015 (visited on 11/12/2025).

Sasaki, H., A. Ikari, K. Terashima, and S. K. S. Kimura (July 1, 1995). "Temperature Dependence of the Electrical Resistivity of Molten Silicon". In: *Japanese Journal of Applied Physics* 34 (7R), p. 3426. ISSN: 1347-4065. DOI: 10.1143/JJAP.34.3426. URL: https://iopscience.iop.org/article/10.1143/JJAP.34.3426/meta (visited on 08/27/2025).

Schmidt, R. and W. Wagner (Dec. 1985). "A New Form of the Equation of State for Pure Substances and Its Application to Oxygen". In: *Fluid Phase Equilibria* 19.3, pp. 175–200. ISSN: 03783812. DOI: 10.1016/0378-3812(85)87016-3. (Visited on 11/03/2025).

Secco, R. A. (Apr. 1, 2017). "Thermal Conductivity and Seebeck Coefficient of Fe and Fe-Si Alloys: Implications for Variable Lorenz Number". In: *Physics of the Earth and Planetary Interiors* 265, pp. 23–34. ISSN: 0031-9201. DOI: 10.1016/j.pepi.2017.01.005. URL: https://www.sciencedirect.com/science/article/pii/S0031920116301832 (visited on 08/08/2025).

Seydel, U. and W. Fucke (1977). "Sub-microsecond pulse heating measurements of high temperature electrical resistivity of the 3d-transition metals Fe, Co, and Ni". In: *Zeitschrift für Naturforschung A* 32.9, pp. 994–1002. ISSN: 1865-7109. DOI: 10.1515/zna-1977-0913. URL: https://www.degruyterbrill.com/document/doi/10.1515/zna-1977-0913/html (visited on 08/11/2025).

Span, R., E. W. Lemmon, R. T. Jacobsen, W. Wagner, and A. Yokozeki (Nov. 2000). "A Reference Equation of State for the Thermodynamic Properties of Nitrogen for Temperatures from 63.151 to 1000 K and Pressures to 2200 MPa". In: *Journal of Physical and Chemical Reference Data* 29.6, pp. 1361–1433. ISSN: 0047-2689, 1529-7845. DOI: 10.1063/1.1349047. (Visited on 11/03/2025).

Span, R. and W. Wagner (Nov. 1996). "A New Equation of State for Carbon Dioxide Covering the Fluid Region from the Triple-Point Temperature to 1100 K at Pressures up to 800 MPa". In: *Journal of Physical and Chemical Reference Data* 25.6, pp. 1509–1596. ISSN: 0047-2689, 1529-7845. DOI: 10.1063/1.555991. (Visited on 11/03/2025).

Suárez-Iglesias, O., I. Medina, M. D. L. Á. Sanz, C. Pizarro, and J. L. Bueno (Oct. 2015). "Self-Diffusion in Molecular Fluids and Noble Gases: Available Data". In: *Journal of Chemical & Engineering Data* 60.10, pp. 2757–2817. ISSN: 0021-9568, 1520-5134. DOI: 10.1021/acs.jced.5b00323. (Visited on 10/07/2025).

Tegeler, Ch., R. Span, and W. Wagner (May 1999). "A New Equation of State for Argon Covering the Fluid Region for Temperatures From the Melting Line to 700 K at Pressures up to 1000 MPa". In: *Journal of Physical and Chemical Reference Data* 28.3, pp. 779–850. ISSN: 0047-2689, 1529-7845. DOI: 10.1063/1.556037. (Visited on 11/03/2025).

Tesfaye, F. and P. Taskinen (2010). *Densities of Molten and Solid Alloys of (Fe, Cu, Ni, Co)-S at Elevated Temperatures - Literature Review and Analysis*. Aalto University Publications in Materials Science and Engineering. ISBN: 978-952-60-3272-6. (Visited on 07/09/2025).

"Thermodynamics Research Center" (Apr. 2009). In: *NIST*. (Visited on 08/14/2025).

Thibodeau, E. (2014). "Modeling the molar volume and electrical conductivity of oxide melts". MA thesis. Montreal, Canada: McGill University. (Visited on 06/26/2023).

Thibodeau, E. (Feb. 2016). "A structural electrical conductivity model for oxide melts". en. In: *METALLURGICAL AND MATERIALS TRANSACTIONS B* 47, pp. 355–383.

Thibodeau, E., A. E. Gheribi, and I.-H. Jung (2016a). "A Structural Molar Volume Model for Oxide Melts Part I: Li2O-Na2O-K2O-MgO-CaO-MnO-PbO-Al2O3-SiO2 Melts—Binary Systems". In: *Metallurgical and Materials Transactions B* 47.2, pp. 1147–1164. DOI: doi:10.1007/s11663-015-0548-y. (Visited on 06/13/2023).

Thibodeau, E., A. E. Gheribi, and I.-H. Jung (2016b). "A Structural Molar Volume Model for Oxide Melts Part II: Li2O-Na2O-K2O-MgO-CaO-MnO-PbO-Al2O3-SiO2 Melts—Ternary and Multicomponent Systems". In: *Metallurgical and Materials Transactions B* 47.2, pp. 1165–1186. DOI: doi:10.1007/s11663-015-0543-3. (Visited on 06/13/2023).

Thibodeau, E., A. E. Gheribi, and I.-H. Jung (2016c). "A Structural Molar Volume Model for Oxide Melts Part III: Fe Oxide-Containing Melts". In: *Metallurgical and Materials Transactions B* 47.2, pp. 1187–1202. DOI: doi:10.1007/s11663-015-0549-x. (Visited on 06/13/2023).

Wagner, W. and A. Pruß (June 2002). "The IAPWS Formulation 1995 for the Thermodynamic Properties of Ordinary Water Substance for General and Scientific Use". In: *Journal of Physical and Chemical Reference Data* 31.2, pp. 387–535. ISSN: 0047-2689, 1529-7845. DOI: 10.1063/1.1461829. (Visited on 11/03/2025).

Watanabe, M., M. Adachi, M. Uchikoshi, and H. Fukuyama (July 1, 2019). "Thermal Conductivities of Fe-Ni Melts Measured by Non-contact Laser Modulation Calorimetry". In: *Metallurgical and Materials Transactions A* 50.7, pp. 3295–3300. ISSN: 1543-1940. DOI: 10.1007/s11661-019-05250-9. URL: https://doi.org/10.1007/s11661-019-05250-9 (visited on 08/06/2025).

Westenberg, A. A. and N. De Haas (May 1, 1963). "Gas Thermal Conductivity Studies at High Temperature. II. Results for O2 and O2-H2O Mixtures". In: *The Physics of Fluids* 6.5, pp. 617–620. ISSN: 0031-9171. DOI: 10.1063/1.1706789. URL: https://doi.org/10.1063/1.1706789 (visited on 11/12/2025).

Westenberg, A. A. and N. DeHaas (Mar. 1, 1962). "Gas Thermal-Conductivity Studies at High Temperature. Line-Source Technique and Results in N2, CO2, and N2-CO2 Mixtures". In: *The Physics of Fluids* 5.3, pp. 266–273. ISSN: 0031-9171. DOI: 10.1063/1.1706610. URL: https://doi.org/10.1063/1.1706610 (visited on 11/12/2025).

Wilke, C. R. (Apr. 1950). "A Viscosity Equation for Gas Mixtures". In: *The Journal of Chemical Physics* 18.4, pp. 517–519. ISSN: 0021-9606, 1089-7690. DOI: 10.1063/1.1747673. (Visited on 10/28/2025).

Yamasue, E., M. Susa, H. Fukuyama, and K. Nagata (May 1, 2003). "Deviation from Wiedemann"Franz Law for the Thermal Conductivity of Liquid Tin and Lead at Elevated Temperature". In: *International Journal of Thermophysics* 24.3, pp. 713–730. ISSN: 1572-9567. DOI: 10.1023/A:1024088232730. URL: https://doi.org/10.1023/A:1024088232730 (visited on 08/13/2025).

Zhao, A. Z. and J. E. Garay (Oct. 1, 2023). "High Temperature Liquid Thermal Conductivity: A Review of Measurement Techniques, Theoretical Understanding, and Energy Applications". In: *Progress in Materials Science* 139, p. 101180. ISSN: 0079-6425. DOI: 10.1016/j.pmatsci.2023.101180. URL: https://www.sciencedirect.com/science/article/pii/S0079642523001123 (visited on 07/11/2025).

Ziman, J. (2001). *Electrons and Phonons: The Theory of Transport Phenomena in Solids*. International Series of Monographs on Physics. OUP Oxford. 554 pp. ISBN: 978-0-19-850779-6. URL: https://books.google.co.za/books?id=UtEy63pjngsC.

Zytveld, J. B. V. (Aug. 1, 1980). "ELECTRICAL RESISTIVITIES OF LIQUID TRANSITION METALS". In: *Le Journal de Physique Colloques* 41.C8, pp. C8–506. ISSN: 0449-1947, 2777-3418. DOI: 10.1051/jphyscol:19808126. URL: http://dx.doi.org/10.1051/jphyscol:19808126 (visited on 07/31/2025).

Glossaries

Acronyms

BF-BOF Blast Furnace-Basic Oxygen Furnace 2

GGS Groeien met Groen Staal i, 2

MQM Modified Quasichemical Model 4, 10, 12–14, 21, 43, 44, 46, 47, 50

REF Reducing Electric Furnace i, 2, 65

Advancing Through Insight